UNIVERSITÀ
DEGLI STUDI
FIRENZE

DOTTORATO DI RICERCA IN
FISICA E ASTRONOMIA

CICLO XXX

COORDINATORE Prof. Raffaello D'Alessandro

Towards atom interferometry beyond the Standard Quantum Limit with strontium atoms

Settore scientifico disciplinare: FIS/03 Fisica della materia

Dottorando

Leonardo Salvi

Leonardo Salvi

Tutore

Prof. Guglielmo M. Tino

Coordinatore

Prof. Raffaello D'Alessandro

Raffaello D'Alessandro

Anni 2014 / 2017

Contents

Abstract

Atom interferometry is a rapidly developing field that finds applications in both applied and fundamental physics. An atom interferometer can be configured to measure, for example, gravity acceleration, gravity gradients or to test the Einstein Equivalence Principle.

The operation of an atom interferometer relies on its large sensitivity to the measured quantities and on the ability to limit systematic effects.

In this thesis, atom interferometry operating with strontium atoms is presented. The chosen atomic species features an inherent robustness against external perturbations that can seriously affect the measurement accuracy. Moreover, atom interferometry experiments are performed through Bragg diffraction, a method that yields an additional immunity to external perturbations and allows to increase the interferometer area with a corresponding increase in the instrument sensitivity.

Our implementations of atomic interferometry were based on a dipole-allowed and a spin-forbidden atomic transition and demonstrated our ability to successfully manipulate momentum states for inertial measurements.

Besides increasing the interferometer area and limiting systematic effects, the ability to measure the accumulated phase shift poses a fundamental limitation when such experiments are performed with uncorrelated particles.

This barrier, the Standard Quantum Limit, can be overcome by generating entangled atomic states with enhanced phase sensitivity. Many methods for the implementation of such states have been successfully demonstrated. However, as they rely on the atomic internal structure, they cannot be directly implemented for superpositions of momentum states. In this thesis, a method that generates states with enhanced sensitivity is considered that is based on the nondestructive measurement of the Doppler effect due to the different velocities of the momentum components. We show that when the momentum difference is large the method performs as well as other demonstrated methods. When the momentum difference is small, altering the atomic response to the measurement through electromagnetically induced transparency can retrieve the phase sensitivity.

In this thesis we also discuss an experimental setup that allows for the implementation of such squeezed momentum states that involves the enhanced interaction of the measuring

light with the atomic ensemble and show that, with realistic parameters, a phase resolution 100 times better than the Standard Quantum Limit can be attained.

Acknowledgements

Even though I decided to write these acknowledgements, I feel that I will never have the ability to express my full gratitude in words.

The person who motivated me through all my career since I was a bachelor student is my supervisor, Guglielmo Tino. Guglielmo always had the ability to find for me a greater challenge. He was always there for any scientific, personal or recreational discussion. In my opinion, he has been leading our group with wise decisions, great ambitions and formidable strength. I thank him for encouraging me in exploring this new field which scared me in the beginning but is currently my passion. I thank him for taking seriously every crazy idea that comes into my mind and I am very glad that, in these last years, our interaction transformed into a fruitful exchange.

Nicola Poli, though not my supervisor, followed closely my activity throughout my whole PhD. The number of discussions that I had with Nicola approaches infinity as we were together through every problem we were facing. I wish to thank him for his patience when I just wanted to complain and I would like to acknowledge all the technical advice that he has been offering, a neverending resource that presents itself as a continuous flow.

I would like to thank the people contributing to our earlier strontium experiments: Tommaso Mazzoni for his rigorous, constant and pleasant approach to science, Xian Zhang for his calm and for reminding us that a problematic experiment is not the worse thing in life. I acknowledge the latest team of the strontium experiment: Ruben Del Aguila for his funny approach which made every day in the lab very pleasant and Liang Hu with whom I shared many important discussions and tough moments and who is one of the most intense hard workers I met.

My experience at the Massachusetts Institute of Technology was forged by the group of Vladan Vuletić. There I met the greatest concentration of good people and great scientists that I could ever imagine. Vladan is definitely one of the greatest masters in this field, his knowledge spans from the most fundamental to the most technical aspects to all of which he gives equal and great value. I believe that I could spend every day discussing with him about science. His abilities to teach even complicated things in a simple way to anyone, to encourage people and to never surrender despite all the difficulties will always be a model to me. I hope that I can transmit at least a fraction of what he gave me

to future promising minds. I am very glad that our interaction reached a considerable symbiosis and I hope that it will only become stronger in time.

I owe a lot to Boris Braverman and Akio Kawasaki who welcomed me in their lab at MIT. I thank Boris for all the moments spent together in trying to reduce the noise of *our favorite laser*, making every instant as pleasant and funny as it was. I thank Akio for his patience in explaining to me all the things I needed to know in the Yb lab.

I thank my mother Paola and my father Sergio for raising me and making me the person I am. My mother assisted me in all the hard and good moments and put her biggest effort in the most important things for our family. Through all the movies that I watched with my father, he was able to form my personal views of humanity. Every artistic discussion with him makes me grow. I am grateful to my sister Margherita, one of the most sensitive and profound people in the world.

My dearest friend Alessio is a constant resource for me. Through all those discussions about science and art, through all those wonderful meals accompanied by our favorite wine and our favorite whiskey and through the climbing woods, we shared all our best moments in life.

There are no words that can express how grateful I am to Giulia. She has always been there for me. Her love and passion for our relationship exceeds all imagination. Despite all the stressing moments in our six years, our connection does not show a single scratch, a unique feature that makes me look forward to more moments spent together. I hope that I have been able to return all the greatest love that she offers.

I trust that my grandparents Ilaria and Francesco would be proud.

Chapter 1

Introduction

Atom interferometers are devices that convert an accumulated phase difference between two separate arms into a measurable population difference [1, 2]. The interferometer can be arranged in such a way that the inferred phase difference carries valuable information about important fundamental interactions. In this way, a large class of inertial measurements can be performed, including the measurement of gravity acceleration [3, 4], gravity gradients [5, 6], gravity curvature [7] and rotations [8, 9]. The applications of such devices span from inertial navigation [10] to the precision measurement of fundamental constants such as the fine structure constant [11, 12] and the Newtonian gravitational constant [13, 14, 15]. Because of the ability to sense gravitational fields, atom interferometers are excellent candidates for tests of General Relativity [16] and in particular of the Einstein Equivalence Principle [17, 18, 19, 20, 21].

Valuable insight into the main features of atom interferometers can be gained by considering the Mach-Zehnder atom interferometer. In its optical counterpart, this interferometer is formed by beam splitters and mirrors that serve to split, reflect and recombine a laser beam. In order to implement the atomic version, it is necessary to realize the equivalent of these optical elements. This is realized by exploiting the interaction of laser radiation with the atomic wavepackets. In particular, through photon absorption and stimulated emission processes, it is possible to transfer momentum to an atomic wavepacket. By tuning the strength and duration of such laser interaction, it is possible to induce coherent superpositions of momentum states, thus building a beam splitter for matter waves. Similarly, the interaction can induce a complete inversion between one momentum state and the other, thus realizing a mirror [22]. The accumulated phase shift is reflected, at the interferometer output, as an interference fringe in the population difference between momentum states. The optical elements can be combined so as to form an atomic Mach-Zehnder interferometer. In a uniform gravitational field with acceleration g, the accumulated phase shift is given by

$$\Phi = k_{\text{eff}} g T^2, \tag{1.1}$$

where k_{eff} is the effective wavenumber of the laser fields that realize the beam splitters and mirrors and is proportional to the momentum transferred to the atoms and T is the time interval between the laser pulses. This equation shows that the accumulated phase shift is linked to gravity's acceleration through the factor $k_{\text{eff}}T^2$, which can be made considerably large when the interaction involves optical photons and the interferometer time is on the order of 100 ms. Equation (1.1) somehow summarizes the main efforts in the field of atom interferometry for inertial measurements. Increasing the wavenumber k_{eff} translates to the implementation of Large Momentum Transfer techniques [23]. Increasing the interaction time T, on the other hand, requires that the coherence of the atomic wavepacket is maintained over the duration of the interferometer so as to preserve the fringe contrast.

In an ideal world, the phase Φ is sensitive to gravity's acceleration only. Unfortunately, this is not the case in real experiments, where many perturbing sources of uncertainty are present. Sources of systematic and poorly measurable errors are external electromagnetic fields that couple to the atomic internal and external dynamics. For this aspect, in particular, there is substantial room for improvement. Indeed, by arranging the interferometer in a suitable way, it is possible to largely suppress these sources of uncertainty.

In our work, we explored an atomic species that is potentially immune to these effects: atomic strontium. In its ground state, bosonic strontium lacks any form of angular momentum, a condition that largely reduces the effects of electromagnetic perturbations in inertial measurements. Moreover, the ^{88}Sr isotope is highly insensitive to s-wave cold collisions, a property that enables long coherence times in atom interferometers.

Laser cooling and manipulation of atomic strontium has become, over the years, a technologically achievable task. Most of the interest is motivated by the availability of a highly stable, ultra-narrow optical transition that constitutes one of the prime candidates for neutral atom-based optical clocks [24, 25].

In this dissertation, the ability to perform atom interferometry with large momentum transfer beam splitters based on Bragg diffraction is established for two optical transitions, a broad dipole-allowed and a narrow intercombination transition. The development of the necessary atom optics tools is discussed and a proof-of-principle implementation of a gravimeter and of a gradiometer is presented.

Another aspect connected to Equation (1.1) is the ability to measure the phase shift Φ. Because a phase shift does not correspond to a physical observable, it can only be *estimated* [26]. An interferometer is *the* process through which this parameter is estimated by conversion to a physically measurable quantity, in our case, the population difference. The process that maps the relative phase into a population difference is inherently affected by a fundamental noise source, the quantum projection noise [27]. This source of uncertainty arises when, after the final beam splitter of the interferometer, the relative population is measured. In general, the output of the interferometer will consist of a set of atoms in a superposition $|\psi\rangle = a_{\downarrow}|{\downarrow}\rangle + a_{\uparrow}|{\uparrow}\rangle$, where $|{\uparrow}\rangle$ and $|{\downarrow}\rangle$ are the two states of the

interferometer and the amplitudes $a_\downarrow$ and $a_\uparrow$ are related to the phase shift Φ[1]. After performing a projective measurement of the population, the state $|\downarrow\rangle$ is measured with probability $|a_\downarrow|^2$ and the state $|\uparrow\rangle$ is measured with probability $|a_\uparrow|^2$. Therefore, the probabilistic nature of the measurement outcome causes noise in the phase measurement. When the atomic states of an ensemble are uncorrelated, the phase noise variance is the sum of the single-atom variances. Therefore, if the sample is formed by N atoms, the noise variance is proportional to N. On the other hand, the signal is also proportional to the number of atoms. This leads to a signal-to-noise ratio $\sqrt{N}$ and to the Standard Quantum Limit (SQL) in phase measurement resolution:

$$\delta\Phi_{\mathrm{SQL}} = \frac{1}{\sqrt{N}}. \tag{1.2}$$

For the way we formulated this argument, it is clear that this limit, also known as the (atom) shot noise limit, arises because of the absence of correlations between the atomic states of different atoms.

The extreme case where all the particles are correlated induces a formidable improvement in the scaling of the phase resolution with atom number. In such an extreme case, one is left with the noise of a single particle while the results of measurements performed on the remaining $N-1$ particles are perfectly correlated with the first one and therefore do not add noise. As a result, the interferometer phase resolution is given by

$$\delta\Phi_{\mathrm{H}} = \frac{1}{N}, \tag{1.3}$$

known as the Heisenberg limit [28].

Our reasoning leads to connect any improvement beyond the SQL to the presence of correlations or multiparticle entanglement in the atomic ensemble.

Research in the field of entanglement has produced various exciting results and several methods have been studied that can generate such correlated states [26, 29]. Among these, the methods that achieve sub-shot noise sensitivity by optical means gained considerable interest [30, 31]. Indeed, they can generate entanglement between distant atoms and therefore do not require high densities that may lead to systematic effects and coherence loss in precision measurements. In the considerable variety of entangled states, criteria that identify those that yield sub-shot noise phase sensitivity have been found. Inside this selected class, spin squeezed states are found to be induced in a number of ways and feature a relatively high robustness. In comparison, the maximally entangled states that yield a phase resolution at the Heisenberg limit, are extremely fragile and their implementation in systems with large number of particles is a long-standing goal.

Among the optical methods, spin squeezed states can be generated by effective nonlinear interactions mediated by light, by transfer of squeezing from light to the atoms or by quantum nondemolition measurements.

[1]The amplitudes are assumed to fulfill the normalization condition $|a_\downarrow|^2 + |a_\uparrow|^2 = 1$.

In this thesis we will mainly focus on measurement-induced spin squeezing. From the above discussion, it would appear that the measurement process constitutes the *problem* rather than the *solution* of noise reduction. However, depending on how a measurement is performed, a wide variety of states can be generated [32, 33]. This process is ultimately due to the fact that the measurement of an observable projects the state into an eigenstate of that observable. Entanglement generation in this case relies on the measurement of a collective variable. After the measurement of a collective variable, squeezing is conditioned to the measurement outcome, because the particular final state is produced in a probabilistic fashion. This means that the outcome cannot be discarded and that it should provide as much information as possible about the induced state. In particular, this requires a large signal-to-noise ratio and a large correlation between the outcome and the state that is actually produced. The first requirement is satisfied when the optical depth of the atomic ensemble is large [34]. The second requirement, on the other hand, is fulfilled if the measurement process does not alter the state in an unpredictable way. Both requirements are fulfilled when the measuring light is passed multiple times through the ensemble, a situation that is achieved in an optical resonator.

Many correlated atomic states can be generated through cavity-enhanced collective measurements [32]. However, to our knowledge, all the methods that induce spin squeezing in atomic ensembles rely on the internal electronic structure. When implementing atom interferometers that are robust against external perturbations, it is desirable to operate the beam splitters and mirrors on transitions that largely suppress these effects. The states that are coupled by atomic Bragg diffraction from a standing-wave meet this requirement as they only differ by their external motion. As a result, the squeezing methods developed up to date are not directly applicable to this case.

In this thesis we propose a probing scheme that is able to resolve the collective population difference between two momentum states through the Doppler effect. The measurement is sensitive to the population difference rather than the population sum as long as the probe operates on a transition that is narrow compared to the Doppler effect. The strontium atom is one of the few species that enables this kind of measurement thanks to the presence of a narrow optical transition. The proposed scheme reaches its optimum performance for large momentum transfer beam splitters and is therefore compatible with state-of-the-art technology. When large momentum transfer cannot be attained, the method can be extended by adding a feature that alters the atomic response in order to simulate the case where the momentum transfer is large. With this addition, our method becomes applicable to a wider variety of atomic species.

This thesis is structured as follows.

In Chapter 2 we elaborate a model for the atom interferometer that describes the dynamics and the spin squeezed states in a single representation. The Standard Quantum Limit of phase estimation is introduced and its relation to uncorrelated states is discussed.

States with enhanced phase sensitivity compared to the shot noise limit are introduced and their relation to entanglement is illustrated. After identifying the squeezed states among all others, the methods for their generation are discussed and some of the numerous experimental achievements are reviewed.

Chapter 4 considers the first step in the implementation of a squeezed strontium atom interferometer i.e. the realization of the beam splitters and mirrors. The theory of Bragg diffraction as opposed to Raman transitions is reviewed and our experimental results are reported.

In Chapter 5 our proposal for squeezing of momentum state superpositions is illustrated with particular reference to the strontium atom. The main theoretical tools are derived in a way that is directly linked to the experimental situation considered where the squeezing measurement is enhanced by an optical cavity. The attainable squeezing is studied in relation to the fundamental limitation related to scattering of photons in free space. A method that alters the atomic response in order to effectively enhance the measurement signal-to-noise ratio through electromagnetically induced transparency is illustrated.

Chapter 6 reports our first efforts in the realization of a setup that can combine Bragg diffraction and squeezing in strontium atoms. A design of the optical resonator that meets the requirements of this experiment is illustrated. The first experimental investigations on the cavity mirrors are reported and the implementation of a laser system for atomic cooling and trapping is presented.

Chapter 2

Spin squeezing in atom interferometry

In this Chapter we will begin by defining a simple even though quite general model of an atom interferometer [1, 2]. We will see that, when the interferometer operates with uncorrelated states, its performance limits are set by the Standard Quantum Limit. Overcoming this limit then requires the generation of correlated or *entangled* states. We will show that these states can be implemented in a number of ways. Finally, we will discuss the main challenges in the implementation of a matter-wave interferometer operating beyond the Standard Quantum Limit.

2.1 A model for the atom interferometer

An interferometer is a device that converts an accumulated phase shift between two separate arms into a measurable population difference between two states. The main goal of an interferometric measurement is the estimation of this phase shift. This can in turn be connected to fundamental and basic physical interactions. Interferometers based on neutral atoms, for example, couple to inertial fields. For a suitable setup, the interferometer phase shift can be made proportional to gravity's acceleration [3, 35].

Every atomic sensor, being an interferometer that measures inertial or electromagnetic fields, or a clock, takes advantage of this conversion between a phase shift and a population difference.

The two arms of the interferometer can be associated with the states $|\uparrow\rangle$ and $|\downarrow\rangle$ of a two-level system, described by a pseudo-spin operator $\hat{\boldsymbol{S}}$. The states $|\uparrow\rangle$ and $|\downarrow\rangle$ are eigenstates of the operator $\hat{S}_z = (|\uparrow\rangle\langle\uparrow| - |\downarrow\rangle\langle\downarrow|)/2$:

$$\hat{S}_z |\downarrow\rangle = -\frac{1}{2} |\downarrow\rangle , \hat{S}_z |\uparrow\rangle = +\frac{1}{2} |\uparrow\rangle . \tag{2.1}$$

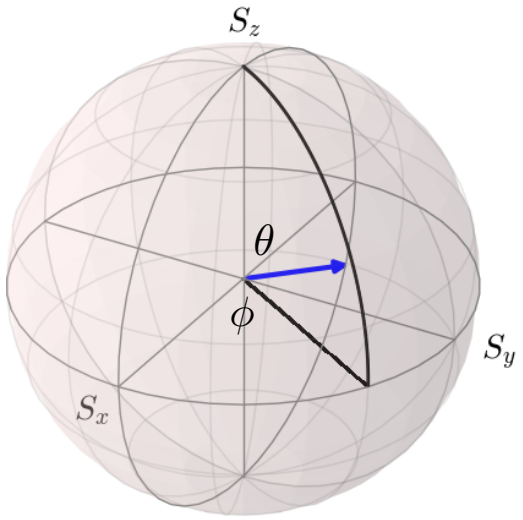

Figure 2.1: Representation of the atomic state of a two-level system on the Bloch sphere. The Bloch vector (blue arrow) forms an angle θ with respect to the z-axis and there is an angle ϕ between the projection of the Bloch vector on the xy plane and the x-axis. The coordinates of the point at the tip of the vector are determined by the expectation values of the spin operators $(\langle \hat{S}_x \rangle, \langle \hat{S}_y \rangle, \langle \hat{S}_z \rangle)$.

On the basis of these eigenstates, a general single-particle state can be written as

$$|\psi\rangle = \sin\frac{\theta}{2}\,|\downarrow\rangle + e^{-i\varphi}\cos\frac{\theta}{2}\,|\uparrow\rangle\,. \tag{2.2}$$

Such a state can be represented as a point on the single-particle Bloch sphere as in Fig. 2.1. We will refer to the Bloch vector as the one connecting the center of the sphere and the point representing the state $|\psi\rangle$. This representation yields the interpretation of the angles θ and ϕ that completely characterize the state $|\psi\rangle$. In particular, the angle θ is related to the populations of the two levels, $P_\downarrow = \sin^2\theta/2$ and $P_\uparrow = \cos^2\theta/2$, whereas ϕ is the phase of the superpositions between the states corresponding to the two levels. This representation is useful in describing the evolution of two-level systems, which is simply equivalent to rotations in the Bloch sphere.

We will now consider the main building blocks of an atom interferometer: the interaction with the laser fields that is used to manipulate the particle states and the phase shift.

We consider the specific case of the interaction of a two-level atom with a laser field. We write the atomic state as $|\psi\rangle = a_\downarrow\,|\downarrow\rangle + a_\uparrow\,|\uparrow\rangle$, where $a_{\downarrow,\uparrow}$ are the amplitudes for the two modes $|\uparrow\rangle$ and $|\downarrow\rangle$. If $\hbar\omega_0$ is the energy difference between the two atomic levels,

which we label $|\downarrow\rangle$ and $|\uparrow\rangle$, the unperturbed Hamiltonian of the system can be written as

$$\hat{\mathcal{H}}_0 = \frac{1}{2}\hbar\omega_0\hat{\sigma}_z, \tag{2.3}$$

where $\hat{\sigma}_z = 2\hat{S}_z$ is the Pauli spin operator with the matrix representation

$$\sigma_z = \begin{pmatrix} 1 & 0 \\ 0 & -1 \end{pmatrix}. \tag{2.4}$$

We next consider an interaction term that couples the two atomic levels through an oscillating field with frequency ω and phase ϕ_L, $\hat{\mathcal{H}}_{\text{int}} = 2\hat{\mathcal{H}}^{(0)}_{\text{int}}\cos(\omega t + \phi_L)$ and define the corresponding Rabi frequency

$$\Omega = 2\frac{|\langle\uparrow|\hat{\mathcal{H}}^{(0)}_{\text{int}}|\downarrow\rangle|}{\hbar}. \tag{2.5}$$

The simplest case of interaction of a laser field with the atoms is the electric dipole interaction, where $\hat{\mathcal{H}}_{\text{int}} = -\hat{\boldsymbol{d}}\cdot\boldsymbol{E}$, where $\hat{\boldsymbol{d}}$ is the atomic electric dipole operator and $\boldsymbol{E}$ the laser's electric field. For simplicity, we consider the laser's electric field oriented along the quantization axis z. In this case we can write the interaction term in the form

$$\hat{\mathcal{H}}_{\text{int}} = -\hbar\Omega\cos(\omega t + \phi_L)(|\uparrow\rangle\langle\downarrow| + |\downarrow\rangle\langle\uparrow|). \tag{2.6}$$

We then consider the transformation to a frame rotating at the laser frequency ω and define the amplitudes $b_{\uparrow,\downarrow}$ such that $a_\downarrow = b_\downarrow e^{i\omega t/2}$ and $a_\uparrow = b_\uparrow e^{-i\omega t/2}$. In this rotating frame we can write the total Hamiltonian as

$$\mathcal{H} = \frac{\hbar}{2}\begin{pmatrix} -\delta & -\Omega e^{-i\phi_L} \\ -\Omega e^{i\phi_L} & \delta \end{pmatrix}, \tag{2.7}$$

where we defined the detuning of the laser field from the atomic resonance $\delta = \omega - \omega_0$ and we neglected terms oscillating at twice the laser frequency (Rotating Wave Approximation).

As a result, the total Hamiltonian can be written as

$$\hat{\mathcal{H}} = -\boldsymbol{\Omega}_R\cdot\hat{\boldsymbol{S}}, \tag{2.8}$$

where $\hat{\boldsymbol{S}} = \hat{\boldsymbol{\sigma}}/2$, $\boldsymbol{\Omega}_R = \delta\boldsymbol{e}_z + \Omega\cos\phi_L\boldsymbol{e}_x + \Omega\sin\phi_L\boldsymbol{e}_y$ is the Rabi frequency vector and $\boldsymbol{e}_i$ is the unit vector in the direction i. The effect of the interaction with the laser field can therefore be pictured as an equivalent rotation of the Bloch vector $\hat{\boldsymbol{S}}$ about $\boldsymbol{\Omega}_R$. The Hamiltonian $\hat{\mathcal{H}}$ is equivalent to that of the precession of a magnetic moment in a magnetic field, where $\hat{\boldsymbol{S}}$ is an effective magnetic moment and $\boldsymbol{\Omega}_R$ is an effective magnetic field.

By applying the commutation relations [36] for the spin operators, $[\hat{S}_i, \hat{S}_j] = i\epsilon_{ijk}\hat{S}_k$, and the Ehrenfest theorem $\frac{d}{dt}\langle\hat{\boldsymbol{S}}\rangle = \langle[\hat{\boldsymbol{S}}, \hat{\mathcal{H}}]\rangle/(i\hbar)$, we obtain the equation of motion for the precession of the spin vector about the Rabi frequency vector,

$$\frac{d}{dt}\langle\hat{\boldsymbol{S}}\rangle = -\boldsymbol{\Omega}_R\times\langle\hat{\boldsymbol{S}}\rangle. \tag{2.9}$$

The frequency of this precession is given by the norm of $\mathbf{\Omega}_R$, defined as the generalized Rabi frequency $\Omega_R = \sqrt{\Omega^2 + \delta^2}$.

The unitary evolution $\hat{U}_\mathrm{p}$ induced by the Hamiltonian (2.8) can also be expressed by using the properties of the Pauli matrices $\hat{\boldsymbol{\sigma}}$ as

$$\hat{U}_\mathrm{p}(t - t_0, \boldsymbol{n}_R) = e^{-i\hat{\mathcal{H}}(t-t_0)/\hbar} = \hat{I}\cos\left[\frac{\Omega_R}{2}(t - t_0)\right] + i\boldsymbol{n}_R \cdot \hat{\boldsymbol{\sigma}} \sin\left[\frac{\Omega_R}{2}(t - t_0)\right], \quad (2.10)$$

where $\hat{I}$ is the identity operator and $\boldsymbol{n}_R(\theta, \phi) = \mathbf{\Omega}_R/\Omega_R$ is the unit vector corresponding the generalized Rabi frequency.

We can now consider the cases that are relevant to atom interferometry, namely the beam splitter and the mirror laser pulses. If the laser is on resonance with the atomic transition, $\delta = 0$, then $\Omega_R = \Omega$. Furthermore, for $\phi_L = 0$, if the initial state lies in the yz plane, it will remain there during the interaction with the laser field. We then have the solution

$$\langle \hat{S}_z(t) \rangle = \langle \hat{S}_z(0) \rangle \cos\Omega t - \langle \hat{S}_y(0) \rangle \sin\Omega t. \quad (2.11)$$

A mirror laser pulse is one that produces population inversion between the two states: starting from the Bloch vector pointing at the south pole, $\langle \hat{S}_z(0) \rangle = -1/2, \langle \hat{S}_y(0) \rangle = 0$, a complete inversion is attained when $\langle \hat{S}_z(0) \rangle = 1/2$ or $\Omega t_\pi = \pi$. Because of this condition, such a pulse is named a π-pulse.

Another important case is the 50-50 beam splitter pulse, which produces an equal superposition of the two spin states. This is attained when $\Omega t_{\pi/2} = \pi/2$ and because of this condition, such a pulse is named a $\pi/2$-pulse.

In terms of the state in eq. (2.2), the expectation value of $\hat{S}_z$ can be written as

$$\langle \hat{S}_z \rangle = \frac{1}{2} \langle \psi | \left(|\uparrow\rangle \langle\uparrow| - |\downarrow\rangle \langle\downarrow| \right) |\psi\rangle = \frac{1}{2}\left(\cos^2\frac{\theta}{2} - \sin^2\frac{\theta}{2}\right) = \frac{1}{2}\cos\theta. \quad (2.12)$$

Therefore, the π-pulse induces the transition $\theta(t = 0) = \pi \rightarrow \theta(t = t_\pi) = 0$ and the $\pi/2$-pulse induces the transition $\theta(t = 0) = \pi \rightarrow \theta(t = t_{\pi/2}) = \pi/2$.

After describing the manipulation of the atomic states by the laser interaction, we now turn our attention to the interactions that take place inside between the interferometer pulses. In general, these interactions can be quantified by a parameter $\Delta\phi$, the phase shift of the interferometer. The main goal of an interferometric measurement is to provide an estimation of $\Delta\phi$. However, because there exists no hermitian operator corresponding to this phase shift, in the interferometer, the measurement is attained by converting this phase shift into a population difference.

The effect of the phase shift in the interferometer can be represented as a rotation of the Bloch vector about the z-axis. The unitary operator that accomplishes such transformation can be written as

$$\hat{U}_\mathrm{ps}(\Delta\phi) = e^{-i\Delta\phi\hat{\sigma}_z/2} = e^{-i\Delta\phi/2} |\uparrow\rangle \langle\uparrow| + e^{i\Delta\phi/2} |\downarrow\rangle \langle\downarrow|. \quad (2.13)$$

To visualize the effect of this transformation we first interpret the phase φ in (2.2) by computing

$$\langle \hat{S}_x \rangle = \frac{1}{2} \sin\theta \cos\varphi \tag{2.14}$$

$$\langle \hat{S}_y \rangle = \frac{1}{2} \sin\theta \sin\varphi. \tag{2.15}$$

These properties and (2.12) are related to the fact that the state (2.2) is the eigenstate of the operator $\hat{\boldsymbol{\sigma}} \cdot \boldsymbol{n}$, where $\boldsymbol{n} = \sin\theta\cos\varphi \boldsymbol{e}_x + \sin\theta\sin\varphi \boldsymbol{e}_y + \cos\theta \boldsymbol{e}_z$ is the unit vector in the Bloch sphere pointing in the direction defined by the angles θ and φ. It is then clear that φ is the phase of quantum superpositions of spin states and that it can be visualized as the angle of the Bloch vector with respect to the x-axis, in the equatorial plane.

The effect of the phase shift operator $\hat{U}_{\rm ps}$ can be computed as

$$\hat{U}_{\rm ps}(\Delta\phi) \left|\psi\right\rangle = e^{i\Delta\phi/2} \sin\frac{\theta}{2} \left|\downarrow\right\rangle + e^{-i(\varphi+\Delta\phi/2)} \cos\frac{\theta}{2} \left|\uparrow\right\rangle = \sin\frac{\theta}{2} \left|\downarrow\right\rangle + e^{-i(\varphi+\Delta\phi)} \cos\frac{\theta}{2} \left|\uparrow\right\rangle, \tag{2.16}$$

where in the last equality we used the fact that states differing by an overall phase factor coincide. The phase shift operator therefore adds the phase $\Delta\phi$ to the superposition (2.2).

We now have the tools to consider the operation of the simplest interferometer, the Ramsey interferometer [37]. In the initial state $\left|\psi_{\rm in}\right\rangle$, the atom is pumped in the ground $\left|\downarrow\right\rangle$ state i.e. at the south pole of the Bloch sphere. A $\pi/2$-pulse is then applied with a phase $\phi_L = \pi/2$ ($\boldsymbol{n}_R = \boldsymbol{e}_y$) and, following the accumulation of the phase $\Delta\phi$, a final $\pi/2$-pulse with phase $\phi_L = 0$ ($\boldsymbol{n}_R = \boldsymbol{e}_x$) converts the accumulated phase shift into a population difference. This final state is attained by the sequence of operations (Fig. 2.2)

$$\begin{aligned} \left|\psi_{\rm fin}\right\rangle &= \hat{U}_p(t_{\pi/2}, \boldsymbol{e}_x) \hat{U}_{\rm ps}(\Delta\phi) \hat{U}_p(t_{\pi/2}, \boldsymbol{e}_y) \left|\psi_{\rm in}\right\rangle \\ &= \frac{1}{2} \left[(1 + ie^{-i\Delta\phi}) \left|\downarrow\right\rangle + (i - e^{-i\Delta\phi}) \left|\uparrow\right\rangle \right] \end{aligned} \tag{2.17}$$

The probabilities for the final state of being in the two spin states are therefore given by

$$P_\downarrow = |\left\langle\downarrow\right| \left.\psi_{\rm fin}\right\rangle|^2 = \frac{1}{2}(1 + \sin\Delta\phi), P_\uparrow = |\left\langle\uparrow\right| \left.\psi_{\rm fin}\right\rangle|^2 = \frac{1}{2}(1 - \sin\Delta\phi), \tag{2.18}$$

and the population difference therefore directly reflects the phase shift:

$$P_\downarrow - P_\uparrow = \sin\Delta\phi. \tag{2.19}$$

These results show that the phase shift manifests itself as an interference fringe or a variation of the relative population between the two states. The most sensitive point where to operate the interferometer corresponds to the condition $\Delta\phi \ll 1$ where $P_\downarrow - P_\uparrow \simeq \Delta\phi$. This condition can be achieved, for example, by tuning the phase of the initial beam splitter pulse. In this case, if the corresponding phase is ϕ', then the unit vector

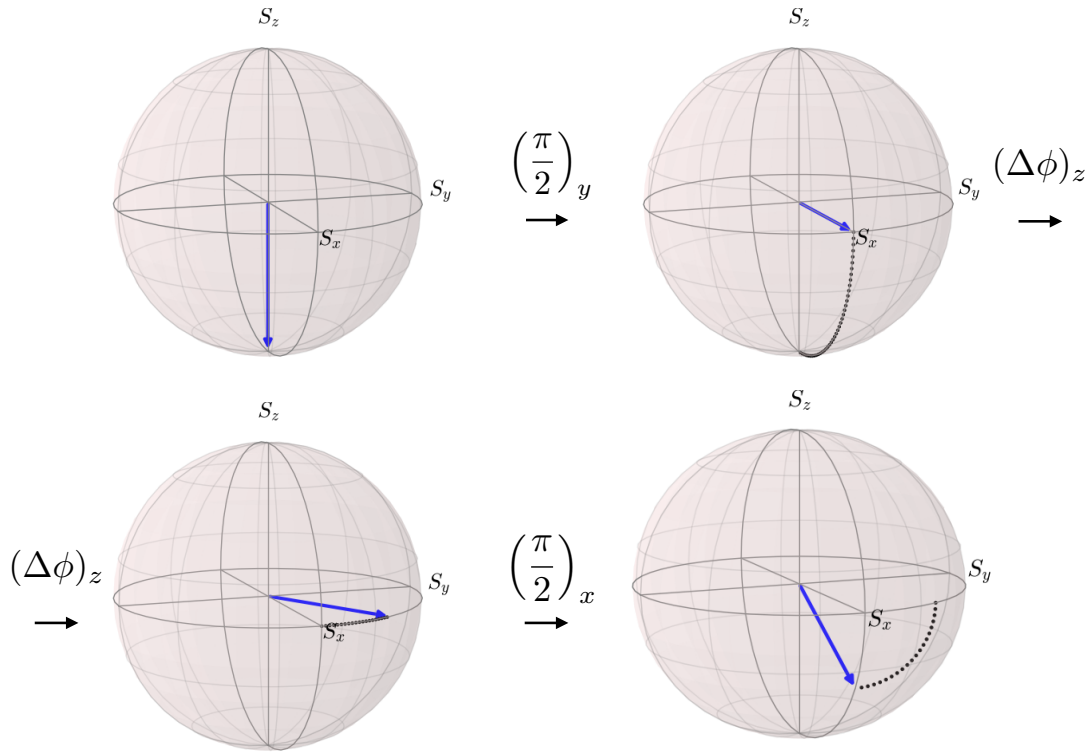

Figure 2.2: Representation of the Ramsey interferometer on the Bloch sphere. The $\pi/2$-pulses are indicated as $\left(\frac{\pi}{2}\right)_k$, where k labels the axis of the rotation. Similarly, the accumulated phase shift is labelled $(\Delta\phi)_z$ thus recalling that it is represented as a rotation about the z-axis.

corresponding to the generalized Rabi frequency is $\boldsymbol{n}_R = \cos\phi'\boldsymbol{e}_x + \sin\phi'\boldsymbol{e}_y$ and the superposition state after the pulse is

$$U_p(t_{\pi/2}, \boldsymbol{n}_R)\,|\psi_{\text{in}}\rangle = \frac{1}{\sqrt{2}}(|\downarrow\rangle + e^{-i(\phi'-\pi/2)}\,|\uparrow\rangle). \tag{2.20}$$

The phase shift measured by the interferometer can therefore meet the condition of maximum sensitivity, $\Delta\phi \ll 1$, because changes in $\Delta\phi$ are equivalent to changes in ϕ'.

In this Section we have described a representation that intuitively explains how the interferometer converts the accumulated phase into a measurable population difference between two states. There is however the essential question about how well it is possible to measure the probabilities $P_\downarrow$ and $P_\uparrow$. With a single particle, the noise in the phase measurement is the quantum projection noise. With more independent particles the limit is still set by the quantum projection noise. However, if more particles are *correlated*, this limit can be overcome. This will be the subject of the following sections.

2.2 Input states in atom interferometry

When an interferometric measurement is performed with a single particle, the phase estimation is limited by the quantum projection noise. To see how this arises, we recall that in the interferometer one can arrange a situation where the phase shift is measured through the relation $\Delta\phi \simeq P_\downarrow - P_\uparrow \propto \langle \hat{S}_z \rangle$. The uncertainty of this measurement is therefore given by the variance of the operator $\hat{S}_z$. This is defined as

$$(\Delta S_z)^2 = \langle \psi_{\text{fin}} | \hat{S}_z^2 | \psi_{\text{fin}} \rangle - \langle \psi_{\text{fin}} | \hat{S}_z | \psi_{\text{fin}} \rangle^2 \tag{2.21}$$

For a generic interferometer output state $|\psi_{\text{fin}}\rangle = a_\downarrow |\downarrow\rangle + a_\uparrow |\uparrow\rangle$, we have $(\Delta S_z)^2 = |a_\uparrow|^2 |a_\downarrow|^2$. The phase resolution in the presence of quantum projection noise can be computed as

$$\delta(\Delta\phi) = \frac{\Delta S_z}{\left| \frac{\partial \langle S_z \rangle}{\partial \Delta\phi} \right|}. \tag{2.22}$$

By using $\langle \hat{S}_z \rangle = -\frac{1}{2} \sin \Delta\phi$, we get $|\partial \langle S_z \rangle / \partial \Delta\phi| = \hbar |a_\downarrow| |a_\uparrow|$ and the phase resolution is therefore $\delta(\Delta\phi) = 1$, independent of the operating point $\Delta\phi$. This result can be interpreted in terms of the fact that the phase sensitivity is proportional to the spin noise ΔS_z. This result, however, holds when the quantum projection noise is the only noise source. In the presence of additional noise, due for example to detection noise, there exists an optimum operating point. We therefore consider an additional noise source $(\Delta S_z)_{\text{add}}$ which we take to be uncorrelated from the quantum projection noise and does not introduce any bias in the phase estimation. For this noise source, therefore, the variances are additive and the phase resolution becomes

$$\delta(\Delta\phi) = \frac{\sqrt{(\Delta S_z)^2 + (\Delta S_z)^2_{\text{add}}}}{\left| \frac{\partial \langle \hat{S}_z \rangle}{\partial \Delta\phi} \right|}. \tag{2.23}$$

It is then straightforward to see that this expression is minimized when $|a_\uparrow|^2 |a_\downarrow|^2$ is maximized. Because $|a_\downarrow|^2 + |a_\uparrow|^2 = 1$, this condition corresponds to that of maximum phase sensitivity $|a_\downarrow|^2 = |a_\uparrow|^2 = 1/2$ [27].

2.2.1 Repeated phase measurements with uncorrelated states and the Standard Quantum Limit

We next consider the case where the interferometric measurement is repeated m times with a single particle and assume that the various repetitions are uncorrelated i.e. the outcome of one measurement does not affect the outcomes of the following measurements. In this case we will consider the random variable S_z to be the sum of the random variables

corresponding to each measurement trial k, $(S_z)_k$. If the independent trials are indistiguishable, then $\langle (S_z)_k \rangle = \langle (S_z)_l \rangle$ and $(\Delta S_z)_k^2 = (\Delta S_z)_l^2$ for $k \neq l$. By making use of the error propagation formula, in the previous results we therefore make the replacements

$$\langle S_z \rangle \to \sum_{k=1}^{m} \langle (S_z)_k \rangle = m \langle S_z \rangle \tag{2.24}$$

$$(\Delta S_z)^2 \to \sum_{k=1}^{m} (\Delta S_z)_k^2 = m(\Delta S_z)^2 \tag{2.25}$$

and the phase resolution is given by

$$\delta(\Delta\phi) = \frac{1}{\sqrt{m}}. \tag{2.26}$$

The phase measurement can also be performed with more than one atom. If the atomic states of different atoms are uncorrelated, then this measurement is equivalent to the repetition of a measurement with a single atom, a number of times equal to the number of atoms. This follows from the fact that the interactions in the interferometer, namely the interaction with the laser field and the phase shift, are *local* operations. This means that the interferometer does not create correlations between particles. Therefore, with m trials of the experiment, each with N atoms, the phase resolution is given by

$$\delta\Delta\phi = \frac{1}{\sqrt{mN}}. \tag{2.27}$$

We now consider the relevant case where a single experiment run is performed with N particles. In this case we define the spin variables corresponding to a single particle with index i: $\hat{\boldsymbol{\sigma}}_i$ the Pauli spin matrices and $\hat{\boldsymbol{S}}_i = \frac{1}{2}\hat{\boldsymbol{\sigma}}_i$ the spin vector. The corresponding collective spin vector is given by $\hat{\boldsymbol{S}} = \sum_{i=1}^{N} \hat{\boldsymbol{S}}_i$. The eigenvalue corresponding to the operator $\hat{\boldsymbol{S}}^2$ is $S(S+1)$, where S can take the values $S = N/2, N/2-1, \cdots, 1/2$ or 0 depending on whether N is odd or even, respectively. For each value of S, the operator $\hat{S}_z$ can take the values $M = -S, \cdots, +S$. These simultaneous eigenstates of $\boldsymbol{S}^2$ and S_z, denoted $|S, M\rangle$ are known as Dicke states. The subspace $S = N/2$ is that of the fully symmetric states. This condition represents the maximum length of the Bloch vector and can also be interpreted in terms of interferometer contrast. An important property is that S is conserved when the interactions do not distinguish between different particles. For example, the interactions in the interferometer described above fulfill this requirement.

The state of N independent (or uncorrelated) atoms with the corresponding Bloch vectors all pointing in the same direction (θ, ϕ) is known as the coherent spin state (CSS) [38] and can be written as

$$|\theta, \phi\rangle = \left(\sin\frac{\theta}{2} |\downarrow\rangle + e^{-i\phi} \cos\frac{\theta}{2} |\uparrow\rangle \right)^{\otimes N} \tag{2.28}$$

This state can also be written in the Dicke basis as

$$|\theta,\phi\rangle = \sum_{M=-S}^{S} |S,M\rangle \langle S,M|\theta,\phi\rangle \,, \tag{2.29}$$

where

$$\langle S,M|\theta,\phi\rangle = \sqrt{\begin{pmatrix} 2S \\ M+S \end{pmatrix}} \cos^{S+M}\frac{\theta}{2} \sin^{S-M}\frac{\theta}{2} e^{-i(S+M)\phi}. \tag{2.30}$$

The CSS is one of the most common states used in atom interferometry, mainly because it is readily obtained by the interaction with the laser fields. Indeed, starting with all the atoms pumped in the ground $|\downarrow\rangle$ state, corresponding to $|\theta=\pi,\phi\rangle$, the state is rotated into any state $|\theta,\phi\rangle$ by the interaction with the laser fields described above.

We can now assume that a particular CSS state $|\theta,0\rangle$ is the output of an atom interferometer. Because of the mapping of phase shift $\Delta\phi$ into population difference, we have $\theta = \Delta\phi + \pi/2$. With this state we can now compute the interferometer phase resolution (2.22).

In order to compute the spin mean value and variance, we note that the expansion (2.29) corresponds to the binomial distribution with probability

$$|\langle S,M|\theta,\phi\rangle|^2 = \begin{pmatrix} 2S \\ M+S \end{pmatrix} \cos^{2(S+M)}\frac{\theta}{2} \sin^{2(S-M)}\frac{\theta}{2}. \tag{2.31}$$

The average is therefore $\langle \hat{S}_z\rangle = -\frac{1}{2}N\sin\Delta\phi$ and the variance $(\Delta S_z)^2 = N\cos^2\frac{\theta}{2}\sin^2\frac{\theta}{2} = \frac{1}{4}N\cos^2\Delta\phi$ so the phase resolution is

$$\delta(\Delta\phi) = \frac{1}{\sqrt{N}}. \tag{2.32}$$

This phase resolution limit is known as the Standard Quantum Limit (SQL) and the corresponding phase noise is known as the shot noise. The simpler reasoning that led to (2.27) would of course suffice. Here we however provided a quantum mechanical description of the state that corresponds to uncorrelated atoms.

We now compare this limit with that expected from the Heisenberg uncertainty relation. In this case, in particular, we are considering a state pointing, in the Bloch sphere, in the positive x direction (we assume $\Delta\phi = 0$ for simplicity) so that the state is an eigenstate of $\hat{S}_x$. The uncertainty relation in this case reads

$$(\Delta S_y)^2(\Delta S_z)^2 \geq \frac{1}{4}|\langle \hat{S}_x\rangle|^2 = \frac{N^2}{16}. \tag{2.33}$$

The variance $(\Delta S_z)^2$ was calculated above. In order to compute $(\Delta S_y)^2$ one can conceptually rotate the state about the x-axis through a $\pi/2$-pulse by applying the operator $\hat{U}_{\rm p}$. In doing so we see that the CSS remains unaltered for any rotation angle. In

other terms, the CSS is a symmetric state about the direction (θ, ϕ). We conclude that $(\Delta S_y)^2 = (\Delta S_z)^2 = N/4$ and that the CSS is a minimum uncertainty state i.e. it saturates the inequality in (2.33).

The uncertainty regions of quantum states can be represented by the Husimi Q function [39]. This is essentially formed by the diagonal elements of the density operator $\hat{\rho}$ in the representation of the coherent spin states $|\theta, \phi\rangle$:

$$Q(\theta, \phi) = \frac{2S+1}{4\pi} \langle \theta, \phi | \hat{\rho} | \theta, \phi \rangle . \tag{2.34}$$

For an atomic state defined by the density matrix $\hat{\rho}$, we define the probability density function $P(\theta, \phi)$ for it to be in the state $|\theta, \phi\rangle$,

$$\hat{\rho} = \int \sin\theta d\theta d\phi P(\theta, \phi) \, |\theta, \phi\rangle \langle \theta, \phi| . \tag{2.35}$$

The Husimi Q function can then be written as

$$\begin{aligned} Q(\theta, \phi) &= \frac{2S+1}{4\pi} \int \sin\theta' d\theta' d\phi' P(\theta', \phi') | \langle \theta, \phi | \theta', \phi' \rangle |^2 \\ &= \frac{2S+1}{4\pi} \int \sin\theta' d\theta' d\phi' P(\theta', \phi') (\cos\Theta/2)^{4S}, \end{aligned} \tag{2.36}$$

where Θ is the angle between the directions of the coherent spin states $|\theta, \phi\rangle$ and $|\theta', \phi'\rangle$ and is given by

$$\cos\Theta = \cos\theta \cos\theta' + \sin\theta \sin\theta' \cos(\phi - \phi'). \tag{2.37}$$

In the limit of large atom numbers, $S \gg 1$, this expression can be approximated by

$$Q(\theta, \phi) \simeq \frac{S}{2\pi} \int \sin\theta' d\theta' d\phi' P(\theta', \phi') \exp\left[-\frac{S}{2}(\theta - \theta')^2 - \frac{S}{2}(\phi - \phi')^2 \sin^2\theta' \right] . \tag{2.38}$$

If we consider the CSS state $\rho = |\theta_0, \phi_0\rangle \langle \theta_0, \phi_0|$, then $P(\theta', \phi') = \delta(\theta' - \theta_0)\delta(\sin\theta'(\phi' - \phi_0))$ and the Q function is expressed by a Gaussian distribution

$$Q(\theta, \phi) = \frac{S}{2\pi} \exp\left[-\frac{S}{2}(\theta - \theta_0)^2 - \frac{S}{2}(\phi - \phi_0)^2 \sin^2\theta_0 \right] . \tag{2.39}$$

This function is represented in Fig. 2.3 for a CSS pointing in the direction $(\theta = \pi/2, \phi = 0)$.

We also note that, whenever the atomic state is a pure state, $\hat{\rho} = |\psi\rangle \langle \psi|$, the Q function can be expressed as

$$Q(\theta, \phi) = \frac{2S+1}{4\pi} | \langle \theta, \phi | \psi \rangle |^2. \tag{2.40}$$

and can therefore be interpreted as an effective probability density function.

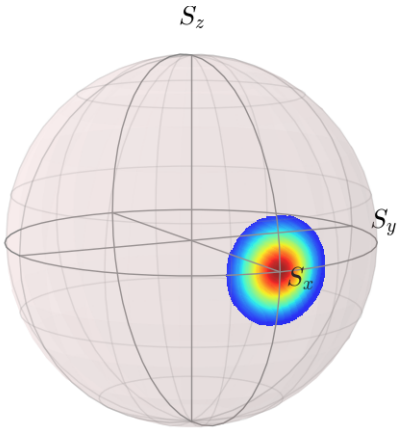

Figure 2.3: Husimi Q function for a coherent spin state pointing in the direction ($\theta = \pi/2, \phi = 0$).

2.2.2 Entanglement and phase measurements beyond the Standard Quantum Limit

From our treatment of the coherent spin state, the one readily attained experimentally, we conclude that it can perform at best at the shot noise limit. There are, however, states that possess phase sensitivities beyond the Standard Quantum Limit. An important example is the NOON state [40] which is a particular Schrödinger-cat state and, for our system, is written as

$$|\psi_{\text{NOON}}\rangle = \frac{1}{\sqrt{2}}(|\uparrow\rangle^{\otimes N} + |\downarrow\rangle^{\otimes N}) = \frac{1}{\sqrt{2}}(|S, S\rangle + |S, -S\rangle), \tag{2.41}$$

where in the second equality the state was written in the Dicke basis. The NOON state is seen to be an equal superposition of two coherent states. This feature is also visible from the corresponding Husimi Q function:

$$Q(\theta, \phi) = \frac{2S+1}{8\pi}\left[\cos^{4S}\left(\frac{\theta}{2}\right) + \sin^{4S}\left(\frac{\theta}{2}\right) + 2\sin^{2S}\left(\frac{\theta}{2}\right)\cos^{2S}\left(\frac{\theta}{2}\right)\cos(2S\phi)\right]. \tag{2.42}$$

This function is plotted in Fig. 2.4 a) and shows two probability peaks at the north and south poles. Additionally, for small S, there is interference between the north and the south regions, represented by the last term proportional to $\cos(2S\phi)$.

The importance of this state stems from its large sensitivity to atomic phase variations. This can be understood by applying the phase shift operator $\hat{U}_{\text{ps}}(\Delta\phi)$,

$$\hat{U}_{\text{ps}}(\Delta\phi)\,|\psi_{\text{NOON}}\rangle = \frac{1}{\sqrt{2}}(|\downarrow\rangle^{\otimes N} + e^{-iN\Delta\phi}\,|\uparrow\rangle^{\otimes N}). \tag{2.43}$$

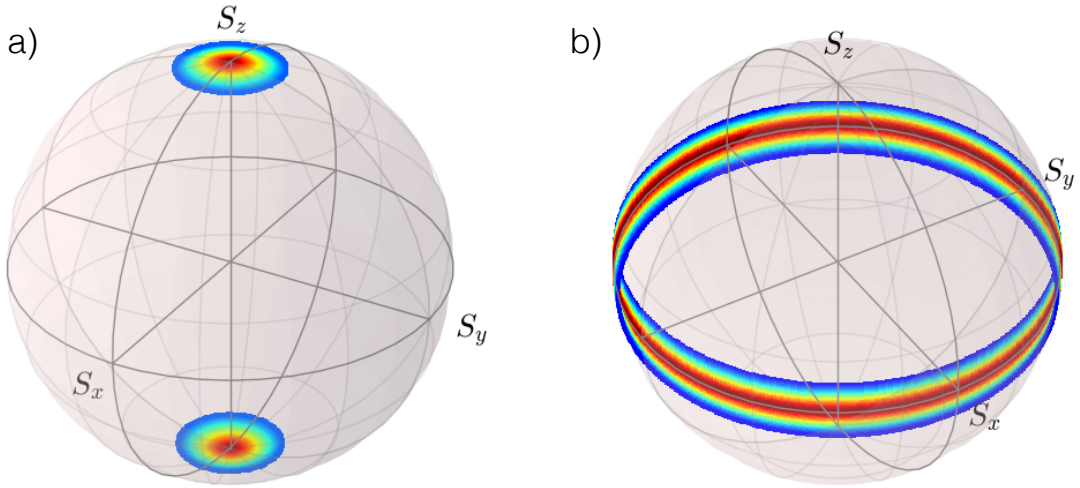

Figure 2.4: Husimi Q function representation of two entangled multiparticle states for $N = 100$. a) NOON state, b) Dicke state $|S, 0\rangle$.

It is then seen that the NOON state accumulates the phase shift N times faster compared to the coherent spin state. The phase shift of the NOON state is measured via the operator [41]

$$\hat{A} = |S, S\rangle \langle S, -S| + |S, -S\rangle \langle S, S| \,, \tag{2.44}$$

whose expectation value is $\langle \psi_{\mathrm{NOON}}|\hat{A}|\psi_{\mathrm{NOON}}\rangle = \cos N\Delta\phi$ and its variance is $(\Delta A)^2 = \sin^2 \Delta\phi$. The phase resolution is therefore

$$\delta\Delta\phi = \frac{(\Delta A)}{|\partial \langle \hat{A} \rangle / \partial \Delta\phi|} = \frac{1}{N}. \tag{2.45}$$

Another important example is that of the Dicke state $|S, M\rangle$ with Husimi Q function

$$Q(\theta, \phi) = \frac{2S+1}{4\pi} \begin{pmatrix} 2S \\ S+M \end{pmatrix} \cos^{2(S+M)}\left(\frac{\theta}{2}\right) \sin^{2(S-M)}\left(\frac{\theta}{2}\right). \tag{2.46}$$

Because the Dicke state is a state where the population between the two spin states is defined, the Husimi Q function is represented by a ring in the Bloch sphere (Fig. 2.4 b)). An interferometric phase measurement with such a state would then proceed as follows. After preparation of the state $|S, 0\rangle$, also known as the twin-Fock state [42], a $\pi/2$-pulse rotates the state into a phase-sensitive state and after a precession, another $\pi/2$-pulse is applied as in a standard Ramsey interferometer. The result is a state with increased variance $(\Delta S_z)^2$ which is proportional to $(\Delta\phi)^2$. A measurement of the relative population variance therefore yields the phase measurement. It can be shown that for small $\Delta\phi$ the phase resolution is [43]

$$\delta\Delta\phi = \frac{\sqrt{2}}{N}. \tag{2.47}$$

We have therefore shown that there are states that can yield phase measurements with a resolution better than the Standard Quantum Limit and that the ability to perform such measurements depends on the measured observable [43]. All these states share the common property of being *entangled* states. This means that the state cannot be expressed as a direct product of single-particle states. In terms of the density matrix, we define the density matrix for the single particle i as $\hat{\rho}_i$. By definition, the collective state $\hat{\rho}$ is entangled if it is not *separable* i.e. if

$$\hat{\rho} \neq \sum_k p_k \hat{\rho}_1^{(k)} \otimes \hat{\rho}_2^{(k)} \otimes \cdots \otimes \hat{\rho}_N^{(k)}, \tag{2.48}$$

where p_k is the probability of being in the state $\hat{\rho}_1^{(k)} \otimes \hat{\rho}_2^{(k)} \otimes \cdots \otimes \hat{\rho}_N^{(k)}$.

2.2.3 Phase resolution limits for separable and entangled states

Among the several entangled states, only a fraction are useful for quantum metrology and can yield measurement precisions better than the shot noise limit. Entanglement is however a necessary condition for beating the shot noise as it was shown in [44] that separable states can perform at most at the shot noise limit. On the other hand, entangled states can yield a phase resolution at the Heisenberg limit $\delta(\Delta\phi) = 1/N$. This can be shown by considering the phase shift operator $\hat{U}_{\text{ps}} = e^{-i\Delta\phi\hat{S}_z}$, where $\hat{S}_z$ is the collective spin operator. The corresponding uncertainty relation can written as [44]

$$\delta(\Delta\phi)\Delta S_z \geq \frac{\hbar}{2\sqrt{m}}, \tag{2.49}$$

where m is the number of repetitions of the measurement. We consider the case where the input state is a separable state and note that, according to (2.49), the best phase resolution is possible when the variance $(\Delta S_z)^2$ is maximized. This is obtained when the input state is a product of superpositions of states corresponding to the maximum and minimum eigenvalues of $\hat{S}_z$, with equal amplitudes i.e. the single-particle state is $|\psi_i\rangle = (|\uparrow\rangle_i + |\downarrow\rangle_i)/\sqrt{2}$. The corresponding variance is $(\Delta S_z)^2 = N/4$ and the bound (2.49) reads

$$(\delta\Delta\phi)_{\text{separable}} \geq \frac{1}{\sqrt{Nm}}. \tag{2.50}$$

This shows that interferometry with separable states can perform at best at the shot noise limit.

We next consider an entangled input state. In this case the variance $(\Delta S_z)^2$ is maximized by the collective state $|\psi\rangle = (|\uparrow\rangle^{\otimes N} + |\downarrow\rangle^{\otimes N})/\sqrt{2}$ and $(\Delta S_z)^2 = N^2/4$. The bound (2.49) therefore reads

$$(\delta\Delta\phi)_{\text{entangled}} \geq \frac{1}{N\sqrt{m}} \tag{2.51}$$

which means that the phase measurement resolution is bounded by the Heisenberg limit.

This reasoning also shows the following facts:

- That the best phase resolution is attained for equal superpositions of states corresponding to the maximum and minimum eigenvalues of the generator $\hat{S}_z$ of the phase shift.
- That the NOON state is the only state that can reach the Heisenberg limit.
- That the prefactor in the phase resolution depends on the eigenvalues of $\hat{S}_z$. If the single-particle spin is s, then the phase resolution limits read

$$(\delta\Delta\phi)_{\text{separable}} \geq \frac{1}{2s\sqrt{Nm}} \text{ and } (\delta\Delta\phi)_{\text{entangled}} \geq \frac{1}{2sN\sqrt{m}} \tag{2.52}$$

  which reduce to (2.50) and (2.51) in the case of the two-level system, $s = 1/2$.

2.2.4 Useful states for quantum metrology and spin squeezing

In the previous Subsection we concluded that entanglement is a necessary condition for phase measurements beyond the Standard Quantum Limit. It has been shown [45] that there exists a quantity, the quantum Fisher information, that provides a necessary condition for multiparticle entanglement and a necessary and sufficient condition for sub-shot-noise phase measurements. Even though this is the most general criterion that identifies states that are useful for quantum metrology, we will only consider a selected class of such states known as *spin squeezed states* [46]. For these states, entanglement correlates the noise of the single particles, resulting in reduced fluctuations for one direction in the Bloch sphere (the *squeezing* direction) at the expense of enhanced fluctuations in the orthogonal direction (the *anti-squeezing* direction).

Depending on the specific application, different parameters can be used to quantify spin squeezing.

For the atom interferometer, the useful parameter was introduced by Wineland [47, 29] and represents essentially the signal-to-noise ratio of the phase measurement that also accounts for the fringe contrast $\mathcal{C}$:

$$\xi_m^2 = \mathcal{C}^2 \frac{N}{(\Delta N)^2}, \tag{2.53}$$

where the fraction is the inverse of the population difference variance $(\Delta N)^2$ normalized to the shot noise N.

The Ramsey interferometer with a squeezed state would then proceed as follows:

- After pumping all the atoms in state $|\downarrow\rangle$, thus producing the coherent spin state $|\theta = \pi, \phi\rangle$, a $\pi/2$-pulse is applied and rotates the state about the y-axis. The resulting CSS state is $|\theta = \pi/2, \phi = 0\rangle$.

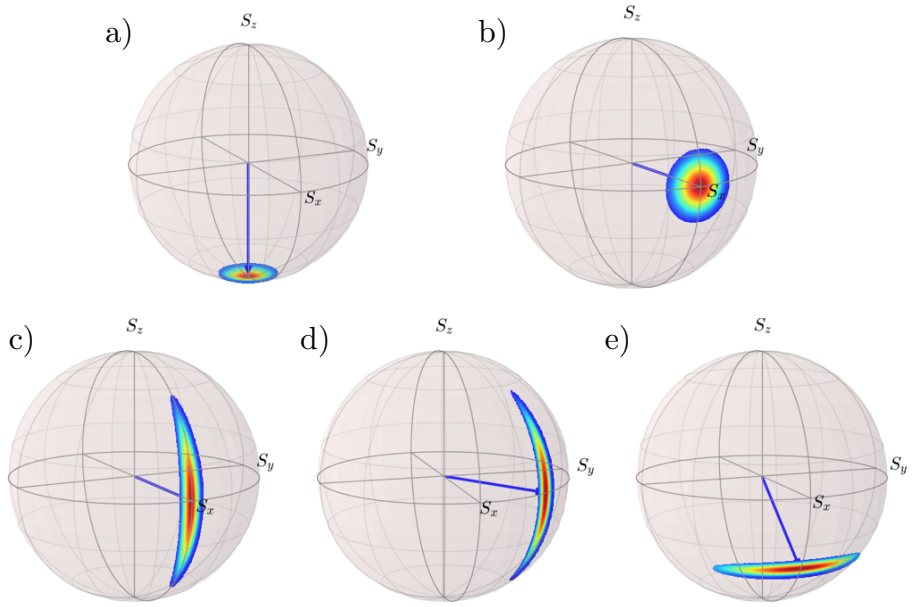

Figure 2.5: Representation of the Ramsey sequence on the Bloch sphere. a) Initial coherent spin state $|\theta = \pi, \phi\rangle$. b) Coherent state after the first $\pi/2$-pulse. c) Spin squeezed state with enhanced phase sensitivity. d) Spin squeezed state after the accumulation of the phase shift $\Delta\phi$. e) Spin squeezed state with reduced relative population uncertainty.

- A *spin squeezing* procedure is applied, thus producing a phase-sensitive state i.e. a state with reduced fluctuations along the phase direction y.
- The precession accumulates the phase shift $\Delta\phi$.
- The final $\pi/2$-pulse maps the accumulated phase shift into a population difference between the two spin states and converts the phase-sensitive state into a state with reduced relative population uncertainty.

Such an adapted Ramsey sequence is illustrated in Fig. 2.5.

2.3 Generation of spin squeezed states

There are several methods that can generate spin squeezed states [29, 26]. A first class of methods relies on the implementation of effective nonlinear interactions that introduce correlations between the elementary spins. This is what was initially proposed by Kitagawa and Ueda [46] who studied the effect of Hamiltonians that are quadratic in the collective spin operators. A second class of methods relies on a pre-measurement of a collective variable that has the ability to project the atomic state into a state with reduced

uncertainty for that variable. In the following we study these mechanisms and attempt to cite the main experimental achievements.

2.3.1 Spin squeezing induced by one-axis twisting and two-axis countertwitsting

In their proposal [46], Kitagawa and Ueda consider a class of unitary transformations in the form

$$\hat{U}(t) = e^{-itF(\hat{S}_z)} \tag{2.54}$$

which are induced by the Hamiltonian $\hat{H} = \hbar F(\hat{S}_z)$ and where $F(\hat{S}_z)$ is a function of the collective spin operator $\hat{S}_z$. It is possible to show that the ladder operators $\hat{S}_\pm = \hat{S}_x \pm i\hat{S}_y$ evolve as

$$\hat{S}_+(t) = \hat{U}^\dagger \hat{S}_+(0)\hat{U} = \hat{S}_+(0)e^{itf(\hat{S}_z)} \tag{2.55}$$

where $f(\hat{S}_z) = F(\hat{S}_z + 1) - F(\hat{S}_z)$ and $\hat{S}_-(t) = [\hat{S}_+(t)]^\dagger$. For the lowest-order nonlinear Hamiltonian $\hat{H} = \hbar\chi\hat{S}_z^2$ we have $f(\hat{S}_z) = 2\chi(\hat{S}_z + 1/2)$. The evolution of the observables $\hat{S}_x$ and $\hat{S}_y$ is then given by

$$\hat{S}_x(t) = \frac{1}{2}\left[\hat{S}_+(0)e^{i\mu(\hat{S}_z+1/2)} + e^{-i\mu(\hat{S}_z+1/2)}\hat{S}_-(0)\right] \tag{2.56}$$

and

$$\hat{S}_y(t) = \frac{1}{2i}\left[\hat{S}_+(0)e^{i\mu(\hat{S}_z+1/2)} - e^{-i\mu(\hat{S}_z+1/2)}\hat{S}_-(0)\right] \tag{2.57}$$

with $\mu = 2\chi t$. These expressions allow us to compute the various expectation values where it is possible to see how the fluctuations are redistributed between the different observables. Because squeezing occurs in an oblique spin component, we introduce the rotation about the x-axis of the spin operators $\overline{\boldsymbol{S}} = e^{i\alpha\hat{S}_x(t)}\hat{\boldsymbol{S}}(t)e^{-i\alpha\hat{S}_x(t)}$ and evaluate the expectation values on the state after the $\pi/2$-pulse in the Ramsey sequence, $|\theta = \pi/2, \phi = 0\rangle$,

$$\langle\overline{S}_x\rangle = S\cos^{2S-1}(\mu/2), \langle\overline{S}_y\rangle = \langle\overline{S}_z\rangle = 0, \tag{2.58}$$

$$(\Delta\overline{S}_x)^2 = \frac{S}{2}\left[2S(1 - \cos^{2(2S-1)(\mu/2)}) - (S - 1/2)A\right], \tag{2.59}$$

$$(\Delta\overline{S}_y)^2 = \frac{S}{2}\left[1 + \frac{1}{2}(S - 1/2)(A + \sqrt{A^2 + B^2}\cos(2\alpha + 2\beta))\right], \tag{2.60}$$

$$(\Delta\overline{S}_z)^2 = \frac{S}{2}\left[1 + \frac{1}{2}(S - 1/2)(A - \sqrt{A^2 + B^2}\cos(2\alpha + 2\beta))\right], \tag{2.61}$$

where $A = 1 - \cos^{2S-2}\mu, B = 4\sin\frac{\mu}{2}\cos^{2S-2}\frac{\mu}{2}$ and $\tan(2\beta) = B/A$. These expressions show that the uncertainty regions of the transformed state are redistributed in an anisotropic way. We can now determine the value of α that minimizes one of the variances in y or z and maximizes the other one. These correspond to the directions of squeezing

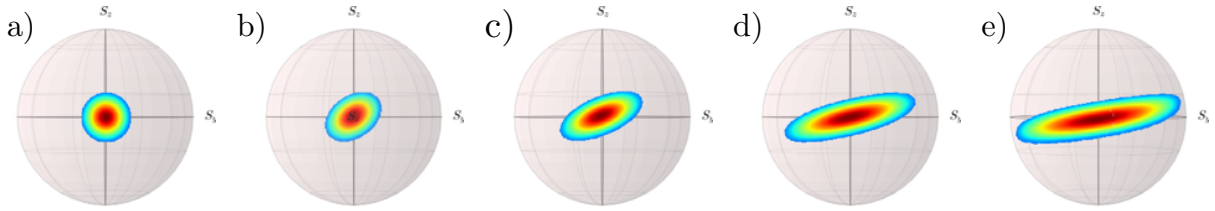

Figure 2.6: Husimi Q function representation on the Bloch sphere of the spin squeezed state induced by the one-axis twisting Hamiltonian for $S = 40$ and a) $\mu = 0$, b) $\mu = 0.02$, c) $\mu = 0.05$, d) $\mu = 0.1$ and e) $\mu = 0.15$

and anti-squeezing. In particular, $(\Delta\overline{S}_y)^2$ is minimized and $(\Delta\overline{S}_z)^2$ is maximized when $\alpha = \pi/2 - \beta$ and viceversa $(\Delta\overline{S}_y)^2$ is maximized and $(\Delta\overline{S}_z)^2$ is minimized when $\alpha = -\beta$. The corresponding variances are given by

$$V_{\pm} = \frac{S}{2}\left\{1 + \frac{1}{2}\left(S - \frac{1}{2}\right)\left[A \pm \sqrt{A^2 + B^2}\right]\right\}, \tag{2.62}$$

where the plus sign corresponds to the maximum variance and the minus sign corresponds to the minimum variance. The Husimi Q function for the spin squeezed state is represented in Fig. 2.6 for different values of the interaction strength μ. Here it is possible to see how the one-axis twisting interaction acts to redistribute the fluctuations: the Hamiltonian $\hat{H} \propto \hat{S}_z^2$ induces a precession about the z-axis by an angle that is proportional to the spin component S_z. As a result, the points of the Husimi function above the equator are rotated in one direction and points below the equator are rotated in the other direction. This process results in the shearing of the uncertainty region.

For $S \gg 1, \mu \ll 1, S\mu^2 \ll 1$, we have the approximate expressions

$$V_+ \approx \frac{S^3\mu^2}{2}, V_- \approx \frac{S}{2}\left(\frac{1}{S^2\mu^2} + \frac{S^2\mu^4}{24}\right), \tag{2.63}$$

where it is seen that the minimum variance decrease with μ is limited by the second term which accounts for the effect of the curvature of the Bloch sphere. It is then seen that the minimum variance $V_{\min}$ is attained for $\mu = \mu_0 = 24^{1/6}S^{-2/3}$ and is given by $V_{\min} \approx \frac{1}{2}\left(\frac{S}{3}\right)^{1/3}$. This result can also be expressed in terms of the squeezing parameter as $\xi_m^2 = (3/4)^{1/3}N^{2/3}$ or in terms of the phase resolution $\delta(\Delta\phi) = 1/(2^{4/3}3^{1/6}N^{5/6})$. We also note that, as μ increases, the state deviates from a minimum uncertainty state (i.e. one that saturates the Heisenberg uncertainty relation) as $4(\Delta S_y)^2(\Delta S_z)^2/|\langle S_x\rangle|^2 \approx 1 + (\mu/\mu_0)^6$ or, in other terms, the anti-squeezing is larger than the squeezing.

The squeezing limits of the one-axis twisting Hamiltonian are set by the curvature of the Bloch sphere and the fact that the squeezing direction does not follow that of a geodesic. This limitation can be overcome by the two-axis countertwisting Hamiltonian

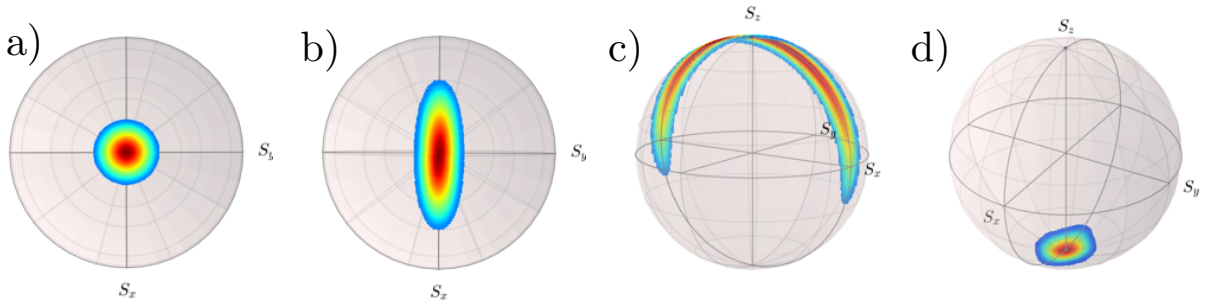

Figure 2.7: Bloch sphere representation of the Husimi Q function for $S = 40$ and for different values of the interaction strength: a) Initial CSS $|0, \phi\rangle$, $\mu = 0$; b) Partially squeezed, $\mu = 0.03$; c) Optimally squeezed, $\mu = 0.06$; d) oversqueezed $\mu = 0.16$: after separating in two peaks, the Husimi Q function becomes concentrated at the south pole.

which induces a twisting of the uncertainty region about two orthogonal axes and in opposite directions. If the initial state is orthogonal to these two axes, then it has been shown [48] that the quantum dynamics generates states with a phase resolution reaching a Heisenberg scaling. For example, the Hamiltonian for the two-axis countertwisting interaction can be written as

$$\hat{H} = \frac{\hbar\chi}{2i}(\hat{S}_+^2 - \hat{S}_-^2) \tag{2.64}$$

which induces twisting about the directions $(\pi/2, \pi/4)$ and $(\pi/2, -\pi/4)$ and the minus sign between the two terms means that the two rotations are in opposite directions. The initial state for spin squeezing would then be, for example $|0, \phi\rangle$ and the squeezed direction would be the y-axis. Because the dynamics of the two-axis countertwisting interaction cannot be solved analytically, we will limit ourselves to a numerical solution of the dynamics and show the results. Specifically, we write the Schrödinger equation $i\hbar\frac{d}{dt}|\psi(t)\rangle = \hat{H}|\psi(t)\rangle$ where we solve for the evolution of the superposition of Dicke states $|\psi(t)\rangle = \sum_{M=-S}^{+S} c_M(t)|S, M\rangle$. In assuming the initial state to be $|0, \phi\rangle$ we take $c_{+S}(0) = 1$ and $c_M(0) = 0$ for $M \neq +S$. The results can then be used to compute the variances of the spin operators and the Husimi Q function. In Fig. 2.7 we plot the Husimi Q function on the Bloch sphere for different values of the interaction strength $\mu = 2\chi t$.

We can now compare the performance of the two squeezing Hamiltonians in terms of metrological gain above the shot noise limit and in terms of the phase resolution. The results are given for $S = N/2 \gg 1$ in the Table 2.1 and in Fig. 2.8.

The one-axis twisting interaction has more potential than the analysis of Kitagawa and Ueda shows. In fact, it has been shown in [49] that, through appropriate transformations, one-axis twisting can be transformed into two-axis countertwisting. Moreover, by a combined twisting-untwisting process, it has been shown that the Heisenberg limit can be approached, in the presence of technical detection noise, by effectively amplifying the

State	**Metrological gain ξ_m^2**	**Phase resolution $\delta(\Delta\phi)$**
Coherent spin state	1	$1/\sqrt{N}$
One-axis twisted	$(3/4)^{1/3}N^{2/3}$	$1/(2^{4/3}3^{1/6}N^{5/6})$
Two-axis countertwisted	$0.54 \times N$	$1.36/N$
Maximally entangled	N	$1/N$

Table 2.1: Comparison of metrological gain and phase resolution for different dynamically squeezed states.

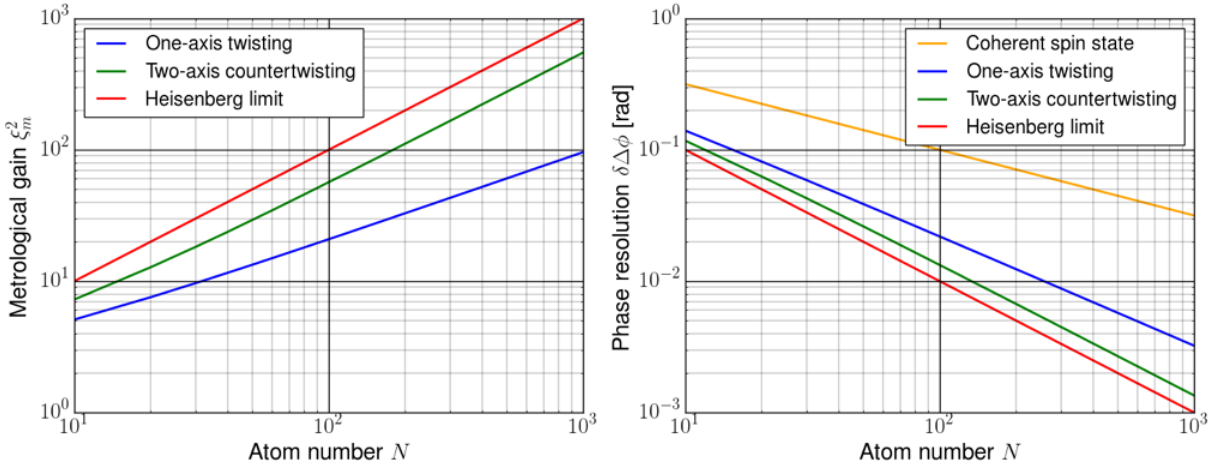

Figure 2.8: Left: comparison of the maximum metrological gain ξ_m^2 attained by the one-axis twisted and two-axis countertwisted states; Right: comparison of the phase resolution attained by the different states: the coherent spin state, the one-axis twisted and the two-axis countertwisted states.

phase signal [50, 51].

2.3.2 Measurement-induced spin squeezing

The measurement process in quantum mechanics can be conceived as a quantum state preparation device [52, 32, 33]. For example, if one is probing a superposition state $|\psi\rangle = a_\downarrow |\downarrow\rangle + a_\uparrow |\uparrow\rangle$ by measuring the variable S_z, then one would find the eigenvalue $+1/2$ with probability $|a_\uparrow|^2$ and the eigenvalue $-1/2$ with probability $|a_\downarrow|^2$. The corresponding states after the measurement would then be $|\uparrow\rangle$ and $|\downarrow\rangle$, respectively. It is therefore clear that the measurement prepared a quantum state, even though the prepared state is undetermined before the measurement i.e. the preparation is conditioned to the measurement outcome.

A measurement can prepare states that are more complex than single-particle states, in particular, entangled states useful for quantum metrology can be prepared by appropriately designed measurements.

To be more practical, we consider the simplest non-trivial case of two particles with spin 1/2 (i.e. two two-level systems). The four possible states of the ensemble can be organized as spin singlet and spin triplet states on the basis $|S, M\rangle$ of the total angular momentum $\boldsymbol{S} = \boldsymbol{S}_1 + \boldsymbol{S}_2$, where $\boldsymbol{S}^2$ and S_z are simultaneously diagonalized. As already mentioned, these are the Dicke states. By using the notation where $|\alpha\rangle_i$ indicates that particle i is in state $|\alpha\rangle$, we have:

$$|0,0\rangle = \frac{|\uparrow\rangle_1 |\downarrow\rangle_2 - |\downarrow\rangle_1 |\uparrow\rangle_2}{\sqrt{2}} \text{ (spin singlet)} \tag{2.65}$$

$$|1,+1\rangle = |\uparrow\rangle_1 |\uparrow\rangle_2 , |1,0\rangle = \frac{|\uparrow\rangle_1 |\downarrow\rangle_2 + |\downarrow\rangle_1 |\uparrow\rangle_2}{\sqrt{2}}, |1,-1\rangle = |\downarrow\rangle_1 |\downarrow\rangle_2 \text{ (spin triplet).} \tag{2.66}$$

We now consider an experiment where we initially pump the two particles in the state $|\downarrow\rangle$ so that $|\psi_{\text{in}}\rangle = |1,-1\rangle = |\downarrow\rangle_1 |\downarrow\rangle_2$. We then apply a $\pi/2$-pulse and bring the state to the equator of the Bloch sphere, therefore generating the coherent spin state $|\theta = \pi/2, \phi = 0\rangle$. In terms of the Dicke states, this is

$$|\theta = \frac{\pi}{2}, \phi = 0\rangle = \frac{1}{2} |S = 1, M = -1\rangle + \frac{1}{\sqrt{2}} |S = 1, M = 0\rangle + \frac{1}{2} |S = 1, M = +1\rangle . \tag{2.67}$$

Let's now assume that we make a measurement $S_{z1} \otimes S_{z2}$ of the relative population of the two particles *separately* and that we get the results $S_{z1} = +1/2, S_{z2} = -1/2$. This situation will occur with a probability 1/4 and will give rise to the final state $|\uparrow\rangle_1 |\downarrow\rangle_2 = (|S = 0, M = 0\rangle + |S = 1, M = 0\rangle)/\sqrt{2}$. The final state of the measurement is therefore a separable state with reduced spin length. This last fact derives ultimately from the type of measurement that distinguishes between the different particles. Indeed, as stated earlier, S is a conserved quantity if the interaction does not distinguish between the particles' labels. We next consider the relevant case where the quantity $S_z = S_{z1} + S_{z2}$ is measured

instead. Here the measurement does not distinguish between the particles because S_z is invariant under the particle exchange $1 \leftrightarrow 2$. As a result, $S = 1$ is a conserved quantity so the state after the measurement has to be one of the triplet states. With the same probability of 1/4 we will find the measurement outcomes $S_z = +1$ and $S_z = -1$ which still correspond to separable states. However, if the measurement outcome is $S_z = 0$, then we prepared the Dicke state $|S = 1, M = 0\rangle$ which is an entangled state. This reasoning shows that our ability to generate entangled states depends on our ability to perform *collective* rather than single-particle measurements.

The first proposal for the generation of entangled states useful for quantum metrology through measurements was provided by Kuzmich, Bigelow and Mandel [53]. In their proposal, the authors considered a system of N two-level atoms (or pseudo-spins 1/2) with the corresponding total angular momentum operator $\boldsymbol{S}$. This system is injected in an interferometer that measures the phase shift $\Delta\phi$. The atomic system is probed with the aid of a similar system, made of n two-mode particles and described by the angular momentum $\boldsymbol{J}$. In practice, $\boldsymbol{J}$ refers to any collection of two-mode particles, for example photons in two polarization states. We assume that the two systems interact for a time Δt through the Hamiltonian

$$H_m = \hbar\Omega_m S_z J_z. \tag{2.68}$$

In the Heisenberg picture, on the operator $\boldsymbol{S}$, the Hamiltonian (2.68) induces a rotation by a J_z-dependent angle and viceversa:

$$\begin{pmatrix} S_x \\ S_y \\ S_z \end{pmatrix}_{\Delta t} = \begin{pmatrix} \cos(\chi J_z) & -\sin(\chi J_z) & 0 \\ \sin(\chi J_z) & \cos(\chi J_z) & 0 \\ 0 & 0 & 1 \end{pmatrix} \begin{pmatrix} S_x \\ S_y \\ S_z \end{pmatrix}_{\text{in}} \tag{2.69}$$

$$\begin{pmatrix} J_x \\ J_y \\ J_z \end{pmatrix}_{\Delta t} = \begin{pmatrix} \cos(\chi S_z) & -\sin(\chi S_z) & 0 \\ \sin(\chi S_z) & \cos(\chi S_z) & 0 \\ 0 & 0 & 1 \end{pmatrix} \begin{pmatrix} J_x \\ J_y \\ J_z \end{pmatrix}_{\text{in}}, \tag{2.70}$$

where the interaction strength is parameterized by $\chi = \Omega_m \Delta t$.

At the output of the interferometer, the operator $\boldsymbol{S}$ is transformed according to $\boldsymbol{S}_{\text{out}} = U^\dagger \boldsymbol{S}_{\text{in}} U$, where $U = e^{-i\Delta\phi S_y} e^{-i\chi S_z J_z}$ is the product of the transformations due to the interaction Hamiltonian H_m and of the mapping of phase shift $\Delta\phi$ to a population difference in the interferometer. We assume that both the atomic and the probe systems are initially prepared in a coherent spin state, $\langle \boldsymbol{S}_{\text{in}} \rangle = N\boldsymbol{e}_x/2, \langle \boldsymbol{J}_{\text{in}} \rangle = n\boldsymbol{e}_x/2$. According to the transformation (2.70), $\langle J_y(\Delta t) \rangle = n \langle \sin(\chi S_{z,\text{in}}) \rangle /2$. For $\chi \Delta S_{z,\text{in}} = \chi\sqrt{N}/2 \ll 1$, this expression can be approximated as $\langle J_y(\Delta t) \rangle \simeq \chi n \langle S_{z,\text{in}} \rangle /2$. The meaning of this relation is that $S_{z,\text{in}}$ can be measured through $J_y(\Delta t)$. As a result, we consider the operator

$$S_z' \equiv S_{z,\text{out}} - \frac{2}{\chi n} J_y(\Delta t) \tag{2.71}$$

which is the difference between the interferometer output and the result of the pre-measurement of $S_{z,\text{in}}$. We now show that this operator has, under certain conditions, reduced fluctuations compared to the shot noise. To compute the phase resolution we need the mean value $\langle S'_z \rangle$ and the variance $(\Delta S'_z)^2$. The mean value can be computed by taking the relation $\langle e^{i\chi S_{z,\text{in}}} \rangle = \cos^N(\chi/2)$ and recalling that $\langle J_y(\Delta t) \rangle \propto \langle \sin(\chi S_{z,\text{in}}) \rangle = \text{Im} \langle e^{i\chi S_{z,\text{in}}} \rangle = 0$ as expected because the average of pre-measurements on a state on the equator of the Bloch sphere vanishes. By using the transformation U defined above, $S_{z,\text{out}} = S_{z,\text{in}} \cos\Delta\phi + \sin\Delta\phi[\cos(\chi J_{z,\text{in}})S_{x,\text{in}} + \sin(\chi J_{z,\text{in}})S_{y,\text{in}}]$. As a result,

$$\langle S'_z \rangle = \frac{N}{2} \sin\Delta\phi \, \langle \cos(\chi J_{z,\text{in}}) \rangle = \frac{N}{2} \sin\Delta\phi \text{Re} \, \langle e^{i\chi J_{z,\text{in}}} \rangle = \frac{N}{2} \sin\Delta\phi \cos^n \frac{\chi}{2}. \tag{2.72}$$

Similarly, the variance is found to be [53]

$$\begin{aligned}(\Delta S'_z)^2 = \frac{N}{4}\cos^2\Delta\phi + \frac{N}{8}\left[N\left(1+\cos^n\chi - 2\cos^{2n}\frac{\chi}{2}\right) + 1 - \cos^n\chi\right]\sin^2\Delta\phi \\ + \frac{1}{2n\chi^2}\left[n(1-\cos^N\chi) + 1 + \cos^N\chi\right] - \frac{N}{\chi}\sin\frac{\chi}{2}\cos^{N-1}\frac{\chi}{2}\cos\Delta\phi.\end{aligned} \tag{2.73}$$

With these expressions we can compute the phase resolution as

$$\delta(\Delta\phi) = \frac{(\Delta S'_z)}{|\partial \langle S'_z \rangle / \partial\Delta\phi|} \simeq \frac{e^{\xi/2}}{N\sqrt{\xi}}, \tag{2.74}$$

where $\xi = n\chi^2/4$ and the minimum $\delta(\Delta\phi)$ is attained for $\xi = 1$. The final expression for the phase resolution is valid when $N\chi^2 \ll n^{-1/3}, N \gg 1, n \gg 1$. Remarkably, the scheme operates near the Heisenberg limit and exhibits a Heisenberg scaling as the minimum phase resolution is $\delta(\Delta\phi)_{\text{min}} = \sqrt{e}/N$. The noise reduction here relies on considering the difference between the final measurement and the initial measurement. While both these terms fluctuate at the shot noise limit, they are correlated and their difference has a fluctuation that is close to the Heisenberg limit. In other terms, the measurement of J_y prepares an atomic spin squeezed state whose mean S_z value fluctuates from trial to trial. However, if the outcome of the pre-measurement is not discarded, the prepared state is useful for the phase shift measurement.

The scheme described above is a case of a quantum nondemolition (QND) measurement. In general, a QND measurement is characterized by a number of criteria that we will briefly review here [54, 29]. As in the previous example, in a QND measurement there are two systems A and P that are characterized by the variables A_α and P_α. A is the *signal* system, the system to be measured or, in the previous case, the atomic system. P is the *probe* system or the system through which A is measured. A QND Hamiltonian can in general be cast in the following form

$$H_{\text{QND}} = H_A + H_P + H_I, \tag{2.75}$$

where H_A represents the dynamics of the signal system independent of the probe, H_B represents the dynamics of the probe system independent of the signal and H_I is the hamiltonian for the interaction of the probe with the signal. Through H_I, information about the signal is gained by measuring the probe. For the case analyzed above, $H_I = H_m = \hbar\Omega_m S_z J_z$. The conditions for a QND measurement of a variable A_α through the probe variable P_β are the following:

- Because A_α is to be measured, the interaction term must depend on a signal operator A_α, $H_I = H_I(A_\alpha)$.

- The measurement is of nondemolition-type (or back action-evading) if the interaction term does not alter the signal, or

$$[H_I, A_\alpha] = 0. \tag{2.76}$$

- In order to allow for information gain about the variable A_α, there has to exist a variable P_β, the measured variable, for which

$$[H_I, P_\beta] \neq 0. \tag{2.77}$$

  In other words, because the measurement relies on a change of P_β, the time derivative $\frac{d}{dt}P_\beta \propto [H_I, P_\beta]$ cannot vanish.

- In order for the successive outcomes of measurements of A_α to be predictable, the signal Hamiltonian must not be a function of A_β, the conjugated variable of A_α. If this was the case, because of the uncertainty relation between A_α and A_β, the successive evolution of A_α would be affected as $\frac{d}{dt}A_\alpha \propto [H_A(A_\beta), A_\alpha]$. This is the case, for example, in the measurement of the position of a free particle. At any given time the position can be measured with an arbitrary precision Δx thus implying a momentum uncertainty $\Delta p \geq \hbar/(2\Delta x)$. The increased momentum uncertainty deriving from a precise position measurement therefore affects the position itself at later times.

The simplest interaction Hamiltonian that fulfills the above requirements is of the form $H_I = CP_\alpha A_\alpha$. The interaction term proposed by Kuzmich, Bigelow and Mandel is exactly of this form.

We next provide a general treatment of the squeezing limits attainable through QND measurements [55]. We consider the measurement of the spin variable S_z through a probe variable that provides a pre-measurement and denote by M_{out} the corresponding measurement outcome. Next to this variable we consider the *unconditional* expectation value $\langle S_z \rangle$ which corresponds to the previous knowledge of the atomic state i.e. before any measurement is performed on the system. This is the case, for example, in the

interferometer, when we produce a coherent spin state pointing on the equator of the Bloch sphere. Here no measurement is performed but we know that $\langle S_z \rangle = 0$ because we applied a $\pi/2$-pulse to a state at the south pole. Based on the knowledge of the unconditional mean and on the result of the pre-measurement, our prediction of S_z, conditioned on the measurement outcome is the weighted average

$$\langle S_z \rangle_{M_{\rm out}} = w M_{\rm out} + (1-w) \langle S_z \rangle . \tag{2.78}$$

The value of the weight w that yields the best prediction is determined by the requirement that the *conditional* variance

$$\begin{aligned} (\Delta S_z)^2_{M_{\rm out}} &\equiv {\rm Var}[w M_{\rm out} + (1-w)\langle S_z \rangle - S_z] = \\ &= w^2 {\rm Var}(M_{\rm out}) + {\rm Var}(S_z) - 2w {\rm Cov}^2(M_{\rm out}, S_z) \end{aligned} \tag{2.79}$$

is minimized. This condition is attained for $w = {\rm Cov}(M_{\rm out}, S_z)/{\rm Var}(M_{\rm out})$ and yields the minimum

$$(\Delta S_z)^2_{M_{\rm out}} = \frac{{\rm Var}(M_{\rm out}){\rm Var}(S_z) - {\rm Cov}^2(M_{\rm out}, S_z)}{{\rm Var}(M_{\rm out})}. \tag{2.80}$$

After exchanging $M_{\rm out}$ and S_z in the above expression, we get the relation

$$(\Delta S_z)^2_{M_{\rm out}} = \frac{{\rm Var}(S_z)}{{\rm Var}(M_{\rm out})} (\Delta M_{\rm out})^2_{S_z} \tag{2.81}$$

between the conditional spin variance and the variance of the measurement outcomes when S_z is fixed. In other words, $(\Delta M_{\rm out})^2_{S_z}$ represents the measurement imprecision and its value determines the strength of the measurement.

We also note that, if the pre-measurement is unbiased, then the average of measurement outcomes with S_z fixed must be equal to S_z itself, $\langle M_{\rm out} \rangle_{S_z} = S_z$. Also, if the noise of the measurement with S_z fixed is independent on the noise of S_z, we have ${\rm Var}(M_{\rm out}) = (\Delta M_{\rm out})^2_{S_z} + {\rm Var}(S_z)$ and (2.81) becomes

$$(\Delta S_z)^2_{M_{\rm out}} = \frac{{\rm Var}(S_z)(\Delta M_{\rm out})^2_{S_z}}{(\Delta M_{\rm out})^2_{S_z} + {\rm Var}(S_z)}. \tag{2.82}$$

The above relation can therefore be used to determine the variance of the state prepared through the pre-measurement if the initial variance ${\rm Var}(S_z)$ and the measurement imprecision $(\Delta M_{\rm out})^2_{S_z}$ are known. In particular, we see that in the weak measurement limit, $(\Delta M_{\rm out})^2_{S_z} \gg {\rm Var}(S_z)$, the variance after the measurement is just the initial variance, $(\Delta S_z)^2_{M_{\rm out}} \simeq {\rm Var}(S_z)$. In the opposite and more relevant case of a strong measurement, $(\Delta M_{\rm out})^2_{S_z} \ll {\rm Var}(S_z)$, the conditional spin variance is set by the measurement imprecision, $(\Delta S_z)^2_{M_{\rm out}} \simeq (\Delta M_{\rm out})^2_{S_z}$.

We conlude that squeezing by QND measurements requires to induce an interaction Hamiltonian H_I that meets the criteria listed above and, in this condition, for a strong measurement, the amount of spin squeezing is determined by the measurement imprecision i.e. the pre-measurement atom number resolution.

2.3.3 Atomic spin squeezing by interaction with squeezed light

Another interesting scheme that can produce spin squeezed states in atomic ensembles involves the interaction with squeezed light. Under certain conditions it is possible to show that spin squeezing can be transferred from the light to the atoms. This scheme was considered in [56, 57] and implemented in [58]. In [57], in particular, the authors consider a V-type atom with one ground state $|0\rangle$ and two excited states $|1\rangle$ and $|2\rangle$. The $0-1$ transition is made to interact with a coherent state of the light and the $0-2$ transition is made to interact with a squeezed vacuum field. In their analysis, the authors consider the case where the amplitude of the coherent field is large compared to the squeezed vacuum fluctuations. In considering the fluctuations of the pseudo-spin system defined by the states $|1\rangle$ and $|2\rangle$, they show that when the squeezed light is completely absorbed and the atomic state is prepared in an eigenstate of S_z, the variance of a spin component in the xy plane is linked to the light field phase variance X^2 by

$$(\Delta S_{xy})^2 = \frac{1}{4}\langle S_z\rangle (4X^2+1). \tag{2.83}$$

If the field driving the $0-2$ transition is a vacuum field, then $X^2 = 1/4$ whereas for a squeezed vacuum $X^2 = 0$, $(\Delta S_{xy})^2 = \langle S_z\rangle /4$ so it is possible to attain 50 % of squeezing. The limiting factor for this scheme is set by atomic spontaneous emission.

A related scheme involving the transfer of squeezing from the light to the atomic ensemble was proposed in [59] in the framework of a Mach-Zehnder atom interferometer.

2.3.4 Experimental implementations of spin squeezed states

In this subsection we will attempt to list the main experimental achievements in the field of spin squeezing. However, because of the variety of techniques to achieve squeezing, the increasing interest in the field and the numerous publications, only a fraction of these results will be illustrated here.

The main distinction between the methods that achieve spin noise reduction can be made in terms of the kind of interaction that induces such reduction.

Spin squeezing methods based on interactions The first class of experiments that we consider is based on atomic interactions in Bose-Einstein condensates (BECs). These methods have become very attractive mainly because of the inherent long coherence times that are possible in a BEC and because of the strong atom-atom interactions that induce nonlinear interactions and therefore spin squeezing.

We start by considering a BEC that is loaded in an optical lattice and is therefore described by the Bose-Hubbard Hamiltonian

$$H = \gamma \sum_{i,j} a_i^\dagger a_j + \sum_i \epsilon_i n_i + \frac{g\beta}{2}\sum_i n_i(n_i-1), \tag{2.84}$$

where a_i is the annihilation operator for an atom in the lattice site i, and $n_i = a_i^\dagger a_i$ is the corresponding number operator. The interaction strength g is related to the s-wave scattering length a_s by $g = 4\pi a_s/m$, $\beta = \int d^3r|\phi(r)|^4$, where ϕ is the atomic wave function and finally we define the tunneling amplitude γ between the lattice sites i and j as

$$\gamma = \int d^3r\phi(r - r_i)\left[-\frac{\hbar^2\nabla^2}{2m} + U(r)\right]\phi(r - r_j), \tag{2.85}$$

where r_i is the position of the i-th lattice site and $U(r)$ is the lattice potential energy. In other words, the Hamiltonian (2.84) describes the tunneling from site i to site j (first term), the atomic energy in site i (second term) and the interaction energy due to collisions (third term).

The ability of this system to reduce the quantum fluctuations in an observable is essentially captured by the superfluid-to-Mott insulator transition [60]. The superfluid phase corresponds to the strong tunneling regime (small lattice depth) where $g\beta/\gamma \ll 1$. In this case, the interaction term (proportional to $g\beta$) is negligible and the ground state of the superfluid system can be written as

$$|\psi_{\mathrm{SF}}\rangle \propto \left(\sum_{i=1}^{M} a_i^\dagger\right)^N |0\rangle \tag{2.86}$$

where N is the number of atoms and M is the number of lattice sites. The superfluid ground state wavefunction therefore describes wavepackets that are spread over the entire lattice with a long-range phase coherence. It can be shown that the on-site atom number fluctuations follow a Poisson distribution, as in a coherent spin state, so that the variance is $(\Delta n_i)^2 = \langle n_i\rangle$.

As the lattice depth (or $g\beta/\gamma$) is increased above a critical point, the system enters the Mott insulator phase. In the most extreme case we would neglect the tunneling term, $\gamma = 0$, and find the system ground state as

$$|\psi_{\mathrm{MI}}\rangle \propto \prod_{i=1}^{M}(a_i^\dagger)^{n_i}\,|0\rangle\,. \tag{2.87}$$

Because this is a product of on-site Fock states, in the Mott insulator phase, the behaviour is opposite to that of the superfluid: exact numbers of atoms are localized at individual lattice sites and as a result, no phase coherence exists among them. The signature of number squeezing was observed in [61] as an increased phase variance. This was measured by releasing the atoms from the optical lattice and by observing the resulting interference.

The essential physics of the above results is captured by a simple two-well model, in which case the Bose-Hubbard Hamiltonian reduces to

$$H = \gamma(a_{\mathrm{L}}^\dagger a_{\mathrm{R}} + a_{\mathrm{R}}^\dagger a_{\mathrm{L}}) + \frac{g\beta}{2}\left[(a_{\mathrm{L}}^\dagger a_{\mathrm{L}})^2 + (a_{\mathrm{R}}^\dagger a_{\mathrm{R}})^2\right], \tag{2.88}$$

where $a_{\mathrm{L}}(a_{\mathrm{R}})$ is the annihilation operator for an atom in the left (right) potential well. This system can be viewed as a two-mode system represented by the two wells. It is therefore possible to associate angular momentum operators to the annihilation operators, according to the Schwinger representation [62]

$$S_x = \frac{1}{2}(a_{\mathrm{L}}^{\dagger}a_{\mathrm{R}} + a_{\mathrm{R}}^{\dagger}a_{\mathrm{L}}), S_y = \frac{1}{2i}(a_{\mathrm{L}}^{\dagger}a_{\mathrm{R}} - a_{\mathrm{R}}^{\dagger}a_{\mathrm{L}}), S_z = \frac{1}{2}(a_{\mathrm{L}}^{\dagger}a_{\mathrm{L}} - a_{\mathrm{R}}^{\dagger}a_{\mathrm{R}}), \tag{2.89}$$

so that the two-well Hamiltonian becomes

$$H = 2\gamma S_x + \chi S_z^2 + \frac{\chi N^2}{4}, \tag{2.90}$$

where $\chi = g\beta$ and N is the total number of atoms. The result is therefore the one-axis twisting Hamiltonian.

Other experiments were able to prove the reduction in atom number number fluctuations directly. For example, in [63], the authors used spin-changing collisions as a nondestructive probe for the presence of atom pairs. In many cases it was observed that number squeezing could extend the coherence times [64]. In [65] an imaging system with a 1 μm resolution was implemented that could resolve the occupation of the sites in an optical lattice and therefore prove atom number squeezing directly by imaging. Interestingly, in this experiment, squeezing was attained between two states of the external atomic motion through the repulsive interactions in a Bose-Einstein condensate.

The first demonstration of an atom interferometer performing beyond the Standard Quantum Limit was reported in [66], where a complete Ramsey sequence was simultaneously performed on atoms trapped in six wells of a one-dimensional optical lattice and in two internal states. In this system, squeezing occurs within the interferometer and in particular in a nonlinear beam splitter. The Hamiltonian describing the interactions of the interferometer can be written as $H = \hbar\Delta\omega_0 J_z + \hbar\chi J_z^2 + \hbar\Omega J_\phi$, where the first term is a precession term describing the atomic free evolution, the second term describes the interaction-induced one-axis twisting and the third term accounts for the spin rotations during atomic state manipulations. By controlling the interaction strength between atoms in the two states and therefore χ through a narrow Feshbach resonance, an atom interferometer operating beyond the Standard Quantum Limit was implemented, with a metrological gain of 8.2 dB.

Spin squeezing in BECs was also demonstrated in an atom chip [67] as a viable option for the implementation of atomic clocks beyond the shot noise limit. In this experiment, an efficient technique that allows tuning of the nonlinear coefficient χ was demonstrated. This was based on the control of the overlap between the wavefunctions of two atomic modes in a state-dependent potential. By spatially separating the two modes in the two internal states, a situation where χ is conveniently large can be reached.

The results reported in [65, 67] are relevant in the field of atom interferometry with spatially separated arms in that they provide squeezing between external degrees of free-

dom. In this thesis, however, we will mainly focus on the generation of squeezed states of the external atomic motion of free particles via optical means. In this situation we attempt to create entanglement useful for quantum metrology *directly* onto the external degrees of freedom i.e. without intermediate steps that rely on internal degrees of freedom. It remains nevertheless true that one can envisage schemes where internal-state entanglement is mapped onto the external atomic motion. While this might extend many experimental implementations, we will consider one such example, when the interferometer is driven on an optical clock transition, as briefly illustrated in Subsection 5.4.2.

Spin squeezing methods based on the interaction with electromagnetic radiation Another important class of experiments that can achieve spin squeezing relies on the interaction between the atomic ensemble and laser light.

Soon after the proposal by the Polzik group [57], squeezing by transfer from light to the atomic ensemble was demonstrated with cesium atoms [58] attaining an improvement of 3 % beyond the Standard Quantum Limit.

One of the most successful techniques that achieve spin squeezing in atomic ensembles is that of quantum nondemolition (QND) measurements. A remarkable implementation of these methods was reported in [68]. In this experiment, a continuous QND measurement was performed by monitoring the Faraday rotation of the magnetic moment of 10^7 cesium atoms. Here a probe laser beam, detuned from the $6S_{1/2}, F = 4$ - $6P_{3/2}$ transition is polarization analyzed by measuring the differential photocurrent of two detectors placed at the output of a polarizing beam splitter. The outcome of the measurement therefore projects the collective state into a state with reduced spin uncertainty and 70 % of noise reduction was observed.

One of the key figures of merit in light-based QND measurements is the atomic optical depth. This parameter can be greatly enhanced through an optical resonator [69]. Indeed, while the above squeezing experiment was performed in free space, in [70], the authors demonstrated a QND measurement of the relative population of the ^{87}Rb clock states $|F = 1, m_F = 0\rangle, |F = 2, m_F = 0\rangle$ in a high-finesse optical cavity. As a result, a 3.8 dB relative population variance reduction compared to the atom shot noise was observed. Cavity-aided QND measurements were also performed in [71]. Here the measurement of the relative population of the two rubidium clock states was attained by tuning the probe laser field between the two optical transitions $|^5S_{1/2}, F = 1, m_F = 0\rangle$ - $|^5P_{3/2}\rangle$ and $|^5S_{1/2}, F = 2, m_F = 0\rangle$ - $|^5P_{3/2}\rangle$. With the laser field also tuned to the slope of the cavity mode, relative population variations between the two clock states are translated into transmitted power variations through variations of the atomic index of refraction. In this experiment, a noise reduction of 3.0 dB was observed. This same measurement scheme also allowed to attain an effectively nonlinear atom-atom interaction mediated by light. The essence of this method can be understood by considering the Hamiltonian for the AC

Stark shift induced by the probe field onto the atoms. When the probe field is detuned halfway between the two optical transitions as described above, the Stark shift is given by $H \propto c^\dagger c S_z$, where $c^\dagger c$ is the operator for the number of intracavity photons and S_z is the collective spin operator. In the linear approximation, tuning the probe field to the slope of the cavity mode induces intracavity power variations that are proportional to S_z, $c^\dagger c \propto S_z$. The effective interaction, $H \propto S_z^2$, therefore induces one-axis twisting through atomic interactions mediated by the intracavity light [72, 73, 74]. This technique was able to demonstrate generation of spin squeezed states of the ^{87}Rb clock states with 5.6 dB improvement compared to the Standard Quantum Limit. This same method was then used to demonstrate a squeezed microwave atomic clock which, for averaging times up to 50 s achieves a given precision 2.8 times faster than a clock operating at the Standard Quantum Limit [75].

Another application of QND-induced squeezed states was implemented in [76]. This experiment consisted in the nondestructive measurement of photon Faraday rotation in order to produce squeezed states. Rapid probing, realized through a series of 1 μs-long measurement pulses, allowed the implementation of a high-bandwidth atomic magnetometer.

An atomic clock beyond the Standard Quantum Limit was also reported in [77], where cesium atoms loaded in a dipole trap were dispersively probed. This was attained by sending two laser beams to the atoms, one off-resonant with the $|6S_{1/2}, F = 3, m_F = 0\rangle$ - $|6P_{3/2}, F' = 2\rangle$ transition and the other off-resonant with the $|6S_{1/2}, F = 4, m_F = 0\rangle$ - $|6P_{3/2}, F' = 5\rangle$ transition. These two frequency components are phase shifted by an amount proportional to the number of atoms in the two clock states. The differential phase shift is then recorded at the output of an optical Mach-Zehnder interferometer. This technique is analogous to the measurement of the Faraday rotation in other experiments. The photons in the two modes can be associated with a spin operator $\boldsymbol{J}$ whose y component is measured via the QND method, as in (2.71).

The presence of many atomic levels in the experiments described here can be regarded as a limit for coherence times in spin squeezed samples because of the presence of loss channels. In this sense, in [78], 1.8 dB of spin squeezing was attained by QND measurements of Faraday rotation of ^{171}Yb atoms. The interest of this result lies in the simple nuclear spin one-half structure in the ground state of these atoms. This results in both reduced decoherence channels and in a highly suppressed sensitivity to external magnetic fields. The reported QND measurements were short (100 ns) compared to the decoherence time. Also, because ^{171}Yb is a promising candidate for optical atomic clocks, after squeezing in the ground state, mapping to the $^1S_0$ - $^3P_0$ clock transition would result in a spin squeezed optical atomic clock.

Measurement-induced spin squeezing does not require the probe field to be off-resonant with an optical transition. Indeed, as we will see in the following of this thesis, the amount

of spin squeezing attainable by optical techniques is ultimately set by the atomic sample optical depth. An important proof of such a resonant regime can be found in [79]. In this work, the relative population measurement is achieved by a frequency measurement. When the mode of an optical cavity is tuned to the resonance of an optical transition, the interaction results in dressed cavity modes corresponding to two cavity transmission peaks with a frequency separation, the vacuum Rabi splitting, proportional to $\sqrt{N}$, the square root of the number of atoms in the ground state. The authors realized a measurement of such a frequency difference in ^{87}Rb atoms through a probe resonant with the $|5S_{1/2}, F = 2\rangle$ - $|5P_{1/2}\rangle$ transition. The vacuum Rabi splitting was then measured by simultaneously scanning two frequency components across the two transmission features. This method measures the number of atoms in the $|\uparrow\rangle = |5S_{1/2}, F = 2\rangle$ state. In order to achieve a complete measurement of S_z, a microwave π-pulse is applied that swaps $|\downarrow\rangle = |5S_{1/2}, F = 1\rangle$ and $|\uparrow\rangle$ so that repeating the Rabi splitting measurement yields the number of atoms in $|\downarrow\rangle$. As a result, a conditional spin squeezing of 3.4 dB was attained. In [80], through a similar setup, up to 10 dB of spin squeezing were observed. The main upgrade consisted in a large suppression of spin-changing (Raman) events induced by the probe field. This was attained by considering the two-level system $|\downarrow\rangle = |5S_{1/2}, F = 1, m_F = +1\rangle$, $|\uparrow\rangle = |5S_{1/2}, F = 2, m_F = +2\rangle$ and by probing on the cyclic $|\uparrow\rangle = |5S_{1/2}, F = 2, m_F = +2\rangle$ - $|\uparrow\rangle = |5P_{3/2}, F' = 3, m_{F'} = +3\rangle$ transition.

Finally, in the same setup it was possible to establish a record in spin squeezing of 17.7 dB by measuring the dispersive frequency shift of the cavity mode tuned to the blue of the $|\uparrow\rangle$ - $|5P_{3/2}, F' = 3, m_{F'} = +3\rangle$ transition [30]. In this work, the transformation of conditional squeezing to deterministic squeezing was also demonstrated by real-time feedback. This consisted in acquiring the outcome of the QND measurement and applying a corresponding microwave rotation of the Bloch vector that produces a target state deterministically, retaining 7.4 dB of spin squeezing. A related scheme using dispersive detection in an optical cavity with homogeneous atom-light coupling allowed 20 dB of spin squeezing [31]. By implementing these techniques, an important step towards the implementation of spin squeezing techniques in separated-arm atom interferometers was taken. In particular, because the spatial inhomogeneity of the probe standing wave in an optical cavity leads to substantial squeezing reduction, letting the atoms fall under gravity can average the probe field spatial dependence and produce spatially homogeneous entanglement. As a result, 11 dB of spin squeezing were attained [81].

2.4 Conclusions and discussion

In this Chapter we established the concept of spin squeezing and its deep relation with multi-particle entanglement. We explored many proposals and implementations of spin

squeezed states in ensembles of neutral atoms and saw that, in some cases, squeezed states can be successfully implemented in Ramsey interferometers as microwave atomic clocks. In this community there is also some effort in order to implement squeezed states of optical atomic clocks which could boost the performance of the world's best clocks [82]. However, only a few of these methods can provide squeezed states that are useful for separate-arm atom interferometers. This will be the subject of the following part of this thesis. In particular, we will consider the atomic system that we consider to be the most promising for atom-interferometry-based gravity measurements: the strontium atom. In the following two Chapters we will illustrate the significant progress which was obtained in our group in manipulating this species in atom interferometers. In particular, this atom offers a simple system that is immune to many external perturbations that affect atom interferometers based on alkaline atoms. Moreover, because of its small scattering cross section, strontium atomic states can preserve their coherence for extremely long times, thereby allowing for long interrogation times. All these properties make this atom a very promising candidate for high-sensitivity atom interferometry. As we will see, however, taking the additional step of implementing strontium squeezed states useful for atom interferometry presents a number of challanges which will be addressed. In particular, because of the electronic structure of the atom and the resulting need to operate an interferometer with momentum states i.e. states differing only by their velocity, we will consider techniques that can produce squeezing for this new class of states. In some sense, our proposed methods inherit the progress done over the years in spin squeezing. For example, the use of the optical cavity to enhance the signal in nondemolition measurements will be a fundamental ingredient. Among the methods available in the literature, we find that the optical schemes are well suited for atom interferometers for precision measurements.

Chapter 3

Properties and laser cooling of strontium atoms

3.1 The strontium atom

Strontium is an alkaline-earth atom with atomic number $Z = 38$ and with very special properties that make it suitable both for experiments of metrology and of quantum simulation. Like many alkaline-earth and alkaline-earth-like atoms, strontium has a number of optical transitions with very different properties. In this atom, nearly all optical transitions can be addressed through current laser technology. Among the optical transitions, the $^1S_0$-$^3P_0$ clock transition has attracted a considerable interest because of its immunity to external perturbations and because of its ultra-narrow linewidth. It is in fact this transition that is employed in today's best atomic clocks [25, 24, 82]. However, up to a few years ago, this atom was never used in atom interferometers for inertial measurements. It is a goal of our group to study the performance of this species in atom interferometers and to develop the necessary tools of atom optics that can allow it to be implemented in today's best atom interferometers.

Nuclear and electronic properties There are four stable isotopes of strontium, three are bosons and one is a fermion. The three bosons have zero nuclear spin whereas the fermion has a relatively large nuclear spin $I = 9/2$. Our work was mainly concentrated on the most abundant ^{88}Sr isotope. Table 3.1 reports the main properties of the four stable isotopes.

There are however more than 20 unstable isotopes of Sr. One of the most important ones is ^{90}Sr, which is produced in nuclear plants and nuclear bombs as a product of the fission of uranium and is extremely dangerous.

As an alkaline-earth element, strontium has an electronic structure with two valence electrons in the outer shell. This structure determines the main properties of the optical

Isotope	**Abundance**	**Mass**	**Nuclear spin**	**Scattering length** (a_0)
^{84}Sr	0.56(1)%	83.913425(3)	0	122.76(9)
^{86}Sr	9.86(1)%	85.909260731(9)	0	798(12)
^{87}Sr	7.00(1)%	86.908877497(9)	9/2	97.37(7)
^{88}Sr	82.58(1)%	87.905612257(10)	0	−2.00(27)

Table 3.1: Main properties of the stable strontium isotopes

transitions in this atom. There are indeed many other atomic systems that share these same properties: the alkaline-earth atoms and the alkaline-earth-like atoms. These are Be, Mg, Ca, Ba, Ra, Zn, Cd, Cn, Yb and No.

The two-electron structure of strontium determines the presence of two nearly independent groups of levels, the singlet states with total electronic spin $S = 0$ and the triplet states with electronic spin $S = 1$. The level diagram and the optical transitions of strontium are shown in Fig. 3.1. Within a single group, one can find relatively broad dipole-allowed transitions. The most important of these transitions is the blue $^1S_0$-$^1P_1$ transition at 461 nm, with a linewidth, measured through photoassociation spectroscopy [83], $\Gamma = 2\pi \times 30.5$ MHz. Because of the large photon scattering rate of this transition, it allows for fast deceleration, cooling and trapping of atoms.

There are however narrow intercombination transitions, where the total spin S changes. The most important of these transitions connect the $^1S_0$ state with the ^3P_J manifold with $J = 0, 1, 2$. Because in these transitions an electron changes spin, they are forbidden by the dipole selection rules. The $^3P_1$ state acquires a finite lifetime due to the spin-orbit interaction whose strength increases for heavier atoms. In Sr it couples the $^3P_1$ and the $^1P_1$ state thereby allowing for a decay through the electric dipole interaction. The resulting lifetime was measured through the spatial decay of the fluorescence in an atomic beam [84] to be 21.3 μs, corresponding to a linewidth $\Gamma = 2\pi \times 7.5$ kHz. This transition allows for efficient optical cooling, called narrow-line cooling where temperatures of about 300 nK can be reached [85, 86]. The properties of this transition also allowed the first demonstration of a degenerate quantum gas by laser cooling [87].

The $^3P_0$ state, also known as the *clock* state because of its implementation in optical atomic clocks, has a very long lifetime. In bosonic strontium, the main radiative decay path is through a two-photon E1M1 (electric dipole and magnetic dipole) transition which can mediate the parity change between the $^1S_0$ and $^3P_0$ states. The resulting lifetime is 5800 years. In the fermion, through hyperfine coupling, the nuclear spin couples the $^3P_0$ state with states that have the same parity and electronic angular momentum $J = 1$. The most important of these are $^1P_1$ and $^3P_1$ which decay through the electric dipole

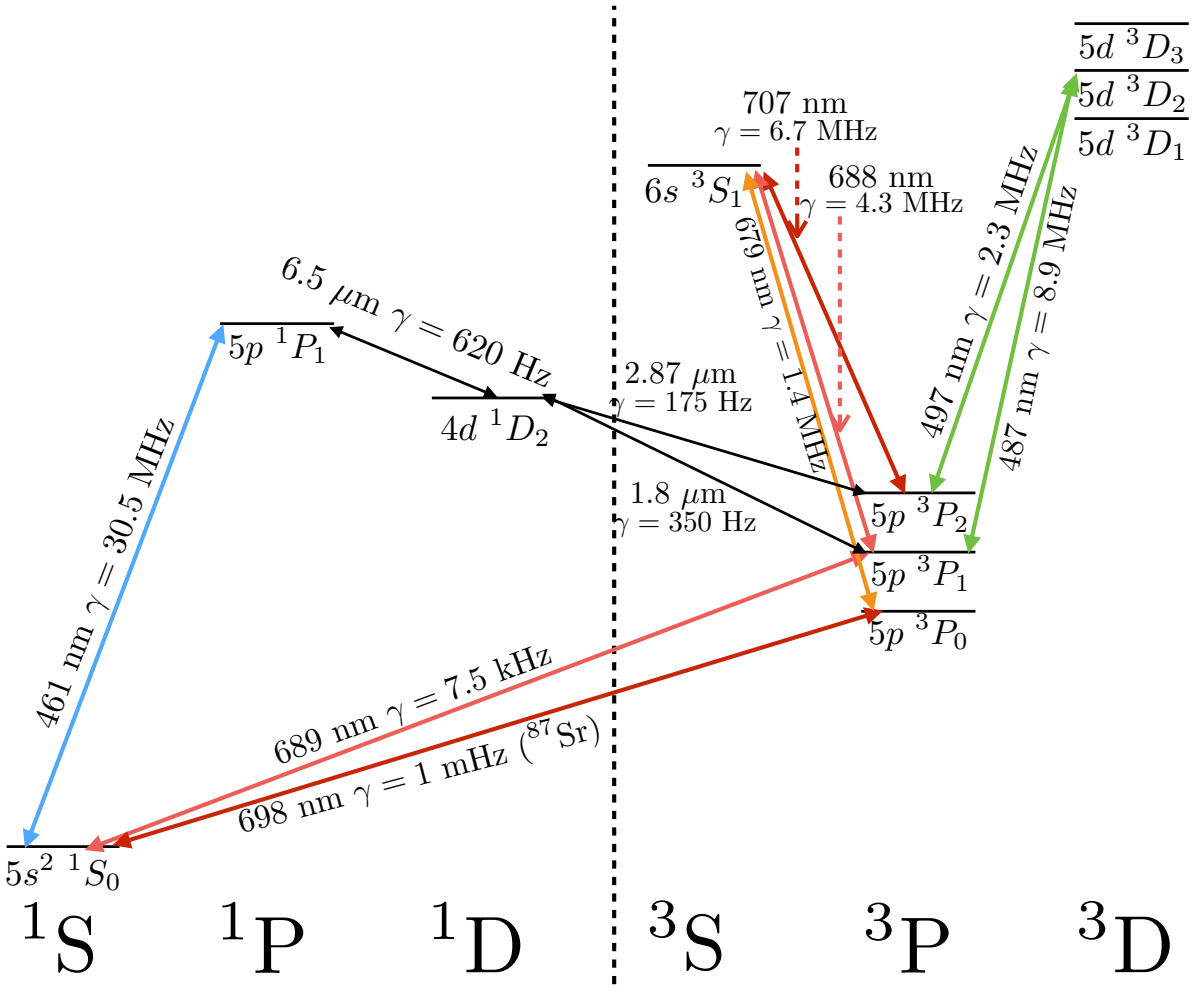

Figure 3.1: Strontium partial level diagram and optical transitions for cooling, trapping, Bragg diffraction and spin squeezing. The transition strengths are reported in terms of the reduced linewidth $\gamma = \Gamma/(2\pi)$, where Γ is the excited state decay rate.

interaction. This results in an estimated lifetime of about 150 s or a linewidth $\Gamma = 2\pi \times 1$ mHz [88].

Finally, the dominant decay channel of the $^3P_2$ state to the ground $^1S_0$ state is through an M2 (magnetic octupole) transition with a predicted lifetime of 1000 s and a measured lifetime of 500 s. Interestingly, this is one of the longest lifetimes ever measured in a laboratory [89]. The measurement was achieved by accumulating the metastable atoms in a magnetic trap and by detecting the rare decay events by trapping the decayed atoms in a magneto-optical trap.

During optical cooling of strontium on the broad $^1S_0$-$^1P_1$ transition, a small fraction of the atoms, 1 out of 150000, is lost, for every photon scattering event, to the metastable $^3P_2$ state through the $^1D_2$ state. While this process can profitably populate the metastable state, it usually limits the lifetime of the cooled and trapped sample. As a result, it is

Transition	λ (nm)	ν (THz)	$\Gamma/(2\pi)$	$I_{\rm sat}$ (mW/cm^2)	$a_{\rm max}/g$	v_r (mm/s)
$^1S_0$-$^1P_1$	460.862	650.504	30.5 MHz	40.7	9.6×10^4	9.9
$^1S_0$-$^3P_1$	689.449	434.829	7.5 kHz	3.0×10^{-3}	16	6.6
$^1S_0$-$^3P_0$	698.446	429.228	1 mHz	4×10^{-10}	2×10^{-6}	6.5
$^3P_0$-$^3S_1$	679.289	441.333	1.4 MHz	0.58	3.0×10^3	6.7
$^3P_1$-$^3S_1$	688.021	435.732	4.3 MHz	1.7	9.1	6.6
$^3P_2$-$^3S_1$	707.202	423.913	6.7 MHz	2.5	1.4×10^4	6.4
$^3P_1$-$^3D_2$	487.385	615.104	8.9 MHz	10	2.7×10^4	9.3
$^3P_2$-$^3D_2$	496.933	603.285	2.3 MHz	2.5	6.7×10^3	9.1

Table 3.2: Properties of the main optical strontium transitions

often necessary to repump the atoms to the ground $^1S_0$ state. This can be achieved in a number of ways. In our experiments we employed one of two options where both make use of dipole-allowed transitions within the triplet states. One possibility is to repump the atoms from the $^3P_2$ state to the $^3P_1$ state through the 707 nm transition that connects to the excited state $5s6s\,^3S_1$. From the $^3P_1$ state the atoms decay back to the ground state. A fraction of the atoms excited to the $^3S_1$ state, however decays to the $^3P_0$ state and a second laser is then added, at 679 nm, resonant with the $^3P_0$ - $^3S_1$ transition. From the $^3S_1$ state, the atoms decay back to $^3P_1$, through the 688 nm transition. Another option is repumping through the $5s5d\,^3D_2$ state with the 497 nm transition. Here a single laser is sufficient and the atoms are pumped to the $^3P_1$ state by decay on the 487 nm transition. All these transitions are dipole-allowed with a linewidth of a few MHz.

In Table 3.2 we report some of the main properties of the strontium optical transitions, including the wavelength λ, the frequency $\nu = c/\lambda$, the linewidth Γ, the saturation intensity $I_{\rm sat} = 2\pi^2\hbar c\Gamma/(3\lambda^3)$, the maximum acceleration arising from radiation pressure in units of gravity acceleration $a_{\rm max}/g = \hbar k\Gamma/(2g)$ and the recoil velocity $v_r = \hbar k/m$, where $k = 2\pi/\lambda$ is the wavenumber and m is the atomic mass.

The vanishing electronic and nuclear angular momenta of the ^{88}Sr isotope in the ground state along with the small s-wave scattering length motivate the interest in implementing atom interferometers with this species. The absence of angular momentum, on the one hand, is a fundamental aspect in the implementation of atomic sensors with an inherent robustness against external electromagnetic perturbations. The small scattering cross section, on the other hand allows for the observation of long coherence times of quantum superpositions [90, 91, 20].

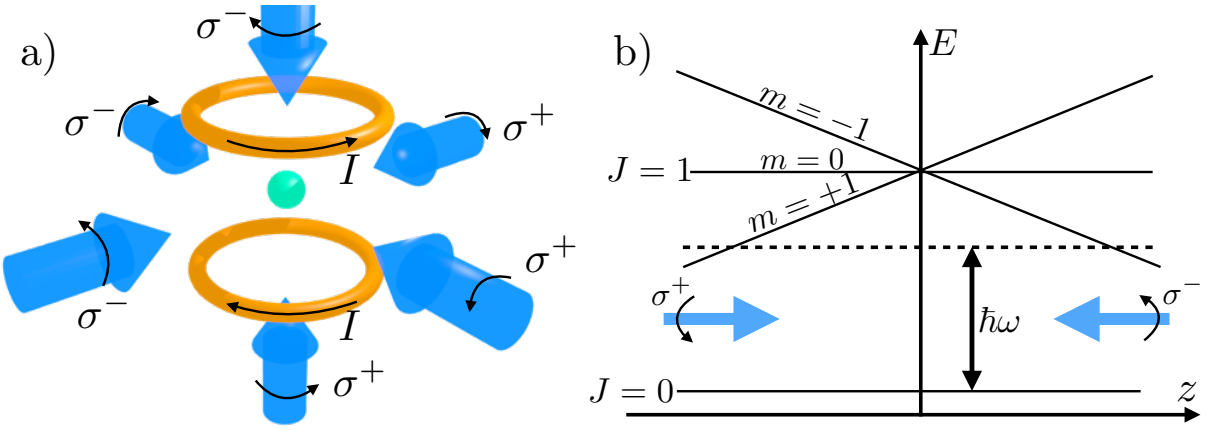

Figure 3.2: a) Schematic representation of the MOT setup with three orthogonal pairs of counterpropagating laser beams with opposite polarizations and the anti-Helmholtz coils used to generate the magnetic field gradient. b) Position-dependent Zeeman shift of the excited state with angular momentum $J = 1$. This condition generates an elastic force that concentrates the atoms at the trap center, with zero magnetic field.

3.2 Laser cooling and trapping of strontium atoms

In order to perform atom interferometry experiments with strontium atoms, it is necessary to reduce the atomic kinetic energy to temperatures on the order of 1 μK, while working with reasonably large atom numbers. This result is achieved in a magneto-optical trap (MOT), through two successive cooling stages, operating on the broad $^1S_0$-$^1P_1$ transition and on the narrow $^1S_0$-$^3P_1$ transition. The goal of the first stage, the so-called *blue MOT*, is to collect a large number of atoms with a relatively large temperature. In the second stage, the *red MOT*, atoms from the blue MOT are further cooled and large densities are reached owing to the narrow linewidth of the red $^1S_0$-$^3P_1$ transition.

3.2.1 Atomic beam slowing and first cooling stage

In a standard setup, the atomic source is provided by a strontium oven which, heated at a temperature $T \simeq$400 °C, produces a well-collimated atomic beam with most probable velocity $v_{\mathrm{mp}} = \sqrt{3k_BT/m} \simeq 400$ m/s.

In order to gain the ability of cooling the atoms, it is necessary to reduce the large velocity v_{mp} to a level where the following cooling stage can capture a sizeable number of atoms. This can be achieved in a Zeeman slower, where combining a spatially varying magnetic field and a laser beam at 461 nm that propagates opposite to the atomic beam results in a substantial velocity reduction. Because of the large atomic deceleration a due to radiation pressure on the $^1S_0$-$^1P_1$ transition (see Table 3.2), the stopping length

$L_{\text{stop}} = v_{\text{mp}}^2/(2a)$ is typically in the range 20-40 cm. However, as the atoms are decelerated, the Doppler effect shifts the resonance frequency and slowing would only be effective on a small part of the overall potential stopping length. The spatially variable magnetic field is used to accordingly shift the atomic resonance in order to compensate the Doppler effect, thus maintaining the atoms on resonance over the full length. As a result of this process, the atomic beam is decelerated to a velocity that does not exceed the capture velocity of the following cooling stage, the blue MOT.

The blue MOT operates on the dipole-allowed $^1S_0$-$^1P_1$ transition and is realized in a standard way [92] by three orthogonal pairs of counterpropagating laser beams, red detuned from atomic resonance, with opposite circular polarizations (see Fig. 3.2). In the presence of a magnetic field gradient, the atomic motion can be described as a damped harmomic oscillator. The final temperature is limited by the rate of spontaneous emission events and is determined by the Doppler limit $T_D = \hbar\Gamma/(2k_B) = 730$ μK [92], where k_B is Boltmann's constant.

In our experiments, with a magnetic field gradient of about 50 G/cm, intensity on the order of the saturation intensity and a red detuning equal to the transition linewidth, we achieve 1×10^8 atoms at a temperature of 1 mK.

As already discussed, the lifetime of the trapped atomic sample is limited by shelving into the $^3P_2$ metastable state. In our experiments, we recycle the lost atoms through two repumping lasers at 679 nm and 707 nm.

3.2.2 Second cooling stage: narrow line cooling

After collecting a large number of atoms in the blue MOT, further cooling is necessary. This is achieved through the $^1S_0$-$^3P_1$ transition at 689 nm which has opposite properties compared to the blue transition. Indeed, the linewidth Γ is comparable to the single-photon recoil frequency. As a result, in the absence of power broadening, one scattering event is sufficient to shift the transition out of resonance through the Doppler effect induced by the photon recoil. As a result, Doppler cooling on this transition can reduce the atomic temperature to the μK level with large atomic densities owing to the reduced resonant photon reabsorption [85]. Moreover, this transition can exert a maximum force that is only 16 times larger than gravity's force (Table 3.2) and is therefore barely sufficient to hold the atoms against gravity.

In Fig. 3.3 a) and b) the qualitative behaviour of the position-dependent force and potential for the blue and the red transitions in a magneto-optical trap is illustrated.

In the blue MOT, the scattering rate is strong enough that gravity acceleration plays a negligible effect (blue lines in Fig. 3.3 a) and b)). In the red MOT, the narrow linewidth causes instead a box-shaped potential whose variation is comparable to the gravity potential, which results in an additional tilt. When equilibrium is reached, the atomic cloud

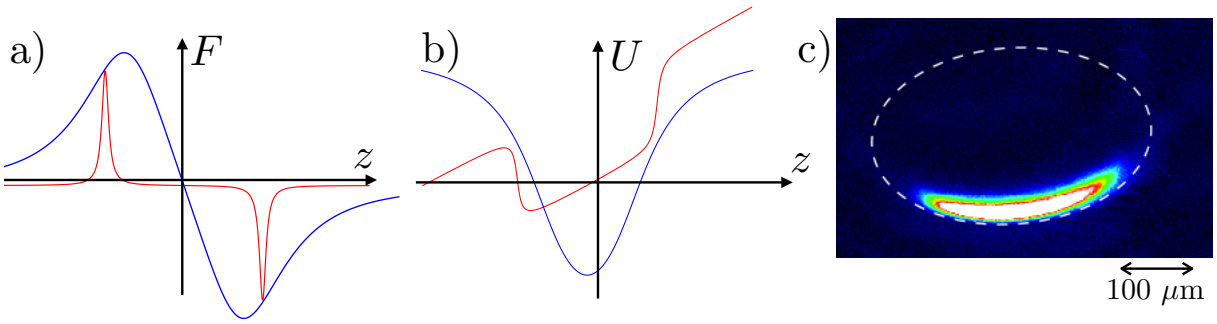

Figure 3.3: a) Position-dependent radiation pressure force in the presence of a magnetic field gradient for the blue transition (blue line) and for the red transition (red line). b) Corresponding potential energy for zero atomic velocity. The z axis is positively oriented in a direction opposite to gravity acceleration. a) and b) only illustrate the qualitative behaviour of the force and the potential and are not to scale. c) Absorption image of the red MOT, flattened because of the gravity force.

is concentrated at the bottom of the tilted square well (red lines in Fig. 3.3 a) and b)) and is flattened due to gravity as seen in Fig. 3.3 c).

In order to effectively transfer the atoms from the blue to the red MOT, an intermediate stage is introduced where the red and the blue MOT beams are simultaneously present. Efficient transfer is obtained by broadening the red laser spectrum, in order to capture the wide range of velocity classes of the blue MOT. In our experiments, the spectrum is broadened for 200 ms through a sinusoidal modulation with 8 MHz modulation depth, resulting in 400 sidebands around the carrier frequency, with an intensity per sideband that is larger than the saturation intensity. At this point, the blue beams are turned off and the broadband phase in maintained for 50 ms. After turning the modulation off, all the optical power is concentrated into the carrier, which broadens the atomic line by power. Subsequently, the intensity is decreased to the saturation intensity and the laser frequency approaches resonance. With a final red detuning of about 200 kHz from atomic resonance, the final temperature can approach the recoil limit $T_r = (\hbar k)^2/(2Mk_B) = 230$ nK, where k is the wavenumber. Remarkably, on the intercombination transition the Doppler temperature $T_D = 180$ nK is smaller than the recoil limit. In our experiments, we achieve a sample of about 5×10^6 atoms at a temperature of 1.2 μK. The size of the atomic cloud (see Fig. 3.3 c)) is 50 μm in the vertical and 300 μm in the horizontal direction full width at half maximum (FWHM).

Chapter 4

Atom interferometry with strontium atoms

In this Chapter we will discuss our main experimental achievements in the implementation of strontium atom interferometers. We will present atom interferometers that operate both on a broad dipole-allowed transition and on a narrow forbidden transition and show that measurements of gravity and of gravity gradients can be implemented. This work contitutes the basis of our proposal for an atom interferometer operating beyond the Standard Quantum Limit.

4.1 Matter-wave interferometry

In an atom interferometer, a wavepacket is coherently split and recombined. At the output of the interferometer, the phase difference accumulated between the two separate arms is transformed into a population difference between two atomic levels. The essence of an atom interferometer is captured by the Mach-Zehnder sequence, where beam splitters are used to split and recombine the wavepacket and mirrors are used to redirect the atomic trajectories.

Many of the features of the Mach-Zehnder interferometer are captured by its optical counterpart which we briefly describe here.

The optical Mach-Zehnder interferometer is represented in Fig. 4.1 a), where a light field with electric field $E(t)$ enters a beam splitter (BS1) and is separated in two arms that are redirected by the mirrors (M) and recombined through the second beam splitter (BS2). The two paths of the interferometer will generally have different lengths z_1 and z_2 so that at the second beam splitter, the two fields will be delayed by a time z_1/c and z_2/c, where c is the speed of light. As a result, because of the superposition principle, one of the outputs of the second beam splitter can be written as

$$E_{\text{out1}}(t) = RT[E(t - z_1/c) + E(t - z_2/c)] \tag{4.1}$$

where R and T are the amplitude reflection and transmission coefficients of the beam splitters, assumed to be identical for the two splitters. The output intensity is then given by

$$I_{\text{out1}} = \frac{1}{2}\varepsilon_0 c|RT|^2 \left\{|E(t_1)|^2 + |E(t_2)|^2 + 2\text{Re}[E^*(t_1)E(t_2)]\right\}, \tag{4.2}$$

where $t_{1,2} = t - z_{1,2}/c$. After averaging over one cycle of the field's oscillation, we get

$$\langle I_{\text{out1}}\rangle = \frac{1}{2}\varepsilon_0 c|RT|^2 \left\{\langle|E(t_1)|^2\rangle + \langle|E(t_2)|^2\rangle + 2\text{Re}\,\langle E^*(t_1)E(t_2)\rangle\right\}. \tag{4.3}$$

The first two terms represent the average intensity of the two arms independently. The third term, the interference term, yields the interference fringes as a function of the delay difference $\tau = t_2 - t_1$. As a result, the interferometer converts a phase shift between the two arms in an intensity variation at the output of the two arms. Because the third term represents the correlation of the field at different times, this is linked to the first-order correlation function $g^{(1)}$. In particular,

$$g^{(1)}(\tau) \equiv \frac{\langle E^*(t)E(t+\tau)\rangle}{\langle|E(t)|^2\rangle}. \tag{4.4}$$

The correlation function $g^{(1)}$ expresses the degree of coherence of the light field i.e. the degree to which the phase of the field is defined. For example, we can consider an ensemble of light emitters at a frequency ω_0 that undergo collisions with the average time between two successive collisions τ_c. For the duration of the collision, the emission frequency will be altered so that at later times the emission frequency will still be ω_0 but the phase changed by a random amount. If we assume that these collisions are instantaneous events, they will correspond to abrupt changes in the phase of $E(t)$. For such emitters, the correlation function can be written as $g^{(1)}(\tau) = e^{-i\omega_0\tau - |\tau|/\tau_c}$. It is seen that on a time scale of τ_c, the correlation function amplitude decays which means that the phase of the field ceases to be predictable.

This simple model of the interferometer displays the main features that are required for its atomic counterpart: 1) the interference is observed because of the superposition principle; 2) the interferometer converts a phase shift into an intensity variation at its output and 3) the amplitude or contrast of the interference signal can only be observed on timescales that are short compared to the decoherence time of the system.

The atomic Mach-Zehnder interferometer shares these properties. The analogy arises because of the validity of the superposition principle for matter waves and because of the conversion between phase shift and population difference. Interference can therefore be observed as long as the atomic wavefunction has a definite phase. This motivates the use of cold atomic samples that are ideally non-interacting.

The atomic Mach-Zehnder interferometer is illustrated in Fig. 4.1 b). An atomic wavepacket is split by a beam splitter $\pi/2$-pulse in two components that, in general, differ

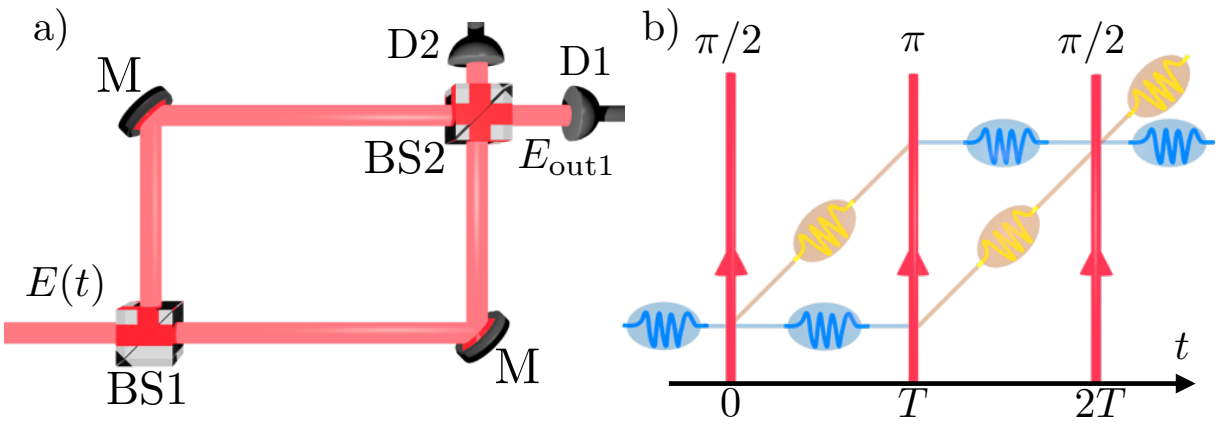

Figure 4.1: Schematic comparison between the optical a) and the atomic b) Mach-Zehnder interferometers. In a) a laser field $E(t)$ is split in two parts by the beam splitter BS1, the mirrors M redirect the beams in order to spatially superimpose at the second beam splitter BS2 where the phase accumulated in the two arms (i.e. the delay difference) is converted into an intensity difference between the two outputs, measured by the photodetectors D1 and D2. In b) an input wavepacket in the internal state $|g\rangle$ (blue) is split at time $t = 0$ by a $\pi/2$ laser pulse in two parts where one component acquired a photon momentum and is in the excited internal state $|e\rangle$ (orange). At $t = T$ a mirror π-pulse exchanges the internal states and the momenta so that at $t = 2T$ the trajectories converge and the final $\pi/2$-pulse converts the phase shift into a population difference.

by their internal state and by their momentum state, owing to the momentum recoil arising from the absorption of a photon. After a separation time T, the wavepackets are reflected by the mirror π-pulse that exchanges the internal and motional states. This causes the trajectories to intersect after an additional time T, where another beam splitter pulse maps the accumulated phase shift between the two arms in a population difference between the two states.

In order to see how the sensitivity to gravity acceleration arises, we consider a simple system where an ensemble of two-level atoms are in free fall and the laser pulses drive single-photon transitions that affect the atom's internal states and motional states. The system Hamiltonian can be written as

$$\mathcal{H} = \mathcal{H}_{\text{at}} + \mathcal{H}_{\text{cm}} + \mathcal{H}_{\text{int}} \tag{4.5}$$

where $\mathcal{H}_{\text{at}} = \hbar\omega_g |g\rangle \langle g| + \hbar\omega_e |e\rangle \langle e|$ is the Hamiltonian for the internal degrees of freedom, and $|g\rangle, |e\rangle$ are the internal ground and excited states, respectively. $\mathcal{H}_{\text{cm}} = \mathcal{H}_{\text{cm}}(\boldsymbol{r}, \boldsymbol{p})$ is the Hamiltonian for the atomic center-of-mass motion, where $\boldsymbol{r}$ and $\boldsymbol{p}$ are the corresponding position and momentum operators. Finally, $\mathcal{H}_{\text{int}}$ represents the dipole interaction with the laser pulses.

We first consider the evolution of the system between the laser pulses, when $\mathcal{H}_{\rm int} = 0$. In this case internal and external dynamics are decoupled and we determine the solution for the center-of-mass component $|\psi_{\rm cm}\rangle$. To do so we move to a reference frame that is falling under gravity through the unitary operator [1]

$$U_c = e^{\frac{i}{\hbar}\int \mathcal{L}dt} e^{-i\boldsymbol{p}\cdot\boldsymbol{r}_c} e^{i\boldsymbol{p}_c\cdot\boldsymbol{r}}, \tag{4.6}$$

where $\boldsymbol{r}_c$ and $\boldsymbol{p}_c$ are the classical position and momentum, solutions of the Lagrange equations with Lagrangian $\mathcal{L}$. Equation (4.6) is the composition of a translation by $\boldsymbol{r}_c$ and a boost by $\boldsymbol{p}_c$. Through the operator U_c we can define the center-of-mass wavefunction in the free-falling reference frame as $|\psi_{\rm cm}\rangle = U_c\,|\phi_{\rm cm}\rangle$. The Schrödinger equation for $|\phi_{\rm cm}\rangle$ is $i\hbar\frac{\partial}{\partial t}\,|\phi_{\rm cm}\rangle = \mathcal{H}'\,|\phi_{\rm cm}\rangle$, where

$$\mathcal{H}' = U_c^\dagger \mathcal{H}_{\rm cm} U_c - i\hbar U_c^\dagger \frac{\partial}{\partial t} U_c. \tag{4.7}$$

By using the relation $U_c^\dagger f(\boldsymbol{r},\boldsymbol{p})U_c = f(\boldsymbol{r}+\boldsymbol{r}_c,\boldsymbol{p}+\boldsymbol{p}_c)$ which holds for an arbitrary analytic function f, one can show that $\mathcal{H}' = \mathcal{H}_2(\boldsymbol{r}+\boldsymbol{r}_c,\boldsymbol{p}+\boldsymbol{p}_c)$, meaning that the transformed Hamiltonian is formed by all the contributions of $\mathcal{H}_{\rm cm}$ that are at least quadratic in position and momentum,

$$\mathcal{H}_{\rm cm}(\boldsymbol{r}+\boldsymbol{r}_c,\boldsymbol{p}+\boldsymbol{p}_c) - \mathcal{H}_2(\boldsymbol{r}+\boldsymbol{r}_c,\boldsymbol{p}+\boldsymbol{p}_c) = \mathcal{H}_{\rm cm}(\boldsymbol{r}_c,\boldsymbol{p}_c) + \nabla_{\boldsymbol{r}}\mathcal{H}_{\rm cm}(\boldsymbol{r}_c,\boldsymbol{p}_c)\cdot\boldsymbol{r} + \nabla_{\boldsymbol{p}}\mathcal{H}_{\rm cm}(\boldsymbol{r}_c,\boldsymbol{p}_c)\cdot\boldsymbol{p}. \tag{4.8}$$

By writing the equations of motion for the position and momentum operators it is possible to see that if $\mathcal{H}_{\rm cm}$ is at most quadratic in position and momentum (or $\mathcal{H}_2$ has only quadratic terms), these equations are the classical equations of motion and in particular it is possible to choose $|\phi_{\rm cm}\rangle$ such that $\langle\boldsymbol{r}\rangle = 0$ and $\langle\boldsymbol{p}\rangle = 0$. This condition corresponds to the semi-classical approximation, where the equations of motion for the expectation values of position and momentum are just the classical equations of motion. When instead $\mathcal{H}_{\rm cm}$ is formed by terms that are higher than second order, the equations of motion depend also on the wavepacket's width in phase space.

We now proceed with the analysis of the Mach-Zehnder interferometer by describing it in terms of the Bloch sphere and by showing that it is conceptually equivalent to the Ramsey interferometer.

We start by considering the two-level system formed by states that differ by their internal atomic energy and by their motional state, which we label $|\alpha,\boldsymbol{p}\rangle$, where $\alpha = g, e$ labels the internal state and the motional state is a plane wave with momentum $\boldsymbol{p}$. In particular, the two states, coupled by the single-photon transition, are $|g,0\rangle \equiv |\downarrow\rangle$ and $|g,\hbar k\rangle \equiv |\uparrow\rangle$, where k is the photon wavenumber and we only consider a one-dimensional motion. We then write the equations of motion in the free-falling frame defined by the transformation (4.6) for the superposition $|\psi\rangle = c_g\,|g,0\rangle + c_e\,|e,\hbar k\rangle$, accounting for (4.7)

and (4.8):

$$i\hbar(\dot{c}_g |g,0\rangle + \dot{c}_e |e,\hbar k\rangle) =$$
$$\hbar\omega_g c_g |g,0\rangle + \hbar(\omega_e + \omega_r)c_e |e,\hbar k\rangle +$$
$$-\frac{\hbar\Omega}{2}\left[e^{i(kz_c-\omega t-\phi)}c_g |e,\hbar k\rangle + e^{-i(kz_c-\omega t-\phi)}c_e |g,0\rangle\right], \tag{4.9}$$

where $z_c = z_c(t)$ is the atomic position, ω is the laser frequency, Ω is the Rabi frequency and $\omega_r = \hbar k^2/(2m)$ is the recoil frequency. In deriving equation (4.9) we neglected terms in $\mathcal{H}_2$ that are quadratic in the position operators and only considered the kinetic energy, $\mathcal{H}_2 \simeq p^2/(2m)$.

In order to provide the connection with the Bloch sphere representation, we define $\omega_0 = \omega_e + \omega_r - \omega_g$ as the frequency of the $|g,0\rangle - |e,\hbar k\rangle$ transition and shift the energy offset such that the Hamiltonian without laser interaction becomes $\hbar\omega_0\sigma_z/2$ with $\sigma_z = |e,\hbar k\rangle\langle e,\hbar k| - |g,0\rangle\langle g,0|$. Also, we neglect the velocity variation during the laser pulse due for example to gravity acceleration and write $z_c(t) \simeq z_c(0) + v_z t$, where v_z is the atomic velocity. As a result, it is natural to define the laser frequency as seen in the free-falling frame i.e. corrected for the Doppler effect, as $\omega_{\rm D} = \omega - kv_z$. Similarly, the laser phase is redefined as $\phi_c = \phi - kz_c(0)$, which carries information about the laser phase and about the atomic position at the time of the pulse. We proceed then as in (2.6) and (2.7) by moving to a frame that is rotating at the laser frequency $\omega_{\rm D}$ by the transformations $c_g = b_g e^{i\omega_{\rm D}t/2}$ and $c_e = b_e e^{-i\omega_{\rm D}t/2}$ and obtain the Hamiltonian

$$\mathcal{H} = -\frac{\hbar}{2}\delta\sigma_z - \frac{\hbar}{2}\Omega\begin{pmatrix} 0 & e^{-i\phi_c} \\ e^{i\phi_c} & 0 \end{pmatrix}, \tag{4.10}$$

which corresponds to (2.7), where $\delta = \omega_{\rm D} - \omega_0$ is the detuning of the laser frequency in the free falling frame from the $|g,0\rangle$-$|e,\hbar k\rangle$ transition. Thus, with the appropriate definitions, the interferometer dynamics can be visualized in the Bloch sphere.

We can now illustrate the formal equivalence between the Mach-Zehnder and the Ramsey interferometer and for simplicity we only account for a uniform gravity acceleration g so that $\mathcal{H}_{\rm cm} = p^2/(2m) + mgz$ and we consider the resonant case $\delta = 0$. After initializing the state in $|\psi_{\rm in}\rangle = |g,0\rangle$, a $\pi/2$-pulse with phase $\frac{\pi}{2} + \phi_{c,\pi/2}$, applied at time $t = 0$ induces the superposition

$$|\psi_{\pi/2}\rangle = U_{\rm p}(t_{\pi/2}, \boldsymbol{n}_R(\theta = \pi/2, \phi = \pi/2 + \phi_{c,\pi/2}))\,|\psi_{\rm in}\rangle = \frac{1}{\sqrt{2}}(|g,0\rangle + e^{-i\phi_{c,\pi/2}}|e,\hbar k\rangle). \tag{4.11}$$

The subsequent evolution between the pulses, where $\Omega = 0$, does not change the wavefunction. At time $t = T$, a π-pulse is applied with phase $\frac{\pi}{2} + \phi_{c,\pi}$ and induces the state

$$|\psi_\pi\rangle = \frac{1}{\sqrt{2}}(|g,0\rangle + e^{-i(\pi+2\phi_{c,\pi}-\phi_{c,\pi/2})}|e,\hbar k\rangle). \tag{4.12}$$

The equivalence with the Ramsey sequence is established by observing that the effect of the π-pulse on a state that lies on the equator of the Bloch sphere is equivalent to the rotation $U_\pi = e^{-i\alpha\sigma_z/2}$ about the z-axis with rotation angle $\alpha = \pi + 2\phi_{c,\pi} - 2\phi_{c,\pi/2}$. The additional π-pulse of the Mach-Zehnder interferometer therefore only adds a phase shift to the final measurement.

After the final $\pi/2$-pulse at time $t = 2T$ with phase $\frac{\pi}{2} + \phi'_{c,\pi/2}$, the accumulated phase is mapped to a population difference,

$$\langle\psi_{\text{fin}}|\sigma_z|\psi_{\text{fin}}\rangle = -\cos\Phi,\ \Phi = \phi'_{c,\pi/2} - 2\phi_{c,\pi} + \phi_{c,\pi/2}. \tag{4.13}$$

This expression for the phase shift Φ displays the main feature of the Mach-Zehnder interferometer as it is proportional to the discretized version of the second derivative of the phase ϕ_c. This can be seen by defining the time-dependent phase as $\phi_c = \phi_c(t)$, so that $\Phi = \phi_c(2T) - 2\phi_c(T) + \phi_c(0) \simeq \frac{\partial^2}{\partial t^2}\phi_c T^2$, where the strict equality holds when $\phi(t)$ is at most a second degree function of t. It is therefore clear that the Mach-Zehnder interferometer measures phase acceleration and is therefore an accelerometer [3, 35]. If the atoms in the interferometer are falling under a uniform acceleration field, then $\phi_c(t) = \phi(t) - kz_c(t)$, where $\phi(t)$ is the laser phase, $z_c(t) = z_c(0) + \dot{z}_c t - \frac{1}{2}gt^2$ is the classical solution to the equation of motion and the interferometer phase accounts for both the laser phase acceleration and gravity acceleration g:

$$\Phi = kgT^2 + \phi(2T) - 2\phi(T) + \phi(0). \tag{4.14}$$

Gravity acceleration and phase are linked by the conveniently large factor kT^2. This potentially large sensitivity can be understood by reinterpreting the interferometer as a device that measures the positions of the atom through the term kz_c on a ruler that has a spacing between the ticks given by the laser wavelength. For optical transitions, where the wavelength is on the order of $\lambda \sim 500$ nm, this translates to very precise gravity measurements. In order to give an impression of such a sensitivity with an optical transition, we consider a single run of a shot-noise-limited interferometer with $N = 10^4$ atoms and with an interrogation time of $T = 100$ ms. The phase resolution due to the shot noise is $\Delta\Phi = 1/\sqrt{N} = 10$ mrad whereas the accumulated phase shift is $\Phi \simeq 10^6$ rad so that the relative uncertainty on gravity acceleration is $\Delta g/g = \Delta\Phi/\Phi \simeq 10^{-8}$. The level of such a sensitivity is already sufficient to resolve the lunar tides.

The accelerometer described here can be extended to various related schemes. For example, multiple spatially separated atomic gravimeters can measure gravity gradients [5, 6] gravity curvature [7].

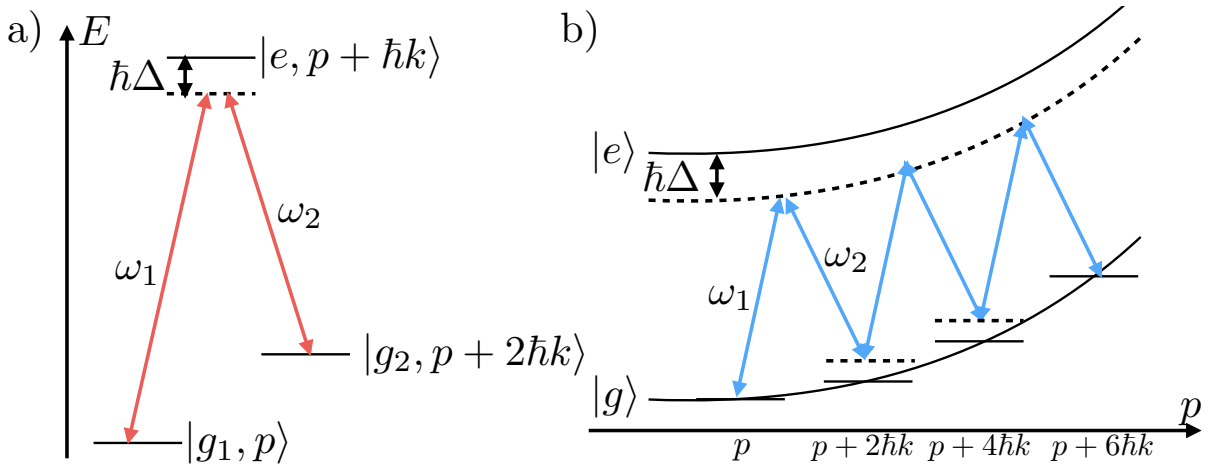

Figure 4.2: Comparison between Raman a) and Bragg b) transitions. In two-photon Raman transitions, two atomic states differing by both the internal and the external motion are coupled. In Bragg diffraction, only the external motion is changed.

4.2 Raman transitions and Bragg diffraction

It is often the case that using a single-photon transition for atom interferometers is inconvenient because of the limited lifetime of the excited state. Although a counterexample for this statement was recently proven in our group [93], many atom interferometers operate on multi-photon transitions, where the population of the optically excited states is kept small.

Raman transitions The first implementations of atom interferometers with separated arms exploited two-photon Raman transitions [35]. A simplified level diagram for this case is shown in Fig. 4.2 a).

The system that we consider is composed of two internal and stable ground states $|g_1\rangle$ and $|g_2\rangle$ and an optically excited state $|e\rangle$. The atomic system is illuminated by a couple of counterpropagating laser beams with frequencies ω_1 and ω_2. Because of the photon recoil, the combined internal and external states $|\alpha, p\rangle$, where $\alpha = g_1, g_2, e$ are considered. Starting from a plane wave with momentum p and in the internal state g_1, $|g_1, p\rangle$, the field with frequency ω_1 and Rabi frequency Ω_1 couples to the excited state $|e, \hbar k\rangle$. Similarly, the counterpropagating field with frequency ω_2 and Rabi frequency Ω_2 couples the excited state to the ground $|g_2, p + 2\hbar k\rangle$ state. Both laser fields are detuned from the transition to the excited state and we define the detunings of the two fields from the excited states as $\Delta_1 = \omega_1 - \omega_{31}$ and $\Delta_2 = \omega_2 - \omega_{32}$, where ω_{31} and ω_{32} are the frequencies of the $|g_1, p\rangle$-$|e, p + \hbar k\rangle$ and $|g_2, p + 2\hbar k\rangle$-$|e, p + \hbar k\rangle$ transitions, respectively.

We first consider the Hamiltonian in the absence of the laser fields

$$\mathcal{H}_{\text{at}} = \hbar\omega_1 \left|g_1, p\right\rangle \left\langle g_1, p\right| + \hbar\omega_2 \left|g_2, p + 2\hbar k\right\rangle \left\langle g_2, p + 2\hbar k\right| + \hbar\omega_3 \left|e, p + \hbar k\right\rangle \left\langle e, p + \hbar k\right| \quad (4.15)$$

and transform the atomic state according to $|\psi\rangle = e^{-i\mathcal{H}_{\text{at}}t/\hbar}|\phi_{\text{at}}\rangle$. We then write the time-dependent Schrödinger equation for $|\phi_{\text{at}}\rangle = c_1 \left|g_1, p\right\rangle + c_2 \left|g_2, p + 2\hbar k\right\rangle + c_3 \left|e, p + \hbar k\right\rangle$ as

$$i\hbar\dot{c}_1 = \frac{\hbar\Omega_1}{2} e^{i(\Delta_1 t + \phi_1)} c_3 \quad (4.16)$$

$$i\hbar\dot{c}_2 = \frac{\hbar\Omega_2}{2} e^{i(\Delta_2 t + \phi_2)} c_3 \quad (4.17)$$

$$i\hbar\dot{c}_3 = \frac{\hbar\Omega_1}{2} e^{-i(\Delta_1 t + \phi_1)} c_1 + \frac{\hbar\Omega_2}{2} e^{-i(\Delta_2 t + \phi_2)} c_2, \quad (4.18)$$

where ϕ_1 and ϕ_2 are the phases of the two laser fields. In the limit where the population of the excited state is kept small, $|\Delta_1|, |\Delta_2| \gg \Omega_1, \Omega_2, |\Delta_1 - \Delta_2|$, it is possible to adiabatically eliminate the excited state amplitude by integrating (4.18) with constant c_1 and c_2 and substituting the result in equations (4.16) and (4.17). Then, by neglecting terms that oscillate at the detunings Δ_i, the system reduces to a soluble two-level problem

$$i\hbar\dot{c}_1 = \hbar\frac{\Omega_1^2}{4\Delta} c_1 + \hbar\frac{\Omega_1\Omega_2}{4\Delta} e^{i(\delta t + \phi_e)} c_2 \quad (4.19)$$

$$i\hbar\dot{c}_2 = \hbar\frac{\Omega_2^2}{4\Delta} c_2 + \hbar\frac{\Omega_1\Omega_2}{4\Delta} e^{-i(\delta t + \phi_e)} c_1, \quad (4.20)$$

where in the coefficients we neglected the difference between Δ_1 and Δ_2 by setting $\Delta_1 \simeq \Delta_2 \equiv \Delta$ and in the complex exponentials we set $\delta \equiv \Delta_1 - \Delta_2$. The effective phase ϕ_e is defined as the difference $\phi_e = \phi_1 - \phi_2$.

If we only look at the second terms of the right-hand side of equations (4.19) and (4.20), these are the same as in the actual two-level system but with an effective (two-photon) Rabi frequency $\Omega_{\text{eff}} = \Omega_1\Omega_2/(2\Delta)$ and the system is driven by an effective laser with frequency $\omega_{\text{eff}} = \omega_1 - \omega_2$, effective wavevector $k_{\text{eff}} = 2k$ and effective phase $\phi_e = \phi_1 - \phi_2$. The first two terms, on the other hand, represent the light shift of the atomic levels. We note that when these are equal, they would merely change the energy offset and therefore not cause an effect. On the other hand, if these terms are different, they change the frequency difference between the two ground states. The light shift terms can cause several difficulties in precision measurements, especially if the intensity profile of the laser beams is considered. In this case, the resulting spatial dependence of the Rabi frequency can cause unwanted interferometer phase shifts.

It is possible to see that by a suitable unitary transformation, this system of equations can be mapped into the Hamiltonian (2.7) with detuning, generalized Rabi frequency and phase given by

$$\delta_e = \delta + \frac{\Omega_1^2}{4\Delta} - \frac{\Omega_2^2}{4\Delta}, \Omega_R = \sqrt{\Omega_{\text{eff}} + \delta_e^2} \text{ and } \phi_e = \phi_1 - \phi_2, \quad (4.21)$$

respectively. A very important feature of two-photon Raman transitions is velocity selectivity [94]. This can be seen by writing the expression for δ as

$$\delta = \Delta_1 - \Delta_2 = \omega_{\text{eff}} - \left(\omega_{21} + \frac{\hbar k_{\text{eff}}^2}{2m} + k_{\text{eff}} v\right), \tag{4.22}$$

where ω_{21} is the transition frequency between the internal $|g_1\rangle$ and $|g_2\rangle$ states and $v = p/m$ is the atomic velocity. Because of the Doppler effect dependence through the term $k_{\text{eff}}v$, for a given detuning δ, the resonance is met for a certain atomic velocity v. The width of the selected velocity class is determined by considering the fraction of excited atoms $P_e = \Omega_{\text{eff}}^2 \sin^2(t\sqrt{\Omega_{\text{eff}}^2 + \delta_e^2}/2)/(\Omega_{\text{eff}}^2 + \delta_e^2)$, setting the π-pulse condition $t_\pi = \pi/\Omega_{\text{eff}}$ and determining the frequency width of the excitation fraction. The full width at half maximum (FWHM) is given by $k_{\text{eff}}(\Delta v)_{\text{FWHM}} \simeq 1.6\pi/t_\pi$. We can give an impression for the velocity selectivity by considering a practical example of a Raman pulse with duration $t_\pi = 100$ μs and with laser wavelength $\lambda = 500$ nm. Then $(\Delta v)_{\text{FWHM}} = 2$ mm/s and for an atomic mass $m = 1.5 \times 10^{-25}$ kg, this corresponds to a temperature $T = m(\Delta v)_{\text{FWHM}}^2/[(8\ln 2)k_B] \simeq 8$ nK.

The phase shift of a Raman-based atom interferometer is written by adapting equation (4.14) with the replacements $k \to k_{\text{eff}}$ and $\phi \to \phi_e$:

$$\Phi = k_{\text{eff}} g T^2 + \phi_e(2T) - 2\phi_e(T) + \phi_e(0). \tag{4.23}$$

Bragg diffraction Multi-photon transitions can be used for the implementation of atom interferometers where the two states differ by their momentum but have no internal excitation. These processes are generally identified as Bragg diffraction because of the analogy with the scattering of X-rays and neutrons off crystals [95]. In atomic Bragg diffraction, the optical lattice formed by two counterpropagating laser fields acts as the diffracting crystal planes and the atomic matter-waves act as the beam of X-rays. In the atom-photon interaction picture, Bragg diffraction is described in terms of combined cycles of absorption and stimulated emission resulting in the net transfer of pairs of photon momenta (Fig. 4.2 b)). Atomic Bragg diffraction was first studied in [96]. The first experimental realization consisted in the diffraction of a collimated atomic beam [97] and, in a related experiment, up to sixth-order Bragg diffraction was observed on a beam of metastable neon atoms [98]. Later on, Bragg diffraction was implemented in laser cooled atomic systems, transferring up to 102 photon recoils and inducing momentum state superpositions with a half-meter scale spatial separation between the wavepackets [23, 99, 100].

In order to describe atomic Bragg diffraction, we consider the same setup as for Raman transitions, with two counterpropagating laser fields with frequencies ω_1 and ω_2 and follow the same procedure. We write the wavefunction as a superposition of atomic states for

the ground and excited states and with momentum differing by $\hbar k_{\text{eff}}$ (Fig. 4.2 b)):

$$|\phi_{\text{at}}\rangle = \sum_n c_{g,n}(t)\,|g, p + n\hbar k_{\text{eff}}\rangle + \sum_n c_{e,n}(t)\,|e, p + n\hbar k_{\text{eff}} + \hbar k\rangle\,. \tag{4.24}$$

As for Raman transitions, we can perform adiabatic elimination of the excited state by assuming that the detuning from the optical transitions is large compared to the single-photon Rabi frequencies and to the frequency difference between the two fields. The result is the system of coupled equations

$$i\hbar\dot{c}_{g,n} = \hbar\left(\frac{\Omega_1^2}{4\Delta} + \frac{\Omega_2^2}{4\Delta}\right)c_{g,n} + \hbar\frac{\Omega_{\text{eff}}}{2}e^{i(\delta_n t+\phi_e)}c_{g,n+1} + \hbar\frac{\Omega_{\text{eff}}}{2}e^{-i(\delta_{n-1}t+\phi_e)}c_{g,n-1}, \tag{4.25}$$

where δ_n is the detuning from the transition $|g, n\rangle$-$|g, n+1\rangle$ which can be expressed in terms of the difference of kinetic energy of the two states as

$$\delta_n = \omega_1 - \omega_2 - \left[\frac{(2n+1)\hbar k_e^2}{2m} + k_{\text{eff}}v\right]. \tag{4.26}$$

These results are similar to those for Raman transitions and, in particular, also Bragg diffraction is velocity selective. There are, however, some important differences. Indeed, because the transitions do not change the internal state, the frequency of the transition between two internal states is absent. For this reason Bragg diffraction is more robust against perturbations such as electromagnetic fields that can alter δ_n and therefore induce an undesired phase shift. This same immunity is reflected in the light shift terms which are the same for every state $|g, p + n\hbar k_{\text{eff}}\rangle$ as long as the conditions for adiabatic elimination hold [101]. Bragg diffraction therefore appears to have a number of advantages compared to two-photon Raman transitions:

- **Immunity to internal energy shifts**: This immunity is valid in the framework of adiabatic elimination and as long as spatial internal energy gradients are small. This means that if the internal atomic energy is position-dependent, the resulting force acting on the atom might still cause undesired systematic effects. This is the case, for example, when magnetic gradients or laser intensity gradients are present during the interferometer.

- **Large-momentum-transfer**: The possibility in Bragg diffraction of transferring several pairs of photon momenta in a single light pulse, generally referred to as Large Momentum Transfer (LMT), enhances the phase sensitivity by increasing the interferometer area. For a Mach-Zehnder interferometer, the phase shift is given by

  $$\Phi_n = nk_{\text{eff}}gT^2 + n(\phi(2T) - 2\phi(T) + \phi(0)). \tag{4.27}$$

  As we will discuss below, this increased sensitivity comes at the price of severe technical requirements which can however be overcome by implementing an appropriate pulse sequence [102].

Regimes of Bragg diffraction Contrary to Raman transitions, in principle Bragg diffraction can couple a large number of momentum components. There are different regimes of Bragg diffraction processes that essentially differ by the number of states that are populated [103]. To gain some insight into the different regimes, we consider a Bragg laser pulse with a given duration τ and with a resulting spectral width $\Delta\omega \sim 1/\tau$. For short enough pulses, the spectral width can be large enough for the Bragg laser to be resonant with several transitions $|g,p\rangle$-$|g,p+n\hbar k_{\text{eff}}\rangle$. For example, for optical transitions, the recoil frequency is on the order of a few 10 kHz, which is the order of magnitude for the frequency difference of the transitions between different momentum states. As a result, pulse durations of 1-10 μs will result in a non-negligible population of various momentum components. Two extreme cases of short pulses with intense fields and of long pulses with weak fields can be considered and correspond to the Raman-Nath and Bragg regimes, respectively.

In the short interaction time limit, the laser is resonant with several transitions. In this case, the small phase shift $|\delta_n t| \ll 1$ in (4.25) for small t yields the Raman-Nath equation

$$i\hbar\dot{c}_{g,n} = \hbar\frac{\Omega_{\text{eff}}}{2}(c_{g,n+1} + c_{g,n-1}). \tag{4.28}$$

We now consider the initial condition where only the zeroth order is populated, $c_{g,0}(0) = 1, c_{g,n}(0) = 0$ for $n \neq 0$. A function that fulfills these conditions can be written in the form

$$c_{g,n} = \frac{1}{2\pi}\int_{-\pi/2}^{3\pi/2} e^{i\zeta(\alpha)t}\cos(n\alpha)d\alpha, \tag{4.29}$$

where ζ is an unknown function.

After substituting into the Raman-Nath equation (4.28), we get $\zeta(\alpha) = -\Omega_{\text{eff}}\cos\alpha$ and by using the integral representation for the Bessel function of order n, $J_n(x) = \frac{1}{2\pi}\int_{-\pi}^{\pi}\exp[i(n\alpha - x\sin\alpha)]d\alpha$, the solution is found to be

$$c_{g,n}(t) = (-i)^n J_n(\Omega_{\text{eff}}t). \tag{4.30}$$

This result shows that in the Raman-Nath regime many diffraction orders are populated as shown in Fig. 4.3.

It is in general possible to implement an atom interferometer operating in the Raman-Nath regime and such an application is described, for example, in [104]. We will however consider an atom interferometer that rather operates in the opposite regime where only two momentum states are populated thus forming a two-level system suitable for the Mach-Zehnder interferometer. This condition is achieved in the Bragg regime corresponding to long interaction times and weak fields. In this regime we reconsider the full equation (4.25) and treat the transition from an initial state corresponding to $n = 0$, $c_{g,0}(0) = 1$ to a target state with Bragg order n. By performing adiabatic elimination

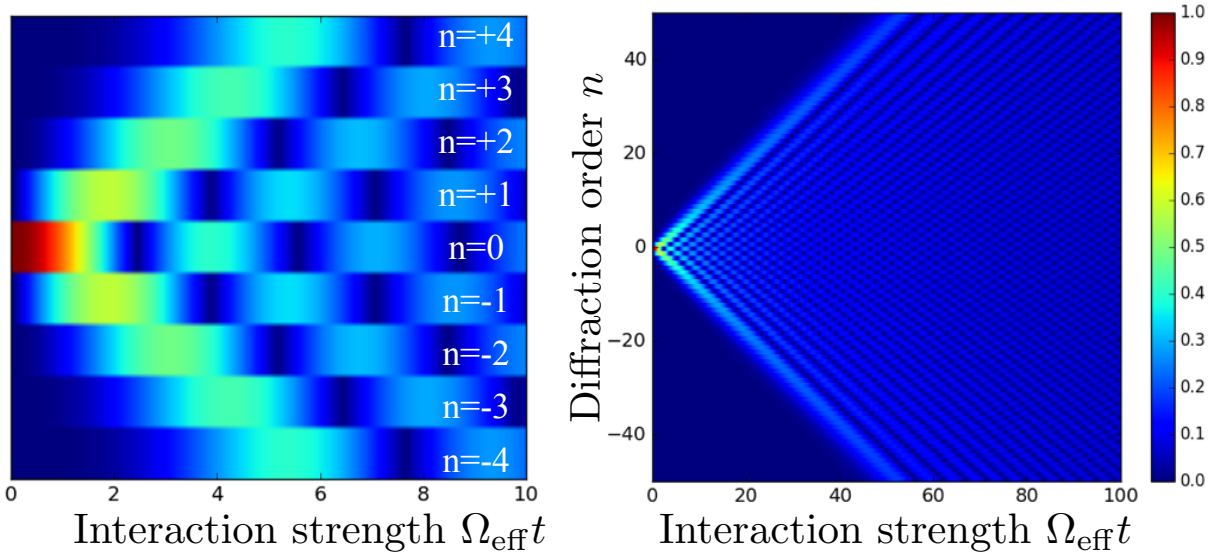

Figure 4.3: Evolution of the amplitude $|c_{g,n}(t)|$ in Raman-Nath diffraction for small interaction strength up to $\Omega_{\text{eff}}t = 10$ (left) and for larger interaction strength up to $\Omega_{\text{eff}}t = 100$ (right). For large $\Omega_{\text{eff}}t$, a large number of diffraction orders are almost equally populated.

of the intermediate states with order k and $0 < k < n$, the system reduces to a two-level system where the coupling strength is quantified by the $2n$-photon Rabi frequency [103, 105]

$$\Omega_{\text{eff}}^{(2n)} = \frac{\Omega_{\text{eff}}^{n}}{(8\omega_r)^{n-1}[(n-1)!]^2}. \tag{4.31}$$

where $\omega_r = \hbar k^2/(2m)$ is the recoil frequency. When the Bragg laser fields are tuned to the resonance of the $|g,0\rangle - |g,n\rangle$ transition, $\omega_{\text{eff}} = 4n\omega_r + k_e v$, the transition probability can be written

$$|c_{g,n}(t)|^2 = \sin^2\left[\frac{1}{2}\int_{-\infty}^{t} \Omega_{\text{eff}}^{(2n)}(t')dt'\right], \tag{4.32}$$

where also the time dependence of the Rabi frequency is considered. The pulse area $\int_{-\infty}^{+\infty} \Omega_{\text{eff}}^{(2n)}(t)dt$ determines the transfer probability between the two momentum states. Operation in the Bragg regime requires the validity of adiabatic elimination. It can be shown [103] that in this regime there is an upper bound to the $2n$-photon Rabi frequency given by

$$\frac{\Omega_{\text{eff}}^{(2n)}}{\omega_r} \ll \frac{(n-1)^n}{2^{n-3}[(n-1)!]^2}. \tag{4.33}$$

For the two-photon Rabi frequency, this limit corresponds to $\Omega_{\text{eff}}^{\max} = 4(n-1)\omega_r$. For small diffraction orders, $n \leq 5$, the upper bound is on the order of the recoil frequency but it rolls off rapidly and for $n = 10$ the ratio at the right-hand side of (4.33) is about 2×10^{-4}. This requirement sets an upper limit to the diffraction order that can be attained in a real atom interferometer with a single pulse. For example, the interaction time could be

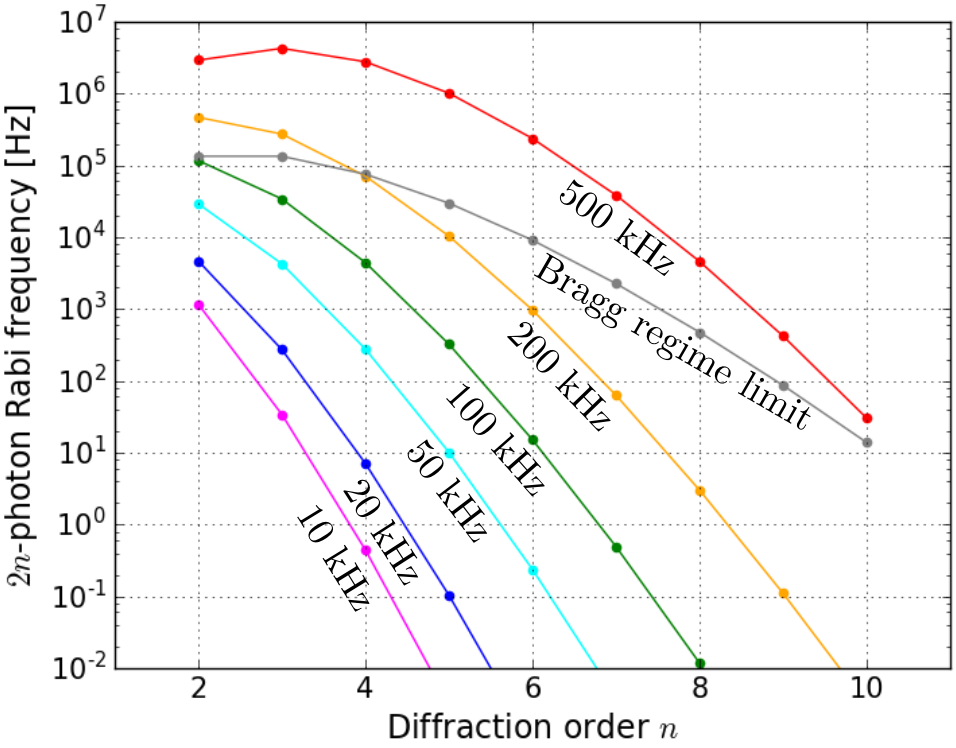

Figure 4.4: Effective $2n$-photon Rabi frequency $\Omega_{\text{eff}}^{(2n)}/(2\pi)$ as a function of the diffraction order n for different values of the two-photon Rabi frequency $\Omega_{\text{eff}}/(2\pi)$: 10 kHz (magenta), 20 kHz (blue), 50 kHz (cyan), 100 kHz (green), 200 kHz (orange), 500 kHz (red). The gray trace indicates the upper limit (4.33) above which the two-level approximation is no longer valid. The specific values refer to the strontium blue transition at 461 nm.

limited by the overall duration of the atom interferometer and by the finite temperature of the atomic cloud which limits the number of atoms in the interferometer[1].

A comparison of the effective $2n$-photon Rabi frequency for different values of the two-photon Rabi frequency Ω_{eff} is plotted in Fig. 4.4, where the upper limit for operation in the Bragg regime is also shown.

Another important consideration in limiting diffraction losses is about the pulse temporal shape. Intuitively, a smooth pulse shape will have a narrower frequency width compared to a *rough* one. For example, in a rectangular pulse, the laser field is abruptly

[1]For example, we can consider an atomic cloud with $N_{\text{in}} = 10^6$ atoms with mass $m = 1.5 \times 10^{-25}$ kg at a temperature of $T = 1$ μK and an effective $2n$-photon Rabi frequency $\Omega_{\text{eff}}^{(2n)} = 2\pi \times 500$ Hz. A π-pulse, with duration $\tau = 1$ ms would then select a velocity width $\Delta v \simeq 1/(k_{\text{eff}}\tau)$, where k_{eff} is the effective wavenumber and we take $\lambda \simeq 500$ nm. For a gaussian initial velocity distribution, the fraction of selectes atoms is

$$\frac{N_{\text{sel}}}{N_{\text{in}}} = \frac{1}{k_{\text{eff}}\tau}\sqrt{\frac{m}{2\pi k_B T}} \simeq 1.5 \times 10^{-3},$$

which gives $N_{\text{sel}} = 1.5 \times 10^3$ and a substantial signal reduction.

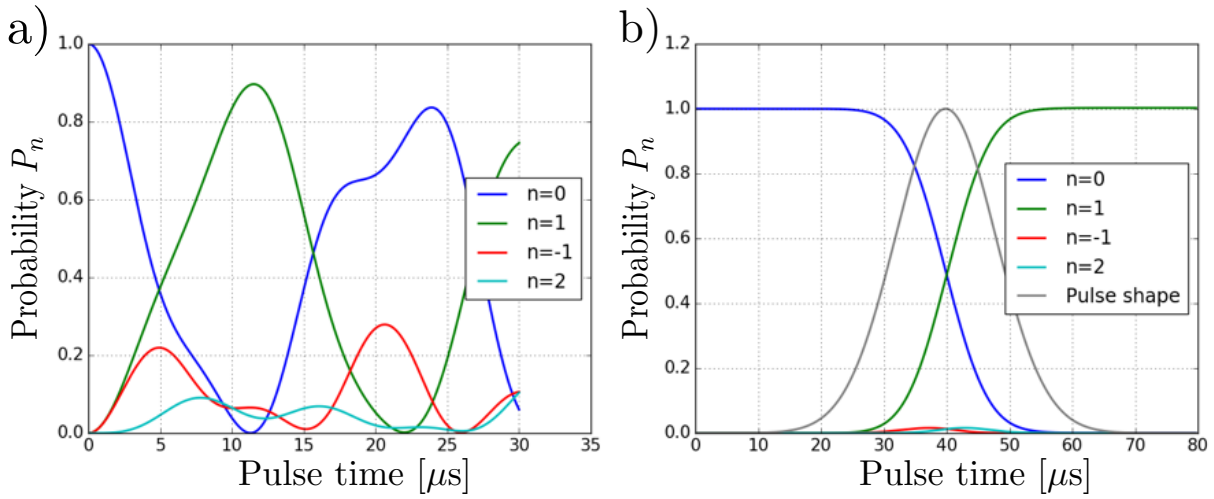

Figure 4.5: Comparison of the losses in Bragg transitions for square and gaussian $f(t) = \exp[-(t-t_0)^2/(2\sigma_t^2)]$ pulses through numerical integration of equation (4.25). The frequency ω_{eff} is tuned to the resonance of the first order $|g,0\rangle$-$|g,\hbar k_{\text{eff}}\rangle$ transition and the losses can be observed in $n=-1$ and $n=2$. a) Evolution during a rectangular pulse with two-photon Rabi frequency $\Omega_{\text{eff}} = 2\pi \times 50$ kHz; b) Evolution during a gaussian pulse with $\sigma_t = 8$ μs and $\Omega_{\text{eff}} = 2\pi \times 25$ kHz. At the end of the pulse, the losses essentially vanish.

switched on and off. This causes the pulse frequency spectrum to have pronounced wings away from the carrier frequency that decay polynomially. On the other hand, in a gaussian pulse, the intensity is gradually turned on and off. This is reflected in the pulse spectrum where the wings decay exponentially. The components of the wings in the pulse spectrum can excite momentum states that are not members of the target two-level system and therefore cause losses.

A comparison between rectangular and gaussian pulses is shown in Fig. 4.5, where it is clear that a gaussian first-order pulse with standard deviation 8 μs and $\Omega_{\text{eff}} = 2\pi \times 25$ kHz is sufficient to largely suppress the losses in other orders. On the other hand, for a rectangular pulse after 30 μs, the losses are still a significant fraction of the total atomic population.

A detailed analysis of the losses in Bragg diffraction can be found in [103]. There it is shown that diffraction losses induce a systematic phase shift on the atomic superposition $\Delta\phi_{\text{loss}}$ and that an upper bound is given by $|\Delta\phi_{\text{loss}}| \leq \sqrt{L}$, where L is the total probability for diffraction losses, i.e. the probability for an atom not to be found in the two target momentum states of the interferometer.

Compared to Raman transitions, where the finite momentum width only limits the pulse efficiency, in Bragg diffraction the momentum width also induces diffraction losses.

The enhanced losses are caused by the velocity dependence of the resonance condition through the Doppler effect. The importance of momentum width in Bragg diffraction has been pointed out and analyzed in [106].

Here we give a simplified result where we assume a gaussian π-pulse envelope function $f(t) = \exp[-(t-t_0)^2/(2\sigma_t^2)]$ and first-order Bragg diffraction. By numerical integration of the equation of motion, it is possible to show that the $|g,0\rangle$-$|g,\hbar k_{\text{eff}}\rangle$ transition probability $p(v)$, where v is the velocity, for $\sigma_t \geq 10$ μs, is well represented by a gaussian function, $p(v) = \exp[-v^2/(2\sigma_\pi^2)]$. The standard deviation σ_π is determined numerically to be related to σ_t by $\sigma_\pi\sigma_t = 23.9$ $\frac{\text{mm}}{\text{s}} \times \mu$s. We also assume that the atomic velocity distribution $f(v)$ is also well represented by a gaussian function, with center velocity v_0 and standard deviation σ_v. Then we can derive a simple result that expresses the efficiency of the π-pulse as

$$E_\pi = \int_{-\infty}^{\infty} p(v)f(v)dv = \frac{\exp\left[-\frac{v_0^2}{2(\sigma_v^2+\sigma_\pi^2)}\right]}{\sqrt{1+\left(\frac{\sigma_v}{\sigma_\pi}\right)^2}}. \tag{4.34}$$

For example, if the Bragg lasers frequency matches the center velocity, we can see that a π-pulse efficiency better than 90% can be achieved if $\sigma_v/\sigma_\pi \leq 0.48$. For a π-pulse with $\sigma_t = 10$ μs, $\sigma_\pi = 0.24$ $\hbar k/m$ and the momentum width should therefore limited to $m\sigma_v \leq 0.12$ $\hbar k$.

4.3 Bragg atom interferometer operating on the dipole-allowed 461 nm transition

In our first implementation of the atomic Mach-Zehnder interferometer, we used the broad dipole-allowed transition at 461 nm to induce Bragg diffraction. In this Section we will present the setup and discuss the main results of our implementation of a strontium gravimeter. Additional details about this experiment can be found in [107, 108]. The results of this and the following sections of this Chapter are to be regarded as the starting point for our proposals for spin squeezed atom interferometers based on strontium atoms.

4.3.1 Experimental setup and sequence

The main setup for laser cooling and trapping and momentum state manipulation is illustrated in Fig. 4.6.

The atomic source is provided by a high-efficiency strontium oven which, heated at a temperature T =430 °C, produces a well-collimated atomic beam with most probable velocity $v_{\text{mp}} \simeq 440$ m/s and a flux of 2×10^{11} atoms/s. The atomic beam is directed to the Zeeman slower, whose operation is outlined in Subsection 3.2.1. There, a two-stage

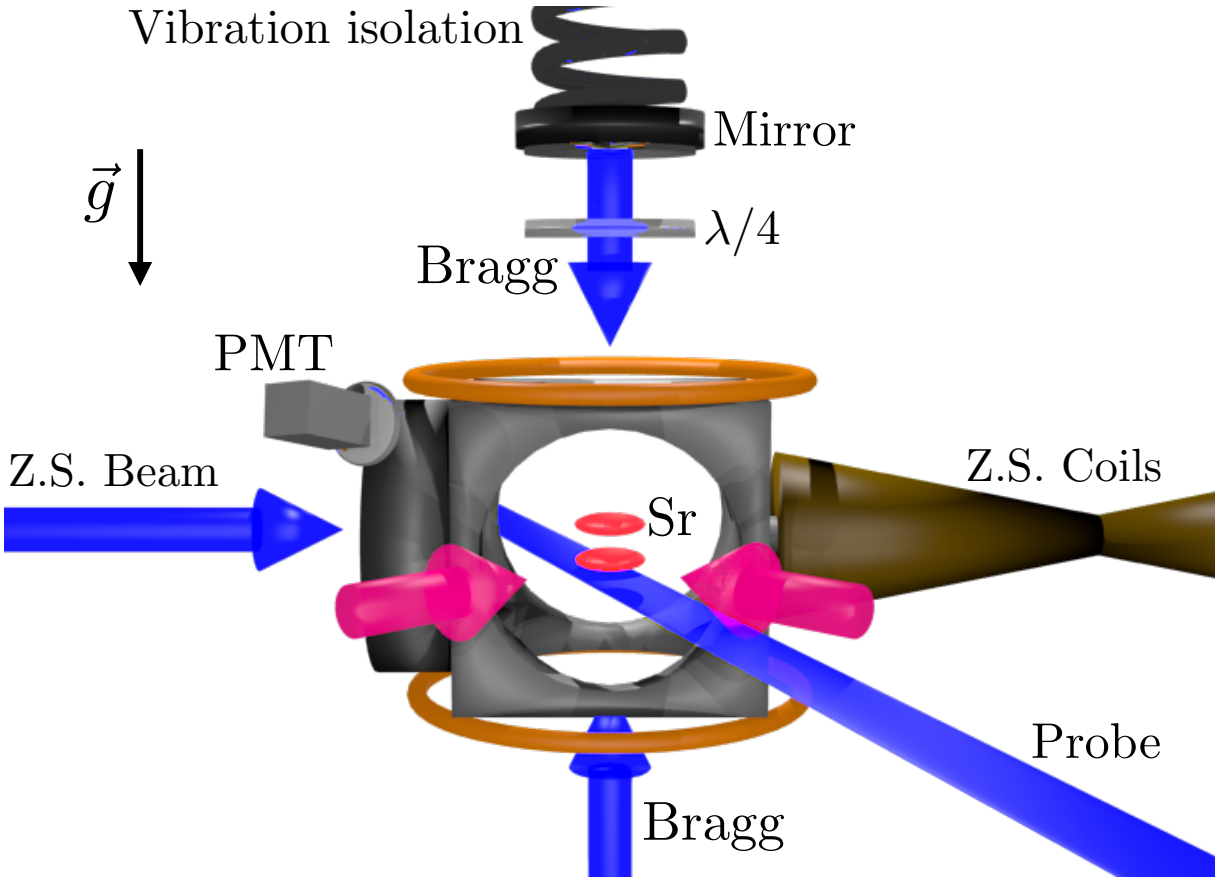

Figure 4.6: Schematic of the experimental setup for the production of the atomic source and its manipulation through Bragg diffraction. Atoms from a high-efficiency oven are decelerated in a Zeeman slower (Z.S.), cooled and trapped through a two-stage magneto-optical trap (MOT): the magenta arrows are the cooling beams and the two rings represent the MOT coils. Bragg diffraction is produced by the two vertical counterpropagating blue beams with orthogonal polarization. The Bragg light is reflected by the mirror suspended on a vibration isolation stage and its polarization is rotated by a $\lambda/4$ waveplate. The atoms with different momentum and vertical spatial separation are depicted as red ellipsoids. The population measurement is performed by resonant excitation through the probe beam and fluorescence collection through a photomultiplier tube (PMT).

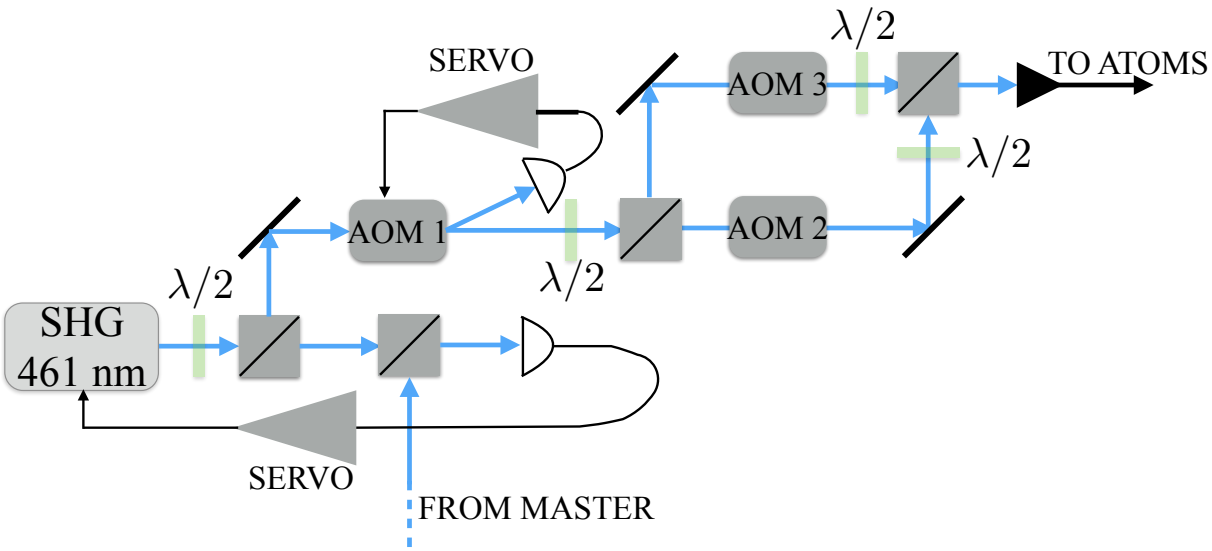

Figure 4.7: Setup for the production of the 461 nm laser light for Bragg diffraction. The blue light is generated by second harmonic generation (SHG) of an amplified 922 nm laser. A part of the light is beated with our reference blue laser to offset lock the laser with a given detuning by acting on the blue laser. The first-order diffracted light from AOM 1 is used for instensity stabilization by acting on the AOM itself. In the following optical Mach-Zehnder interferometer, the light with orthogonal polarizations is amplitude and frequency controlled by AOM 2 and AOM 3. After recombination, the light is sent to the vacuum chamber through a polarization-maintaining optical fiber.

magneto-optical trap (MOT) is performed [85, 86]. The first stage produces a sample of 10^8 atoms at a temperature of 1 mK in 1 s. Further cooling is attained through the second stage, the *red MOT* (see Section 3.2). Here a sample of 2×10^6 atoms at a temperature of 1.2 μK is produced with a size of 300 μm on the horizontal direction and of 50 μm on the vertical direction full width at half maximum (FWHM).

Bragg diffraction is induced by a pair of counterpropagating laser beams at 461 nm, with frequency close to the $^1S_0$-$^1P_1$ resonance. The optical setup for the Bragg beams production is shown in Fig. 4.7.

We generate the blue light with an output power of 230 mW by cavity-enhanced frequency doubling of an amplified 922 nm laser. In order to induce Bragg diffraction while suppressing scattering of photons into free space, we need to introduce a detuning of the blue laser from atomic resonance that is large compared to the natural linewidth. This is achieved by combining a part of the blue light with that of our reference cooling laser. The detected beatnote frequency is compared with a stable oscillator in a phase and frequency detector which outputs an error signal used for locking the blue laser. By tuning the frequency of the oscillator we can set the detuning from resonance of the

Bragg laser in the range 2-8 GHz. Most of the light is directed to the acousto-optic modulator AOM 1 which is used for intensity stabilization by detecting the first-order diffracted light. By acting on the AOM RF drive amplitude, we are able to stabilize the zeroth order intensity. This stabilization stage is necessary for our frequency doubled laser because enhancement cavity vibrations and crystal temperature variations cause output intensity noise. The zeroth order light is then directed to an optical Mach-Zehnder interferometer, where the two Bragg frequencies ω_1 and ω_2 are produced. The frequency difference $\omega_1 - \omega_2$ and the phase difference between the two lasers are tuned through the two acousto-optic modulators AOM 2 and AOM 3 in the two interferometer arms. The two AOMs are also used for pulse shaping during the atom interferometer. The two parts are then recombined in a polarizing beam splitter and the resulting beam is coupled into a single-mode polarization-maintaining optical fiber. The fiber output is directed to the atoms after being collimated to a waist ($1/e^2$ intensity radius) $w = 2.5$ mm. It is then sent vertically (to within 1 mrad) into the vacuum chamber and to the atoms. The counterpropagating Bragg beam is obtained by retroreflection on a mirror that is supported on a vibration isolation platform from MinusK Technology (MinusK 25BM-4). The residual mirror vibrations and tilt are monitored by a triaxial accelerometer (Episensor ES-T) and a tiltmeter (Applied Geomechanics Tuff Tilt 420). A double pass through a quarter waveplate is used to produce polarizations that are orthogonal to those of the upward-propagating beam. Through this setup, we create two couples of traveling optical lattices, one upward propagating and the other downward propagating with velocity $|\omega_1 - \omega_2|/k_{\text{eff}}$.

The output of the interferometer is measured after separating the wavepackets corresponding to the two momentum states in time of flight by resonant excitation though a thin sheet of blue light (the probe beam). The resulting fluorescence is collected on a photomultiplier tube (PMT). Alternatively, although not shown in Fig. 4.6, we shine resonant blue light onto the atoms and detect the resulting spatial absorption profile through a CCD camera.

After the production of the trapped atomic sample, the atoms are released from the MOT and a sequence of Bragg π pulses is applied that provides vertical velocity selection and launch (left of Fig. 4.8). After the selection and launch stages, we produce a sample with a vertical momentum spread of 0.2 $\hbar k$ FWHM and a vertical average momentum of 40 $\hbar k$. The measured high-efficiency Rabi oscillations are plotted in the right of Fig. 4.8. The preparation sequence allows for a total time of flight of 150 ms and for high-efficiency interferometer pulses.

After the preparation of the atomic ensemble, a Mach-Zehnder $\pi/2 - \pi - \pi/2$ pulse sequence is performed. In the following Subsection we give the main experimental results in terms of the interferometer contrast and sensitivity.

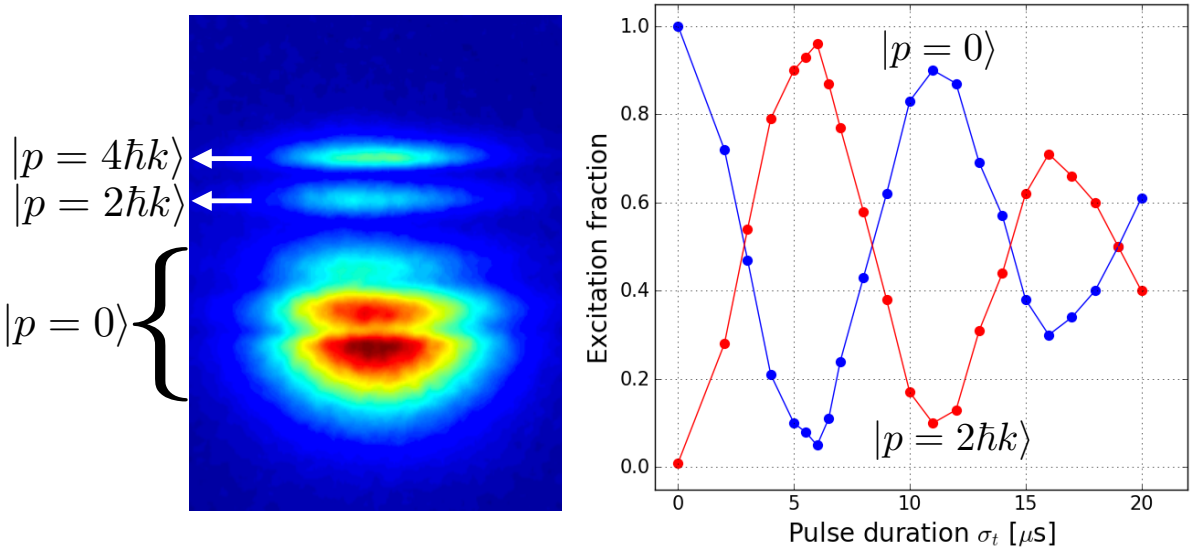

Figure 4.8: Left: absorption image of the diffracted atomic cloud from the falling red MOT. Two clouds corresponding to the excited $|p = 2\hbar k\rangle$ and $|p = 4\hbar k\rangle$ momentum states are visible. Right: Rabi oscillation for first-order Bragg diffraction through Gaussian pulses with standard deviation σ_t.

4.3.2 Experimental results

Interferometer contrast The interferometer contrast was measured by scanning the relative phase between the two Bragg laser beams at the last $\pi/2$-pulse. The measured contrast is plotted on the left of Fig. 4.9 for first, second and third order Bragg diffraction as a function of the interferometer time T. By performing numerical simulations of the interferometer dynamics with the known atomic cloud and beam parameters, we confirmed the intuitive fact that, for short interferometer times, the contrast is limited by the finite vertical momentum width and by scattering of photons into free space. On the other hand, for long interferometer times, the contrast is limited by the finite size of the Bragg laser beams due to the horizontal expansion. These effects result in an inhomogeneous interaction of the atoms with the Bragg lasers. For increasing diffraction order, the contrast drop with interferometer time T becomes more pronounced because of the critical dependence of the $2n$-photon Rabi frequency on the laser intensity profile. These results can be considerably improved through technically feasibile upgrades. On the basis of our numerical simulations, the use of laser sources with enhanced output power and an accurate optimization of the beam intensity and phase profiles are sufficient to provide large interferometer contrast. More work still needs to be done in the direction of further cooling the atomic ensemble, thereby reducing the detrimental effects of horizontal expansion.

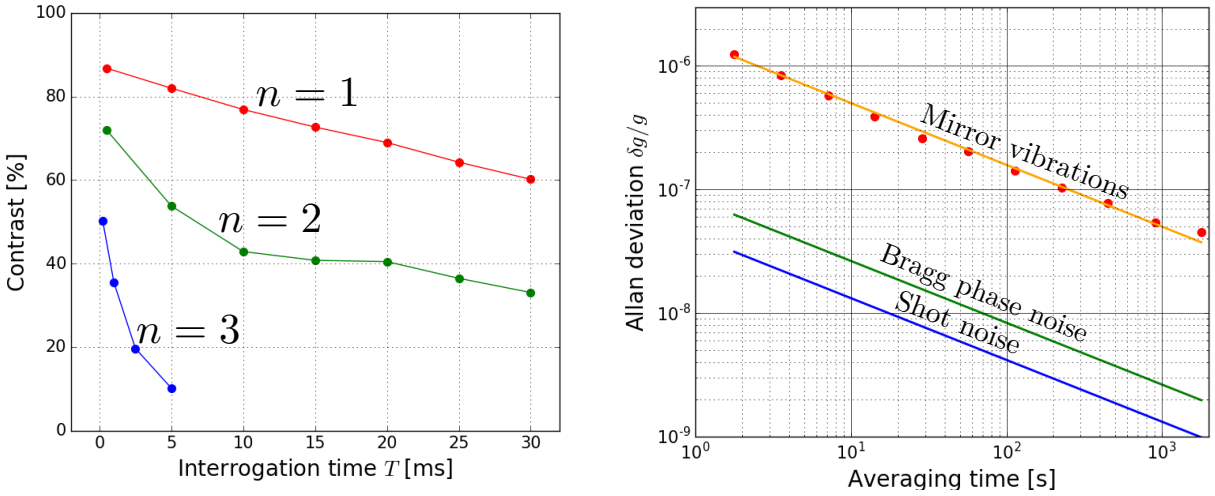

Figure 4.9: Left: fringe contrast of the interferometer for first ($n = 1$), second ($n = 2$) and third ($n = 3$) order Bragg diffraction. Right: Sensitivity of the atomic gravimeter. The dominant noise source is due to mirror vibrations. Smaller contributions arise from Bragg laser phase noise and atom shot noise.

Our work however shows that the reduced temperatures and cloud size attainable with strontium atoms lead to a large contrast with a relatively small laser beam transverse size.

Interferometer sensitivity The interferometer sensitivity was determined through repeated atomic phase measurements where we set the operating point at the fringe slope. This measurement allowed the determination of the Allan deviation for different averaging times (right of Fig. 4.9). By operating with an interferometer time $T = 30$ ms and an experiment cycle time of 1.7 s, we found a relative sensitivity to gravity acceleration variations $\delta g/g = 1.5 \times 10^{-6}$ at 1 s of averaging time. By averaging for $\tau = 2000$ s, we attained a sensitivity $\delta g/g = 4 \times 10^{-8}$. This result only slightly differs from the prediction $\delta g/g = 1.5 \times 10^{-6}/\sqrt{\tau} = 3.4 \times 10^{-8}$ based on the assumption of pure white phase noise.

The measured sensitivity limits are dominated by the residual retroreflecting mirror vibrations. By computing the sensitivity limits based on the reading of our accelerometer, we found the contribution 380 mrad/$\sqrt{\tau}$ due to mirror vibrations which matches the measured sensitivity. The Bragg laser phase noise was measured to yield a contribution of 20 mrad/$\sqrt{\tau}$ whereas the shot noise limit for 1×10^5 atoms is 10 mrad/$\sqrt{\tau}$ [107].

Because our experiments were aimed at the demonstration of a large-momentum-transfer Bragg interferometer with strontium atoms, we did not implement state-of-the-art technology for the suppression of the residual retroreflecting mirror vibrations [3]. These techniques will be implemented in future experiments and we foresee no complication in accessing the atom shot noise limit at least for interferometers with short interrogation

times. On the other hand, it is important to note that in our experiments we did not investigate the performance for longer interferometer times because of the limited size of the vacuum chamber.

4.4 Bragg atom gradiometer operating on the $^1S_0$-$^3P_1$ intercombination transition

In a later experiment, detailed in [109, 110], we explored the possibility of implementing an atom interferometer operating on the $^1S_0$-$^3P_1$ intercombination transition at 689 nm. This transition is easily accessible with current laser technology, where optical amplifiers as well as continuous-wave titanium-sapphire lasers exist. The unique feature of this transition lies in its narrow linewidth $\Gamma = 2\pi \times 7.5$ kHz. On the one hand, the small value of Γ allows to shift the laser frequency by many linewidths with a simple acousto-optic modulator. Such a modulator can readily switch from atomic resonance to the dispersive regime where the photon scattering rate is strongly suppressed. This allows the implementation of multi-photon Bragg transitions as well as dipole traps and optical lattices with the same laser source. For example, a 200 MHz AOM shifts the laser frequency by 2.7×10^4 Γ. For the blue transition, the same shift in units of the linewidth would be obtained by a detuning of 820 GHz, where laser locking by beatnote detection becomes challenging and other methods need to be implemented[2]. Even if such methods are implemented, a fast switching of the laser frequency by such a large amount is hardly feasibile. On the other hand, the linewidth of the 689 nm transition is large enough that laser stabilization can be attained by standard saturated absorption spectroscopy [108].

4.4.1 Experimental setup and sequence

The setup of the experiment is similar to that employed for Bragg diffraction on the dipole-allowed transition in that the MOT stage and the fluorescence detection methods are the same.

The setup for the red Bragg lasers is illustrated in Fig. 4.10 and consists of an optically-amplified laser at 689 nm with an emission linewidth of about 100 Hz. These favorable noise properties are attained by locking an extended-cavity diode-laser to a high-finesse optical resonator through the Pound-Drever-Hall method. The long-term drift of the optical cavity length is compensated by an additional locking stage performed by locking the piezo-actuated cavity to the saturated-absorption spectroscopy signal from a strontium heat pipe. The resulting laser light is used for the operation of the red MOT stage. A

[2]Stable locking with large frequency differences can be attained, for example, with a high-resolution wavemeter, a frequency comb or a transfer cavity.

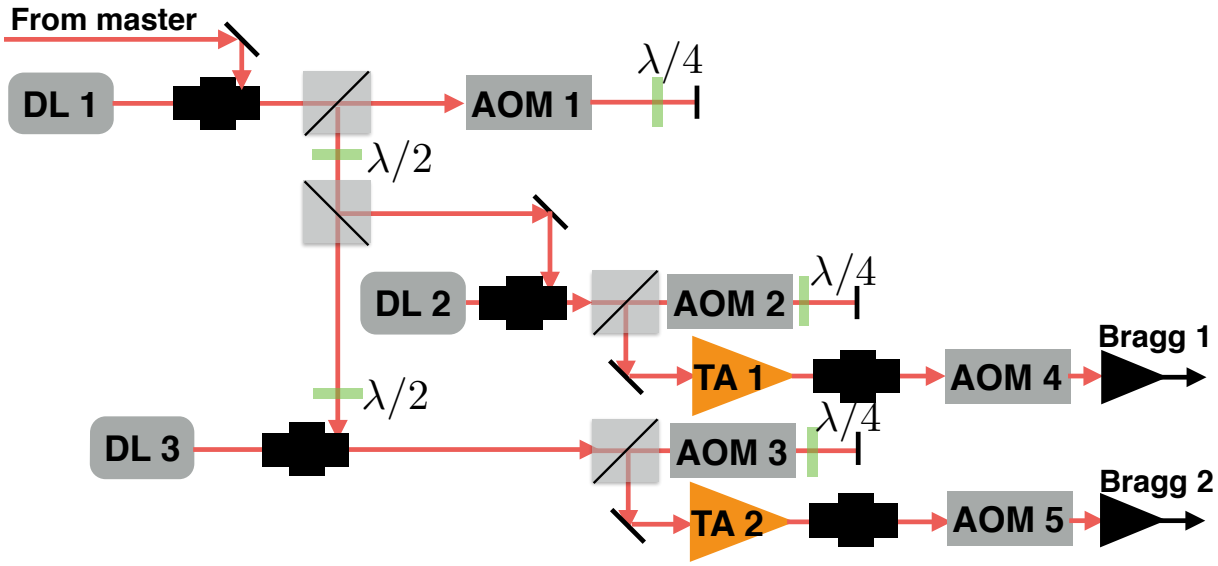

Figure 4.10: Optical scheme for the production of the laser beams for Bragg diffraction on the $^1S_0$-$^3P_1$ transition. A first diode laser (DL1) is optically injected from the master source, frequency shifted by AOM1 and injects two additional lasers (DL2 and DL3), both frequency shifted (AOM2 and AOM3) and amplified by two tapered amplifiers (TA1 and TA2). The final modulators AOM4 and AOM5 are used to temporally shape the Bragg pulses.

fraction of the light is used to optically inject a set of laser diodes and tapered amplifiers for the production of Bragg diffraction. This set consists of a first diode laser, optically injected by the master laser. The output of this laser is passed through an AOM which sets the general detuning from atomic resonance in the range $-1.3\times10^4\ \Gamma < \Delta < +1.9\times10^4\ \Gamma$. The AOM output is then used to optically inject two laser diodes that independently seed two tapered amplifiers. This couple forms the two Bragg laser beams. Before seeding the tapered amplifiers, the output of the two laser diodes is frequency shifted by two AOMs used to control the phase and frequency difference between the Bragg beams. Finally, the temporal shape of the laser pulses is tuned by two independent AOMs. The laser light is then coupled in two polarization-maintaining optical fibers and the output is collimated to a 2.3 mm waist with an output power of 80 mW per beam.

After releasing the MOT, the atoms are loaded into a vertical optical lattice with a depth $U = 20E_r$ (where E_r is the recoil energy) formed by the two Bragg beams with a 95 MHz red detuning from atomic resonance. This lattice is used to launch the atoms upwards. Because only a fraction of the atoms is captured by this first launch, there is a residual falling cloud which is subsequently trapped in a second stage optical lattice and launched vertically. After a set of Bragg selection and launch pulses, the atomic sample is formed by two clouds with a momentum difference of $4\hbar k$ (where k is the laser

wavenumber) and a $0.15\hbar k$ momentum width. This procedure allows to operate a second-order Bragg interferometer. In particular, by defining p_0 as the momentum of the lower cloud, the upper cloud with a momentum $p_0+4\hbar k$ is coupled to the state with momentum p_0, whereas the lower cloud is coupled to the state with momentum $p_0 + 4\hbar k$. These two clouds have a separation or baseline that is set by the time interval between the two successive launch stages. The result of this preparation stage is a pair clouds with 5×10^5 atoms each and a separation between 2.7 cm and 3.6 cm. This sample is then injected into a Mach-Zehnder atom interferometer and the output is used to measure the difference in gravity acceleration between the two cloud positions.

Because of the limited size of the vacuum chamber used in our experiments, both the gradiometer baseline and the interrogation time T are limited. Therefore, the current setup does not allow to attain a sizeable signal for the measurement of the Earth gravity gradients. In order to characterize the instrument sensitivity, we added a feature by inserting a difference between the general detuning of the $\pi/2$-pulses and that of the π-pulse of the interferometer. This method [111] induces an artificial gradient given by $\Gamma_{\mathrm{a}} = 2\Delta k_{\mathrm{eff}}/(k_{\mathrm{eff}}T^2)$, where k_{eff} is the effective wavenumber and Δk_{eff} is the effective wavenumber variation resulting from the frequency jump.

4.4.2 Experimental results

Interferometer contrast Our measurements showed that the atom interferometer operated on the red intercombination transition has a better performance compared to the blue dipole-allowed transition, as shown in Fig. 4.11. The main difference is the ability to reach an extremely large detuning from atomic resonance compared to the natural linewidth while keeping a relatively large four-photon Rabi frequency $\Omega_{\mathrm{eff}}^{(4)} = 2\pi \times 20$ kHz. In particular, we observed that, for a detuning 1.3×10^4 Γ and a beam waist 2.3 mm, we can attain a contrast $\mathcal{C} = 0.42$ for a $T = 80$ ms atom interferometer with a decay time constant of 130 ms. Bragg diffraction on the blue transition, in comparison, yielded a smaller contrast and a faster decay rate with a time constant of 39 ms.

Interferometer sensitivity Also in this case, the phase sensitivity of the interferometer was characterized by the Allan deviation. We found that the phase sensitivity is 210 mrad at 1 s, corresponding to a gradient sensitivity 5×10^{-4} s^{-2}. After a τ =1000 s averaging time, we reached a sensitivity to gravity gradients of 1.5×10^{-5} s^{-2} which is consistent with the prediction 5×10^{-4} s$^{-2}/\sqrt{\tau}$ and shows that the phase fluctuations have a white noise character. The sensitivity of our interferometer is limited by the size of the vacuum chamber and by the detection efficiency.

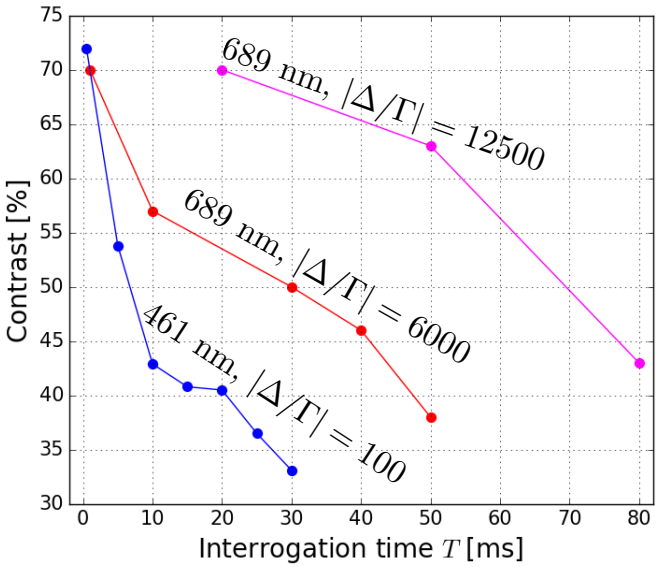

Figure 4.11: Comparison of the fringe contrast as a function of the interrogation time T and in different conditions. Blue points: second-order Bragg diffraction experiment performed on the blue $^1S_0$-$^1P_1$ transition with detuning $|\Delta/\Gamma| = 100$. The other curves refer to the measured contrast for the interferometer operated on the intercombination transition, for different values of the detuning $|\Delta/\Gamma| = 6000$ (red points) and $|\Delta/\Gamma| = 12500$ (magenta points). Note that the linewidths Γ refer to the specific transition used.

Sensitivity to magnetic fields Bosonic strontium in the $^1S_0$ ground state is expected to have a negligible sensitivity to external magnetic fields. This enhanced robustness against electromagnetic perturbations is expected because of the vanishing electronic and nuclear angular momenta. As a result, no linear Zeeman effect is expected for atoms in the ground state. It is found that the dominant shift of the ground state is given by the so-called diamagnetic term [112], proportional to the square of the vector potential. The calculation of such an effect requires the knowledge of the spatial part of the wavefunction of the atomic electrons. A reasonable estimate of this effect is obtained by using the optimized Slater orbitals [113]. A full calculation using the most advanced wavefunctions [114] for the atomic electrons yields a frequency shift $\Delta\nu = 36e^2a_0^2B^2/(8m_eh)$, where e is the electron charge, a_0 is the Bohr radius, B is the magnetic field intensity, m_e is the electron mass and h is Planck's constant. This shift amounts to $\Delta\nu = 5.4$ mHz/G^2. In comparison, for Rb atoms, the shift is 288 Hz/G^2 or 5×10^4 times larger.

In our experiments, we verified the insensitivity to such perturbations by applying intense magnetic field gradients.

Interestingly, we found that in our experiment configuration, we are able to apply a gradient of 50 G/cm and a magnetic field difference between the positions of the two atomic clouds of almost 200 G. According to our estimates, in these conditions it should

be possible to induce a considerably large gradiometer phase shift of more than 500 mrad which is well above our level of sensitivity. This measurement could thus determine an experimental measurement for such a small magnetic shift through its mechanical effect on the atomic trajectories. It should be however noted that, for precision gravity measurements and in standard conditions, the effect is hardly observable and is not expected to yield important systematic uncertainties.

4.5 Conclusions

In this Chapter, the implementation of Bragg diffraction in atom interferometers is discussed. Atom interferometers were implemented both on the dipole-allowed and on the intercombination transition and considerable values of the interferometer contrast have been observed.

Large values of the contrast were attained when operating on the red intercombination line. We attribute the superior performance of this transition to the narrow linewidth of the transition and to the availability of large amounts of laser power. The narrow linewidth allows to detune the laser from the optical transition by many linewidths in a straightforward manner, whereas the availability of laser power can induce reasonably large Rabi frequencies. The laser system that is necessary to implement the interferometer on the red transition is nevertheless rather involved as it requires a number of laser sources to attain optical pre-amplification and final amplification. In this chain, stability of the single units is essential and somewhat hard to maintain. For example, the injection of our slave lasers and the noise of the master laser were critical aspects that caused a sizeable waste of time and effort. Additionally, it is well known that tapered amplifiers suffer from a wide and intense background of amplified spontaneous emission. This is, to our knowledge, the main limitation to achieving long lattice lifetimes with a laser so close to atomic resonance. While the laser spectrum can be filtered through optical cavities, cleaner solutions exist, though more expensive, such as the Titanium-Sapphire laser or a frequency-doubled infrared Raman laser. These solutions will be explored in the near future. While in standard conditions the interferometer operated on the red transition, as is the blue transition, does not sense external magnetic fields, the large first-order Zeeman effect of the excited state can cause complications. Indeed, a magnetic field might shift one of the Zeeman sublevels closer to the laser frequency thus changing the contrast loss rate in a polarization-dependent manner. Even if we did not carefully explore this aspect, the presence of a nearby photoassociation line might have caused additional complications and enhanced sensitivity to laser polarization.

The blue transition, on the other hand, does not allow to achieve large detunings (in units of the linewidth) while switching the frequency by large amounts. A large detuning

can be attained, in principle, but then, if necessary, the optical lattice trap should be implemented with a separate laser. This choice probably represents the most stable solution if one is constrained by a low budget.

Because these experiments were mainly focused on providing a proof-of-principle of the feasibility of atom interferometers with strontium atoms, the state-of-the-art was not reached. However, technologically achievable improvements will boost the performance of these interferometers. At least for atomic gradiometers, it is expected that the atom shot noise limit is attainable. Moreover, the high level of insensitivity to external magnetic fields has been established.

In the next Chapter, we consider a method that allows to generate squeezed momentum states for atom interferometry that is applicable to both transitions considered in this Chapter, even if we will make explicit reference to the dipole-allowed transition. There is no fundamental reason to choose this transition aside from the facts that Bragg diffraction is achievable in a quite simple way and that it provides a good momentum state separation, owing to the small wavelength. If a better stability of the red laser system can be achieved, this might represent a better choice.

Chapter 5

Squeezing on momentum states for atom interferometry

In this Chapter we enter the core of this thesis. We will describe a method for the implementation of squeezed momentum states of strontium atoms for Bragg interferometry [115]. This study is motivated by the following facts:

- Strontium atoms are among the best candidates for precision metrology. This has been demonstrated both for optical lattice clocks based on neutral atoms approaching the 10^{-19} relative precision [82] as well as for atom interferometers in our group. Aside from being accessible with current technology, strontium atoms have unique features that make them insensitive to external perturbations, an essential requirement for precision measurements. Moreover, the strontium optical transitions span a natural linewidth range that extends over more than eleven decades, allowing to perform experiments in different regimes including the production of degenerate gases by laser cooling [87].

- In our group we successfully implemented large momentum transfer beam splitters and mirrors based on Bragg diffraction for atom interferometry. We operated atom interferometer experiments both on a dipole-allowed transition and on a narrow intercombination transition. We demonstrated that strontium Bragg atom interferometers are largely insensitive to external perturbations and attained large values of fringe contrast, indicating the persistence of atomic coherence over considerably long time scales.

- In our experiments, the limits to the atom interferometer sensitivity were purely technical and can be overcome with current technology both for gravimeters [3] and for gradiometers where the atom shot noise limit has been reached [13]. A further improvement in the sensitivity can be obtained by reducing the quantum fluctuations below the Standard Quantum Limit.

- As large momentum transfer atom interferometers operate with two states that differ by their linear momentum while having the same electronic part, overcoming the shot noise limit requires to elaborate a set of methods which can produce squeezed momentum states. This has remained so far a formidable task.

In this Chapter we illustrate a method to induce squeezed momentum states whose potential is increased in the presence of a ring resonator. We begin by providing the theoretical tools for the understanding and the derivation of the main results. We then consider the nondestructive measurement of the population difference between two momentum states through the Doppler effect. Being a collective measurement, it projects the ensemble state into a state that is close to an eigenstate of the measured observable and therefore produces spin squeezing according to the treatment performed in Subsection 2.3.2. Although we mainly focus on nondestructive measurements, most of the methods described here can produce dynamic squeezing as in [72, 73]

We show that squeezing based on the Doppler effect is limited to large Bragg diffraction orders for optical transitions and that by appropriately modifying the atomic medium properties, the method can reach a squeezing limit for small diffraction orders that is as good as for large diffraction orders.

5.1 General treatment of the interaction of a system with a heat bath

In this Section we provide the main theoretical framework that allows to analyze the problem of the interaction between an atomic system with a radiation field. This treatment is suitable for a consistent description of an ensemble of atoms interacting with the light circulating in an optical resonator and of the damping of both the atomic and radiation systems. We follow the input-output theory outlined in [116, 117] and adapt the notation to the specific problem of interest for spin squeezing experiments.

We consider a system interacting with a heat bath comprised of a large number of harmonic oscillators. We restrict our discussion to the relevant case where the following three assumptions are fulfilled:

1. the interaction between the system and the heat bath is linear;
2. the rotating-wave approximation is made;
3. the interaction strength of the system with the heat bath is independent of the energy being exchanged between the two parts.

We define $\hat{b}(\omega)$ as the annihilation operator for a quantum of the harmonic oscillator of the bath with frequency ω and $\hat{c}$ as an operator of the system through which the system

and the bath interact. Because the bath has a large number of degress of freedom (or modes), we employ the continuum approximation and consider the commutation relation $[\hat{b}(\omega), \hat{b}^\dagger(\omega')] = \delta(\omega - \omega')$, where $\delta(x)$ is the Dirac delta function. The total Hamiltonian, describing the free energies of the system, of the bath and of their interaction can be written as $\hat{\mathcal{H}} = \hat{\mathcal{H}}_{\rm S} + \hat{\mathcal{H}}_{\rm B} + \hat{\mathcal{H}}_{\rm I}$. $\hat{\mathcal{H}}_{\rm S}$ is the Hamiltonian for the system,

$$\hat{\mathcal{H}}_{\rm B} = \int_{-\infty}^{\infty} \hbar\omega \hat{b}^\dagger(\omega)\hat{b}(\omega)d\omega \tag{5.1}$$

describes the free energy of the bath and

$$\hat{\mathcal{H}}_{\rm I} = i\int_{-\infty}^{\infty} \hbar g(\omega)\left[\hat{b}^\dagger(\omega)\hat{c} - \hat{c}^\dagger\hat{b}(\omega)\right]d\omega \tag{5.2}$$

describes the linear interaction of the system with the heat bath with the frequency-dependent interaction strength $\hbar g(\omega)$.

We now follow a standard procedure aimed at describing the system dynamics where the interaction with the bath is described by effective driving and damping terms.

The Heisenberg equation of motion for the observable $\hat{A}$ reads $i\hbar\frac{d}{dt}\hat{A} = [\hat{A}, \hat{\mathcal{H}}]$. We write this equation for the bath operator $\hat{b}(\omega)$ and for an arbitrary system operator $\hat{a}$,

$$\frac{d}{dt}\hat{b}(\omega) = -i\omega\hat{b}(\omega) + g(\omega)\hat{c} \tag{5.3}$$

$$\frac{d}{dt}\hat{a} = -\frac{i}{\hbar}[\hat{a}, \hat{\mathcal{H}}_{\rm S}] + \int_{-\infty}^{\infty} g(\omega)\left\{\hat{b}^\dagger(\omega)[\hat{a}, \hat{c}] - [\hat{a}, \hat{c}^\dagger]b(\omega)\right\}d\omega. \tag{5.4}$$

Next we formally integrate equation (5.3),

$$\hat{b}(\omega) = e^{-i\omega(t-t_0)}\hat{b}_0(\omega) + g(\omega)\int_{t_0}^{t} e^{-i\omega(t-t')}\hat{c}(t')dt' \tag{5.5}$$

and insert the result in (5.4) thus obtaining the Langevin equation:

$$\begin{aligned}\frac{d}{dt}\hat{a} = &-\frac{i}{\hbar}[\hat{a}, \hat{\mathcal{H}}_{\rm S}] + \int_{-\infty}^{\infty} g(\omega)\left\{e^{i\omega(t-t_0)}\hat{b}_0^\dagger(\omega)[\hat{a}, \hat{c}] - e^{-i\omega(t-t_0)}[\hat{a}, \hat{c}^\dagger]b_0(\omega)\right\} \\ &+ \int_{-\infty}^{\infty} d\omega g^2(\omega)\int_{t_0}^{t} dt'\left\{e^{i\omega(t-t')}\hat{c}^\dagger(t')[\hat{a}, \hat{c}] - e^{-i\omega(t-t')}[\hat{a}, \hat{c}^\dagger]\hat{c}(t')\right\},\end{aligned} \tag{5.6}$$

where $\hat{b}_0(\omega)$ is the value of $\hat{b}(\omega)$ at the initial instant of time t_0. Up to this point, the equations of motion describe a linear (1) interaction between the system and the bath in the rotating wave approximation (2). We next introduce the third assumption that the coupling strength is independent of frequency. This is known as the Markov approximation which we express in the form $g(\omega) = \sqrt{\gamma/(2\pi)}$ and show that γ can be interpreted as a damping rate. The equation of motion (5.6) for the operator $\hat{a}$ then takes the form

$$\frac{d}{dt}\hat{a} = -\frac{i}{\hbar}[\hat{a}, \hat{\mathcal{H}}_{\rm S}] - \left\{[\hat{a}, \hat{c}^\dagger]\left[\frac{\gamma}{2}\hat{c} + \sqrt{\gamma}\hat{b}_{\rm in}\right] - \left[\frac{\gamma}{2}\hat{c}^\dagger + \sqrt{\gamma}\hat{b}_{\rm in}^\dagger\right][\hat{a}, \hat{c}]\right\}, \tag{5.7}$$

where $\hat{b}_{\rm in}$ is the input field, defined as the Fourier transform of $\hat{b}(\omega)$

$$\hat{b}_{\rm in}(t) = \frac{1}{\sqrt{2\pi}} \int_{-\infty}^{\infty} \hat{b}_0(\omega) e^{-i\omega(t-t_0)} d\omega. \tag{5.8}$$

The input field satisfies the commutation relation $[\hat{b}_{\rm in}(t), \hat{b}_{\rm in}^\dagger(t')] = \delta(t-t')$.

Similarly, we define the output field

$$\hat{b}_{\rm out}(t) = \frac{1}{\sqrt{2\pi}} \int_{-\infty}^{\infty} \hat{b}_1(\omega) e^{-i\omega(t-t_1)} d\omega \tag{5.9}$$

where $\hat{b}_1$ is the bath operator evaluated at the final instant of time t_1 with $t_1 > t > t_0$. By considering the result of the formal integration (5.5), we rewrite it with the replacements $t_0 \to t$ and $t \to t_1$ and solve for $\hat{b}(\omega)$:

$$\hat{b}(\omega) = \hat{b}_1(\omega) e^{-i\omega(t-t_1)} - g(\omega) \int_t^{t_1} e^{-i\omega(t-t')} \hat{c}(t') dt'. \tag{5.10}$$

This result, along with (5.5) allows to obtain the relation between the input and output operators. This is achieved by integrating $\hat{b}(\omega)$ over the frequency domain and by using (5.5) and (5.10):

$$\frac{1}{\sqrt{2\pi}} \int_{-\infty}^{\infty} \hat{b}(\omega) = \hat{b}_{\rm in} + \frac{\sqrt{\gamma}}{2} \hat{c} = \hat{b}_{\rm out} - \frac{\sqrt{\gamma}}{2} \hat{c} \tag{5.11}$$

or

$$\hat{b}_{\rm out} = \hat{b}_{\rm in} + \sqrt{\gamma} \hat{c}. \tag{5.12}$$

We now show that equation (5.7) gives an effective description for the interaction of the system with the heat bath in terms of damping at a rate γ. To show this we consider a system formed by a harmonic oscillator described by the annihilation operator $\hat{a}$ with $[\hat{a}, \hat{a}^\dagger] = 1$ and assume that the system has been previously excited so that $\hat{a}(t = t_0) = \hat{a}_0$. If $\hat{a}$ is the operator through which the system interacts with the heat bath, we also have $\hat{a} = \hat{c}$. The system Hamiltonian is just the free energy of the harmonic oscillator, $\hat{\mathcal{H}}_{\rm S} = \hbar\omega_c \hat{c}^\dagger \hat{c}$. The equation of motion for $\hat{c}$ is

$$\frac{d}{dt}\hat{c} = -i\omega_c \hat{c} - \frac{\gamma}{2}\hat{c} \tag{5.13}$$

and has the solution $\hat{a}(t) = \hat{a}_0 e^{-i(\omega_c - i\gamma/2)(t-t_0)}$ that is, the amplitude of the harmonic oscillator field decays with a rate $\gamma/2$.

Similarly, the equation of motion for the number operator $\hat{n} = \hat{c}^\dagger \hat{c}$ is

$$\frac{d}{dt}\hat{n} = -\gamma \hat{n}, \tag{5.14}$$

with solution $\hat{n}(t) = \hat{n}_0 e^{-\gamma(t-t_0)}$, where $\hat{n}_0 = \hat{a}_0^\dagger \hat{a}_0$ is the initial number of quanta in the harmonic oscillator. As a result, the number operator decays with a rate γ.

The terms proportional to $\sqrt{\gamma}$ represent the external driving of the system. For a coherent drive with amplitude β and frequency ω, corresponding to $\hat{b}_0(\omega') = \sqrt{2\pi}\beta\delta(\omega' - \omega)$, we have $\langle \hat{b}_{\text{in}} \rangle = \beta e^{-i\omega(t-t_0)}$ and the equation of motion for $\hat{c}$ reads

$$\frac{d}{dt}\langle \hat{c} \rangle = -i\left(\omega_c - i\frac{\gamma}{2}\right)\langle \hat{c} \rangle - \sqrt{\gamma}\beta e^{-i\omega(t-t_0)} \tag{5.15}$$

The solution with the initial condition $\langle c(t = t_0) \rangle = 0$ is

$$\langle \hat{c}(t) \rangle = -i\frac{\sqrt{\gamma}\beta}{\Delta + i\frac{\gamma}{2}} e^{-i\omega(t-t_0)} \left[1 - e^{i(\Delta + i\gamma/2)(t-t_0)}\right], \tag{5.16}$$

where we have defined the detuning $\Delta = \omega - \omega_c$. This result reveals the main properties of the driven system:

- system decay and system driving are connected in that the oscillator amplitude is proportional to $\sqrt{\gamma}$;
- the solution reaches its steady state after a time interval $\Delta t \gg 1/\gamma$ after which the solution no longer contains the component oscillating at the natural frequency ω_c and only oscillates at the drive frequency ω;
- the excitation profile features a resonance at the natural frequency ω_c with a lorentzian full width at half maximum γ.

The two systems considered in this Chapter, photons and atoms, can be described by this model. For photons, the model describes the light in a single mode of an optical resonator with resonance frequency ω_c and linewidth γ. Similarly, an atomic two-level system far from population saturation can be described as a harmonic oscillator where the resonance frequency ω_c corresponds to the energy of the transition between ground and excited states and γ is the linewidth of the transition.

5.2 Equations of motion for photons and atoms

The tools developed in the previous Section are directly applicable to the description of the interaction of an ensemble of atoms with the light circulating in an optical cavity in the presence of damping. We first consider the two systems, photons and atoms separately.

5.2.1 Photons in an optical cavity

As already discussed, (5.15) can be directly adapted to describe the motion of the annihilation operator $\hat{c}$ for the system formed by the photons in a single mode at frequency ω_c. This model describes photons in an optical cavity. Because γ is the photon number

(or optical power) decay rate, we set $\gamma = \kappa$, where κ is the cavity mode linewidth and is related to the free spectral range $\Delta\nu_{\mathrm{FSR}}$ and the finesse $\mathcal{F}$ by $\kappa = 2\pi\Delta\nu_{\mathrm{FSR}}/\mathcal{F}$. Equation (5.15) describes a single-mode optical cavity that is coupled to the environment on one side only, that is, only one mirror has a partial transmission and no other losses are present. The model can be generalized to describe the real situation where multiple inputs and outputs are present. In particular, we consider the practical case where two mirrors have finite transmission and there are additional intracavity losses. We can then consider three heat baths described by the operators $\hat{b}^{(i)}(\omega)$ with coupling strength $g_i(\omega) = \sqrt{\kappa_i/(2\pi)}$ for $i = 1, 2, 3$. The coupling strengths g_i for $i = 1, 2$ describe the coupling through the two partially transmitting mirrors whereas g_3 describes the losses and therefore does not contribute to the external driving of the optical cavity. The interaction Hamiltonian (5.2) can then be rewritten in the form

$$\hat{\mathcal{H}}_{\mathrm{I}} = i \sum_{i=1,2,3} \hbar \sqrt{\frac{\kappa_i}{2\pi}} \int_{-\infty}^{\infty} d\omega \left[\hat{b}^{(i)\dagger}(\omega)\hat{c} - \hat{c}^{\dagger}\hat{b}^{(i)}(\omega) \right]. \tag{5.17}$$

The Langevin equation then takes the form

$$\frac{d}{dt}\hat{a} = -\frac{i}{\hbar}[\hat{a}, \hat{\mathcal{H}}_{\mathrm{S}}] - \frac{\kappa}{2}\left([\hat{a}, \hat{c}^{\dagger}]\hat{c} - \hat{c}^{\dagger}[\hat{a}, \hat{c}]\right) - \sum_{i=1,2} \sqrt{\kappa_i} \left([\hat{a}, \hat{c}^{\dagger}]\hat{b}^{(i)}_{\mathrm{in}} - \hat{b}^{(i)\dagger}_{\mathrm{in}}[\hat{a}, \hat{c}] \right), \tag{5.18}$$

where $\kappa = \kappa_1 + \kappa_2 + \kappa_3$.

The input-output relation (5.12) determines the output fields. In particular, we consider driving the optical cavity from side 1 so that $\hat{b}^{(1)}_{\mathrm{in}}$ represents the driving field and no field is present on the second side. The transmitted field is then expressed as

$$\hat{b}^{(2)}_{\mathrm{out}} = \sqrt{\kappa_2}\hat{c}, \tag{5.19}$$

whereas the reflected field is given by

$$\hat{b}^{(1)}_{\mathrm{out}} = \hat{b}^{(1)}_{\mathrm{in}} + \sqrt{\kappa_1}\hat{c}. \tag{5.20}$$

This last expression has the clear interpretation as a superposition between the light reflected by the input mirror and the light that is coupled into the cavity and is transmitted by the same mirror.

5.2.2 Atomic ensembles

The damping equation for an atomic ensemble can be derived through steps that are similar to those that led to the Langevin equation (5.7). In this case the bath is formed by the photon modes that differ by the wavevector $\boldsymbol{k}$ and the polarization $\boldsymbol{e}_p$. By defining $\hat{b}_{\boldsymbol{k},p}$ as the corresponding annihilation operator, the bath Hamiltonian is written

$$\hat{\mathcal{H}}_{\mathrm{B}} = \sum_{\boldsymbol{k},p} \hbar\omega_k \hat{b}^{\dagger}_{\boldsymbol{k},p}\hat{b}_{\boldsymbol{k},p}, \tag{5.21}$$

where $\hbar\omega_k$ is the energy of a photon with wavenumber k. In determining the interaction with an atomic ensemble, we consider first a single two-level atom with resonance frequency ω_0 and define $|g\rangle$ and $|e\rangle$ the ground and excited states, respectively. We then consider the ladder operators $\hat{\sigma}_- = |g\rangle\langle e|$ and $\hat{\sigma}_+ = |e\rangle\langle g|$. The interaction Hamiltonian in the electric dipole and rotating-wave approximations of the atom with the bath of modes of the electromagnetic field is given by [118]

$$\hat{\mathcal{H}}_{\mathrm{I}} = i\hbar \sum_{\boldsymbol{k},p} g_k \boldsymbol{e}_p \cdot \boldsymbol{e}_d (\hat{b}^\dagger_{\boldsymbol{k},p}\hat{\sigma}_- - \hat{\sigma}_+ \hat{b}_{\boldsymbol{k},p}), \tag{5.22}$$

where $g_k = \sqrt{\omega_k \mu^2/(2\epsilon_0 \hbar V)}$ is the single-photon Rabi frequency with $\omega_k = ck$, $\boldsymbol{\mu} = |\langle e|\hat{\boldsymbol{\mu}}|g\rangle|\boldsymbol{e}_d$ the electric dipole moment matrix element, V the quantization volume. The polarization unit vector is denoted as $\boldsymbol{e}_p$.

We then find the equation of motion for the operator $\hat{b}_{\boldsymbol{k},p}$ and integrate it formally:

$$\hat{b}_{\boldsymbol{k},p} = g_k \boldsymbol{e}_p \cdot \boldsymbol{e}_d \int_{t_0}^{t} e^{-i\omega_k (t-t')} \hat{\sigma}_-(t') dt'. \tag{5.23}$$

Here we neglect the input field $\hat{b}_{\boldsymbol{k},p}(0)$ at the initial instant of time $t = t_0$ because for the case considered in this Chapter, the atom is driven through the cavity field. The equation of motion for the arbitrary system operator $\hat{a}$ then reads

$$\frac{d}{dt}\hat{a} = -\frac{i}{\hbar}[\hat{a}, \hat{\mathcal{H}}_{\mathrm{S}}] + \sum_{\boldsymbol{k},p} g_k \boldsymbol{e}_p \cdot \boldsymbol{e}_d \left(\hat{b}^\dagger_{\boldsymbol{k},p}[\hat{a}, \hat{\sigma}_-] - [\hat{a}, \hat{\sigma}_+]\hat{b}_{\boldsymbol{k},p} \right). \tag{5.24}$$

By substituting (5.23) into (5.24) we get the final atomic damping equation. In order to attain this, we follow the Wigner-Weisskopf approach [119] and make the continuum approximation by the replacement

$$\sum_{\boldsymbol{k},p} |\boldsymbol{e}_p \cdot \boldsymbol{e}_d|^2 \to 2\frac{V}{(2\pi)^3} \int |\boldsymbol{e}_p \cdot \boldsymbol{e}_d|^2 d\Omega_s \int_0^{+\infty} \frac{\omega^2}{c^3} d\omega = \frac{V}{3\pi^2} \int_0^{+\infty} \frac{\omega^2}{c^3} d\omega. \tag{5.25}$$

The resulting Langevin equation of motion is

$$\frac{d}{dt}\hat{a} = -\frac{i}{\hbar}[\hat{a}, \hat{\mathcal{H}}_{\mathrm{S}}] + \frac{\Gamma}{2}\left(\hat{\sigma}_+[\hat{a}, \hat{\sigma}_-] - [\hat{a}, \hat{\sigma}_+]\hat{\sigma}_- \right), \tag{5.26}$$

where

$$\Gamma = \frac{\omega_0^3 \mu^2}{3\pi\epsilon_0 \hbar c^3} \tag{5.27}$$

is the decay rate of the optical transition.

The formalism described in this Subsection also allows to establish the formal equivalence of the atomic system with that of harmonic oscillators when the population is far from saturation. We first note that $[\hat{\sigma}_-, \hat{\sigma}_+] = -\hat{\sigma}_z$, where $\hat{\sigma}_z = |e\rangle\langle e| - |g\rangle\langle g|$ is the operator corresponding to the population difference. If the atom is weakly driven by a light field, the population of the excited state is negligible and we can make the replacement $\hat{\sigma}_z \to -1$. As a result, $[\hat{\sigma}_-, \hat{\sigma}_+] = 1$ and σ_- behaves the same way as the annihilation operator for the light field.

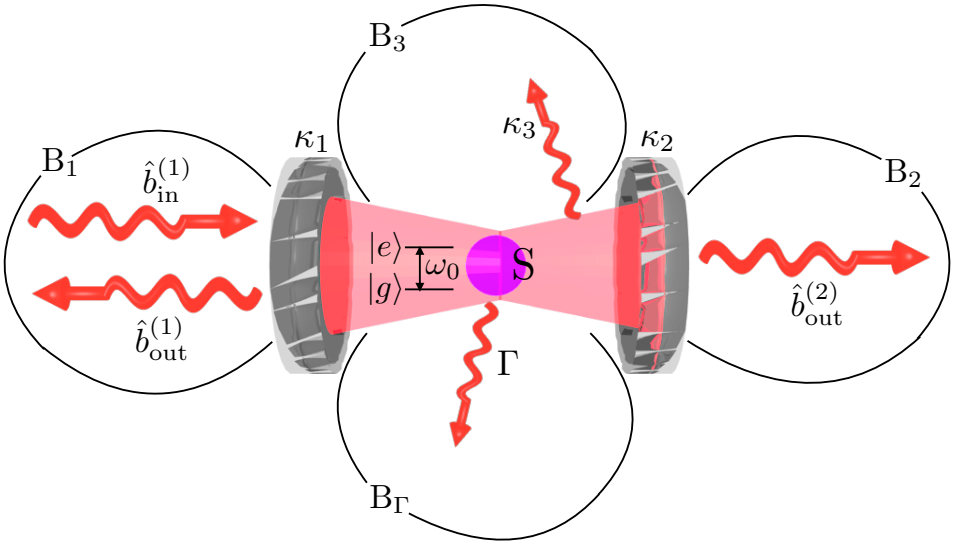

Figure 5.1: Schematic representation of the coupled atoms-cavity system S and of its environment. The bath is formed by four parts. B_1 is the bath of the modes on the input side with $\hat{b}^{(1)}_{\rm in}$ the incident field, $\hat{b}^{(1)}_{\rm out}$ the reflected field and the coupling strength is given by κ_1. Similarly, the bath on the output side is denoted by B_2, is coupled to S with a strength κ_2 and contains the transmitted field $\hat{b}^{(2)}_{\rm out}$. The undetected intracavity losses form the bath B_3. The atomic ensemble, on the other hand emits photons in the bath B_Γ at a rate Γ.

5.2.3 Atom-cavity system

A schematic representation of the coupled atoms-cavity system S embedded in the environment formed by the modes of the free electromagnetic field is shown in Figure 5.1. In building up the complete picture for the interaction of the system with the environment, we decompose the bath into four parts:

- B_1 is the bath formed by the modes of the incident field $\hat{b}^{(1)}_{\rm in}$ and of the reflected field $\hat{b}^{(1)}_{\rm out}$. The rate of photons transmitted from the input mirror is κ_1
- B_2 is the bath formed by the modes of the transmitted field $\hat{b}^{(2)}_{\rm out}$.
- B_3 is the bath formed by the modes of the light that is lost because of intracavity losses. These include losses from scattering and absorption from the cavity mirrors. The rate of such losses is κ_3.
- B_Γ is the bath formed by the modes of the light that is scattered from the atoms into free space at a rate Γ.

By combining the results of the previous sections, we can write the Langevin equation of motion for the system formed by a two-level atom and the light circulating in the

optical cavity:

$$\frac{d}{dt}\hat{a} = -\frac{i}{\hbar}[\hat{a}, \hat{\mathcal{H}}_{\rm S}] + \frac{\kappa}{2}\left(\hat{c}^\dagger[\hat{a},\hat{c}] - [\hat{a},\hat{c}^\dagger]\hat{c}\right) + \frac{\Gamma}{2}\left(\hat{\sigma}_+[\hat{a},\hat{\sigma}_-] - [\hat{a},\hat{\sigma}_+]\hat{\sigma}_-\right) \\ -\sqrt{\kappa_1}\left([\hat{a},\hat{c}^\dagger]\hat{b}^{(1)}_{\rm in} - \hat{b}^{(1)\dagger}_{\rm in}[\hat{a},\hat{c}]\right), \tag{5.28}$$

where $\kappa = \kappa_1 + \kappa_2 + \kappa_3$ and we give the physical significance to the operator $\hat{c}$ as the annihilation operator for the intracavity light field, with $[\hat{c}, \hat{c}^\dagger] = 1$.

The generalization of this equation to the case of an ensemble of N two-level atoms is straightforward. We assume that photon scattering into free space from the different atoms populates different modes of the free electromagnetic field in B_Γ. This assumption is correct in the continuum limit where B_Γ is formed by an infinite amount of modes. As a result, an atom scatters photons independently of all the others and we need to make the replacement

$$\frac{\Gamma}{2}\left(\hat{\sigma}_+[\hat{a},\hat{\sigma}_-] - [\hat{a},\hat{\sigma}_+]\hat{\sigma}_-\right) \to \frac{\Gamma}{2}\sum_{i=1}^{N}\left(\hat{\sigma}_{i+}[\hat{a},\hat{\sigma}_{i-}] - [\hat{a},\hat{\sigma}_{i+}]\hat{\sigma}_{i-}\right), \tag{5.29}$$

where $\hat{\sigma}_{i-}$ and $\hat{\sigma}_{i+}$ are the ladder operators for the i-th atom.

We are now in a position to write the equations of motion for the system variables $\hat{c}$ and $\hat{\sigma}_- = \sum_{i=1}^{N}\hat{\sigma}_{i-}$ with the cavity incident coherent field amplitude at frequency ω $\langle\hat{b}^{(1)}_{\rm in}\rangle = \beta e^{-i\omega t}$. We consider the system Hamiltonian formed by the free atomic energy, by the free energy of the intracavity electromagnetic field and by their interaction in a Jaynes-Cummings form:

$$\hat{\mathcal{H}}_{\rm S} = \frac{\hbar\omega_0}{2}\hat{\sigma}_z + \hbar\omega_c\hat{c}^\dagger\hat{c} + \hbar g(\hat{c}^\dagger\hat{\sigma}_- + \hat{\sigma}_+\hat{c}), \tag{5.30}$$

where ω_0 is the atomic resonance frequency, ω_c is the cavity resonance frequency, $2g$ is the single-photon Rabi frequency, $g = \sqrt{\omega_0\mu^2/(2\epsilon_0\hbar V)}$, μ is the electric dipole matrix element and V is the cavity mode volume. The cavity mode volume is $V = V_{\rm sw} = \pi w^2 L/4$ for a linear (standing-wave) cavity with length L and mode waist w and $V = V_{\rm rw} = \pi w^2 L_{\rm rt}/2$ for a ring (running-wave) cavity with round-trip length $L_{\rm rt}$[1]. Using the expression for $\hat{\mathcal{H}}_{\rm S}$,

[1]For a TEM_{00} Gaussian profile, the mode volume is defined as the volume integral with cross-sectional (xy) area weighted by the Gaussian intensity factor and with the axial (z) part weighted by the longitudinal intensity factor. For a linear (standing-wave) cavity with length L we account for the longitudinal intensity variation due to the standing-wave pattern and write, for $L \gg \lambda_0$, where λ_0 is the light wavelength,

$$V_{\rm sw} = \int_{-\infty}^{\infty}dx\int_{-\infty}^{\infty}dy e^{-2\frac{x^2+y^2}{w^2}}\int_0^L \sin^2\left(\frac{2\pi}{\lambda_0}z\right)dz = \frac{1}{4}\pi w^2 L$$

For a ring (running-wave) cavity, on the other hand, the intensity is uniform along the cavity axis, therefore

$$V_{\rm rw} = \int_{-\infty}^{\infty}dx\int_{-\infty}^{\infty}dy e^{-2\frac{x^2+y^2}{w^2}}\int_0^{L_{\rm rt}}dz = \frac{1}{2}\pi w^2 L_{\rm rt}.$$

the equations of motion are

$$\frac{d}{dt}\hat{c} = -i\left(\omega_c - i\frac{\kappa}{2}\right)\hat{c} - ig\hat{\sigma}_- - \sqrt{\kappa_1}\hat{b}_{\text{in}}^{(1)} \tag{5.31}$$

$$\frac{d}{dt}\hat{\sigma}_- = -i\omega_0\hat{\sigma}_- + \frac{\Gamma}{2}\sum_{i=1}^{N}\hat{\sigma}_{iz}\hat{\sigma}_{i-} + ig\hat{\sigma}_z\hat{c} \tag{5.32}$$

where $\hat{\sigma}_{iz} = |e\rangle_i \langle e|_i - |g\rangle_i \langle g|_i$ and $\hat{\sigma}_z = \sum_{i=1}^{N}\hat{\sigma}_{iz}$. As we already discussed in the previous Subsection, we express the equations of motion in the weak driving (low saturation) limit, where the population difference operators are replaced as $\hat{\sigma}_{iz} \to -1$ and $\hat{\sigma}_z \to -N$. We take the expectation values of the operators in the rotating frame at the frequency ω of the driving field: $\hat{c} = \hat{\tilde{c}}e^{-i\omega t}, \hat{\sigma}_- = \hat{\tilde{\sigma}}_- e^{-i\omega t}$. The incident field is expressed by $\langle \hat{b}_{\text{in}}^{(1)} \rangle = \beta e^{-i\omega t}$, where β is the field amplitude with units of $\sqrt{\text{photons/s}}$. Finally, the equations of motion for the expectation values in the rotating frame are

$$\frac{d}{dt}\tilde{c} = i\left(\delta + i\frac{\kappa}{2}\right)\tilde{c} - ig\tilde{\sigma}_- - \sqrt{\kappa_1}\beta \tag{5.33}$$

$$\frac{d}{dt}\tilde{\sigma}_- = i\left(\Delta + i\frac{\Gamma}{2}\right)\tilde{\sigma}_- - iNg\tilde{c}, \tag{5.34}$$

where $\tilde{c} = \langle \hat{\tilde{c}} \rangle, \tilde{\sigma}_- = \langle \hat{\tilde{\sigma}}_- \rangle, \delta = \omega - \omega_c$ is the detuning from cavity resonance and $\Delta = \omega - \omega_0$ is the detuning from atomic resonance.

The homogeneous part of equations (5.33) and (5.34) has the normal mode frequencies given by

$$\overline{\omega}_\pm = \frac{\Delta + \delta \pm \sqrt{(\Delta+\delta)^2 + 4Ng^2}}{2}. \tag{5.35}$$

In the limit $|\Delta + \delta| \gg 2g\sqrt{N}$ with $\Delta + \delta$ positive, $\overline{\omega}_+ \to (\Delta+\delta), \overline{\omega}_- \to 0$ whereas for $\Delta + \delta$ negative, $\overline{\omega}_+ \to 0, \overline{\omega}_- \to (\Delta + \delta)$. When the condition $\Delta + \delta = 0$ is satisfied the degeneracy is lifted by the vacuum Rabi splitting [79, 120, 121] $\overline{\omega}_+ - \overline{\omega}_- = 2g\sqrt{N}$.

Another important feature of equations (5.33) and (5.34) is their steady-state solution which is found when the time derivatives vanish:

$$\tilde{\sigma}_- = \frac{Ng\tilde{c}}{\Delta + i\frac{\Gamma}{2}} \tag{5.36}$$

and

$$\tilde{c} = -i\frac{2\frac{\sqrt{\kappa_1}}{\kappa}\beta}{\frac{2\delta}{\kappa} + N\eta\mathcal{L}_d(\Delta) + i[1 + N\eta\mathcal{L}_a(\Delta)]} \tag{5.37}$$

where we defined the absorption $\mathcal{L}_a$ and dispersion $\mathcal{L}_d$ profiles as [34]

$$\mathcal{L}_a(\Delta) = \frac{\Gamma^2}{\Gamma^2 + 4\Delta^2} \quad \mathcal{L}_d(\Delta) = -\frac{2\Delta\Gamma}{\Gamma^2 + 4\Delta^2} \tag{5.38}$$

and the single-atom cooperativity $\eta = 4g^2/(\kappa\Gamma)$. It is important to notice that, despite its appearance, the single-atom cooperativity is an essentially geometric parameter. This can

be seen by recalling the expressions of the single-photon Rabi frequency $2g$ from (5.30) and of Γ (5.27). The cavity mode linewidth is given by $\kappa = 2\pi\Delta\nu_{\rm FSR}/\mathcal{F}$, where $\Delta\nu_{\rm FSR}$ is the free spectral range of the optical cavity and $\mathcal{F}$ is the cavity finesse. The free spectral range is given by $\Delta\nu_{\rm FSR} = c/(2L)$ for a linear cavity and $\Delta\nu_{\rm FSR} = c/L_{\rm rt}$ for a ring cavity. By also accounting for the expression for the cavity mode volume, it is found that the single-atom cooperativity is the same for the linear and the ring cavities:

$$\eta = \frac{4g^2}{\kappa\Gamma} = \frac{24\mathcal{F}}{\pi k^2 w^2}, \tag{5.39}$$

where $k = 2\pi/\lambda_0$. The geometric nature of this expression can be understood by recalling that the solid angle $\Delta\Omega$ subtended by a Gaussian beam in the far field is proportional to $(k^2w^2)^{-1}$. Therefore, the single-atom cooperativity η is proportional to the effective solid angle. The cavity finesse $\mathcal{F}$ then has the effect of enhancing the effective solid angle [34] despite the fact that the real solid angle is usually rather small [122].

With the result (5.37), the output fields $\hat{b}^{(1)}_{\rm out}$ and $\hat{b}^{(2)}_{\rm out}$ can be expressed. The transmitted field is given by (5.19) as

$$\langle \hat{b}^{(2)}_{\rm out} \rangle = \sqrt{\kappa_2}\,\langle \hat{c} \rangle = -i\frac{2\frac{\sqrt{\kappa_1\kappa_2}}{\kappa}\beta e^{-i\omega t}}{\frac{2\delta}{\kappa} + N\eta\mathcal{L}_d(\Delta) + i[1 + N\eta\mathcal{L}_a(\Delta)]}. \tag{5.40}$$

The output transmitted power is maximized, for negligible intracavity losses ($\kappa_3 = 0$), when the transmission from the input and output mirrors is equal, $\kappa_1 = \kappa_2 = \kappa/2$. Then the ratio of transmitted to incident photon flux is

$$\frac{P_{\rm tr}}{P_{\rm in}} = \frac{|\,\langle \hat{b}^{(2)}_{\rm out} \rangle\,|^2}{|\beta|^2} = \frac{1}{\left[\frac{2\delta}{\kappa} + N\eta\mathcal{L}_d(\Delta)\right]^2 + \left[1 + N\eta\mathcal{L}_a(\Delta)\right]^2}. \tag{5.41}$$

This function is plotted in Fig. 5.2 a) for the empty cavity and, in the presence of atoms, for different values of the collective cooperativity $N\eta$. The single cavity resonance transmission peak is split, in the presence of the atoms, by the vacuum Rabi splitting $\overline{\omega}_+ - \overline{\omega}_- = 2g\sqrt{N} = \sqrt{N\eta\kappa\Gamma}$. This feature is also shown in Fig. 5.2 c) which plots the transmitted power fraction as a function of the detuning of the laser from the bare cavity resonance $\delta = \omega - \omega_c$ and as a function of the detuning of the laser from the bare atomic resonance $\Delta = \omega - \omega_0$. The figure shows the characteristic avoided crossing resulting from the atom-cavity coupling.

When the laser is far detuned from atomic resonance, such that $N\eta\mathcal{L}_a(\Delta) \ll 1$, the dominant effect is a dispersive shift of the cavity resonance frequency $\delta\omega_c$ which, in units of half the cavity linewidth, is given by $\frac{\delta\omega_c}{\kappa/2} = -N\eta\mathcal{L}_d(\Delta)$.

Similar properties are shared by the reflected field, whose expression is derived from equation (5.20) as

$$\langle \hat{b}^{(1)}_{\rm out} \rangle = \left\{1 - 2i\frac{\kappa_1}{\kappa}\frac{1}{\frac{2\delta}{\kappa} + N\eta\mathcal{L}_d(\Delta) + i[1 + N\eta\mathcal{L}_a(\Delta)]}\right\}\beta e^{-i\omega t} \tag{5.42}$$

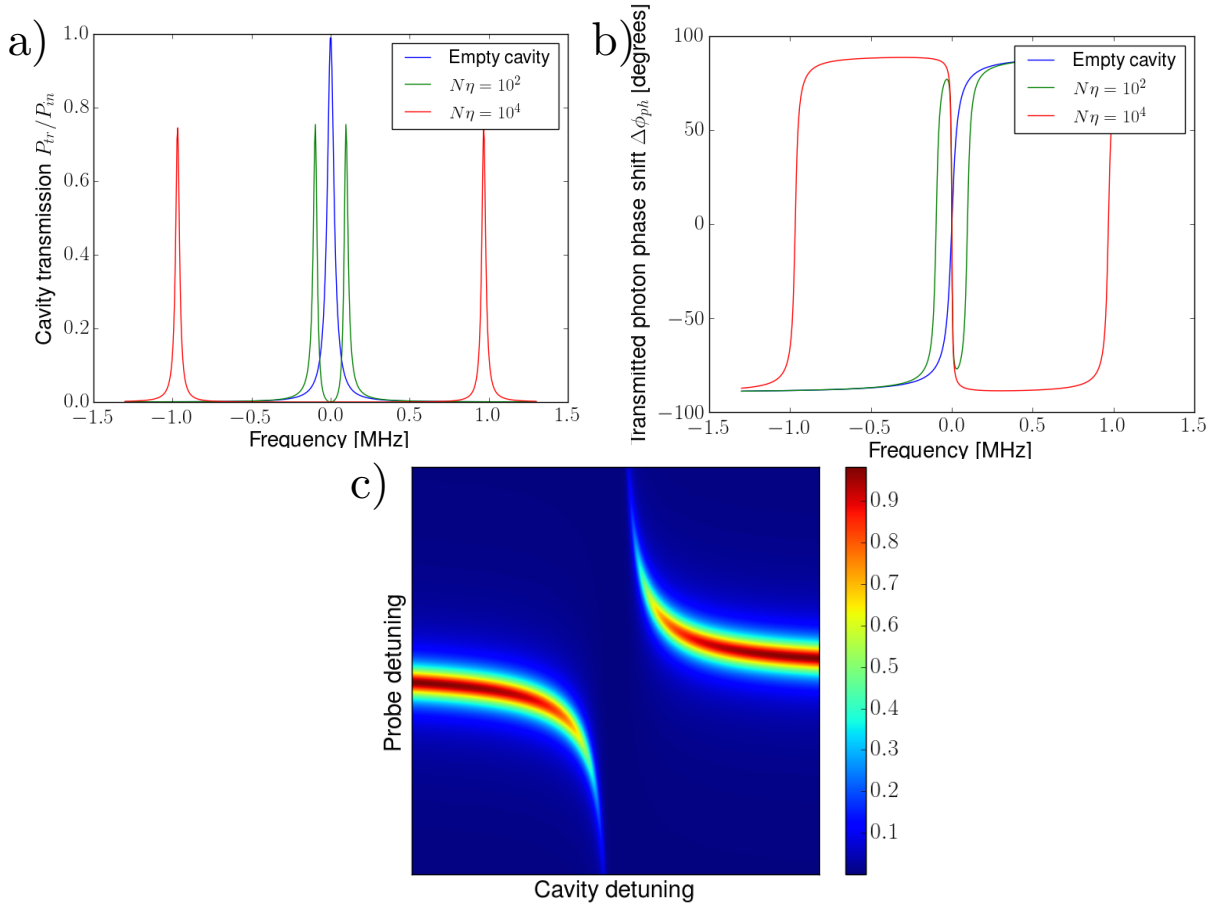

Figure 5.2: Cavity response spectra in the presence and in the absence of coupling with an atomic ansemble. a) cavity transmission spectrum with $\delta = \Delta$ for the empty cavity and for two values of the collective cooperativity, $N\eta = 10^2$ and $N\eta = 10^4$. The plots correspond to the case $\kappa_1 = \kappa_2 = \kappa/2 = 2\pi \times 50$ kHz. b) Transmitted photon phase shift compared to the phase on resonance with the bare cavity resonance. c) Transmitted intensity density plot for varying cavity detuning δ and probe detuning Δ.

We note that the reflected power vanishes on resonance for the symmetric case $\kappa_1 = \kappa_2 = \kappa/2$ and is independent of frequency for $\kappa_1 = \kappa, \kappa_2 = 0$, when both the intracavity losses and the transmission from the mirrors other than the input are negligible.

5.2.4 Scattering of photons into free space and decoherence

Following the notation adopted in Subsection 5.2.2, the total number of photons scattered into free space per atom is the number operator $\hat{b}^\dagger_{\boldsymbol{k},p}\hat{b}_{\boldsymbol{k},p}$ summed over all possible wavevectors $\boldsymbol{k}$ and polarizations p or

$$\hat{n}_{\rm sc} = \sum_{\boldsymbol{k},p} \hat{b}^\dagger_{\boldsymbol{k},p}\hat{b}_{\boldsymbol{k},p}. \tag{5.43}$$

By considering the bath Hamiltonian (5.22), one can write the Langevin equation for $\frac{d}{dt}\hat{n}_{\rm sc}$ and, by applying the Wigner-Weisskopf procedure, one can find the photon scattering rate per atom

$$\frac{d}{dt}\langle\hat{n}_{\rm sc}\rangle = \Gamma|\langle\hat{\sigma}_{i-}\rangle|^2. \tag{5.44}$$

This formula expresses the known fact that the scattering rate is the product of the atomic linewidth and of the excited state population. This result can be explicited, in steady state, by using the results (5.36) for $N = 1$ and (5.37) as

$$\frac{d}{dt}\langle\hat{n}_{\rm sc}\rangle = \frac{4\eta\frac{\kappa_1}{\kappa}\mathcal{L}_a(\Delta)}{\left[\frac{2\delta}{\kappa} + N\eta\mathcal{L}_d(\Delta)\right]^2 + \left[1 + N\eta\mathcal{L}_a(\Delta)\right]^2}P_{\rm in}, \tag{5.45}$$

where $P_{\rm in}$ is the incident photon flux.

For many experiments where the preservation of the atomic coherence is of paramount importance, it is essential to quantify the effect of scattering of photons into free space. Here we show that, if nothing else, free space scattering reduces the coherence of atomic superpositions. To show this we consider a slightly different system and accordingly adapt the notation. We consider a two-level system formed by the two stable levels $|\uparrow\rangle$ and $|\downarrow\rangle$ in the atomic ground state with energy difference $\hbar\delta\omega$. These could be, for example, two states of the ground hyperfine structure of alkali atoms. We next consider the case where one atom is illuminated by a laser beam in free space that is resonant with the transition, at frequency ω_e, from $|\downarrow\rangle$ to an optically excited state $|e\rangle$. We further assume that the atom is initially prepared in an equal superposition of the two ground states and that the transition $|\downarrow\rangle - |e\rangle$ is closed. In order to quantify the loss of coherence, we use the ladder operator $\hat{\sigma}_{g-} = |\downarrow\rangle\langle\uparrow|$. The optical transition from $|\downarrow\rangle$ to $|e\rangle$ is described by the ladder operators $\hat{\sigma}_- = |\downarrow\rangle\langle e|$ and $\hat{\sigma}_+ = |e\rangle\langle\downarrow|$. For a laser field with frequency ω and amplitude β, we can write the system Hamiltonian as

$$\hat{\mathcal{H}}_{\rm S} = \frac{\hbar\delta\omega}{2}\hat{\sigma}_{gz} + \hbar\beta g(\hat{\sigma}_- e^{i\omega t} + \hat{\sigma}_+ e^{-i\omega t}). \tag{5.46}$$

For notational convenience we also define the operators for the transition $|\uparrow\rangle - |e\rangle$ as $\hat{\sigma}'_- = |\uparrow\rangle\langle e|$ and $\hat{\sigma}'_+ = |e\rangle\langle\uparrow|$ and write the operators in a rotating frame as $\hat{\sigma}_{g-} = \hat{\tilde{\sigma}}_{g-}e^{-i\delta\omega t}$ and $\hat{\sigma}'_+ = \hat{\tilde{\sigma}}'_+ e^{i(\omega-\delta\omega)t}$. We obtain the closed system of equations

$$\frac{d}{dt}\hat{\tilde{\sigma}}_{g-} = ig\beta\hat{\tilde{\sigma}}'_+ \tag{5.47}$$

$$\frac{d}{dt}\hat{\tilde{\sigma}}'_+ = -i\left(\Delta - i\frac{\Gamma}{2}\right)\hat{\tilde{\sigma}}'_+ + ig\beta\hat{\tilde{\sigma}}_{g-}, \tag{5.48}$$

where $\Delta = \omega - \omega_e$ is the detuning from the optical $|\downarrow\rangle - |e\rangle$ transition. The solution for the coherence $\tilde{\sigma}_{g-} = \langle\hat{\tilde{\sigma}}_{g-}\rangle$ is found to be

$$\tilde{\sigma}_{g-}(t) = \tilde{\sigma}_{g-}(0)\exp\left(-\frac{2g^2\beta^2}{\Gamma + 2i\Delta}t\right). \tag{5.49}$$

The expression in the argument of the exponential function can be divided in two terms corresponding to the real and imaginary parts:

$$\frac{2g^2\beta^2}{\Gamma + 2i\Delta} = \frac{2g^2\beta^2}{\Gamma}[\mathcal{L}_a(\Delta) + i\mathcal{L}_d(\Delta)] \tag{5.50}$$

The imaginary part in (5.50) accounts for the light shift of the level $|\downarrow\rangle$ by the light field. The real part accounts for the coherence loss as it reduces the magnitude of the coherence between the two levels of the ground state $|\tilde{\sigma}_{g-}|$. The corresponding expression is seen to be equal to the total number of photons scattered into free space per atom n_{sc}:

$$|\sigma_{g-}(t)| = |\sigma_{g-}(0)|e^{-n_{\mathrm{sc}}}. \tag{5.51}$$

The scaling $e^{-n_{\mathrm{sc}}}$ is then also valid for the interferometer contrast, $\mathcal{C} = e^{-n_{\mathrm{sc}}}$ if no other sources of decoherence are present.

Contrast loss is the only effect on a superposition of atomic states when the transition is closed. In this case, after scattering a photon, an atom ends up in the ground state superposition with a phase that varies randomly between scattering events. Contrast loss in this picture is therefore caused by dephasing. There are, however, other detrimental effects of free space scattering. For example, scattering can cause atom loss because of the imparted photon recoil. Another situation arises when the transition is not closed. In this case, if the final atomic state is not one of the two spin states $|\downarrow\rangle$ or $|\uparrow\rangle$, the atom is lost. If, on the other hand, the atom is not lost, Raman scattering can occur, where the processes $|\downarrow\rangle \rightarrow |e\rangle \rightarrow |\uparrow\rangle$ and $|\uparrow\rangle \rightarrow |e\rangle \rightarrow |\downarrow\rangle$ are possible. Here Raman scattering has the effect of randomizing the population between the two spin states and is clearly a limitation for optically-induced spin squeezing.

5.3 A method for the implementation of squeezed momentum states with strontium atoms

In the previous Chapter we discussed our results concerning the implementation of atom interferometers based on Bragg diffraction. We saw that large momentum transfer can be attained both on a broad dipole-allowed transition and on a narrow intercombination transition. Bragg atom interferometry has an inherent robustness against external perturbations because the two *spin* states only differ by the center-of-mass momentum. This immunity is even more pronounced in ^{88}Sr atoms, where the ground state is essentially a pure scalar with a formidable immunity to external magnetic fields and cold collisions. The performance of these two interferometers is currently limited by technical aspects that do not represent a limit in principle. For this kind of interferometer, the tools to overcome the atom shot noise limit are however missing. In this and in the following

sections, we will present a method that can extend the current spin squeezing technology to a new class of states i.e. momentum superpositions. We will show that the narrow intercombination $^1S_0$-$^3P_1$ transition allows to perform nondestructive measurements of the atomic population in two momentum states and compute the attainable metrological gain.

5.3.1 Basic scheme for momentum state collective measurements in the atom interferometer

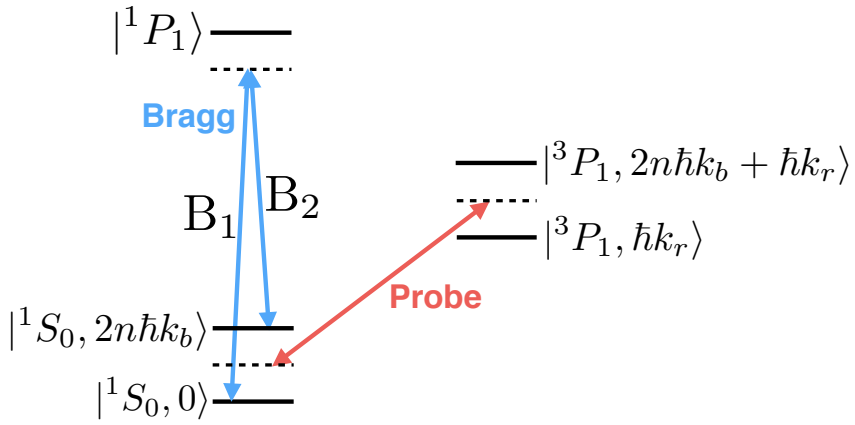

Figure 5.3: Level diagram and relevant transitions for a collective measurement of the population difference between the two momentum states coupled by the Bragg diffraction process. Bragg diffraction is induced by the Bragg beams B_1 and B_2 that operate on the $^1S_0$-$^1P_1$ transition (blue arrows). The population difference is probed by operating on the $^1S_0$-$^3P_1$ intercombination transition (red arrow).

The proposed scheme is illustrated in Fig. 5.3, where we consider the collective measurement of the population difference between the two momentum states coupled by Bragg diffraction. We label the atomic states with the notation $|\chi, p\rangle$ where χ labels the internal electronic state and p labels the center-of-mass momentum in the reference frame moving with the free-falling non-diffracted wavepacket. We consider the momentum states $|^1S_0, 0\rangle$ and $|^1S_0, 2n\hbar k_b\rangle$ coupled by n-th order Bragg diffraction on the dipole-allowed $^1S_0$-$^1P_1$ transition at λ_b =461 nm, where $k_b = 2\pi/\lambda_b$ is the wavenumber of the Bragg lasers. In our discussion we will assume that diffraction losses are negligible, a condition that, as seen in the previous Chapter, can be attained with gaussian pulses with a duration larger than about 10 μs.

The squeezing method relies on resolving the Doppler effect due to the different speed of the two momentum components. For dipole-allowed transitions, however, the Doppler

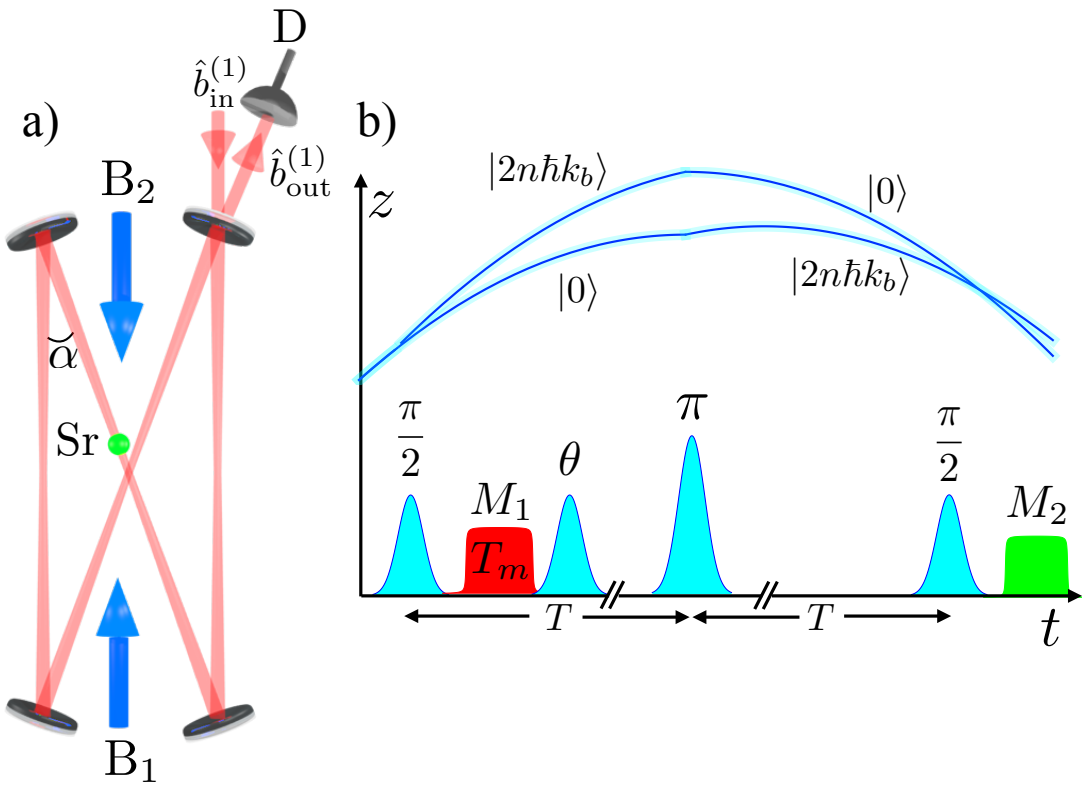

Figure 5.4: Schematic of the setup with the cavity-enhanced collective measurement integrated in the interferometer in free space. a) Optical ring cavity, where the momentum state superposition is probed by the red beams, with angle α with respect to gravity, as the atoms cross the cavity mode volume. The probe field $\hat{b}_{\text{in}}^{(1)}$ is incident on one side of the cavity and the reflected field $\hat{b}_{\text{out}}^{(1)}$ is measured by the photodetector D. The momentum states are manipulated through the counterpropagating blue Bragg beams B_1 and B_2. b) Interrogation sequence and atomic trajectories in a $\pi/2 - \pi - \pi/2$ Mach-Zehnder interferometer. The blue gaussian curves indicate Bragg pulses. The pulse labelled θ rotates the state into a phase-sensitive state. The squeezing pre-measurement is performed in M_1 with duration T_m and the final measurement is performed in M_2.

splitting, of the order of 10-100 kHz, is hidden by the large linewidth on the order of 10 MHz. Probing on a dipole-allowed transition therefore can only provide information about the total atom number rather than about the population difference. The linewidth $\Gamma = 2\pi \times 7.5$ kHz of the $^1S_0$-$^3P_1$ intercombination transition at $\lambda_r = 689$ nm of strontium is however small enough to perform as a probe that can resolve the Doppler splitting [123]. For the scheme illustrated in Fig. 5.3, the splitting between the optical transitions $|^1S_0, 0\rangle - |^3P_1, \hbar k_r\rangle$ and $|^1S_0, 2n\hbar k_b\rangle - |^3P_1, 2n\hbar k_b + \hbar k_r\rangle$, where $k_r = 2\pi/\lambda_r$, is considered and amounts to $2\delta\omega_r = k_r \frac{2n\hbar k_b}{M} = 2\pi n \times 28.6$ kHz, where M is the atomic mass.

The collective measurement of the population difference between the two momentum states can be enhanced through an optical cavity. A setup that is compatible with an atom interferometer in free fall is illustrated in Fig. 5.4 a). When, during the atomic trajectories, the ensemble crosses the cavity mode volume, probing is performed through the red beam at $\lambda_r = 689$ nm circulating in the ring resonator[2]. The probe light is coupled from one side of the cavity and the reflected field is measured by a photodetector. The atomic trajectories and interrogation sequence, with the integrated squeezing pre-measurement, are illustrated in Fig. 5.4 b). The basic sequence is formed by a $\pi/2 - \pi - \pi/2$ Mach-Zehnder interferometer. After the first $\pi/2$-pulse, which prepares the coherent momentum superposition, the squeezing measurement M_1 is performed and the state is subsequently rotated into a phase-sensitive state. The final measurement is performed in M_2 and can, in principle, be performed by fluorescence collection as we already demonstrated (see Chapter 4 and [107]).

5.3.2 Measurement resolution

In the following, measurements of the cavity reflected field $\hat{b}^{(1)}_{\text{out}}$ (Fig. 5.4 a)) are considered and the sensitivity to atom number fluctuations between momentum states is computed. As such measurements provide collective information without distinguishing between individual atoms, they project the ensemble into a collective state which corresponds to the measurement outcome, as discussed in 2.3.2. This process can produce conditionally squeezed atomic momentum states.

We treat the two momentum states as a spin-1/2 system and describe the ensemble by a total spin $S = N/2$, where N is the atom number. The population difference between the two momentum states is then $2S_z$.

According to (2.53), we quantify the attainable metrological gain ξ_m by the ratio between the contrast squared $\mathcal{C}^2$ and the relative population variance $(2\Delta S_z)^2$ normalized

[2]In principle, in computing the Doppler splitting $2\delta\omega_r$, we should take into account the finite angle α between the oblique cavity beam and gravity acceleration. We will assume that the corresponding factor $\cos\alpha$ introduces a negligible reduction of $2\delta\omega_r$

to the atom shot noise variance $2S$:

$$\xi_m = \frac{S}{2(\Delta S_z)^2}\mathcal{C}^2. \tag{5.52}$$

The squeezing pre-measurement of S_z can be achieved by arranging a situation where the atom-light interaction is dispersive and the two momentum states are associated with opposite variations of the index of refraction and shift the cavity resonance frequency in opposite directions. When the cavity resonance frequency ω_c is tuned halfway between the two optical transitions, atoms in the two momentum states produce opposite shifts of the cavity resonance frequency that can be detected via the phase shift $\Delta\phi_{\rm ph}$ of the light reflected from the cavity.

By using the tools developed in the previous sections of this Chapter, we now compute the photon phase shift induced in the presence of the momentum state superposition.

We start by considering a single atomic transition at frequency ω_0, a single cavity resonance at frequency ω_c and a driving laser field with frequency ω_r and amplitude $\langle \hat{b}_{\rm in}^{(1)} \rangle = \beta e^{-i\omega_r t}$. The linewidths of the cavity mode and of the atomic transition are given by κ and Γ, respectively. We recall the definitions of the detuning from cavity resonance $\delta = \omega_r - \omega_c$ and of the detuning from atomic resonance $\Delta = \omega_r - \omega_0$. We denote by $2g$ the single-photon Rabi frequency and by $N\eta = 4g^2N/(\kappa\Gamma)$ the collective cooperativity. By applying the result (5.42),

$$\langle \hat{b}_{\rm out}^{(1)} \rangle = \left\{ 1 - 2i\frac{\kappa_1}{\kappa}\frac{1}{\frac{2\delta}{\kappa} + N\eta\mathcal{L}_d(\Delta) + i[1 + N\eta\mathcal{L}_a(\Delta)]} \right\} \beta e^{-i\omega_r t}. \tag{5.53}$$

We note that in the ideal case of a lossless cavity, $\kappa_1/\kappa = 1$, and in the absence of atomic absorption, the reflected optical power is independent of frequency and every photon is collected by the photodetector. This is clearly the most desirable situation as it provides the maximum signal. The reflected light undergoes a phase shift that is determined by the presence of the atomic ensemble. This phase shift can be measured for example through a variant of the Pound-Drever-Hall method [124]. This relies on forming a spectrum composed of a strong carrier out of cavity resonance and of a weak sideband at the frequency of the probe laser ω_r. The phase measurement is achieved by detecting the interference between the sideband and the carrier.

From this point on we consider the actual level scheme for squeezing of momentum states and extend the simple two-level scheme to the two transitions $|^1S_0, 0\rangle - |^3P_1, \hbar k_r\rangle$ and $|^1S_0, 2n\hbar k_b\rangle - |^3P_1, 2n\hbar k_b + \hbar k_r\rangle$. As the polarizabilities for the two optical transitions are additive [34], we make the replacements[3]

$$N\mathcal{L}_a(\Delta) \to \left(\frac{N}{2} - S_z\right)\mathcal{L}_a(\delta\omega_r) + \left(\frac{N}{2} + S_z\right)\mathcal{L}_a(-\delta\omega_r) = N\mathcal{L}_a(\delta\omega_r) \tag{5.54}$$

[3]Even though this is a fact that ultimately derives from the linear atomic response, it can be derived in a straightforward and consistent manner by generalizing the Langevin equations of motion (5.33) and (5.34) to the case of multiple atomic transitions.

$$N\mathcal{L}_d(\Delta) \to \left(\frac{N}{2} - S_z\right)\mathcal{L}_d(\delta\omega_r) + \left(\frac{N}{2} + S_z\right)\mathcal{L}_d(-\delta\omega_r) = -2S_z\mathcal{L}_d(\delta\omega_r), \tag{5.55}$$

where we used the fact that $\mathcal{L}_a$ and $\mathcal{L}_d$ are even and odd functions, respectively. With this result, we compute the interference signal that arises from the superposition of the local oscillator carrier with amplitude $\beta_{\rm LO}e^{-i[(\omega_r-\omega_{\rm LO})t+\phi_{\rm LO}]}$ and of the sideband with amplitude $\langle\hat{b}^{(1)}_{\rm out}\rangle$. Having defined the local oscillator phase $\phi_{\rm LO}$, we take β and $\beta_{\rm LO}$ to be real numbers. The flux of reflected photons can be written, when the probe laser is on resonance with the bare cavity resonance, $\delta = 0$, as

$$\beta^2_{\rm det} = \langle\hat{b}^{(1)}_{\rm out}\rangle^2 + \beta^2_{\rm LO} + \left\{\beta\beta_{\rm LO}e^{i(\omega_{\rm LO}t+\phi_{\rm LO})}\left[1 - \frac{2i\frac{\kappa_1}{\kappa}}{i[1+N\eta\mathcal{L}_a(\delta\omega_r)] - 2S_z\eta\mathcal{L}_d(\delta\omega_r)}\right] + c.c.\right\} \tag{5.56}$$

The two terms in curly brackets account for the interference between the two fields, which we denote as the *signal* $\mathcal{S}$ and can be written as

$$\frac{\mathcal{S}}{T_m} = 2\beta\beta_{\rm LO}\frac{2\frac{\kappa_{\rm in}}{\kappa} - 1 - N\eta\mathcal{L}_a(\delta\omega_r)}{1+N\eta\mathcal{L}_a(\delta\omega_r)}\cos(\omega_{\rm LO}t + \phi_{\rm LO} + \pi - \Delta\phi_{\rm ph}), \tag{5.57}$$

where T_m is the measurement time duration and $\mathcal{S}$ has units of number of photons. The signal phase shift $\Delta\phi_{\rm ph}$ is given by

$$\Delta\phi_{\rm ph} = 4\frac{\kappa_{\rm in}}{\kappa}\frac{S_z\eta\mathcal{L}_d(\delta\omega_r)}{[2\frac{\kappa_{\rm in}}{\kappa} - 1 - N\eta\mathcal{L}_a(\delta\omega_r)][1+N\eta\mathcal{L}_a(\delta\omega_r)]}, \tag{5.58}$$

where this expression is valid for $\delta\omega_r \gg |S_z|\Gamma$. For an initial coherent state that is an equal superposition of the two momentum states, a limit on S_z can be estimated by the shot noise fluctuations, so that $\delta\omega_r \gg \Gamma\sqrt{N}/2$.

By mixing the detected electronic signal with the local oscillator source and by appropriately tuning the local oscillator phase, the last term in eq. (5.57) equals $\Delta\phi_{\rm ph}$. As a result, the population difference can be detected via the phase shift of the light emerging from the cavity.

In order to determine the photon shot noise limited atom number resolution $2\Delta S_z$, we first note that for an initial coherent state with the same population in the two momentum states, $S_z = 0$ for an average over different experiment runs. Therefore, we can compute the photon shot noise variance as $\mathcal{N}^2 = (\langle\hat{b}^{(1)}_{\rm out}\rangle^2 + \beta^2_{\rm LO})T_m \simeq \beta^2_{\rm LO}T_m$. The condition that the phase shift measurement is at the photon shot noise is expressed as $(\mathcal{S}/\mathcal{N})^2 = 1$.

Since the main, and fundamental, limitation on attainable squeezing is set by scattering into free space, we convert the number of incident photons in the probe field $n_{\rm in} = \beta^2 T_m$ into the number of photons scattered into free space per atom $n_{\rm sc}$. This conversion can be achieved by using the result in equation (5.45), and by setting $n_{\rm sc} = \frac{d}{dt}\langle\hat{n}_{\rm sc}\rangle T_m$:

$$\frac{n_{\rm sc}}{n_{\rm in}} = \frac{4\eta\frac{\kappa_1}{\kappa}\mathcal{L}_a(\delta\omega_r)}{[1+N\eta\mathcal{L}_a(\delta\omega_r)]^2}. \tag{5.59}$$

The squared atom number resolution $(2\Delta S_z)^2$, normalized to the atom shot noise variance $2S$ is then set by the condition $(\mathcal{S}/\mathcal{N})^2 = 1$ and reads

$$\frac{2(\Delta S_z)^2}{S} = \frac{[1 + N\eta\mathcal{L}_a(\delta\omega_r)]^2\mathcal{L}_a(\delta\omega_r)}{4N\eta\frac{\kappa_1}{\kappa}n_{\rm sc}[\mathcal{L}_d(\delta\omega_r)]^2}. \tag{5.60}$$

The term $\kappa_{\rm in}/\kappa$ can be seen as the fraction of detected-to-incident photons and is therefore interpreted as the detection efficiency ϵ_d. In the definition of the detection efficiency, we include the effect of cavity losses, of detector quantum efficiency and of any additional loss in the path from the cavity input mirror to the photodetector.

5.3.3 Squeezing limits from photon scattering into free space

After the scattering of a photon by one atom, the momentum superposition is destroyed and the associated recoil causes the trajectory to deviate from the vertical direction. The resulting losses cause a random imbalance $2(\Delta S_z)_{\rm sc}$ of the populations in the two momentum states.

We compute the resulting population imbalance arising from scattering $p_{\rm sc} = Nn_{\rm sc}$ photons into free space in the regime where $p_{\rm sc} \ll N$. According to the binomial distribution, the probability for scattering k photons from $|^1S_0, 0\rangle$ and $p_{\rm sc} - k$ photons from $|^1S_0, 2n\hbar k_b\rangle$ is given by

$$P_k = \frac{1}{2^{p_{\rm sc}}}\begin{pmatrix} p_{\rm sc} \\ k \end{pmatrix}, \tag{5.61}$$

where the probability for scattering from one of the two momentum states is set to 1/2. The mean and variance are given by $\langle k\rangle = p_{\rm sc}/2$ and $\mathrm{Var}(k) = p_{\rm sc}/4$, respectively. The atom number variance increase due to free space scattering can then be written as $(2\Delta S_z)^2_{\rm sc} = \mathrm{Var}(p_{\rm sc} - 2k)$ or

$$(2\Delta S_z)^2_{\rm sc} = p^2_{\rm sc} + 4\mathrm{Var}(k) + 4\langle k\rangle^2 - 4p_{\rm sc}\langle k\rangle = p_{\rm sc}. \tag{5.62}$$

The squeezing limit can then be determined by summing the atom number resolution of the measurement given by eq. (5.60) and the variance increase $2(\Delta S_z)^2_{\rm sc}/S$. This gives the total atom number variance normalized to the atom shot noise as

$$\left[\frac{2(\Delta S_z)^2}{S}\right]_{\rm tot} = \frac{[1 + N\eta\mathcal{L}_a(\delta\omega_r)]^2\mathcal{L}_a(\delta\omega_r)}{4N\eta\epsilon_d n_{\rm sc}[\mathcal{L}_d(\delta\omega_r)]^2} + n_{\rm sc}. \tag{5.63}$$

The above expression reaches a minimum at the optimum value of $n_{\rm sc}$ given by

$$n^{\rm opt}_{\rm sc} = \sqrt{\frac{[1 + N\eta\mathcal{L}_a(\delta\omega_r)]^2\mathcal{L}_a(\delta\omega_r)}{4N\eta\epsilon_d[\mathcal{L}_d(\delta\omega_r)]^2}}. \tag{5.64}$$

The squeezing limit is then derived by setting $n_{\rm sc} = n^{\rm opt}_{\rm sc}$ in (5.63):

$$\left[\frac{2(\Delta S_z)^2}{S}\right]_{\rm opt} = \sqrt{\frac{[1 + N\eta\mathcal{L}_a(\delta\omega_r)]^2\mathcal{L}_a(\delta\omega_r)}{N\eta\epsilon_d[\mathcal{L}_d(\delta\omega_r)]^2}}. \tag{5.65}$$

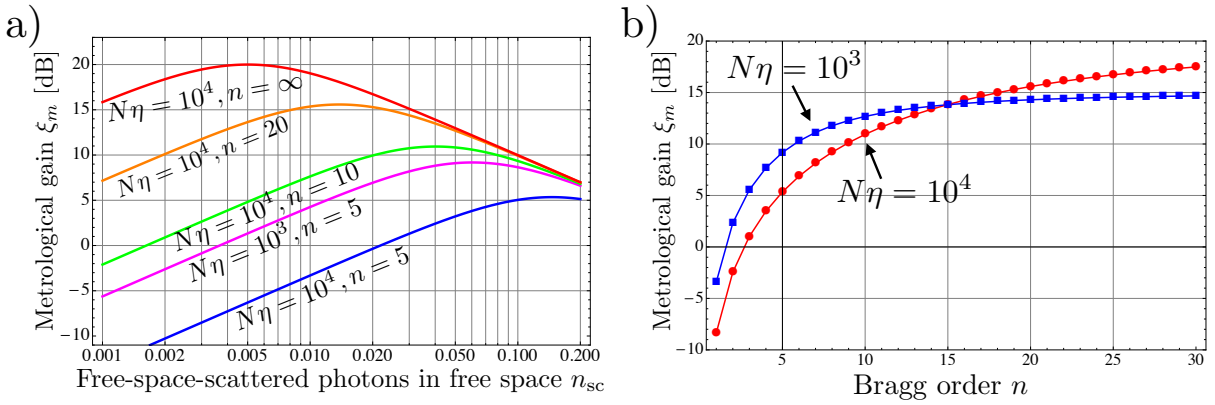

Figure 5.5: Dependence of the metrological gain on the main parameters. a) Metrological gain as a function of the number of photons scattered into free space per atom n_{sc} for different values of the collective cooperativity $N\eta$ and for different Bragg diffraction orders. b) Metrological gain as a function of the Bragg diffraction order for $N\eta = 10^3$ (blue squares) and $N\eta = 10^4$ (red circles).

and in the dispersive limit $N\eta\mathcal{L}_a(\delta\omega_r) \ll 1$, the metrological gain saturates at the value $\xi_m = \sqrt{N\eta\epsilon_d}$.

The effect of dephasing discussed in subsection 5.2.4 in this case where losses dominate is not the main limitation to the attainable squeezing. This statement remains valid when $n_{sc}^{opt} \ll 1$, a condition that is fulfilled in the dispersive regime when the collective cooperativity $N\eta$ is large. In this case, the contrast $\mathcal{C} = e^{-n_{sc}} \simeq 1$. In general, additional limitations to the attainable squeezing level arise because of the curved nature of the Bloch sphere. However, for the squeezing levels and atom numbers considered in this thesis and for many experimental realizations, such effects yield negligible gain loss [125] and, as such, their discussion is deferred to Appendix A.

The metrological gain, as computed from (5.65), is plotted in Fig. 5.5 as a function of n_{sc} and of the diffraction order n. When $N\eta$ lies in the range $10^3 - 10^4$, there is significant gain if $n > 5$, a condition typically met by large-momentum-transfer atom interferometers [100]. Indeed, for small n, the optical transitions are not sufficiently resolved in frequency space compared to the atomic linewidth, which prevents operating in the dispersive regime of atom-light interaction and leads to substantial absorption and squeezing reduction. Mathematically, this fact is expressed by the term $[1 + N\eta\mathcal{L}_a(\delta\omega_r)]^2\mathcal{L}_a(\delta\omega_r)$ in equation (5.65) which represents the effect of cavity-enhanced atomic absorption. In general, the condition for operating in the dispersive regime can be written as $n \gg 0.3 \times \sqrt{N\eta}$, which shows that, in order to avoid absorption, a larger Doppler splitting is required. This aspect is clear from Fig. 5.5, where it is shown that the gain for small diffraction orders is larger when $N\eta$ is smaller.

As discussed in Section 4.2, achieving large diffraction orders in a single pulse can be challenging in real atom interferometers because of the long interaction times required to operate in the Bragg regime. The Bragg pulse shape and frequency can however be optimized in a way that produces highly efficient Bragg diffraction also for large diffraction orders [102]. This result however comes at the cost of pulse durations that lie in the range 100 μs - 1 ms. The delay between the initial $\pi/2$-pulse and the squeezing pre-measurement can then increase the spatial separation between the wavepackets corresponding to the two momentum states. For a finite cavity mode volume, this might cause the two wavepackets to be probed with different efficiencies, which is fundamentally undesirable as the process would distinguish between different atoms and reduce squeezing [126].

It would, on the other hand, be desirable to extend the range of validity of our method to small diffraction orders and large atom numbers. If it were possible to provide such an extension, the scheme would still not be limited to small diffraction orders. Indeed, the squeezing measurement could be performed, for example, after a first-order $\pi/2$-pulse and the momentum splitting could be further increased by successive Bragg pulses. Clearly, a possibility is to probe on transitions that are narrower than the strontium intercombination line. Even though such an approach is possible at least in principle, the measurement time T_m would increase. This fact arises because reaching $n_{\mathrm{sc}}^{\mathrm{opt}}$ in equation (5.64) with negligible population in the optically excited state requires a longer measurement.

In the following Subsection we propose and analyze a method that can modify the atomic response to the probe field in such a way that the squeezing measurement operates in the dispersive regime.

5.3.4 Squeezing enhancement by electromagnetically induced transparency

In this Section we propose a scheme that enhances the signal-to-noise ratio of momentum state collective measurements also at small Bragg diffraction orders n, with a large collective cooperativity $N\eta$. As the main limitation in this regime is the spoiling of the cavity finesse by atomic absorption, we consider a scheme where coupling of the decaying $^3P_1$ state to the metastable $^3P_0$ state with a much longer lifetime results in electromagnetically induced transparency (EIT) at the original cavity resonance frequency [127, 128, 129, 130, 131, 132]. The $^3P_1$-$^3P_0$ coupling can be attained through two-photon Raman coupling via the $^3S_1$ intermediate state with the two copropagating Raman lasers R_1 and R_2 at 679 nm ($^3P_0$–$^3S_1$ transition) and 688 nm ($^3P_1$–$^3S_1$ transition), respectively, as illustrated in Fig. 5.7.

In order to capture the essence of EIT in this condition, the center-of-mass motion can be neglected, we adopt a density matrix approach and assume that the probe field is a classical coherent field. After deriving the modified atomic response features, the

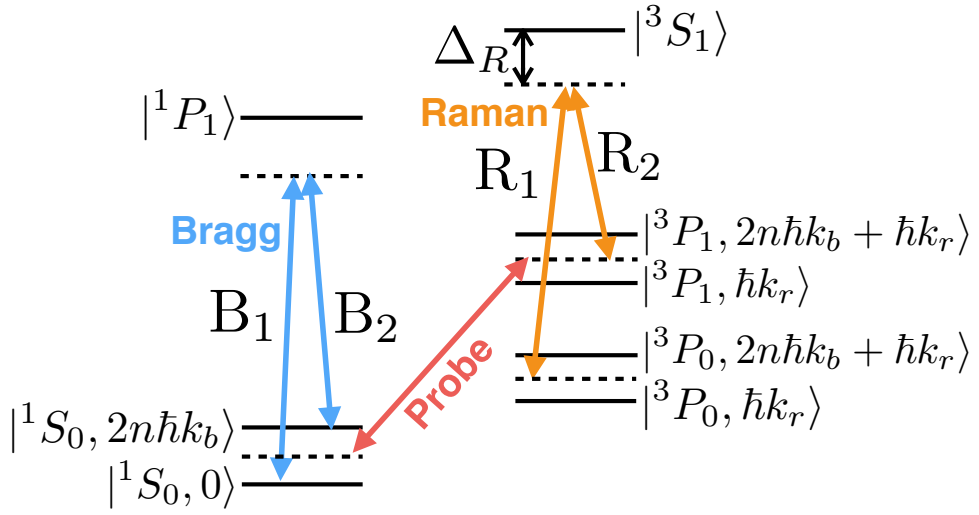

Figure 5.6: Relevant level diagram for probing on the $^1S_0$-$^3P_1$ intercombination transition with EIT coupling through the two-photon $^3P_1$-$^3P_0$ transition. The two-photon Raman transition is induced by a couple of copropagating laser beams at 679 nm and 688 nm that are detuned from the transition to the $^3S_1$ state.

generalization to momentum states and to the cavity field is straightforward.

In practice, we consider a linear probe polarization that couples the $|^1S_0\rangle$ and $|^3P_1, m_J = 0\rangle$ states and two Raman beams R_1 and R_2 with Rabi frequencies Ω_{R1} and Ω_{R2}, respectively. The field R_1, with frequency ω_1, couples the states $|^3P_1, m_J = 0\rangle$ and $|^3S_1, m_J = +1\rangle$, whereas the field R_2, with frequency ω_2, couples the states $|^3P_0\rangle$ and $|^3S_1, m_J = +1\rangle$. For notational convenience, we make the replacements $|^1S_0\rangle \to |a\rangle$, $|^3P_1, m_J = 0\rangle \to |b\rangle$, $|^3P_0\rangle \to |c\rangle$, $|^3S_1, m_J = +1\rangle \to |d\rangle$ and write the Hamiltonian as

$$\mathcal{H} = \hbar\omega_a |a\rangle\langle a| + \hbar\omega_b |b\rangle\langle b| + \hbar\omega_c |c\rangle\langle c| + \hbar\omega_d |d\rangle\langle d| + \frac{\hbar\Omega_p}{2}(|b\rangle\langle a| e^{-i\omega_r t} + |a\rangle\langle b| e^{i\omega_r t})$$

$$+\frac{\hbar\Omega_{R1}}{2}(|d\rangle\langle b| e^{-i\omega_1 t} + |b\rangle\langle d| e^{i\omega_1 t}) + \frac{\hbar\Omega_{R2}}{2}(|d\rangle\langle c| e^{-i\omega_2 t} + |c\rangle\langle d| e^{i\omega_2 t}), \tag{5.66}$$

where $\hbar\omega_i$ is the unperturbed atomic energy of state $|i\rangle$, ω_r is the probe frequency and Ω_p the corresponding Rabi frequency.

Using first-order perturbation theory[4] for the weak probe field, $\Omega_p \ll \Gamma$, we can write

[4]In perturbation theory, we define the Hamiltonian $\mathcal{H} = \mathcal{H}_0 + \mathcal{H}_1$, where $\mathcal{H}_0$ is the unperturbed Hamiltonian and $\mathcal{H}_1$ is the perturbation. The solution for the density operator is expressed as the series

$$\hat{\rho} = \sum_{n=0}^{\infty} \hat{\rho}^{(n)}$$

where $\hat{\rho}^{(n)}$ is the n-th order solution given by

$$\frac{d}{dt}\hat{\rho}^{(n)} = -\frac{i}{\hbar}[\mathcal{H}_0, \hat{\rho}^{(n)}] - \frac{i}{\hbar}[\mathcal{H}_1, \hat{\rho}^{(n-1)}].$$

the closed set of equations of motion for the matrix elements of the density operator $\hat{\rho}$ as

$$\dot{\rho}_{ab} = i\omega_{ba}\rho_{ab} - \frac{\Gamma}{2}\rho_{ab} + i\frac{\Omega_{\mathrm{R1}}}{2}\rho_{ad}e^{-i\omega_1 t} + i\frac{\Omega_p}{2}e^{i\omega_r t} \tag{5.67}$$

$$\dot{\rho}_{ac} = i\omega_{ca}\rho_{ac} + i\frac{\Omega_{\mathrm{R2}}}{2}\rho_{ad}e^{-i\omega_2 t} \tag{5.68}$$

$$\dot{\rho}_{ad} = i\omega_{da}\rho_{ad} + i\frac{\Omega_{\mathrm{R1}}}{2}\rho_{ab}e^{i\omega_1 t} + i\frac{\Omega_{\mathrm{R2}}}{2}\rho_{ac}e^{i\omega_2 t}, \tag{5.69}$$

where $\omega_{ij} = \omega_i - \omega_j$ is the frequency of the transition $|j\rangle \rightarrow |i\rangle$. We now consider the relevant case where the detuning of the Raman fields from resonance is large compared to the excited $^3S_1$ state decay rate and compared to the the single-photon Rabi frequencies Ω_{R1} and Ω_{R2}. In this regime it is possible to adiabatically eliminate the excited $^3S_1$ state, in a way that is similar to that adopted in Section 4.2. This is performed by defining in (5.69) the new variables $\sigma_{ab} = \rho_{ab}e^{-i\omega_{ba}t}$, $\sigma_{ac} = \rho_{ac}e^{-i\omega_{ca}t}$, $\sigma_{ad} = \rho_{ad}e^{-i\omega_{da}t}$ and by observing that σ_{ab} and σ_{ac} are slowly varying compared to σ_{ad}. The resulting equation can be directly integrated:

$$\sigma_{ad} = \frac{\Omega_{\mathrm{R1}}}{2\Delta_{\mathrm{R}}}e^{i\Delta_1 t}\sigma_{ab} + \frac{\Omega_{\mathrm{R2}}}{2\Delta_{\mathrm{R}}}e^{i\Delta_2 t}\sigma_{ac}, \tag{5.70}$$

where $\Delta_1 = \omega_1 - \omega_{db}$, $\Delta_2 = \omega_2 - \omega_{dc}$ and in the denominators we set $\Delta_1 \simeq \Delta_2 \equiv \Delta_{\mathrm{R}}$ by neglecting the difference between the detunings of the two lasers. Substitution into equations (5.67) and (5.68) yields the effective three-level equations of motion

$$\dot{\rho}_{ab} = i\omega'_{ba}\rho_{ab} - \frac{\Gamma}{2}\rho_{ab} + i\frac{\Omega_p}{2}e^{i\omega_r t} + i\frac{\Omega_{\mathrm{eff}}}{2}\rho_{ac}e^{i\delta t} \tag{5.71}$$

$$\dot{\rho}_{ac} = i\omega'_{ca}\rho_{ac} + i\frac{\Omega_{\mathrm{eff}}}{2}\rho_{ab}e^{-i\delta t}. \tag{5.72}$$

Here $\Omega_{\mathrm{eff}} = \Omega_{\mathrm{R1}}\Omega_{\mathrm{R2}}/(2\Delta_{\mathrm{R}})$ is the effective two-photon Rabi frequency, $\delta = \omega_2 - \omega_1$ is the frequency difference of the two Raman lasers and $\omega'_{ba} = \omega_{ba} + \Omega^2_{\mathrm{R1}}/(4\Delta_{\mathrm{R}})$, $\omega'_{ca} = \omega_{ca} + \Omega^2_{\mathrm{R2}}/(4\Delta_{\mathrm{R}})$ are the transition frequencies corrected for the AC Stark shift of the Raman fields.

In order to show the presence of electromagnetically induced transparency, we solve (5.71) and (5.72) for the steady state solution. This is achieved by defining $\rho_{ab} = \tilde{\sigma}_{ab}e^{i\omega_r t}$ and $\rho_{ac} = \tilde{\sigma}_{ac}e^{i(\omega_r - \delta)t}$ and by setting $\dot{\tilde{\sigma}}_{ab} = \dot{\tilde{\sigma}}_{ac} = 0$. The coherence between states $|a\rangle$ and $|b\rangle$ is then found to be

$$\rho_{ab} = i\frac{\Omega_p/2}{\frac{\Gamma}{2} + i\left(\Delta - \frac{\Omega^2_{\mathrm{eff}}}{4(\Delta - \delta')}\right)}e^{i\omega_r t}, \tag{5.73}$$

where $\Delta = \omega_r - \omega'_{ba}$ and δ' is the two-photon Raman detuning given by

$$\delta' = \delta - \left(\omega_{bc} + \frac{\Omega^2_{\mathrm{R1}}}{4\Delta_{\mathrm{R}}} - \frac{\Omega^2_{\mathrm{R2}}}{4\Delta_{\mathrm{R}}}\right). \tag{5.74}$$

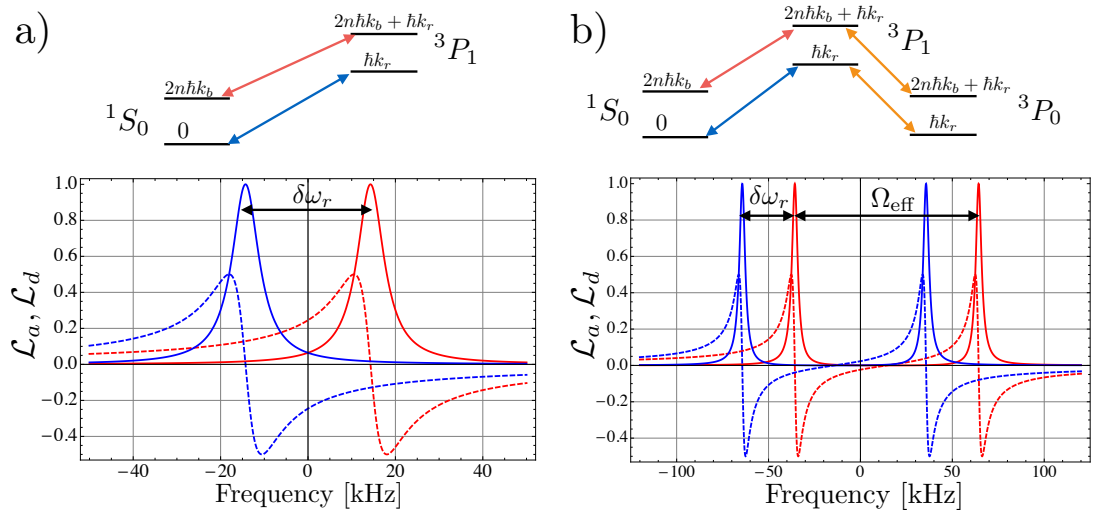

Figure 5.7: Atomic absorption ($\mathcal{L}_a$, solid line) and dispersion ($\mathcal{L}_d$ dashed line) profiles with and without EIT coupling for first-order Bragg diffraction. The light phase measurement is performed with the probe laser tuned halfway between the two bare resonances. a) Absorption and dispersion from the two optical transitions between momentum states without EIT coupling. The level diagram identifies the optical transitions by their color. b) Absorption and dispersion with EIT coupling. The coupling to the $^3P_0$ state is illustrated by the orange arrows and the coupling strength is $\Omega_{\text{eff}} = 2\pi \times 100$ kHz.

The coherence between the states $|a\rangle$ and $|b\rangle$, expressed by equation (5.73), can be directly connected to the expectation value of the ladder operator given in equation (5.36). The comparison is made by recalling that both results hold for the steady-state response of a two-level system and by observing that, for a single atom $N = 1$, $\langle\hat{\sigma}_-\rangle = \rho_{ba} = (\rho_{ab})^*$. Moreover, the probe Rabi frequency is expressed as $\Omega_p = 2g\tilde{c}$. In the presence of EIT coupling, equation (5.36) can be rewritten in the form

$$\tilde{\sigma}_- = \frac{g\tilde{c}}{\left(\Delta - \frac{\Omega_{\text{eff}}^2}{4(\Delta-\delta')}\right) + i\frac{\Gamma}{2}}. \tag{5.75}$$

Therefore, in the presence of EIT, the results given in the previous sections are obtained formally by replacing the detuning from atomic resonance Δ with the effective detuning Δ_E:

$$\Delta \to \Delta_E = \Delta - \frac{\Omega_{\text{eff}}^2}{4(\Delta - \delta')}. \tag{5.76}$$

The increased effective detuning can allow to operate a collective measurement in the dispersive regime thus reaching the optimum squeezing level.

The modified atomic response in the presence of electromagnetically induced transparency with two momentum states can be understood from Fig. 5.7. Without EIT and for small Bragg diffraction orders, atomic absorption halfway between the two resonances

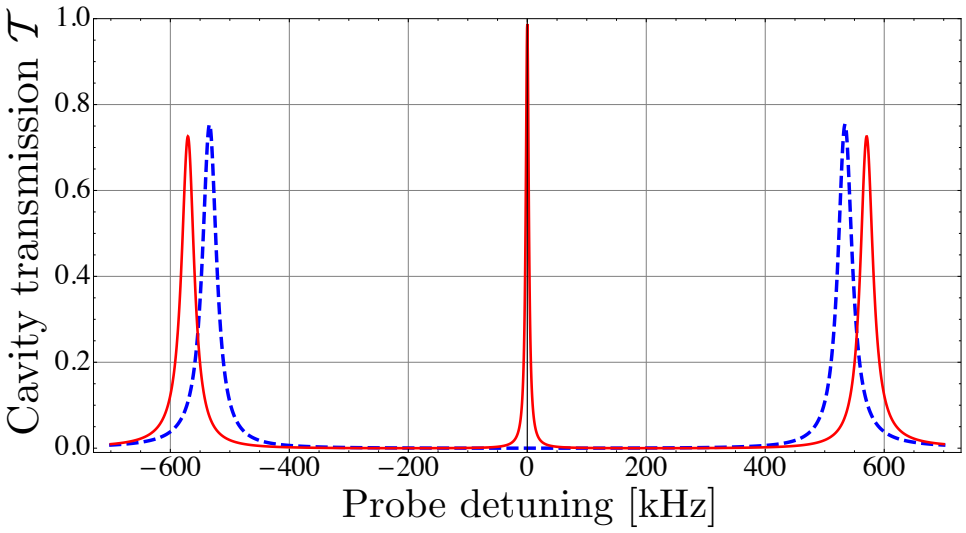

Figure 5.8: Cavity transmission spectrum with (red solid line) and without (blue dashed line) Raman coupling to the $^3P_0$ state for $\Omega_{\text{eff}} = 2\pi \times 400$ kHz, $N\eta = 3 \times 10^3$ and $n = 1$. The two lateral peaks correspond to the vacuum Rabi splitting for $\kappa = 2\pi \times 50$ kHz. The population measurement is performed at the frequency of the transparency region which corresponds to a linewidth of $\kappa_{\text{EIT}} = 2\pi \times 6$ kHz.

limits the number of transmitted photons and thus the signal to noise ratio of the squeezing measurement. As already discussed, in the optical cavity, absorption is enhanced by the factor $[1+N\eta\mathcal{L}_a(\delta\omega_r)]^2\mathcal{L}_a(\delta\omega_r)$ in (5.65). This would then mean that substantial gain would be observed for a small optical depth $N\eta$ and one is left with little interferometer phase resolution. In the presence of EIT on Raman resonance $\delta' = 0$, the single atomic resonance is split by the coupling with the metastable $^3P_0$ state. This effect opens a transparency window, shown in Fig. 5.7 b), for both optical transitions connecting the $^1S_0$ and $^3P_1$ states. With the probe field tuned between the two bare resonances, the intersection between the two transparency windows can lead to a substantial increase in the measurement signal to noise ratio. The increased transmission of the optical cavity at the frequency of the probe laser is shown in Fig. 5.8 for the effective Rabi frequency $\Omega_{\text{eff}} = 2\pi \times 400$ kHz. Mathematically, following (5.76), this situation translates into the definition of the effective Doppler splitting $\delta\omega_E = \delta\omega_r - \Omega_{\text{eff}}^2/(4\delta\omega_r)$. When the two-photon Rabi frequency Ω_{eff} is large, $\Omega_{\text{eff}}^2 \gg \Gamma\delta\omega_r\sqrt{N\eta}$, EIT allows to operate in the dispersive regime where, in (5.65), $[1 + N\eta\mathcal{L}_a(\delta\omega_E)]^2\mathcal{L}_a(\delta\omega_E)/[\mathcal{L}_d(\delta\omega_E)]^2 \to 1$.

As a result, the optimum number of photons scattered into free space (5.64) and the optimum metrological gain (5.65) are obtained, in the presence of EIT, by the replacement $\delta\omega_r \to \delta\omega_E$.

The attainable metrological gain with Raman coupling to the $^3P_0$ state is plotted in

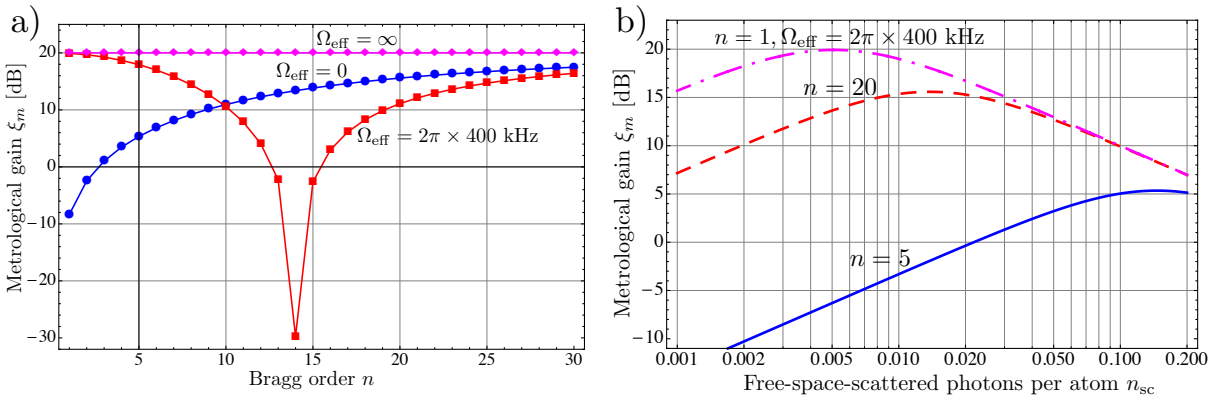

Figure 5.9: Metrological gain as a function of the number of photons scattered into free space per atom $n_{\rm sc}$ (a)) and as a function of the Bragg diffraction order (b)) with and without EIT coupling. The figures show that electromagnetically induced transparency allows to attain the optimum squeezing for small diffraction orders and large atom numbers. Values are plotted for $N\eta = 10^4$ and for a perfect detection efficiency $\epsilon_d = 1$.

Fig. 5.9 and should be compared to Fig. 5.5 where the coupling is absent. The comparison shows that with EIT and for small diffraction orders, the attainable squeezing is as good as for the large diffraction order limit.

We conclude this subsection with a few remarks:

- **Velocity selectivity of Raman transitions**

  In deriving the atomic response to the Raman coupling, we neglected the velocity selectivity of Raman transitions as discussed in Section 4.2. This effect could, at least in principle, cause a different coupling in the $|^3P_1, \hbar k_r\rangle - |^3P_0, \hbar k_r\rangle$ and the $|^3P_1, 2n\hbar k_b + \hbar k_r\rangle - |^3P_0, 2n\hbar k_b + \hbar k_r\rangle$ transitions. However, if the Raman beams are copropagating in the direction of the Bragg beams, the frequency difference between these two transitions is $\Delta\omega = \Delta k_R \frac{2n\hbar k_b}{M}$, where Δk_R is the difference in the wavenumbers of the Raman lasers. For the transitions considered here we have $\Delta\omega = 2\pi n \times 380$ Hz. For small diffraction orders and large $\Omega_{\rm eff}$, this splitting cannot be resolved if the measurement time duration is on the order of 100 μs. In the following we will show that this duration is sufficient to reach the optimum gain. Moreover, if large diffraction orders are used, this splitting can be suppressed or even eliminated by illuminating the atomic sample orthogonally to the Bragg beams.

- **Requirements on the effective two-photon Rabi frequency**

  The condition $\Omega_{\rm eff}^2 \gg \Gamma\delta\omega_r\sqrt{N\eta}$ that allows to operate in the dispersive regime is more readily met when the population is probed on a narrow transition rather

than on a broad transition. Moreover, a larger Doppler splitting $\delta\omega_r$ also sets more stringent requirements on Ω_{eff}. As a result, it is expected that the proposed EIT scheme becomes more accessible experimentally when both Γ and n are small. In this case, achieving large Ω_{eff} is less demanding in terms of laser power. A remarkable feature is that the conditions on Ω_{eff} are less severe in terms of collective cooperativity because the minimum required Rabi frequency scales as $(N\eta)^{1/4}$.

- **Photon scattering into free space induced by the Raman lasers**

  Because the detuning of the Raman lasers from the single-photon transitions is finite, it is important to ensure that the EIT coupling does not add noise or decoherence through scattering into free space. We therefore provide a criterion for the choice of the Raman laser configuration that avoids additional scattering into free space from the excited $^3S_1$ state. We start by computing the average $^3S_1$ population in the limit $\Omega_{\text{R1}}, \Omega_{\text{R2}} \ll |\Delta_{\text{R}}|$ as

$$P(^3S_1) = \frac{\Omega_{\text{R1}}^2 + \Omega_{\text{R2}}^2}{4\Delta_{\text{R}}^2} P_{\text{exc}}, \tag{5.77}$$

  where P_{exc} is the average population of the $^3P_1$ state and we accounted for the fact that, in the presence of Raman coupling, P_{exc} is also the average population of the $^3P_0$ state. We then assume that $\Omega_{\text{R1}} = \Omega_{\text{R2}} \equiv \overline{\Omega}_{\text{R}}$ and that n_{sc}^L is the upper limit for the number of photons per atom scattered into free space by decay from the $^3S_1$ state. The corresponding limit on the ratio $\overline{\Omega}_{\text{R}}/\Delta_{\text{R}}$ between the single-photon Rabi frequency and the Raman detuning is then estimated as

$$\left(\frac{\overline{\Omega}_{\text{R}}}{\Delta_{\text{R}}}\right)_L = \sqrt{\frac{2n_{\text{sc}}^L}{\Gamma_T P_{\text{exc}} T_m}}, \tag{5.78}$$

  where $\Gamma_T = 2\pi \times 12.4$ MHz is the total decay rate from the $^3S_1$ state and T_m is the squeezing measurement time duration.

  Because we assumed, throughout our discussion, that the probe field is weak enough that the population P_{exc} of the $^3P_1$ state is not saturated, the EIT coupling can be attained with smaller detuning Δ_{R} compared to standard implementations of Raman transitions, where the population of the coupled states is of the order of unity. This means that large two-photon Rabi frequencies can be reached, as long as the conditions for adiabatic elimination of the $^3S_1$ state hold.

- **Implementation to atoms with different electronic structure**

  As long as the excited state of the probing transition is coupled to a long-lived state, our EIT method is expected to work, at least in principle. It can, for example, be implemented on alkali atoms. In this case, the hyperfine structure in the ground

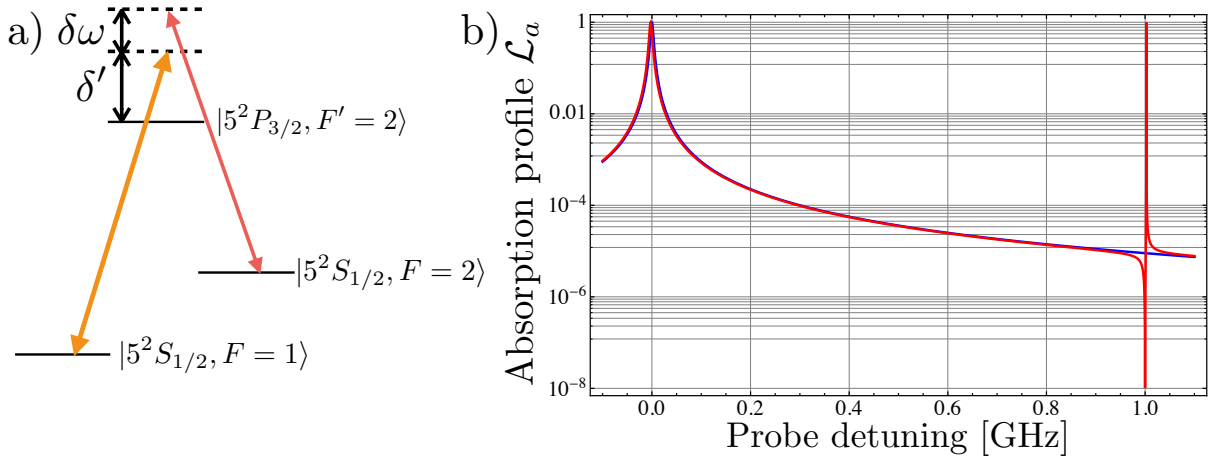

Figure 5.10: Scheme for the implementation of a synthetic narrow absorption line in Rb atoms. a) Level diagram, orange arrow: pump field, red arrow: probe field, δ': detuning of the pump field from the bare atomic resonance, $\delta\omega$: detuning from the two-photon Raman transition. b) Absorption profile with (red line) and without (blue line) EIT coupling with $\Omega_{\text{eff}} = 2\pi \times 100$ MHz and $\delta' = 2\pi \times 1$ GHz. The effective linewidth of the synthetic resonance is $\Gamma_{\text{eff}} = \Gamma_{\text{Rb}}(\Omega_{\text{eff}}/2\delta') = 2\pi \times 15$ kHz for a bare linewidth $\Gamma_{\text{Rb}} \simeq 2\pi \times 6$ MHz.

state offers the possibility to perform the EIT coupling with a single laser. In ^{87}Rb atoms, for example, probing of the momentum state superposition can be implemented on the $|5^2S_{1/2}, F = 2\rangle - |5^2P_{3/2}, F' = 2\rangle$ transition whereas EIT coupling can be implemented on the $|5^2S_{1/2}, F = 1\rangle - |5^2P_{3/2}, F' = 2\rangle$ transition (Fig. 5.10). The notation used to describe EIT can be adapted to describe this case. Here, the detuning of the coupling laser from atomic resonance is δ' and the corresponding single-photon Rabi frequency is Ω_{eff}. The probe detuning from the bare atomic resonance is Δ. By substituting in the absorption profile $\mathcal{L}_a$ the expression for the effective detuning (5.76) it is possible to see that, in the limit $\Omega_{\text{eff}} \ll \delta'$, the single atomic line is split in two resonances at the probe detunings $\Delta_- = -\Omega_{\text{eff}}^2/(4\delta')$ and $\Delta_+ = \delta' + \Omega_{\text{eff}}^2/(4\delta')$. The first resonance, at $\Delta = \Delta_-$, describes the AC Stark shift of the atomic transition whereas the second resonance, at $\Delta = \Delta_+$, occurs near the two-photon Raman resonance as shown in Fig. 5.10 b). By considering small frequency deviations ($\delta\omega$ in Fig. 5.10 a)) about Δ_+, it is seen that this describes a synthetic atomic transition with a reduced linewidth $\Gamma_{\text{eff}} = \Gamma[\Omega_{\text{eff}}/(2\delta')]^2$, where Γ is the bare atomic linewdith. EIT thus creates a resonance with a tunable linewidth that can be used to probe the population of momentum state superpositions [133].

5.3.5 Estimation of attainable squeezing with realistic experimental parameters

With realistic values for the various parameters, our method is applicable to strontium atoms with the current technology. Specifically, we consider an optical cavity where one of the foci has a waist $w_0 = 150$ μm, at the position where the atoms cross the cavity mode volume. With a cavity finesse $F = 2.5 \times 10^4$ and at the wavelength $\lambda_r = 689$ nm, we get a single-atom cooperativity $\eta = 6F\lambda_r^2/(\pi^3 w_0^2) \approx 0.1$ [34]. We then consider $N \approx 10^5$ atoms occupying a volume with a linear size of about 30 μm. With these parameters, the collective cooperativity is $N\eta \approx 10^4$. The maximum possible Bragg diffraction order with our method is set by the condition that the transit time of the wavepackets corresponding to the two momentum states through the cavity beam waist is larger than the time duration of the collective measurement. We estimate the useful transit time as the one taken by a wavepacket with speed $n\hbar k/M$ to cross one tenth of the effective mode waist. Because the atoms are crossing the cavity beam vertically, the effective mode waist is $w_0/\sin\alpha$. We therefore estimate the maximum Bragg diffraction order as $n_{\max} = Mw_0/(10\hbar k T_m \sin\alpha)$, where T_m is the measurement time duration. With $\alpha \approx 0.4$ rad and $T_m \approx 200$ μs we get $n_{\max} = 10$. However, the maximum Bragg order can be made considerably larger by a suitable design of the cavity geometry, where w_0 is made larger and α is made smaller. The measurement time is set by the requirement that the number of photons scattered into free space is sufficient to provide the optimum metrological gain. By considering a collective cooperativity $N\eta = 10^4$, first-order diffraction $n = 1$, a Raman coupling strength $\Omega_{\text{eff}} = 2\pi \times 400$ kHz, a measurement time $T_m = 200$ μs and a detection efficiency $\epsilon_d = 1$, we conclude that the optimum number of photons scattered into free space per atom is $n_{\text{sc}}^{\text{opt}} = 5 \times 10^{-3}$, corresponding to the excited state population $P_{\text{exc}} = n_{\text{sc}}/(\Gamma T_m) = 5 \times 10^{-4}$. In this case it is possible to achieve a metrological gain of 20 dB.

5.4 Other methods for squeezing in atom interferometers

In this Section we attempt to propose alternative methods that can produce squeezed states for atom interferometers. We state the possible procedures through which a collective population measurement can be realized but we do not perform a quantitative analysis. A deeper treatment is left for future theoretical and experimental investigation.

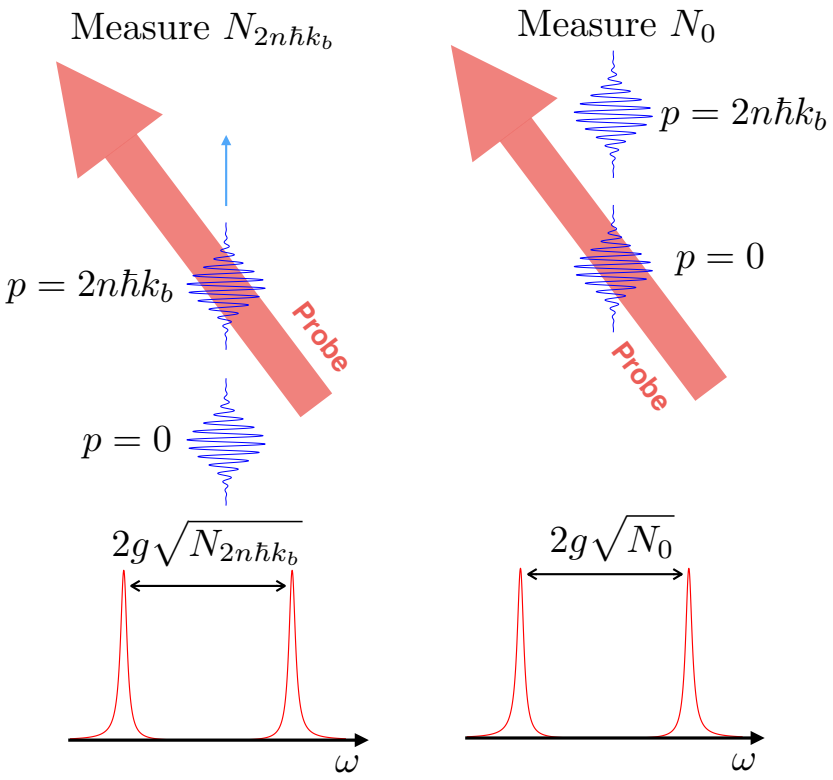

Figure 5.11: Procedure for the measurement of the population of two momentum states as the corresponding wavepackets separately travel through the cavity mode volume. The collective population is measured by the vacuum Rabi splitting.

5.4.1 Momentum state population measurements for spatially separated wavepackets

When the velocity difference between the momentum states of the atom interferometer is large enough, after a certain time-of-flight, the corresponding wavepackets can be spatially separated. In this case, one can arrange a situation where the two wavepackets are probed separately by the measuring light as they cross the cavity mode volume at different times.

As in Fig. 5.11, when the first wavepacket with momentum $p = 2n\hbar k_b$[5] crosses the probe beam, the corresponding number of atoms $N_{2n\hbar k_b}$ is measured through the vacuum Rabi splitting $2g\sqrt{N_{2n\hbar k_b}}$. After this, an additional measurement N_0 on the non-diffracted cloud can be performed. This procedure allows to measure the difference in the populations of the two momentum states. Although this result can in principle be obtained by a single measurement, in practice one needs the double measurement in order to account for atom number fluctuations between different experiment runs. If spatial effects are not

[5]We recall that momenta are written in the reference frame that is falling with the non-diffracted atomic cloud and not in the laboratory reference frame.

an issue, the precision of the nondestructive measurement is that of the vacuum Rabi splitting [79].

5.4.2 Collective population measurements in an atom interferometer based on the optical clock transition

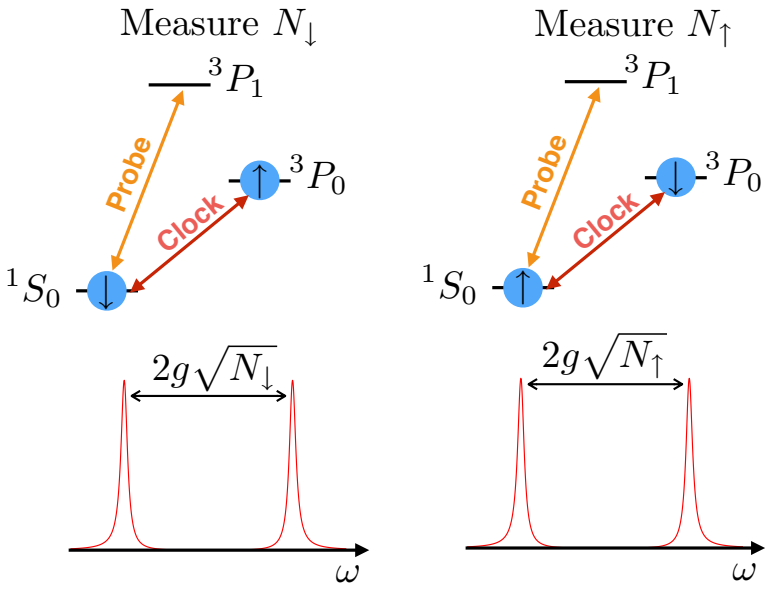

Figure 5.12: Collective measurement of the population of the states connected by the $^1S_0$-$^3P_0$ clock transition. After the generation of a coherent superposition, the number $N_\downarrow$ of atoms in $^1S_0$ is measured by the Rabi splitting. The populations are then flipped by a π-pulse and the measurement is repeated thus giving the number $N_\uparrow$ of atoms in the $^3P_0$ state.

In a recent work, our group demonstrated the first atom interferometer operating on the single-photon optical clock transition [93] with very promising applications to fundamental measurements [134]. An atom interferometer such as this one, where, like in Raman transitions, the internal and external degrees of freedom are entangled, can be equipped with the tools for squeezing. The simplest scheme resembles that of the previous Subsection. Here, after the preparation of the coherent superposition between the $^1S_0$ and $^3P_0$ states, a nondestructive probe can be performed on the $^1S_0$-$^3P_1$ transition where the vacuum Rabi splitting is measured. The number of atoms in the $^3P_0$ state is then measured by applying a π-pulse on the clock transition that flips the populations. After an additional Rabi splitting measurement, the atom number difference is computed in such a way that the influence of total atom number fluctuation is suppressed.

5.5 Conclusions

In this Chapter, a method for squeezing of momentum state superpositions has been presented. The method can yield the best performance when the momentum difference is large enough that the squeezing measurement has a large signal to noise ratio. By adding the feature of electromagnetically induced transparency, squeezing is retrieved also for small momentum separations and large atom numbers. We have shown that this scheme can reasonably and realistically be implemented in real experiments. In this Chapter, moreover, we cited a few alternative options that can be realized in atom interferometers and that can allow for phase resolutions beyond the Standard Quantum Limit.

If these methods were implemented in a real system, they would lead to many attractive experiments, where it is possible to study the features of atom interferometry with correlated atomic sources.

For this reason, in the next Chapter the design of a setup that is suitable for squeezing experiments is discussed.

Chapter 6

Experiment design for squeezing on momentum states

The proposed methods for squeezing in atom interferometers rely on collective measurements of the atomic populations. The attainable metrological gain depends on the optical depth of the atomic ensemble which we quantify through a key parameter: the collective cooperativity $N\eta$. Maximizing this parameter requires, on the one hand, large atomic densities and on the other hand a large single-atom cooperativity η. As seen from equation (5.39), the single-atom cooperativity η depends on the probe mode waist and on the cavity finesse. As a result, a great improvement in the attainable squeezing can be attained in an optical resonator with a large finesse. However, for experiments involving atoms in free flight, it is essential to find a compromise between a mode waist that is small enough to provide a large η but that is also large enough to yield a homogeneous interaction between the probe field and the atomic ensemble.

In this Chapter we discuss a possible experimental realization that can face the demanding even though achievable requirements of our proposed squeezing methods.

In the first part of the Chapter, the main requirements for the cavity geometry and a realistic solution are discussed. An auxiliary optical cavity design used for testing the final geometry is also considered and the present stage of our work is discussed.

In the second part of this Chapter, we will report on the realization of a laser system that will be used for laser cooling and trapping of strontium atoms. The other laser systems for cooling, trapping and probing in the optical cavity will be discussed and a suitable laser scheme for EIT coupling is illustrated.

6.1 Optical cavity and vacuum system

6.1.1 Requirements on the optical cavity and determination of the optimum geometry

On the basis of the discussion that was carried out in the previous Chapter, we can list the main requirements that the optical resonator should satisfy.

1 Ring resonator

Because the atoms are in free flight during the squeezing measurement, it is important to ensure that the coupling of the probe field with the atomic ensemble is uniform and constant throughout the duration of the squeezing measurement. The simplest optical resonator that can be conceived is a linear cavity. Despite its simplicity, a two-mirror cavity has a mode profile that is formed by a standing wave. If implemented in an experiment in free flight conditions, it would cause spatially inhomogeneous entanglement which could be totally washed out at the detection of the final interferometer output [126]. Time averaging of the standing wave profile can result in a homogeneous entanglement [81]. However, this result required a dipole trap to limit the transverse atomic expansion while averaging is performed. For the proposed methods, it would be preferable to avoid additional complications and work intead with an inherently homogeneous mode profile. Such a requirement is satisfied by the ring resonators, where the light travels in one direction only and does not exhibit spatial intensity profiles on the scale of an optical wavelength. For such ring resonators, the length scale of the inhomogeneity is set by the much wider transverse mode profile.

2 Bow-tie ring cavity

The squeezing measurement proposed in the previous Chapter is based on resolving the Doppler splitting due to the different momentum states. The splitting signal is maximized when the cavity probe has a large component along the vertical direction. By adding to this the requirement that the reflection on the cavity mirrors is close to normal incidence, as is typical, a three-mirror ring cavity does not appear to be the best choice. The four-mirror bow-tie cavity illustrated in Fig. 5.4 a), on the other hand, seems to satisfy our needs: the atomic cloud can exit the cavity volume and the reflection on the mirrors is close to normal incidence.

3 Mode waist size

A small mode waist w allows to attain a large single-atom cooperativity because $\eta \propto 1/w^2$. However, if the atomic cloud has a linear size that is larger than w, there is no advantage in choosing a small waist because the collective cooperativity would

be rougly invariant. This is easily understood for a uniform atomic cloud, where the effective number of atoms that interact with the probe beam scales as w^2. Then $N\eta$ is independent of w. A large mode waist on the other hand ensures a homogeneous interaction throughout the measurement time duration. It is therefore clear that the best procedure is to implement a cavity with a mode waist that is comparable with the linear size of the atomic cloud. Given the size of our cooled strontium cloud after the red MOT stage, we estimate that the mode waist should lie in the range $w = 100 - 200$ μm.

4 Mode waist position

As in Fig. 5.4 a), the most convenient position to probe the atomic ensemble is near the crossing of the two beams. The exact crossing should be avoided because there, the interference of the crossing beams causes a standing wave pattern.

5 Sensitivity to misalignment

Given the number of optical components and the somewhat complex geometry of the bow-tie resonator, the cavity setup should be chosen with a pronounced robustness against misalignment.

6 Cavity finesse

After taking care of the geometric constraints that ensure a large collective cooperativity, its overall value is set by the cavity finesse. This forces us to work with high-reflectivity mirrors which in turn means that the mirrors should be protected from any source of contamination.

7 Mechanical stability

Because, in our proposals, the absolute probe frequency is important, the length of the cavity has to be stabilized to an external reference and a good passive stability is desirable. This implies using piezo actuators for fast and fine control of the length as well as a temperature control stage that improves the long term stability. The design of the cavity should minimize the effect of environmental vibration noise. If vibration damping materials are used, they should be elastic enough to provide sufficient damping but also stiff enough such that the alignment of the probe beam incident onto the cavity is maintained. These aspects are also connected to the cavity finesse and to the cavity length. We recall that the cavity linewidth κ is the ratio of the free spectral range $\Delta\omega_{\mathrm{FSR}} = 2\pi c/L_{\mathrm{rt}}$ to the finesse $\mathcal{F}$, where L_{rt} is the round-trip length. Locking the frequency of the cavity to better than κ with a given vibration noise then requires that the finesse is not too large nor the cavity too long.

8 Mirror transmission

Squeezing induced by measurement requires the photon detection efficiency to be as large as possible. The photodetector efficiency is certainly a factor but it is not the only one. An important contribution comes from the intracavity losses. For the scheme detailed in the previous Chapter, the probe light is detected from the reflection of the input mirror. Here the contribution to the detection efficiency is expressed by the factor κ_1/κ contained in equation (5.60) which expresses the ratio of detected to incident photons. In other terms, for the input mirror, the transmission has to be much larger than the total photon loss. The extreme case where $\kappa_1 = \kappa$ is that of a one-sided cavity, where all the light enters and exits from a single mirror.

9 Optical and atomic access

During the interferometer, the atomic wavepackets should have the possibility of entering and exiting the cavity volume without encountering physical obstacles. Moreover, the cavity structure should allow to have enough optical access for the laser beams required for cooling, trapping, Bragg diffraction and EIT coupling. As a result, the cavity structure should be designed in such a way that it poses no physical obstacle for all these tasks.

10 Sensitivity to magnetic fields

The cavity structure should be engineered so that strong forces due to the MOT magnetic fields are avoided.

The cavity geometry was studied by means of the ABCD matrices for Gaussian beams [135, 136]. In our calculations, we separate the treatment between the sagittal plane (orthogonal to the cavity plane) and the tangential plane (parallel to the cavity plane). For a given plane and at each point, the Gaussian beam is completely determined by the complex parameter q which is related to the local wavefront curvature radius R and to the local waist w by

$$\frac{1}{q} = \frac{1}{R} - i\frac{\lambda}{\pi w^2}, \tag{6.1}$$

where λ is the wavelength of the light. The transformation rule for a gaussian beam from q_{in} to q_{out} when passing through an optical element with a 2×2 ABCD matrix is given by $q_{\text{out}} = (Aq_{\text{in}} + B)/(Cq_{\text{in}} + D)$. When an optical cavity is described by an ABCD round-trip matrix, the self-consistency condition for the field to reproduce itself after one round-trip is $q = (Aq + B)/(Cq + D)$. According to the definition (6.1), a self-consistent field only exists when the imaginary part of $1/q$ is negative or $(D - A)^2 + 4BC < 0$. Because the ABCD matrices have unity determinant, this condition can be rewritten as

$$|A + D| < 2, \tag{6.2}$$

which determines the subset of the *stable cavities* i.e. those where a Gaussian beam reproduces itself. As expected, the cavity needed for our experiment will be determined in this class.

The calculation of the round-trip ABCD matrix in the bow-tie cavity uses the following three matrices:

$$\mathcal{M}_f(d) = \begin{pmatrix} 1 & d \\ 0 & 1 \end{pmatrix}, \mathcal{M}_t(R_m, \theta) = \begin{pmatrix} 1 & 0 \\ -\frac{2}{R_m \cos\theta} & 1 \end{pmatrix}, \mathcal{M}_s(R_m, \theta) = \begin{pmatrix} 1 & 0 \\ -\frac{2\cos\theta}{R_m} & 1 \end{pmatrix}, \tag{6.3}$$

which describe free propagation through a distance d ($\mathcal{M}_f$), reflection through a mirror with radius of curvature R_m with incidence angle θ in the tangential ($\mathcal{M}_t$) and in the sagittal ($\mathcal{M}_s$) planes, respectively. The product of these matrices is used to compute the round-trip matrices in the tangential and in the sagittal planes in order to establish whether the cavity is stable according to (6.2).

The ABDC round-trip matrices can also be used to quantify the sensitivity to misalignment [137, 138]. In order to do so, the ABCD matrix is replaced with the generalized 3×3 matrix

$$\mathcal{M} = \begin{pmatrix} A & B & \Delta x \\ C & D & \Delta\alpha \\ 0 & 0 & 1 \end{pmatrix}, \tag{6.4}$$

where Δx and $\Delta\alpha$ represent an effective offset and an effective tilt of the optical axis resulting from the misalignment of the optical element. The error vector $(\Delta x, \Delta\alpha)$ is the null vector when the system is aligned. If one mirror is tilted by a small angle δ with respect to the aligned configuration, the optical axis deviates from the original angle by 2δ, therefore the error vector reads $(0, 2\delta)$. If, on the other hand, the mirror is offset by an amount b that is small compared to the mirror radius of curvature R_m, the optical axis is tilted and the error vector is $(0, 2b/R_m)$. For a ring cavity, one has to distinguish between the tangential and the sagittal planes. If the mirror offset occurs in the tangential plane, then one should use for R_m the effective radius of curvature $R_m \cos\theta$ whereas in the sagittal plane the effective radius of curvature is $R_m/\cos\theta$. The mirror offsets considered here are in the direction that is transverse compared to the optical axis. To first order in the mirror offsets, longitudinal displacements only affect the cavity mode structure and not the optical axis. In order to establish the sensitivity to misalignment, the round-trip matrix is computed as products of matrices of the form (6.4) and the round-trip values of Δx and $\Delta\alpha$ are computed. With this information, the resulting offset x_0 and tilt V_0 of the cavity optical axis can be determined as

$$x_0 = \frac{(1-D)\Delta x + B\Delta\alpha}{2-A-D}, V_0 = \frac{(1-A)\Delta\alpha + C\Delta x}{2-A-D}. \tag{6.5}$$

This result shows that a diverging sensitivity to misalignment is attained when $(A+D) \to +2$. On the opposite stability edge, $(A+D) \to -2$, the cavity reaches its minimum

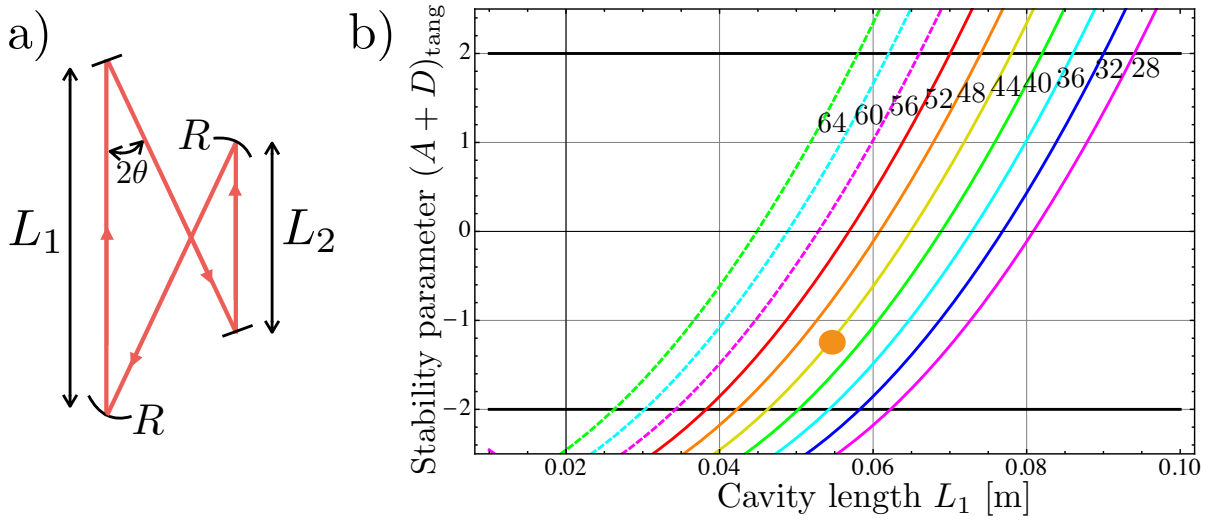

Figure 6.1: a) Schematic of the optical ring cavity represented as a trapezoid where two opposite mirrors have radius of curvature R and the remaining two mirrors are flat. The length of the first arm is L_1 and the other parallel arm has length L_2. The angle of incidence on the mirrors is θ. b) Stability parameter $A + D$ for the tangential plane as a function of L_1. The curves refer to different values of L_2 expressed by the numbers on the plot in mm. Values are plotted for $R = 50$ mm and $\theta = 0.2$ rad. The orange circle identifies our chosen geometry.

sensitivity to misalignment. The interpretation of this criterion in terms of the Gouy phase shift yields a useful rule of thumb for the design of robust optical resonators. The round-trip Gouy phase can be written as

$$\phi_{\mathrm{G}} = \arccos\left(\frac{A+D}{2}\right). \tag{6.6}$$

At the robust edge $(A + D) \to -2$, the Gouy phase shift is $\phi_{\mathrm{G}} = \pi$. For simplicity, we divide the ring cavity into tightly focused arms and into collimated arms. In a collimated arm, the accumulated Gouy phase is negligible whereas, in a tightly focused arm, the accumulated Gouy phase is π. As a result, if the cavity is formed by an odd number of tightly focused arms, the accumulated Gouy phase is approximately π (modulo 2π) and the resonator is robust against misalignment. If, on the other hand, the number of tightly focused arms is even, the accumulated Gouy phase is 2π, corresponding to $(A+D) \to +2$ i.e. the sensitivity to misalignment diverges.

In our cavity design, we will consider a setup with two curved and two flat mirrors that produce a mode with two foci, one with a large waist and the other with a smaller waist. This results essentially in a single tightly focused arm.

After exploring the parameter space, we determined a suitable geometry that fulfills most of our requirements. With reference to Fig. 6.1 a), we considered a geometry where

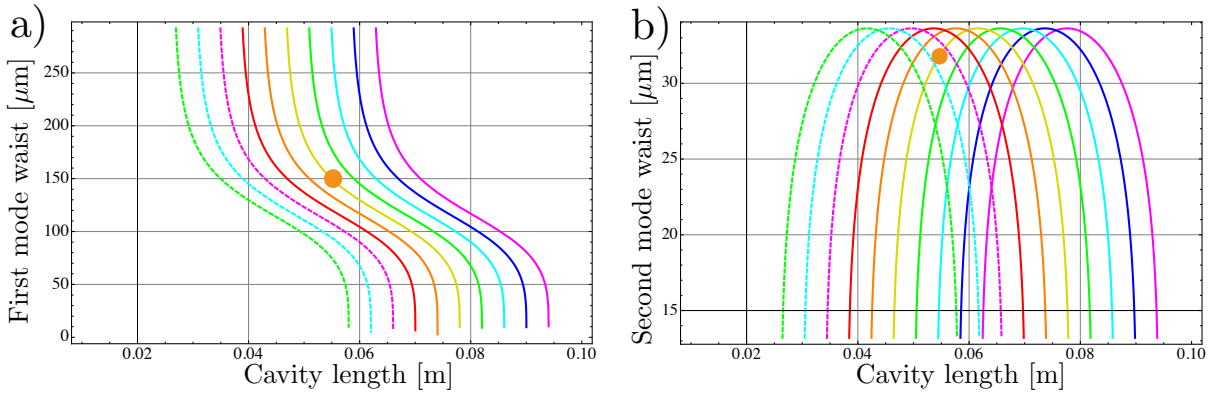

Figure 6.2: Mode waist as a function of the length of the first arm L_1 and for different values of the length of the parallel arm L_2. The orange circles identify our chosen geometry. a) Waist in the second (oblique) arm b) Waist in the fourth (oblique) arm.

the two curved mirrors have a radius of curvature of R =50 mm, the length of the first vertical arm is L_1 = 55 mm and the second is L_2 =44 mm long. The angle of incidence on the cavity mirrors is set to θ =0.2 rad (11.5°). In Fig. 6.1 b), the stability parameter $A + D$ is plotted for the tangential plane. The behaviour in the sagittal plane has only a slight difference. The plot shows that for the chosen geometry (orange circle), the stability parameter is smaller than -1, indicating a cavity that is robust against misalignment.

In Fig. 6.2 the mode waist for the two oblique arms is plotted. The chosen cavity geometry exhibits one large waist of about 150 μm and a second smaller waist of about 30 μm. As anticipated, this situation corresponds to a single tightly focused arm, which guarantees robustness against misalignment. The large waist lies in a range that is comparable with the size of our laser cooled atomic cloud after the red MOT stage.

Fig. 6.3 shows the spatial mode structure. The two foci are located near the crossing points of the two beams and are almost aligned at the vertical midpoint as required.

In going back to the list of ten requirements for the cavity design, the chosen geometry is seen to fulfill requirements 1 through 5.

6.1.2 Design of the optical ring cavity and of the vacuum system

Having determined a suitable geometry for the optical resonator, the next step is to provide a design which satisfies the requirements 6 through 10 of the previous Subsection.

Cavity mirrors As already discussed, our geometric requirements can be satisfied by a ring cavity with two curved and two flat mirrors. The curved mirrors should have a radius of curvature of 50 mm. Moreover, all the mirrors need to be quite small in order to guarantee sufficient optical and atomic access.

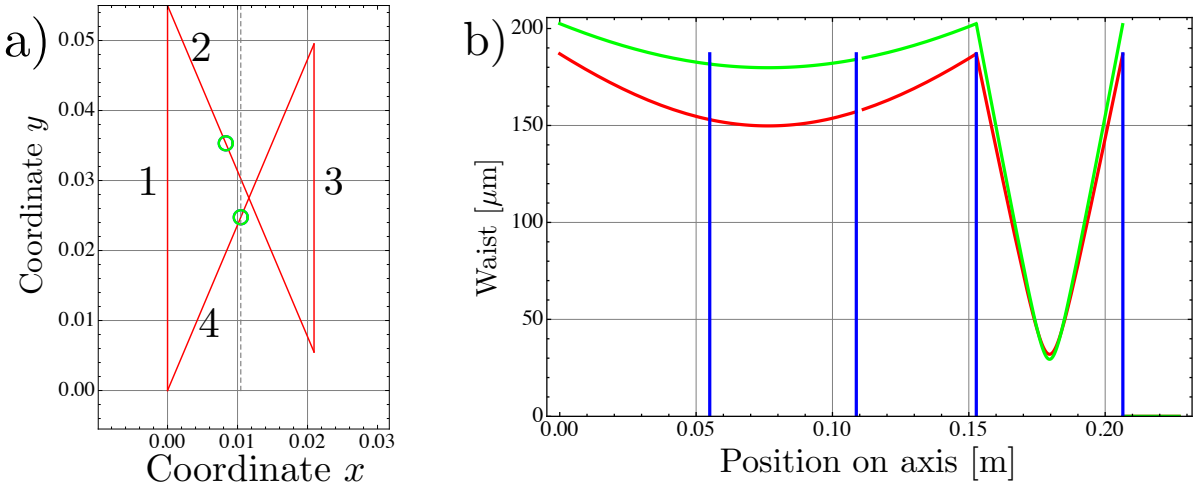

Figure 6.3: a) Computed cavity geometry. The numbers on the plot label the arms of the ring cavity and the green cricles identify the waist positions. The upper waist (in arm 2) is the largest whereas the lower (arm 4) is the smallest. The dashed line indicates the midpoint, where the atomic trajectories are likely to be. b) Evolution of the cavity waist along the optical axis. Red line: waist on the tangential plane. Green line: waist on the sagittal plane. Blue vertical lines: mirror positions.

Thanks to our interaction with the National Physical Laboratory (NPL in the UK), where a strontium experiment is being built, we were able to make a single coating run for the high-reflectivity (HR) mirrors. The mirror substrates have been manufactured by Reasearch Electro-Optics while the coating run was performed by Fivenine optics (both in Boulder, Colorado). The manufactured mirror substrates have a cylindrical shape with a 7.75 mm diameter and a 4 mm thickness and are therefore small enough to yield enough optical and atomic access. The diameter, on the other hand, is large enough to ensure that a beam with at most a 200 μm waist (see Fig. 6.3) does not suffer from significant diffraction losses, at least when the cavity is close to the optimum alignment. For the relevant wavelengths, the substrates are antireflection (AR) coated on the transmissive side in order to avoid etalon effects inside the substrates. The spectrometer data of transmission (HR coated side) for our high-reflectivity mirrors, as measured by Fivenine optics, are given in Fig. 6.4. At the wavelength of the $^1S_0$-$^3P_1$ intercombination transition, the transmission is 33 ppm. According to measurements performed at NPL, the loss per mirror amounts to 26 ppm. This should yield a cavity finesse of 50000 for the two-mirror linear cavity and a finesse of 25000 for the four-mirror bow-tie cavity.

Cavity structure and parts Our current design of the optical cavity support structure is illustratred in Fig. 6.5. The optical cavity is held on a ring spacer, made in 316L

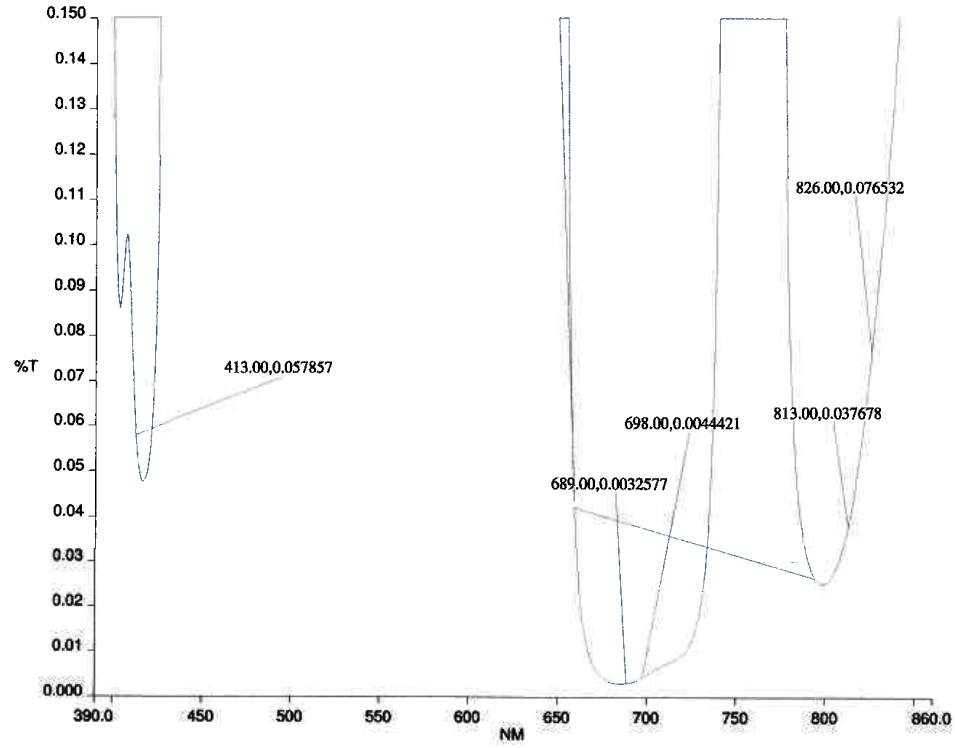

Figure 6.4: Spectrometer data of our high-reflectivity mirrors. %T indicates the mirror transmission. Particular values of T at certain wavelengths λ that are relevant for strontium experiments are indicated in the form λ[nm], T[%].

stainless steel, that is connected to a ultra-high vacuum (UHV) CF100 flange through four plastic pillars. The pillars are made of PEEK plastic, a high-performance polymer [139] that features good mechanical properties, relatively high temperature operation and compatibility with UHV. This material has a Young modulus of 3.6 GPa which is conveniently smaller compared to 193 GPa for 316L stainless steel. This holding structure can therefore provide an effective vibration damping system and prevent transmission of deformations from the CF100 flange.

The steel spacer is ring-shaped, a choice that roughly reproduces the symmetry of the optical cavity. Finite-element computations showed that under the effect of vibrations, the structure with the holders undergoes a mostly common-mode motion which has little effect on the overall cavity length. From the numerical computations, the sensitivity of the cavity resonance frequency to vertical accelerations is computed to be 4 MHz/g, where g is gravity's acceleration.

With our triaxial accelerometer (Episensor ES-T), we measured the acceleration noise of the optical table on the ground. The corresponding power spectral density is plotted in Fig. 6.6. By integrating the noise density over the bandwidth of the accelerometer (200 Hz), we obtain an rms noise value of 2.5×10^{-4} g which corresponds to a 1 kHz

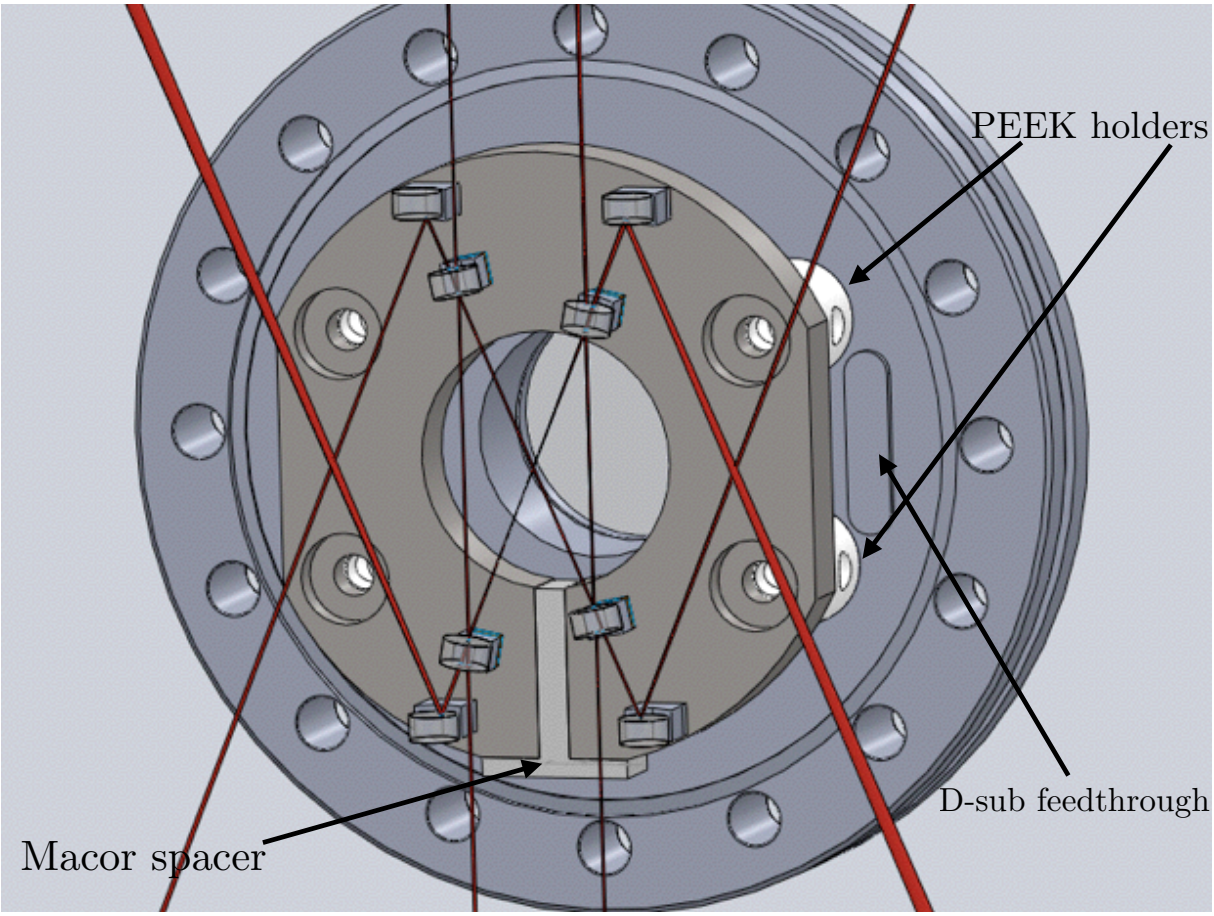

Figure 6.5: Cavity structure design. The circular cavity spacer is supported onto a CF100 ultra-high vacuum flange by four pillars made of PEEK plastic. The optical cavity is formed by the four mirrors close to the central hole. The additional external mirrors redirect the light in order to collect it from the vacuum viewports. All the mirrors are glued onto a V-shaped support. Two of the cavity mirrors are mounted on piezo actuators. Temperature control is provided by four heaters formed as sheets that are glued on the back of the spacer. The D-sub feedthrough provides the necessary electrical connections for the piezos and the heaters. The macor spacer interrupts most of the Eddy currents from varying magnetic fields.

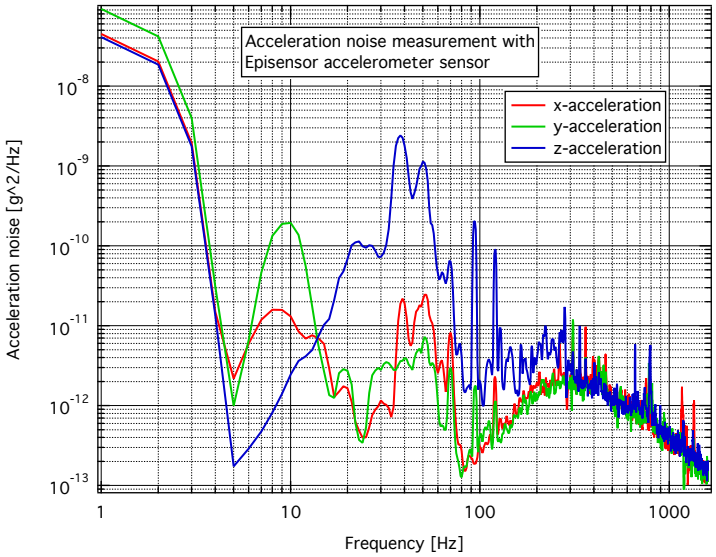

Figure 6.6: Power spectral density measurement of acceleration noise in our optical table performed through the Episensor tri-axial accelerometer.

rms fluctuation of the cavity resonance frequency. This value is tolerable for moderate cavity finesse. It is also expected that by floating the table, the acceleration noise will be substantially reduced. The estimated cavity frequency noise suggests that locking the cavity should not be a formidable task.

In Fig. 6.5, the four internal mirrors form the optical cavity. The mirrors will be glued to four V-shaped supports. Two of these supports are rigidly connected to the ring spacer and the remaining two are connected to piezoelectric actuators. The two piezos (Noliac NAC2402-H2.3) are formed by a square-shaped stack that has a 5 mm side length, a dimension that is perfectly compatible with that of the mirrors. When a voltage is applied to the electrodes, the piezos undergo a shear motion. In order to avoid large dc electric fields in the vacuum chamber, the piezos were ordered without the top and bottom insulating plates that were originally present. In this way it is possible to electrically ground the two plates, while the high-voltage electrode remains between them and electric fields are mainly confined to this region. An important feature of these actuators is their large (unloaded) resonance frequency of 725 kHz. In the presence of the light mass formed by the mirrors and the V-supports, it is expected that these piezos can be driven at relatively large frequencies, thus attaining large vibration and acoustic noise suppression.

The ring spacer is interrupted for a length of a few mm by inserting a piece of electrically insulating material named Macor. The interruption is made in order to suppress strong Eddy currents that could be induced during the experiment runs, when the MOT quadrupole fields are varied. This material is a glass-ceramic whose coefficient of thermal

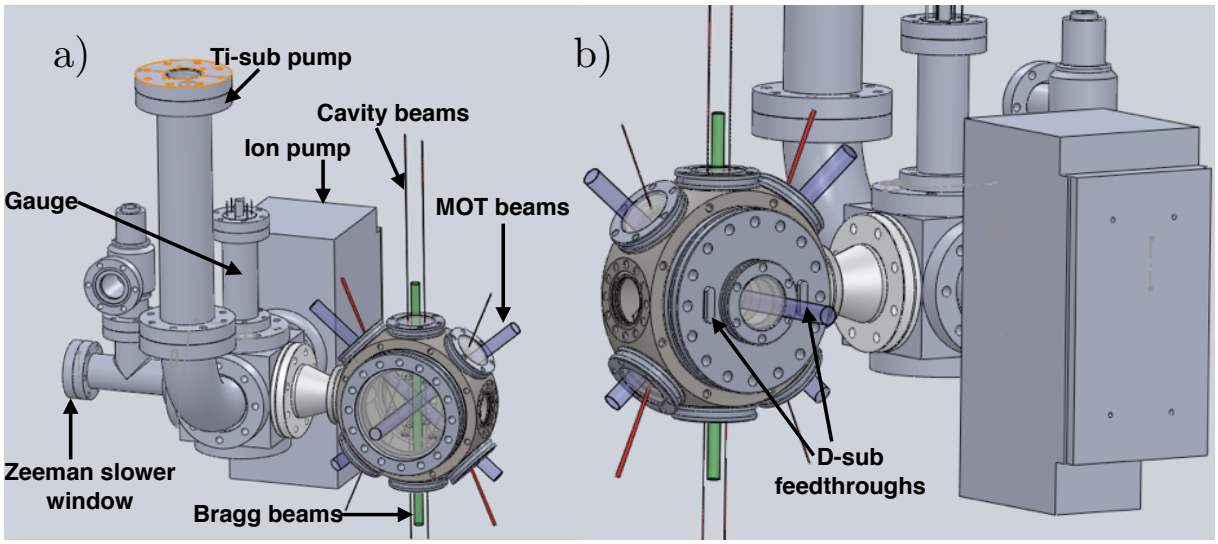

Figure 6.7: a) Front view of the vacuum system with the chamber containing the optical cavity and the pumping section with a titanium-sublimation pump, an ion pump and a vacuum gauge. The atomic source and the Zemman slower coils are not represented. b) Back view of the CF100 flange, where the two D-sub feethroughs are visible.

expansion matches well that of the 316L steel, even though the thermal conductivity is smaller by one order of magnitude.

In order to perform a coarse cavity length tuning and to provide long-term stability, we plan to implement a temperature control through four kapton-foil heaters that are glued on the back of the cavity spacer. The temperature is then measured by two probes.

The various electrical wires connecting the piezo actuators, the heaters and the temperature sensors, along with the common cavity ground, are brought out of the chamber through two D-sub vacuum feedthroughs.

The complete setup with the surrounding vacuum system and the important laser beams is represented in Fig. 6.7. The optical cavity is enclosed in a spherical octagon vacuum chamber. On one side, the chamber is connected to a pumping section, where an ion pump and a titanium-sublimation pump maintain the vacuum.

6.1.3 Tests of the cavity geometry with high-reflectivity mirrors

In order to verify the mirror properties and the cavity geometry, a series of low-cost experimental investigations are being performed.

The first test was performed by manufacturing an aluminum block with holes for the screws of standard mirror mounts. With a suitable adaptor, we were able to perform a first test of the mirrors through a linear near-confocal 5 cm cavity. The mirrors used for this experiment were two curved mirrors with 50 mm radius of curvature. The aluminum

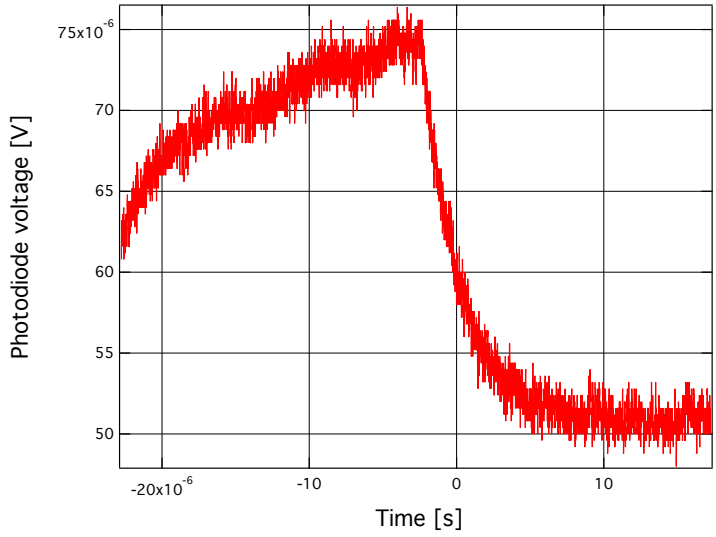

Figure 6.8: Typical cavity ring-down transmission signal after rapidly switching off the incident light. By averaging over signals of this form, the photon lifetime was measured to be $\tau_p = 2.6$ μs corresponding to a cavity finesse $\mathcal{F} \simeq 45000$ and a linewidth $\kappa = 1/\tau_p = 2\pi \times 61$ kHz.

block can be covered by walls in order to suppress air flow and a thermistor can be added that is centered with respect to the cavity structure. With two peltier cells between the aluminum block and the optical table, we were able to obtain a sufficient cavity resonance frequency stability. This allowed to measure the cavity finesse at the wavelength of the $^1S_0$-$^3P_1$ intercombination transition through the ring-down method. The measurement was realized by rapidly turning off the light that is incident onto the cavity and by observing the decay of the light transmission with a rate κ equal to the cavity linewidth, as seen in Fig. 6.8. The fast switching was obtained by a double-pass through an acousto-optic modulator. The resulting rise and fall time of the incident optical power were measured to be smaller than 50 ns. After averaging over 110 repetitions of the ring-down measurement, we found a cavity mode linewidth $\kappa \simeq 2\pi \times 61$ kHz and a finesse $\mathcal{F} \simeq 45000$, in good agreement with that expected from the transmission and loss measurements performed by Fivenine optics and NPL. The setup used to measure the mirror reflectivity is illustrated in Fig. 6.9 a), where the mirrors are supported on standard mounts that are fixed to a temperature stabilized aluminum block.

The next step of our tests is the implementation of a complete ring cavity prototype as shown in Fig. 6.9 b). The cavity will be supported on the same aluminum block as the linear cavity already tested. In this setup we will add two piezo actuators in order to rapidly tune the cavity length. These investigations will allow to verify the main features of the cavity such as the stability, the transverse mode structure and the beam waist of

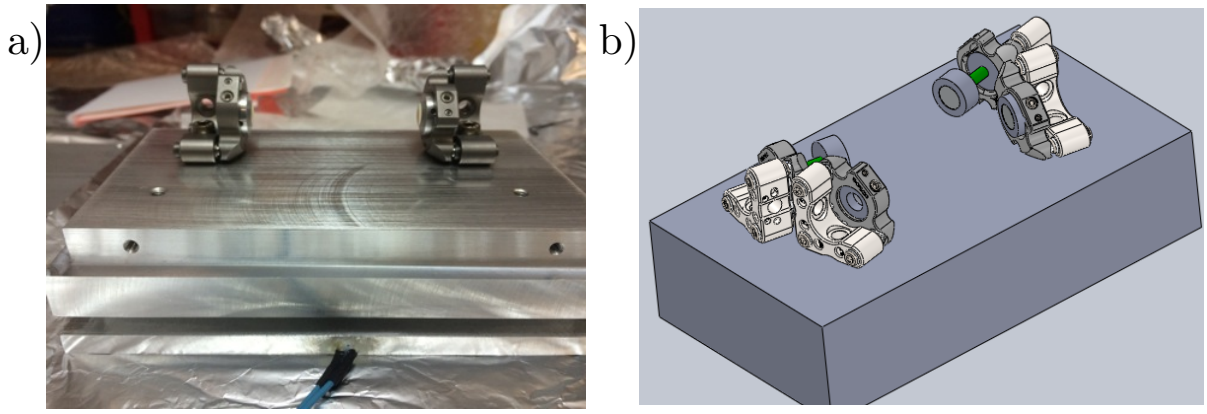

Figure 6.9: a) Setup for the measurement of the reflectivity of the cavity mirrors on a temperature stabilized aluminum block. This same support structure can be used as in b) to test the final ring cavity geometry. Here the green cylinders are piezo actuators used for fine length tuning.

the transmitted light. This work will allow, in particular, to verify that the cavity foci are at the expected positions. Moreover, the ability to lock the cavity length to an external reference will be investigated by implementing a Pound-Drever-Hall locking scheme [124].

From the point of view of our calculations, the cavity geometry and its properties seem to fulfill all the requirements for the proposed squeezing experiment. After our test measurements, the final cavity design will be finalized and the first tests in vacuum will be performed.

There are still two requirements that need to be satisfied for the final design which are under investigation. The first is the ability to glue the mirrors on their supports while avoiding contamination, maintaining alignment and avoiding to overheat the structure. Many vacuum epoxies only cure at high temperature. This restricts our choice to a smaller class of epoxies, namely Torrseal and VacSeal.

The second aspect that will be considered is increasing the transmission of one of the mirrors in order to maximize the ratio κ_1/κ, as is necessary to reach a high detection efficiency.

6.2 Laser systems

6.2.1 Laser system at 461 nm for laser cooling and trapping

An important part of our experiment is the production of the cooled and trapped strontium atomic cloud. We therefore started to build a laser for the first cooling stage on the dipole-allowed $^1S_0$-$^1P_1$ transition. In this experiment, we chose to implement the recently

developed blue laser diodes [140]. In particular, quite recently, blue diode lasers with AR coating on the front facet have been developed. This allows to build an external-cavity diode laser (ECDL) system that performs as the master reference source for all our 461 nm lasers.

If properly implemented, this system would represent a great simplification compared to the more common frequency-doubled laser sources. These frequency-doubled lasers usually have a high quality and large output power. They however suffer from being bulky systems that are often expensive and painful to align.

The ECDL system is formed by an AR-coated diode laser (Nichia, NDBA116T) a 4.5 mm aspheric collimation lens and a 1800 grooves/mm diffraction grating in the Littrow configuration. The grating is glued onto a support that is bent by the force exerted by a piezo actuator used for fine frequency tuning. The baseplate supporting the grating and the diode is thermally stabilized by a peltier cell and the temperature is sensed by a thermistor located right below the diode. The laser does not exhibit single-frequency continuous-wave emission without the external cavity. In assembling this laser it was noted that the laser threshold is critically dependent on the alignment of the collimation lens and of the diffraction grating. This criticality appears more pronounced for this laser than, for example, for our red 689 nm lasers. As a result, the mechanical design of the assembly might need to be reviewed in future work. Nevertheless, exept for the usual mode hopping behaviour, the laser operates in a single mode with the external cavity. In normal operation, the output power is about 20 mW at 120 mA supply current and at the wavelength of the atomic transition. After an optical isolator, about 15 mW are available for the atomic spectroscopy and stabilization and for injection locking of other diode lasers.

The optical setup for atomic spectroscopy, atomic state probing, slowing in the Zeeman Slower and MOT beams is depicted in Fig. 6.10 along with the frequency scheme used to perform the various tasks. This setup essentially reproduces the optimized one that was already implemented in our strontium experiments [108].

About 1 mW of laser light is used for frequency stabilization on the saturated absorption signal of a Sr heat pipe, after a double pass through an acousto-optic modulator (AOM 1). About 5 mW of optical power are directed to AOM 2 and are used for probing of the atomic states. The remaining light is used to optically inject two additional diode lasers that amplify the laser light. The output power of these lasers (Nichia, NDB4216) can reach up to 100 mW. One of the injected lasers is used for the Zeeman slower beam and the other for the MOT beams.

The atomic spectroscopy is performed by modulating the master laser current at 10 MHz and by sending the modulated light to the spectroscopy cell where a pump-probe configuration is realized. After a double-pass through the cell, the light is detected by a fast photodiode. The corresponding signal is mixed with a phase shifted replica of

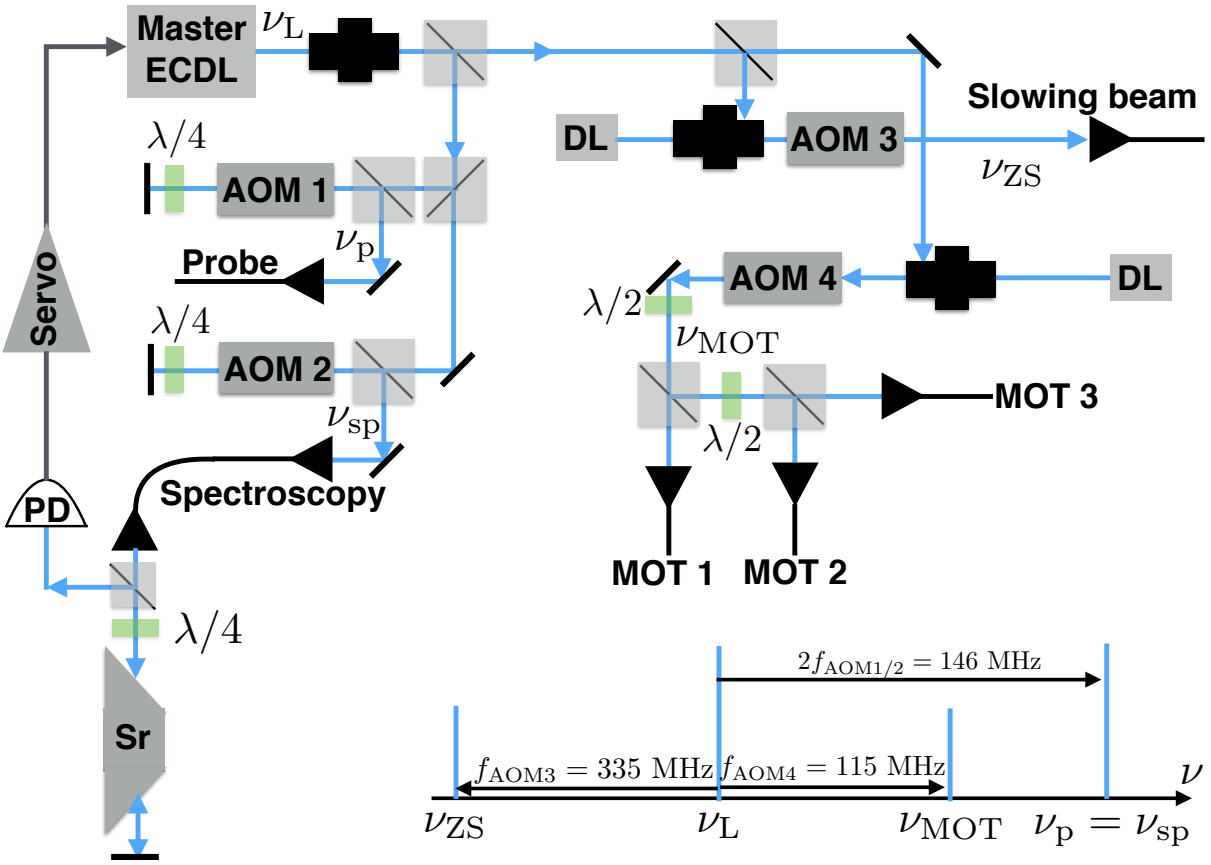

Figure 6.10: Schematic of the optical setup for the production of the blue laser light. The master laser ECDL is locked to a saturated-absorption signal on a Sr heat pipe. The same light is used for probing the atomic states after the interferometer and to optically inject two additional lasers (DL). This amplified light is used for slowing of the atomic beam and for the MOT. At the bottom right, the frequency scheme is illustrated. ν_{ZS}: Slowing beam frequency, ν_{MOT}: MOT beams frequency, ν_p: Probe beam frequency, ν_{sp}: Spectroscopy beam frequency.

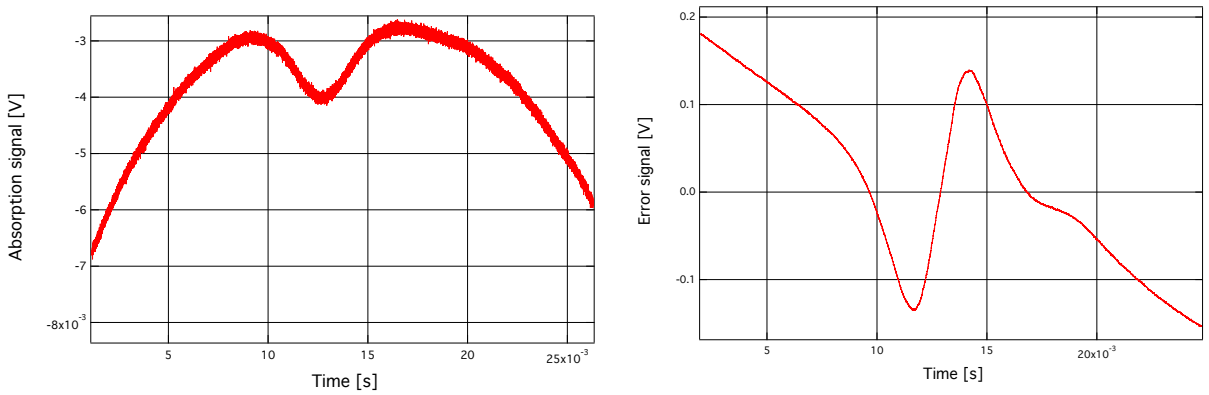

Figure 6.11: Atomic spectroscopy on the 461 nm transition while scanning the laser piezo. Left: saturated absorption dip as measured through the dc channel of the photodiode. Right: error signal for laser locking. The small contribution from ^{86}Sr is visible in the error signal.

the 10 MHz source in a phase detector. The output signal provides a wide dispersive profile that is centered at the resonance frequency of the ^{88}Sr $^1S_0$-$^1P_1$ transition. The saturated absorption and dispersive error signal are shown in Fig. 6.11 for an average over 32 measurements obtained by scanning the master piezo. The error signal also shows the presence of the ^{86}Sr transition which is shifted by 126 MHz due to the isotope shift. This knowledge allows to estimate a spectroscopy linewidth FWHM of 80 MHz.

The error signal is fed to a PI controller that acts on the master piezo in order to lock the laser. Additionally, having a direct way to tune the laser frequency through the supply current, a fast feedback is implemented. This is obtained by combining, in a bias-tee, the 10 MHz modulation and the error signal. Here, the error signal is filtered by a low-pass filter at 150 kHz corner frequency. The fast feedback substantially increases the locking bandwidth and allows to accordingly boost the PI integral gain, thus achieving an enhanced robustness against vibrations and acoustic noise. In these conditions, the laser linewidth can be estimated by the residual rms noise of the error signal and from the knowledge of the spectroscopic linewidth. The locked laser linewidth is about 1 MHz, mainly limited by a white noise pedestal from an internal photodiode amplifier.

6.2.2 Other laser systems

In this Subsection, a brief description of other standard laser systems for the experiment is provided.

Red laser system for cooling, trapping and probing As already discussed, a laser system for interacting with the intercombination transition is important for three reasons:

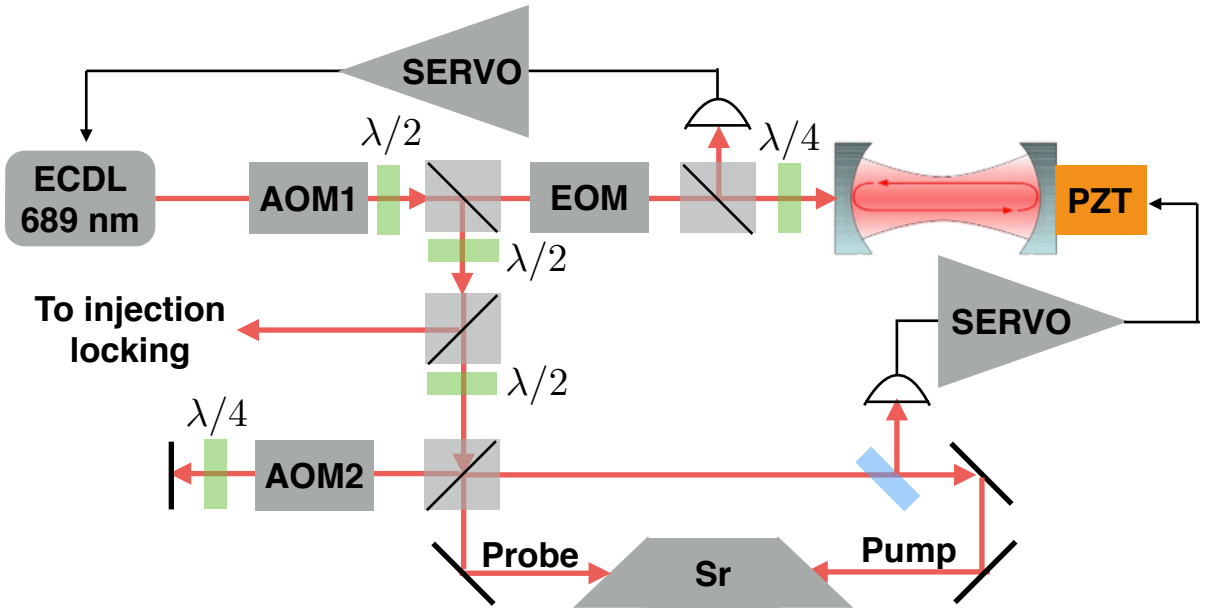

Figure 6.12: Schematic of the master source at 689 nm. The extended-cavity diode-laser (ECDL) is locked to the high finesse cavity and the cavity length is stabilized on the atomic spectroscopy. AOM: acousto-optic modulator, EOM: electro-optic (phase) modulator, $\lambda/2$: half-wave plate, $\lambda/4$: quarter-wave plate.

the implementation of the second cooling stage (the red MOT), probing on momentum states and, eventually, for Bragg diffraction. Here a system that performs the first two tasks is illustrated. For Bragg diffraction, a system similar to that described in Section 4.4 can be implemented. In our experiment, we will use the laser source already developed for the Bragg diffraction experiments.

A schematic representation of this laser source is given in Fig. 6.12. As we already mentioned, the master laser source is provided by an extended-cavity diode laser at 689 nm in the Littrow configuration. Like the blue laser diode, the diffraction grating is glued on a support that can be bent by the pressure of a piezoelectric transducer. In the presence of optical feedback from the diffraction grating, the linewidth is about 200 kHz. In order to interact with the intercombination transition, the linewidth needs to be further reduced. This is achieved by locking the laser to a high-finesse optical cavity through the Pound-Drever-Hall (PDH) method [124]. The optical cavity has a finesse $\mathcal{F} = 7800$ and a free spectral range 1.5 GHz, corresponding to a mode linewidth of 190 kHz. The cavity is formed by two mirrors glued on a quartz support with low thermal expansion coefficient. Moreover, it is contained in a cylindrical-shaped metal enclosure kept under vacuum and sustained on a rubber support for vibration isolation [141]. The PDH locking is implemented by modulating the laser phase through an electro-optic modulator (EOM) at 10 MHz. The error signal for locking is obtained by demodulating

the detected cavity reflected light. Under locking conditions, the locked laser linewidth is estimated to be on the order of 100 Hz. Because the optical cavity is not stable on the long term, additional stabilization is provided by direct saturated absorption spectroscopy on the intercombination line. This is attained in a strontium heat pipe heated at a temperature of 430°C. The spectroscopy pump beam comes from an 80 MHz AOM whose frequency is modulated at 100 kHz. The counterpropagating probe beam is detected on a low-noise amplified photodiode and the error signal is obtained by demodulation with the 100 kHz reference. The spectroscopy error signal is then used to feed back on the length of the high-finesse cavity through a piezo transducer. A fraction of the stabilized light of this source is then used to optically inject other laser diodes in order to provide power amplification.

The amplified light can then be used to perform the various tasks. For the implementation of the red MOT, the light from an injected laser diode is frequency controlled through an AOM and split into three parts to form the MOT beams.

The light can also be used to probe the momentum state population difference through the optical cavity. Although the optimum scheme will be determined experimentally, the laser spectrum will be manipulated through a phase modulator in order to perform the task of locking the science cavity length and to probe the atomic ensemble.

For how the squeezing experiment was conceived, it is clear that, in the ideal case, no light other than the probe light should be present in the cavity. This might add difficulties if it is necessary to keep the cavity locking during the probing procedure as additional locking light might introduce important light shifts that alter the interferometer performance. However, in typical conditions, we expect that the cavity locking light should be turned off for 1 ms only, where cavity vibrations should not be an important issue. If cavity vibrations limit the attainable squeezing through the added photon phase shift, locking could be performed through off-resonant light perhaps locked on a high-order spatial mode of the optical cavity, where the intensity at the center of the beam is negligible.

Green repuming laser For the operation of the blue MOT, it is necessary to recycle the atoms shelved in the $^3P_2$ metastable state. In this experiment, repumping will be achieved through a single laser at 497 nm (see Section 3.1). Because, for our knowledge, no laser diode emits directly at this wavelength, frequency doubling from a 994 nm laser is necessary.

The laser system is formed by an extended-cavity diode laser emitting about 20 mW at 994 nm. The laser is used to inject a tapered amplifier yielding more than 200 mW output power. After coupling into an optical fiber, the infrared light is passed through a fiber-coupled wavelength conversion module from NTT electronics, which can provide up to 20 mW of light at 497 nm. Even for a beam waist of 1 cm, this power yields a saturation

parameter $s = I/I_{\text{sat}} \simeq 5$, more than sufficient to saturate the $^3P_2$-$^3D_2$ transition and provide efficient repumping. In our experiment we will also attempt to lock the laser to the atomic spectroscopy performed on a hollow cathode lamp (Laser Galvatron, Hamamatsu) through the DAVLL (Dichroic Atomic Vapor Laser Lock) locking method [142], which is expected to yield a large signal-to-noise ratio and a sizeable capture range.

6.2.3 EIT laser system

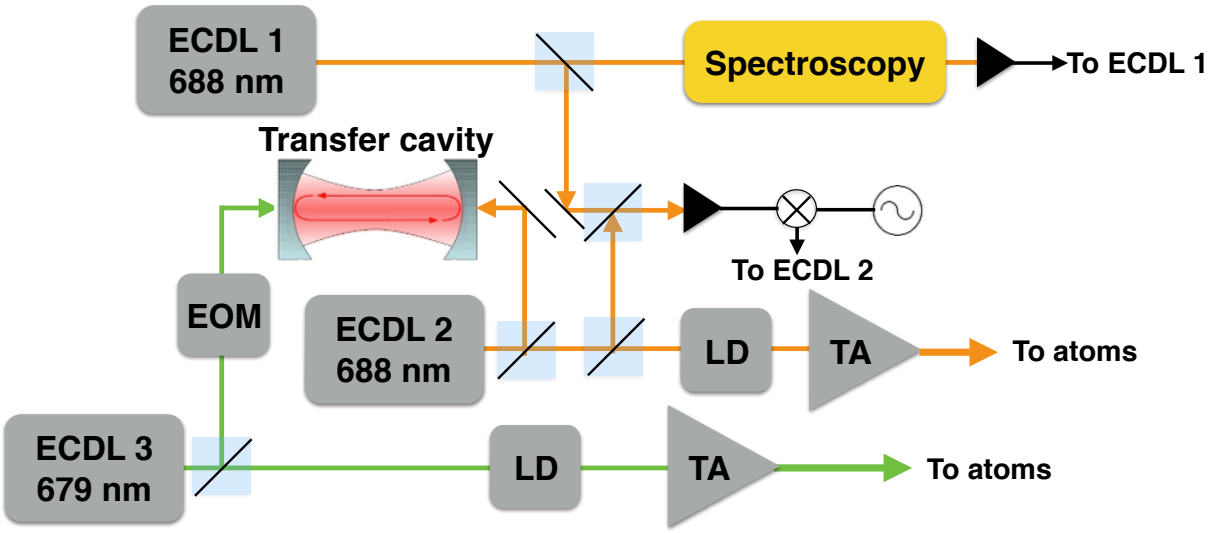

Figure 6.13: Simplified scheme of the EIT laser system. Light at 688 nm is indicated as orange and the light at 679 nm is indicated as green. ECDL 1 at 688 nm is locked to the atomic spectroscopy and optically beated with ECDL 2, to provide the necessary detuning from resonance. The light of ECDL 2 is preamplified by injection locking on a laser diode (LD) and amplified by a tampered amplifier (TA). ECDL 2 is also used to reference the transfer cavity. ECDL 3 at 679 nm is passed through a phase modulator (EOM) and locking is performed on a sideband. Its light is amplified as for ECDL 2.

Squeezing on momentum states on the intercombination transition is limited by atomic absorption. As discussed in Chapter 5, the signal-to-noise ratio can be substantially recovered through electromagnetically induced transparency (EIT). In order to obtain a stable signal from the probe laser, with strontium atoms, two lasers with different wavelength (679 nm and 688 nm) need to be phase locked. This can be achieved through the simplified scheme represented in Fig. 6.13. The setup is formed by an extended-cavity diode laser (ECDL) at 688 nm whose frequency is referenced to the atomic spectroscopy on a hollow cathode lamp, for example through the DAVLL method. A second ECDL at 688 nm is locked to the first through an optical beatnote. This second ECDL is then detuned from atomic resonance as required to drive the Raman transitions (see Section 4.2). This

light is used to reference an optical cavity which transfers the stability to the 679 nm laser by bridging the large frequency gap between the two lasers. The light at 679 nm is also generated by an ECDL. In this case, a part is passed through a phase modulator which generates sidebands in the laser spectrum. The frequency component of one of the sidebands can be stabilized to the transfer cavity. With this scheme, both detunings of the 688 nm laser and of the 679 nm laser can be tuned at will and their difference can be set in order to reach two-photon Raman resonance, a necessary condition for EIT.

Subsequently, the lights at the two wavelengths are preamplified by optical injection on two laser diodes and power amplified through two tapered amplifiers. Because a similar setup with tapered amplifiers at similar wavelengths was implemented for Bragg diffraction on the intercombination line (see Section 4.4), we expect rather large output power levels of about 100 mW per beam. This setup should therefore allow to attain considerably large coupling Rabi frequencies of $\Omega_{\text{eff}} \sim 2\pi \times 100$ kHz.

An important technical issue in implementing this laser system lies in quantifying the required phase and frequency stability of the lasers. In particular, for a 200 μs interrogation time, such requirements should not be severe. If necessary, however, an alternative scheme can be implemented where the laser system is referenced to the 689 nm laser through an additional transfer cavity.

Chapter 7

Conclusions and perspectives

In this thesis, squeezing of momentum state superpositions induced by Bragg diffraction in strontium atoms is studied and a suitable scheme is proposed.

In this work, we demonstrated that Bragg diffraction with strontium atoms is now a reality and that, with additional technical efforts, the shot noise limit, at least for atomic gradiometers, can be reached. Given the inherent robustness of ^{88}Sr atoms against external perturbations and their low collisional rates, this atom appears to be a prime candidate in atom interferometry for inertial measurements. From this starting point, an additional tool that allows to surpass the Standard Quantum Limit is studied. This method relies on resolving the Doppler effect due to the momentum state superposition induced by Bragg diffraction. A narrow-linewidth transition can resolve the Doppler effect and provide a collective nondestructive measurement of the population difference between momentum states. A setup involving an optical ring resonator is considered that can boost the signal-to-noise ratio of collective measurements by a factor of the order of the cavity finesse. However, the collective measurement can produce sufficient signal only for large momentum transfer beam splitters. This requirement is consistent with state-of-the-art technology but might be a complication in certain situations. Moreover, large diffraction orders require a resonator geometry that might be challenging to realize. A feature that can extend the validity of our method to small diffraction orders and large atom numbers is considered. This relies in altering the atomic response to the probe field through electromagnetically induced transparency obtained by coupling the optically excited state to a state with much longer lifetime. Remarkably, with this addition, our method is extendable to atoms where narrow transitions are not naturally available. With this method, a scaling of the phase resolution $\delta\phi \propto N^{-3/4}$ is predicted and is limited by atom loss due to photon scattering into free space.

After identifying the requirements for the experimental implementation of our method, a suitable design of the optical resonator has been discussed and the first tests of its geometry are being performed.

If realized, this experiment could boost the capability of atom interferometers to measure inertial interactions.

Another source of interest lies in exploring the properties of squeezed momentum states and, for example, whether other nonclassical states such as Schrödinger cat states or Dicke states can be induced in real systems.

Appendices

Appendix A

Estimation of the curvature effects of the Bloch sphere

For a spin squeezed state prepared along the x direction, when the uncertainty in the S_z component of the collective atomic pseudospin is reduced as a result of squeezing, the orthogonal component S_y features an enhanced uncertainty due to the Heisenberg uncertainty principle, an effect known as antisqueezing. As long as the atomic interferometer is operated in such a way that the relevant phase information can be extracted from S_z alone, antisqueezing does not degrade the phase sensitivity.

There are however two effects that can degrade the sensitivity, both related to the curvature of the Bloch sphere. From an intellectual point of view, one of these effects can be compared to the measurement of the position of a free particle already discussed in Subsection 2.3.2. There we argued that, after a precise position measurement, because of the subsequent momentum spread, the position itself becomes uncertain at later times.

In the case of the atomic pseudospin, antisqueezing can reduce the effective Bloch vector length (i.e. the contrast) and, after phase accumulation in the interferometer, the enhanced uncertainty in S_y will contribute to the final uncertainty in S_z. In the following we will attempt to provide an estimation of these effects through a geometrical approach which is sufficient to yield an order of magnitude of such effects.

Contrast reduction

For a minimum uncertainty atomic state oriented along the x direction of the Bloch sphere, the Heisenberg uncertainty relation between the variances $(\Delta S_y)^2$ and $(\Delta S_z)^2$ can be written as

$$(\Delta S_y)^2(\Delta S_z)^2 = \frac{S^2}{4}. \tag{A.1}$$

As a result, the phase uncertainty $\delta(\Delta\phi)_{\mathrm{A}}$ corresponding to the antisqueezed component is the angle subtended at the origin of the Bloch sphere by a segment of length ΔS_y, given

by

$$\delta(\Delta\phi)_{\rm A} = \frac{\Delta S_y}{S} = \frac{1}{2\Delta S_z}, \tag{A.2}$$

an expression that is valid for $\Delta S_y \ll S$.

The corresponding reduction of the mean spin length, $S - \langle S_x \rangle$, can then be estimated as

$$S - \langle S_x \rangle = S[1 - \cos\delta(\Delta\phi)_{\rm A}] \simeq S\frac{\delta(\Delta\phi)_A^2}{2} = \frac{S}{8(\Delta S_z)^2}. \tag{A.3}$$

The fractional length reduction yields the contrast reduction

$$1 - \mathcal{C} = \frac{S - \langle S_x \rangle}{S} = \frac{1}{8(\Delta S_z)^2}. \tag{A.4}$$

This expression shows that contrast reduction is a small effect for large atom numbers even when the squeezing is rather pronounced. For example, we may consider a realistic atom number $N = 2S = 10^4$ and a squeezing factor $(S/2)/(\Delta S_z)^2 = 100$ (or 20 dB of spin squeezing), which corresponds to a contrast reduction of 0.5 %. According to the definition of the metrological gain ξ_m given in (5.52), this amounts to a negligible loss of 0.04 dB.

Uncertainty after phase accumulation

In a similarly geometric fashion, the enhanced phase uncertainty at the output of the interferometer can be derived. The added uncertainty is the projection, along the z direction, of the segment of length $S - \langle S_x \rangle$ as given in (A.3). After accumulation of the interferometer phase $\Delta\phi$, for $\Delta\phi \ll 1$, the final uncertainty in S_z is given by the quadrature sum

$$\Delta S_z^f = \sqrt{(\Delta S_z)^2 + \left(\frac{S}{8(\Delta S_z)^2}\Delta\phi\right)^2}. \tag{A.5}$$

This expression gives rise to a loss factor $1 - S^2(\Delta\phi)^2/[64(\Delta S_z)^6]$ for the gain ξ_m. If one is aiming at the achievement of spin squeezing at the level of 20 dB with 10^4 atoms, then the contribution of technical noise sources should be reduced below the level $\delta(\Delta\phi)_{\rm tech} = 1$ mrad. In this condition, the average shift $\Delta\phi$ can be made to vanish in a stable way, for example, by adjusting the relative phase of the Bragg pulses. In this case, the squeezing reduction is at the level of 0.0001 dB. With a modest squeezing reduction of 1.25 dB and the same number of atoms, phase excursions of up to $\Delta\phi = 100$ mrad can be measured with the same number of atoms. With a realistic number of atoms $N = 10^5$, this reduction is suppressed to the level of 0.11 dB.

We finally wish to add that these geometric considerations were confirmed through numerical computations involving squeezed states formed by superpositions of Dicke states weighted by a gaussian amplitude function of M, the eigenvalue of S_z. This form for the amplitude function is justified in general for large atom numbers, $N \gg 1$, a condition that is the most relevant in this thesis.

Bibliography

[1] *Atom Interferometry.* edited by G. M. Tino and M. A. Kasevich (Società Italiana di Fisica and IOS Press, Amsterdam, 2014).

[2] Alexander D. Cronin, Jörg Schmiedmayer, and David E. Pritchard. Optics and interferometry with atoms and molecules. *Rev. Mod. Phys.*, 81:1051–1129, Jul 2009.

[3] Achim Peters, Keng Yeow Chung, and Steven Chu. Measurement of gravitational acceleration by dropping atoms. *Nature*, 400(6747):849–852, Aug 1999.

[4] Zhong-Kun Hu, Bu-Liang Sun, Xiao-Chun Duan, Min-Kang Zhou, Le-Le Chen, Su Zhan, Qiao-Zhen Zhang, and Jun Luo. Demonstration of an ultrahigh-sensitivity atom-interferometry absolute gravimeter. *Phys. Rev. A*, 88:043610, Oct 2013.

[5] J. M. McGuirk, G. T. Foster, J. B. Fixler, M. J. Snadden, and M. A. Kasevich. Sensitive absolute-gravity gradiometry using atom interferometry. *Phys. Rev. A*, 65:033608, Feb 2002.

[6] F. Sorrentino, Q. Bodart, L. Cacciapuoti, Y.-H. Lien, M. Prevedelli, G. Rosi, L. Salvi, and G. M. Tino. Sensitivity limits of a Raman atom interferometer as a gravity gradiometer. *Phys. Rev. A*, 89:023607, Feb 2014.

[7] G. Rosi, L. Cacciapuoti, F. Sorrentino, M. Menchetti, M. Prevedelli, and G. M. Tino. Measurement of the Gravity-Field Curvature by Atom Interferometry. *Phys. Rev. Lett.*, 114:013001, Jan 2015.

[8] F. Riehle, Th. Kisters, A. Witte, J. Helmcke, and Ch. J. Bordé. Optical Ramsey spectroscopy in a rotating frame: Sagnac effect in a matter-wave interferometer. *Phys. Rev. Lett.*, 67:177–180, Jul 1991.

[9] T. L. Gustavson, P. Bouyer, and M. A. Kasevich. Precision Rotation Measurements with an Atom Interferometer Gyroscope. *Phys. Rev. Lett.*, 78:2046–2049, Mar 1997.

[10] Kinematic sensors employing atom interferometer phases. 2008. US Patent 7317184.

[11] David S. Weiss, Brenton C. Young, and Steven Chu. Precision measurement of the photon recoil of an atom using atomic interferometry. *Phys. Rev. Lett.*, 70:2706–2709, May 1993.

[12] Andreas Wicht, Joel M Hensley, Edina Sarajlic, and Steven Chu. A Preliminary Measurement of the Fine Structure Constant Based on Atom Interferometry. *Physica Scripta*, 2002(T102):82, 2002.

[13] G. Rosi, F. Sorrentino, L. Cacciapuoti, M. Prevedelli, and G. M. Tino. Precision measurement of the Newtonian gravitational constant using cold atoms. *Nature*, 510(7506):518–521, Jun 2014.

[14] M. Prevedelli, L. Cacciapuoti, G. Rosi, F. Sorrentino, and G. M. Tino. Measuring the Newtonian constant of gravitation G with an atomic interferometer. *Philosophical Transactions of the Royal Society of London A: Mathematical, Physical and Engineering Sciences*, 372(2026), 2014.

[15] J. B. Fixler, G. T. Foster, J. M. McGuirk, and M. A. Kasevich. Atom Interferometer Measurement of the Newtonian Constant of Gravity. *Science*, 315(5808):74–77, 2007.

[16] C. W. Misner, K. S. Thorne, and J. A. Wheeler. *Gravitation*. Freeman, 1973.

[17] Sebastian Fray, Cristina Alvarez Diez, Theodor W. Hänsch, and Martin Weitz. Atomic Interferometer with Amplitude Gratings of Light and Its Applications to Atom Based Tests of the Equivalence Principle. *Phys. Rev. Lett.*, 93:240404, Dec 2004.

[18] A. Bonnin, N. Zahzam, Y. Bidel, and A. Bresson. Simultaneous dual-species matter-wave accelerometer. *Phys. Rev. A*, 88:043615, Oct 2013.

[19] D. Schlippert, J. Hartwig, H. Albers, L. L. Richardson, C. Schubert, A. Roura, W. P. Schleich, W. Ertmer, and E. M. Rasel. Quantum Test of the Universality of Free Fall. *Phys. Rev. Lett.*, 112:203002, May 2014.

[20] M. G. Tarallo, T. Mazzoni, N. Poli, D. V. Sutyrin, X. Zhang, and G. M. Tino. Test of Einstein Equivalence Principle for 0-Spin and Half-Integer-Spin Atoms: Search for Spin-Gravity Coupling Effects. *Phys. Rev. Lett.*, 113:023005, Jul 2014.

[21] Lin Zhou, Shitong Long, Biao Tang, Xi Chen, Fen Gao, Wencui Peng, Weitao Duan, Jiaqi Zhong, Zongyuan Xiong, Jin Wang, Yuanzhong Zhang, and Mingsheng Zhan. Test of Equivalence Principle at 10^{-8} Level by a Dual-Species Double-Diffraction Raman Atom Interferometer. *Phys. Rev. Lett.*, 115:013004, Jul 2015.

[22] Pierre Meystre. *Atom Optics*. Springer Series on Atomic, Optical, and Plasma Physics, 2001.

[23] Sheng-wey Chiow, Tim Kovachy, Hui-Chun Chien, and Mark A. Kasevich. $102\hbar k$ Large Area Atom Interferometers. *Phys. Rev. Lett.*, 107:130403, Sep 2011.

[24] Andrew D. Ludlow, Martin M. Boyd, Jun Ye, E. Peik, and P. O. Schmidt. Optical atomic clocks. *Rev. Mod. Phys.*, 87:637–701, Jun 2015.

[25] Hidetoshi Katori. Optical lattice clocks and quantum metrology. *Nat Photon*, 5(4):203–210, Apr 2011.

[26] L. Pezzè, A. Smerzi, M. K. Oberthaler, R. Schmied, and P. Treutlein. Non-classical states of atomic ensembles: fundamentals and applications in quantum metrology. *ArXiv e-prints*, September 2016.

[27] D. J. Wineland, J. J. Bollinger, and W. M. Itano. Squeezed atomic states and projection noise in spectroscopy. *Phys. Rev. A*, 50:67–88, 1994.

[28] Vittorio Giovannetti, Seth Lloyd, and Lorenzo Maccone. Advances in quantum metrology. 5:222 EP –, Mar 2011. Review Article.

[29] Jian Ma, Xiaoguang Wang, C.P. Sun, and Franco Nori. Quantum spin squeezing. *Physics Reports*, 509:89 – 165, 2011.

[30] Kevin C. Cox, Graham P. Greve, Joshua M. Weiner, and James K. Thompson. Deterministic Squeezed States with Collective Measurements and Feedback. *Phys. Rev. Lett.*, 116:093602, Mar 2016.

[31] Onur Hosten, Nils J. Engelsen, Rajiv Krishnakumar, and Mark A. Kasevich. Measurement noise 100 times lower than the quantum-projection limit using entangled atoms. *Nature*, 529(7587):505–508, Jan 2016.

[32] Robert McConnell, Hao Zhang, Jiazhong Hu, Senka Cuk, and Vladan Vuletic. Entanglement with negative Wigner function of almost 3,000 atoms heralded by one photon. *Nature*, 519(7544):439–442, Mar 2015. Letter.

[33] Wenlan Chen, Jiazhong Hu, Yiheng Duan, Boris Braverman, Hao Zhang, and Vladan Vuletić. Carving Complex Many-Atom Entangled States by Single-Photon Detection. *Phys. Rev. Lett.*, 115:250502, Dec 2015.

[34] Haruka Tanji-Suzuki, Ian D. Leroux, Monika H. Schleier-Smith, Marko Cetina, Andrew T. Grier, Jonathan Simon, and Vladan Vuletić. Interaction between Atomic Ensembles and Optical Resonators: Classical Description. *Adv. At. Mol. Opt. Phys.*, 60:201, 2011.

[35] Mark Kasevich and Steven Chu. Atomic interferometry using stimulated Raman transitions. *Phys. Rev. Lett.*, 67:181–184, Jul 1991.

[36] Albert Messiah. *Quantum Mechanics*. Dover Publications, 1961.

[37] Norman F. Ramsey. A Molecular Beam Resonance Method with Separated Oscillating Fields. *Phys. Rev.*, 78:695–699, Jun 1950.

[38] F. T. Arecchi, Eric Courtens, Robert Gilmore, and Harry Thomas. Atomic Coherent States in Quantum Optics. *Phys. Rev. A*, 6(6):2211–2237, Dec 1972.

[39] C. T. Lee. Q representation of the atomic coherent states and the origin of fluctuations in superfluorescence. *Phys. Rev. A*, 30:3308–3310, Dec 1984.

[40] Barry C. Sanders. Quantum dynamics of the nonlinear rotator and the effects of continual spin measurement. *Phys. Rev. A*, 40:2417–2427, Sep 1989.

[41] Christopher C. Gerry and R. A. Campos. Generation of maximally entangled photonic states with a quantum-optical Fredkin gate. *Phys. Rev. A*, 64:063814, Nov 2001.

[42] M. J. Holland and K. Burnett. Interferometric detection of optical phase shifts at the Heisenberg limit. *Physical Review Letters*, 71:1355–1358, August 1993.

[43] Taesoo Kim, Olivier Pfister, Murray J. Holland, Jaewoo Noh, and John L. Hall. Influence of decorrelation on Heisenberg-limited interferometry with quantum correlated photons. *Phys. Rev. A*, 57:4004–4013, May 1998.

[44] Vittorio Giovannetti, Seth Lloyd, and Lorenzo Maccone. Quantum Metrology. *Phys. Rev. Lett.*, 96:010401, Jan 2006.

[45] Luca Pezzé and Augusto Smerzi. Entanglement, Nonlinear Dynamics, and the Heisenberg Limit. *Phys. Rev. Lett.*, 102:100401, Mar 2009.

[46] Masahiro Kitagawa and Masahito Ueda. Squeezed spin states. *Phys. Rev. A*, 47:5138–5143, Jun 1993.

[47] D. J. Wineland, J. J. Bollinger, W. M. Itano, F. L. Moore, and D. J. Heinzen. Spin squeezing and reduced quantum noise in spectroscopy. *Phys. Rev. A*, 46:R6797–R6800, Dec 1992.

[48] Dariusz Kajtoch and Emilia Witkowska. Quantum dynamics generated by the two-axis countertwisting hamiltonian. *Phys. Rev. A*, 92:013623, Jul 2015.

[49] Y. C. Liu, Z. F. Xu, G. R. Jin, and L. You. Spin Squeezing: Transforming One-Axis Twisting into Two-Axis Twisting. *Phys. Rev. Lett.*, 107:013601, Jun 2011.

[50] Emily Davis, Gregory Bentsen, and Monika Schleier-Smith. Approaching the Heisenberg Limit without Single-Particle Detection. *Phys. Rev. Lett.*, 116:053601, Feb 2016.

[51] Hosten, O. and Krishnakumar, R. and Engelsen, N. J. and Kasevich, M. A. Quantum phase magnification. *Science*, 352(6293):1552–1555, 2016.

[52] M. J. Holland, M. J. Collett, D. F. Walls, and M. D. Levenson. Nonideal quantum nondemolition measurements. *Phys. Rev. A*, 42:2995–3005, Sep 1990.

[53] A. Kuzmich, N. P. Bigelow, and L. Mandel. Atomic quantum non-demolition measurements and squeezing. *EPL (Europhysics Letters)*, 42(5):481, 1998.

[54] Marlan O. Scully and M. Suhail Zubairy. *Quantum Optics*. Cambridge University Press, Sep 1997.

[55] Monika Helene Schleier-Smith. *Cavity-enabled spin squeezing for a quantum-enhanced atomic clock*. PhD thesis, Massachusetts Institute of Technology. Dept. of Physics, 2011.

[56] G. S. Agarwal and R. R. Puri. Cooperative behavior of atoms irradiated by broadband squeezed light. *Phys. Rev. A*, 41:3782–3791, Apr 1990.

[57] A. Kuzmich, Klaus Mølmer, and E. S. Polzik. Spin Squeezing in an Ensemble of Atoms Illuminated with Squeezed Light. *Phys. Rev. Lett.*, 79:4782–4785, Dec 1997.

[58] J. Hald, J. L. Sørensen, C. Schori, and E. S. Polzik. Spin Squeezed Atoms: A Macroscopic Entangled Ensemble Created by Light. *Phys. Rev. Lett.*, 83:1319–1322, Aug 1999.

[59] Stuart S. Szigeti, Behnam Tonekaboni, Wing Yung S. Lau, Samantha N. Hood, and Simon A. Haine. Squeezed-light-enhanced atom interferometry below the standard quantum limit. *Phys. Rev. A*, 90:063630, Dec 2014.

[60] Markus Greiner, Olaf Mandel, Tilman Esslinger, Theodor W. Hansch, and Immanuel Bloch. Quantum phase transition from a superfluid to a Mott insulator in a gas of ultracold atoms. *Nature*, 415(6867):39–44, Jan 2002.

[61] C. Orzel, A. K. Tuchman, M. L. Fenselau, M. Yasuda, and M. A. Kasevich. Squeezed States in a Bose-Einstein Condensate. *Science*, 291(5512):2386–2389, 2001.

[62] Jun John Sakurai and Jim Napolitano. *Modern Quantum Mechanics*. Addison-Wesley, 2011.

[63] Fabrice Gerbier, Simon Fölling, Artur Widera, Olaf Mandel, and Immanuel Bloch. Probing Number Squeezing of Ultracold Atoms across the Superfluid-Mott Insulator Transition. *Phys. Rev. Lett.*, 96:090401, Mar 2006.

[64] G.-B. Jo, Y. Shin, S. Will, T. A. Pasquini, M. Saba, W. Ketterle, D. E. Pritchard, M. Vengalattore, and M. Prentiss. Long Phase Coherence Time and Number Squeezing of Two Bose-Einstein Condensates on an Atom Chip. *Phys. Rev. Lett.*, 98:030407, Jan 2007.

[65] J. Esteve, C. Gross, A. Weller, S. Giovanazzi, and M. K. Oberthaler. Squeezing and entanglement in a Bose-Einstein condensate. *Nature*, 455(7217):1216–1219, Oct 2008.

[66] C. Gross, T. Zibold, E. Nicklas, J. Estève, and M. K. Oberthaler. Nonlinear atom interferometer surpasses classical precision limit. *Nature*, 464(7292):1165–1169, Apr 2010.

[67] Max F. Riedel, Pascal Böhi, Yun Li, Theodor W. Hänsch, Alice Sinatra, and Philipp Treutlein. Atom-chip-based generation of entanglement for quantum metrology. *Nature*, 464(7292):1170–1173, Apr 2010.

[68] A. Kuzmich, L. Mandel, and N. P. Bigelow. Generation of Spin Squeezing via Continuous Quantum Nondemolition Measurement. *Phys. Rev. Lett.*, 85:1594–1597, Aug 2000.

[69] Anne E. B. Nielsen and Klaus Mølmer. Atomic spin squeezing in an optical cavity. *Phys. Rev. A*, 77:063811, Jun 2008.

[70] Igor Teper, Geert Vrijsen, Jongmin Lee, and Mark A. Kasevich. Backaction noise produced via cavity-aided nondemolition measurement of an atomic clock state. *Phys. Rev. A*, 78:051803, Nov 2008.

[71] Monika H. Schleier-Smith, Ian D. Leroux, and Vladan Vuletić. States of an Ensemble of Two-Level Atoms with Reduced Quantum Uncertainty. *Phys. Rev. Lett.*, 104:073604, Feb 2010.

[72] Monika H. Schleier-Smith, Ian D. Leroux, and Vladan Vuletić. Squeezing the collective spin of a dilute atomic ensemble by cavity feedback. *Phys. Rev. A*, 81:021804, Feb 2010.

[73] Ian D. Leroux, Monika H. Schleier-Smith, and Vladan Vuletić. Implementation of Cavity Squeezing of a Collective Atomic Spin. *Phys. Rev. Lett.*, 104:073602, Feb 2010.

[74] Krzysztof PawÅowski, JÃ©rÃ´me EstÃ¨ve, Jakob Reichel, and Alice Sinatra. Limits of atomic entanglement by cavity feedback: From weak to strong coupling. *EPL (Europhysics Letters)*, 113(3):34005, 2016.

[75] Ian D. Leroux, Monika H. Schleier-Smith, and Vladan Vuletić. Orientation-Dependent Entanglement Lifetime in a Squeezed Atomic Clock. *Phys. Rev. Lett.*, 104:250801, Jun 2010.

[76] M. Koschorreck, M. Napolitano, B. Dubost, and M. W. Mitchell. Sub-Projection-Noise Sensitivity in Broadband Atomic Magnetometry. *Phys. Rev. Lett.*, 104:093602, Mar 2010.

[77] Anne Louchet-Chauvet, Jürgen Appel, Jelmer J Renema, Daniel Oblak, Niels Kjaergaard, and Eugene S Polzik. Entanglement-assisted atomic clock beyond the projection noise limit. *New Journal of Physics*, 12(6):065032, 2010.

[78] T. Takano, M. Fuyama, R. Namiki, and Y. Takahashi. Spin Squeezing of a Cold Atomic Ensemble with the Nuclear Spin of One-Half. *Phys. Rev. Lett.*, 102:033601, Jan 2009.

[79] Zilong Chen, Justin G. Bohnet, Shannon R. Sankar, Jiayan Dai, and James K. Thompson. Conditional Spin Squeezing of a Large Ensemble via the Vacuum Rabi Splitting. *Phys. Rev. Lett.*, 106:133601, Mar 2011.

[80] J. G. Bohnet, K. C. Cox, M. A. Norcia, J. M. Weiner, Z. Chen, and J. K. Thompson. Reduced spin measurement back-action for a phase sensitivity ten times beyond the standard quantum limit. 8:731 EP –, Jul 2014. Article.

[81] Kevin C. Cox, Graham P. Greve, Baochen Wu, and James K. Thompson. Spatially homogeneous entanglement for matter-wave interferometry created with time-averaged measurements. *Phys. Rev. A*, 94:061601, Dec 2016.

[82] S. L. Campbell, R. B. Hutson, G. E. Marti, A. Goban, N. Darkwah Oppong, R. L. McNally, L. Sonderhouse, J. M. Robinson, W. Zhang, B. J. Bloom, and J. Ye. A Fermi-degenerate three-dimensional optical lattice clock. *Science*, 358(6359):90–94, 2017.

[83] Masami Yasuda, Tetsuo Kishimoto, Masao Takamoto, and Hidetoshi Katori. Photoassociation spectroscopy of ^{88}Sr: Reconstruction of the wave function near the last node. *Phys. Rev. A*, 73:011403, Jan 2006.

[84] R. Drozdowski, M. Ignaciuk, J. Kwela, and J. Heldt. Radiative lifetimes of the lowest $^3P^1$ metastable states of Ca and Sr. *Zeitschrift fur Physik D Atoms Molecules Clusters*, 41:125, 1997.

[85] Hidetoshi Katori, Tetsuya Ido, Yoshitomo Isoya, and Makoto Kuwata-Gonokami. Magneto-Optical Trapping and Cooling of Strontium Atoms down to the Photon Recoil Temperature. *Phys. Rev. Lett.*, 82:1116–1119, Feb 1999.

[86] Kurt R. Vogel, Timothy P. Dinneen, Alan Gallagher, and John L. Hall. Narrow-Line Doppler Cooling of Strontium to the Recoil Limit. *IEEE Transactions on Instrumentation and Measurement*, 48:618–621, Apr 1999.

[87] Simon Stellmer, Benjamin Pasquiou, Rudolf Grimm, and Florian Schreck. Laser Cooling to Quantum Degeneracy. *Phys. Rev. Lett.*, 110:263003, Jun 2013.

[88] Robin Santra, Kevin V. Christ, and Chris H. Greene. Properties of metastable alkaline-earth-metal atoms calculated using an accurate effective core potential. *Phys. Rev. A*, 69:042510, Apr 2004.

[89] Masami Yasuda and Hidetoshi Katori. Lifetime Measurement of the $^3P_2$ Metastable State of Strontium Atoms. *Phys. Rev. Lett.*, 92:153004, Apr 2004.

[90] G. Ferrari, N. Poli, F. Sorrentino, and G. M. Tino. Long-Lived Bloch Oscillations with Bosonic Sr Atoms and Application to Gravity Measurement at the Micrometer Scale. *Phys. Rev. Lett.*, 97:060402, Aug 2006.

[91] N. Poli, F.-Y. Wang, M. G. Tarallo, A. Alberti, M. Prevedelli, and G. M. Tino. Precision Measurement of Gravity with Cold Atoms in an Optical Lattice and Comparison with a Classical Gravimeter. *Phys. Rev. Lett.*, 106:038501, Jan 2011.

[92] Harold J. Metcalf and Peter van der Straten. *Laser Cooling and Trapping*. Springer, 1999.

[93] L. Hu, N. Poli, L. Salvi, and G. M. Tino. Atom interferometry with the Sr optical clock transition. *ArXiv e-prints*, August 2017.

[94] Kathryn Moler, David S. Weiss, Mark Kasevich, and Steven Chu. Theoretical analysis of velocity-selective Raman transitions. *Phys. Rev. A*, 45:342–348, Jan 1992.

[95] W. H. Bragg and W. L. Bragg. The Reflection of X-rays by Crystals. *Proceedings of the Royal Society of London A: Mathematical, Physical and Engineering Sciences*, 88(605):428–438, 1913.

[96] V. P. Chebotayev, B. Ya. Dubetsky, A. P. Kasantsev, and V. P. Yakovlev. Interference of atoms in separated optical fields. *J. Opt. Soc. Am. B*, 2(11):1791–1798, Nov 1985.

[97] Peter J. Martin, Bruce G. Oldaker, Andrew H. Miklich, and David E. Pritchard. Bragg scattering of atoms from a standing light wave. *Phys. Rev. Lett.*, 60:515–518, Feb 1988.

[98] David M. Giltner, Roger W. McGowan, and Siu Au Lee. Theoretical and experimental study of the Bragg scattering of atoms from a standing light wave. *Phys. Rev. A*, 52:3966–3972, Nov 1995.

[99] Holger Müller, Sheng-wey Chiow, Quan Long, Sven Herrmann, and Steven Chu. Atom Interferometry with up to 24-Photon-Momentum-Transfer Beam Splitters. *Phys. Rev. Lett.*, 100:180405, May 2008.

[100] T. Kovachy, P. Asenbaum, C. Overstreet, C. A. Donnelly, S. M. Dickerson, A. Sugarbaker, J. M. Hogan, and M. A. Kasevich. Quantum superposition at the half-metre scale. *Nature*, 528(7583):530–533, Dec 2015.

[101] E. Giese, A. Friedrich, S. Abend, E. M. Rasel, and W. P. Schleich. Light shifts in atomic Bragg diffraction. *Phys. Rev. A*, 94:063619, Dec 2016.

[102] Tim Kovachy, Sheng-wey Chiow, and Mark A. Kasevich. Adiabatic-rapid-passage multiphoton Bragg atom optics. *Phys. Rev. A*, 86:011606, Jul 2012.

[103] Holger Müller, Sheng-wey Chiow, and Steven Chu. Atom-wave diffraction between the Raman-Nath and the Bragg regime: Effective Rabi frequency, losses, and phase shifts. *Phys. Rev. A*, 77:023609, Feb 2008.

[104] E. M. Wright and P. Meystre. Theory of an atomic interferometer in the Raman-Nath regime. *Optics Communications*, 75:388–396, March 1990.

[105] Bruce W. Shore. *The Theory of Coherent Atomic Excitation, Multilevel Atoms and Incoherence*. Wiley, Feb 1990.

[106] S S Szigeti, J E Debs, J J Hope, N P Robins, and J D Close. Why momentum width matters for atom interferometry with Bragg pulses. *New Journal of Physics*, 14(2):023009, 2012.

[107] T. Mazzoni, X. Zhang, R. Del Aguila, L. Salvi, N. Poli, and G. M. Tino. Large-momentum-transfer Bragg interferometer with strontium atoms. *Phys. Rev. A*, 92:053619, Nov 2015.

[108] Tommaso Mazzoni. *Atom Interferometry with fermionic and bosonic isotopes of strontium for precision gravity measurement and test of the Equivalence Principle*. PhD thesis, Università degli Studi di Firenze, 2015.

[109] R. P. Del Aguila, T. Mazzoni, L. Hu, L. Salvi, G. M. Tino, and N. Poli. Bragg gravity-gradiometer using the $^1S_0$-$^3P_1$ intercombination transition of ^{88}Sr. 2017. Submitted to New J. Phys.

[110] Ruben Pablo del Aguila. *Bragg interferometry with ultracold strontium for gravity measurements*. PhD thesis, Università degli Studi di Firenze, 2017.

[111] Albert Roura, Wolfgang Zeller, and Wolfgang P Schleich. Overcoming loss of contrast in atom interferometry due to gravity gradients. *New Journal of Physics*, 16(12):123012, 2014.

[112] B. H. Bransden and C. J. Joachain. *Physics of Atoms and Molecules*. Prentice Hall, 2003.

[113] E. Clementi, D. L. Raimondi, and W. P. Reinhardt. Atomic Screening Constants from SCF Functions. II. Atoms with 37 to 86 Electrons. *The Journal of Chemical Physics*, 47(4):1300–1307, 1967.

[114] M. Safronova, Private communication.

[115] L. Salvi, N. Poli, V. Vuletic, and G. M. Tino. Squeezing on momentum states for atom interferometry. *ArXiv e-prints*, August 2017. Submitted to Physical Review Letters.

[116] C. W. Gardiner and M. J. Collett. Input and output in damped quantum systems: Quantum stochastic differential equations and the master equation. *Phys. Rev. A*, 31:3761–3774, Jun 1985.

[117] Crispin Gardiner and Peter Zoller. *Quantum Noise*. Springer, 2004.

[118] Rodney Loudon. *The Quantum Theory of Light*. Clarendon Press, Oxford, 1973.

[119] V. Weisskopf and E Wigner. Berechnung der naturlichen Linienbreite auf Grund der Diracschen Lichtteorie. *Zeit. f. Phys*, 63:54, 1930.

[120] G. S. Agarwal. Vacuum-Field Rabi Splittings in Microwave Absorption by Rydberg Atoms in a Cavity. *Phys. Rev. Lett.*, 53:1732–1734, Oct 1984.

[121] Yifu Zhu, Daniel J. Gauthier, S. E. Morin, Qilin Wu, H. J. Carmichael, and T. W. Mossberg. Vacuum Rabi splitting as a feature of linear-dispersion theory: Analysis and experimental observations. *Phys. Rev. Lett.*, 64:2499–2502, May 1990.

[122] P. M. Alsing, D. A. Cardimona, and H. J. Carmichael. Suppression of fluorescence in a lossless cavity. *Phys. Rev. A*, 45:1793–1803, Feb 1992.

[123] G. Ferrari, P. Cancio, R. Drullinger, G. Giusfredi, N. Poli, M. Prevedelli, C. Toninelli, and G. M. Tino. Precision Frequency Measurement of Visible Intercombination Lines of Strontium. *Phys. Rev. Lett.*, 91:243002, Dec 2003.

[124] R. W. P. Drever, J. L. Hall, F. V. Kowalski, J. Hough, G. M. Ford, A. J. Munley, and H. Ward. Laser phase and frequency stabilization using an optical resonator. *Applied Physics B*, 31(2):97–105, Jun 1983.

[125] Zilong Chen, Justin G. Bohnet, Joshua M. Weiner, Kevin C. Cox, and James K. Thompson. Cavity-aided nondemolition measurements for atom counting and spin squeezing. *Phys. Rev. A*, 89:043837, Apr 2014.

[126] Jiazhong Hu, Wenlan Chen, Zachary Vendeiro, Hao Zhang, and Vladan Vuletić. Entangled collective-spin states of atomic ensembles under nonuniform atom-light interaction. *Phys. Rev. A*, 92:063816, Dec 2015.

[127] Stephen E. Harris. Electromagnetically Induced Transparency. *Physics Today*, 50:36–42, 1997.

[128] S. E. Harris. Lasers without inversion: Interference of lifetime-broadened resonances. *Phys. Rev. Lett.*, 62:1033–1036, Feb 1989.

[129] G. Müller, M. Müller, A. Wicht, R.-H. Rinkleff, and K. Danzmann. Optical resonator with steep internal dispersion. *Phys. Rev. A*, 56:2385–2389, Sep 1997.

[130] Gessler Hernandez, Jiepeng Zhang, and Yifu Zhu. Vacuum Rabi splitting and intracavity dark state in a cavity-atom system. *Phys. Rev. A*, 76:053814, Nov 2007.

[131] Haibin Wu, J. Gea-Banacloche, and Min Xiao. Observation of Intracavity Electromagnetically Induced Transparency and Polariton Resonances in a Doppler-Broadened Medium. *Phys. Rev. Lett.*, 100:173602, May 2008.

[132] Tobias Kampschulte, Wolfgang Alt, Stefan Brakhane, Martin Eckstein, René Reimann, Artur Widera, and Dieter Meschede. Optical Control of the Refractive Index of a Single Atom. *Phys. Rev. Lett.*, 105:153603, Oct 2010.

[133] We thank James K. Thompson for pointing out that our proposed EIT scheme can be extended to a broader class of atomic transitions than we originally thought.

[134] Peter W. Graham, Jason M. Hogan, Mark A. Kasevich, and Surjeet Rajendran. New Method for Gravitational Wave Detection with Atomic Sensors. *Phys. Rev. Lett.*, 110:171102, Apr 2013.

[135] H. Kogelnik and T. Li. Laser Beams and Resonators. *Appl. Opt.*, 5(10):1550–1567, Oct 1966.

[136] A. E. Siegman. *Lasers*. University Science Books, 1986.

[137] Henning Carstens, Simon Holzberger, Jan Kaster, Johannes Weitenberg, Volodymyr Pervak, Alexander Apolonski, Ernst Fill, Ferenc Krausz, and Ioachim Pupeza. Large-mode enhancement cavities. *Opt. Express*, 21(9):11606–11617, May 2013.

[138] A Gerrard and J. M. Burch. *Introduction to Matrix Methods in Optics*. Wiley, 1975.

[139] A. Murari and A. Barzon. Ultra High Vacuum Properties of Some Engineering Polymers. *IEEE Transactions on Dielectrics and Electrical Insulation*, 11(4), August 2004.

[140] Yosuke Shimada, Yuko Chida, Nozomi Ohtsubo, Takatoshi Aoki, Makoto Takeuchi, Takahiro Kuga, and Yoshio Torii. A simplified 461-nm laser system using blue laser diodes and a hollow cathode lamp for laser cooling of Sr. *Review of Scientific Instruments*, 84(6):063101, 2013.

[141] Nicola Poli. *Raffreddamento ed intrappolamento di atomi di stronzio: verso un nuovo standard di frequenza nella regione ottica*. PhD thesis, Università degli Studi di Firenze, 2005.

[142] Kristan L. Corwin, Zheng-Tian Lu, Carter F. Hand, Ryan J. Epstein, and Carl E. Wieman. Frequency-stabilized diode laser with the Zeeman shift in an atomic vapor. *Appl. Opt.*, 37(15):3295–3298, May 1998.